

Electronic Thesis and Dissertation Repository

8-16-2013 12:00 AM

Electrochemiluminescence of Thienyltriazoles, Iridium Complexes, Au₂₅ Clusters and PbS Nanoparticles

Kalen N. Swanick
The University of Western Ontario

Supervisor
Zhifeng Ding
The University of Western Ontario

Graduate Program in Chemistry
A thesis submitted in partial fulfillment of the requirements for the degree in Doctor of Philosophy
© Kalen N. Swanick 2013

Follow this and additional works at: <https://ir.lib.uwo.ca/etd>

 Part of the [Analytical Chemistry Commons](#)

Recommended Citation

Swanick, Kalen N., "Electrochemiluminescence of Thienyltriazoles, Iridium Complexes, Au₂₅ Clusters and PbS Nanoparticles" (2013). *Electronic Thesis and Dissertation Repository*. 1539.
<https://ir.lib.uwo.ca/etd/1539>

This Dissertation/Thesis is brought to you for free and open access by Scholarship@Western. It has been accepted for inclusion in Electronic Thesis and Dissertation Repository by an authorized administrator of Scholarship@Western. For more information, please contact wlsadmin@uwo.ca.

Electrochemiluminescence of Thienyltriazoles, Iridium Complexes, Au₂₅ Clusters
and PbS Nanoparticles

(Thesis format: Integrated Article)

by

Kalen N. Swanick

Graduate Program in Chemistry

A thesis submitted in partial fulfillment
of the requirements for the degree of
Doctor of Philosophy

The School of Graduate and Postdoctoral Studies
The University of Western Ontario
London, Ontario, Canada

© Kalen N. Swanick 2013

Abstract

Electrogenerated chemiluminescence or electrochemiluminescence (ECL), produces light in the vicinity of a working electrode by the excited species of a luminophore formed via electron transfer between radical cations and anions, which are electrogenerated. In order for the ECL system to be efficient, the radicals must be stable in solution. This can be enhanced by adding co-reactants such as benzoyl peroxide (BPO) and tri-*n*-propylamine (TPrA) that produce strong oxidizing or reducing radicals upon redox reactions. ECL pairs electrochemical and spectroscopic methods and is a powerful analytical technique that is highly sensitive and selective.

A comprehensive, mechanistic study of ECL generation *via* annihilation and co-reactant paths has been completed for modified deoxycytidine (dC) nucleosides, thienyltriazole ligands, metal complexes containing iridium(III) and ruthenium(II), Au₂₅ clusters, and boron-dipyrromethene (BDY) capped PbS nanoparticles (NPs). Spooling ECL spectroscopy was developed during this thesis work, and was used to future understand sophisticated mechanisms for ECL generation, tuning and controlling.

Specifically, the electrochemistry and spectroscopy of four modified dC nucleosides were studied to correlate their electronic structures with blue ECL. Four thienyltriazole ligands were synthesized and their electrochemical properties were analyzed and relative efficiencies determined. Eight iridium(III) complexes, four containing aryltriazole cyclometalated ligands, were found to show bright ECL while three iridium(III) complexes containing two dimethylamino substituents on the 2,2'-bipyridine ligand displayed self-enhancing ECL intensity up to 16 times with multiple excited states for light emission. A soft salt containing Ir(III) Ru(II) Ir(III) complexes demonstrated electronic communication between the [Ru]²⁺ and [Ir]⁻ moieties thus reducing the energy required to produce ECL. Au₂₅ clusters were discovered to emit in the near-infrared (NIR) region in both annihilation and co-reactant paths. Co-reactant BPO resulted in multiple strong excited states and the ECL mechanisms were elucidated using our newly developed spooling ECL spectroscopy. And lastly, BDY-capped PbS NPs were investigated in the generation of both visible and NIR ECL via annihilation and co-reactant routes.

Keywords

electrogenerated chemiluminescence • electrochemiluminescence • electrochemistry • photoluminescence • spooling ECL spectroscopy • electronic structures • ECL efficiency • deoxycytidine • thienyltriazoles • iridium complexes • Au₂₅ clusters • BODIPY capped PbS nanoparticles

Co-Authorship Statement

This thesis includes material from five previously published manuscripts presented in Chapters 2, 3, 4.1, 5.2, and 6.1. Also included in this thesis is material from three submitted manuscripts presented in Chapters 4.2, 5.1, and 5.3. And lastly, material from the data of two in-preparation manuscripts in Chapters 6.2 and 7.

The article presented in Chapter 2 was published and co-authored by K. N. Swanick, D. W. Dodd, J. T. Price, A. L. Brazeau, N.D. Jones, R. H. E. Hudson, and Z. Ding (*Phys. Chem. Chem. Phys.* **2011**, *13*, 17405-17412). All of the electrochemistry and ECL work was performed by KNS. X-ray diffraction data was collected and solved by M. Jennings. Theoretical calculations were conducted by ALB. KNS was responsible for writing the manuscript, which was edited and finalized by ZD.

The work described in Chapter 3 was published in an article co-authored by K. N. Swanick, J. T. Price, N.D. Jones, and Z. Ding (*J. Org. Chem.* **2012**, *77*, 5646-5655). All of the syntheses, spectroscopic data, electrochemistry, ECL, and theoretical calculations were performed by KNS. X-ray diffraction data was collected and solved by JTP and A. Borecki. Mass spectrometry data was collected by D. Hairsine. The experimental work and spectroscopic data were completed under the supervision of NDJ, and later taken over by ZD for the electrochemistry, ECL and theoretical calculations. The manuscript was written by KNS, first read by NDJ, then edited and finalized by ZD.

Chapter 4.1 was published in a communication co-authored by K. N. Swanick, S. Ladouceur, E. Zysman-Colman, and Z. Ding (*Chem. Commun.* **2012**, *48*, 3179-3181). All of the ECL work was performed by KNS. The manuscript was written by KNS, edited by EZC and ZD and finalized by ZD.

Chapter 4.2 has been submitted for publication co-authored by K. N. Swanick, S. Ladouceur, E. Zysman-Colman, and Z. Ding (**2013**, submitted). All of the ECL work was performed by KNS. The manuscript was written by KNS, edited by SL, EZC, and ZD, and finalized by ZD.

Chapter 5.1 has been accepted for publication co-authored by S. Ladouceur, K. N. Swanick, S. Gallagher-Duval, Z. Ding, and E. Zysman-Colman (*Eur. J. Inorg. Chem.* **2013**, accepted, DOI: 10.1002/ejic.201300849). All of the CV and ECL work was performed by KNS. The syntheses and spectroscopic data were performed by SL, SGD, A. M. Soliman and M. Sandroni. Theoretical calculations were conducted by EZC. The manuscript was written by SL for the synthesis, KNS for the CV and ECL and EZC for the introduction and edited by SL, EZC, and ZD. Only part of the introduction was included in this chapter, and was written by EZC and edited by ZD. All of the CV and ECL work was included in Chapter 5.1, and was written by KNS.

The material presented in Chapter 5.2 was published in a communication co-authored by K. N. Swanick, S. Ladouceur, E. Zysman-Colman, and Z. Ding (*Angew. Chem. Int. Ed.* **2012**, *51*, 11079-11082). All of the CV and ECL work was performed by KNS. The manuscript was written by KNS, with introduction contributions from EZC and ZD, edited by SL, EZC, and ZD, and finalized by ZD.

Chapter 5.3 has been submitted for publication co-authored by K. N. Swanick, M. Sandroni, Z. Ding, and E. Zysman-Colman (**2013**, submitted). All of the CV and ECL work was performed by KNS. The manuscript was written by KNS, with introduction contributions from EZC and ZD, edited by MS, EZC, and ZD, and finalized by ZD.

The work described in Chapter 6.1 was published in a communication co-authored by K. N. Swanick, M. Hesari, M. S. Workentin, and Z. Ding (*J. Am. Chem. Soc.* **2012**, *134*, 15205-15208). The synthesis and UV-vis spectroscopic data were done by MH. The visible and NIR PL spectroscopic data were performed by KNS and MH. All of the CV and ECL work was performed by KNS. The manuscript was written by KNS, edited by MS, MSW, and ZD, and finalized by ZD.

The manuscript for Chapter 6.2 is currently in preparation and co-authored by M. Hesari, K. N. Swanick, M. S. Workentin, and Z. Ding. The annihilation CV and ECL were done by KNS and MH. All of the CV and ECL work using BPO as the co-reactant was performed by KNS. This portion of the chapter was edited by ZD.

The manuscript for Chapter 7 is currently in preparation and co-authored by K. N. Swanick, J.-S. Lu, S. Wang, and Z. Ding. All of the CV and ECL work was performed by KNS. This chapter was edited by ZD.

Acknowledgments

I would like to first thank my supervisor, Dr. Zhifeng Ding for encouraging me to pursue a Ph.D. in chemistry at Western. As I reflect on my path towards achieving this degree, I have been fortunate to work in a variety of disciplines of chemistry within the Chemistry Department, with many professors and graduate students. Back in 2007, I enrolled in the undergraduate chemistry thesis project working with Dr. Nathan D. Jones and Dr. Robert H. E. Hudson, synthesizing modified deoxycytidine nucleosides, along with former graduate students Dr. David W. Dodd, and Dr. Jacquelyn T. Price. This project sparked my interest in research and I was given the opportunity to continue my research with Dr. Jones as a master's candidate in 2008. Dr. Jones' enthusiasm for chemistry helped motivate me and challenged my skills in research. He would come into the lab every day saying "it's a great day for chemistry." The Jones group family created a positive and fun environment that every graduate student should experience. I thank all my Jones group members for two fun years together. When Dr. Jones resigned the following year, Dr. Ding asked me to consider continuing my studies and transfer into the Ph.D. program. After giving it much thought, I decided it was a great chance to explore electrochemistry and analytical techniques, a big shift from synthesis. Thankfully the transition from synthesis to analysis was smooth and I joined a great lab that has been supportive and motivating for the past four years. I have appreciated the opportunities Dr. Ding has given me to present my research in Canada and internationally. I have enjoyed our discussions and ideas to develop new techniques in the field of ECL. I would like to thank all Ding group members, past and present, for being great friends, for listening to countless presentations, and for creating a fun working environment.

Thank you to all staff members of the Chemistry department, especially to Yves Rambour for making all of our electrochemical cells and working electrodes, and to the electronic shop, John Vanstone and Jon Aukema for assembling all of the parts to my electrochemical cells, for fixing our instruments, and for building pieces for the instruments that I have used.

I would like to thank my committee members, Dr. Wujian Miao, Dr. Paul Charpentier, Dr. Styliani Conostas, and Dr. Yining Huang, for reading my thesis, attending my defense, and for their valuable feedback.

I have been very fortunate to collaborate with many research groups from Western and from other universities in Canada and China. I'd like to start by thanking Dr. Robert H. E. Hudson at Western, Dr. Brian L. Pagenkopf at Western, Dr. Mark S. Workentin at Western, Dr. Jonathan Veinot at the University of Alberta, Dr. Suning Wang at Queen's University, Dr. Yi-Tao Long at East China University of Science and Technology, and Eli Zysman-Colman at L'Université de Sherbrooke. I'd like to thank the following graduate students who have helped contribute to our publications, to Dr. David W. Dodd, Dr. Jacquelyn T. Price, Dr. Allison L. Brazeau, Mr. Sébastien Ladouceur, Mr. Mahdi Hesari, Mr. Shawn Gallagher-Duval, Dr. Martina Sandroni, Dr. Mahmoud Moustafa, Ms. Leah Coumont, and Mr. Jia-shen Lu. I'd like to thank Dr. Paul J. Ragogna at Western for letting me use his glove box to prepare all samples for ECL studies and to Dr. Robert H. E. Hudson for use of his UV-Visible spectrometer and fluorimeter. I would also like to take the time and thank Dr. Martin J. Stillman for giving me the opportunity to help organize and run two conferences up north in Parry Sound, ON. I had a great time at the 3rd and 4th Georgian Bay International Conference on Bioinorganic Chemistry (CanBIC) at the Charles W. Stockey Centre. Thank you to Western University and NSERC for funding.

I'd like to thank my friends and former roommates who have been supportive and have taken the time to drive up to London for visits. It has been a long ten years at Western, however, I have created so many lasting friendships at the university and am thankful to my friends who I have known since junior high and high school. To my forever "roomies" Mandy and Ling, I'm so grateful to have such amazing friends that would memorize the periodic table with me on the bus (Mandy) just so I could ace my test, would cook amazing dinners together, go to Florida, and so instrumental helping out at my wedding.

Thank you to my mom, Gail Oikawa, and dad, Brent Swanick, for being amazing parents, for always supporting me, for allowing me to achieve all of my passions and goals in life, and for believing there is no end to education. To my sister Mariko, thank you for being a great sister, for travelling to the conference with me in Europe, and for looking after the

puppies, Bella and Cail, when I had work to complete or needed a vacation! I would like to thank my in-laws, Polly and Bob McDonald, for welcoming me into their home and for countless dinners, vacations at the cottage and out west, and for their son, my husband Brad. I am so lucky to have such a large extended family with my sister-in-laws Mary and Jessica and brother-in-laws Mike and Jeff. Being away from home for the past ten years has been hard at times, missing my loving grandparents, Nana and Papa, Margaret Oikawa and Mack Oikawa, my aunts, uncles, and cousins. I cherish the times we are able to get together, and I am looking forward to spending more time with everyone. I would like to dedicate this thesis to my Baba, Mary Swanick, who recently passed away in July, a great supporter of my graduate studies, and to my Grandad, Robert Swanick, who is also in heaven, but would have been so proud to have his granddaughter receive a Ph.D. in Chemistry.

Always wanting to own a dog, then having Bella, my charismatic 5 year old dog, forever changed my life. I met my husband, Brad, at puppy class when we both enrolled our dogs, Bella and Cail, because we were first time dog owners. I thank Cail and Bella for changing my life for the better and uniting Brad and I.

Finally, I would like to thank my husband Brad McDonald. You are my everything, and I appreciate all the things you have done for me to help me make it through my degree and in life. Thank you for being so patient, it seems like this Ph.D. has taken forever to achieve, however, I have always had you to come home to after work and have always had you to cheer me up and remind me to relax and enjoy life. I love you with all my heart, now and forever. I would also like to thank our little baby on the way that has been patiently waiting to enter this world. You have been such a good baby, not giving me any morning sickness or nausea, staying up late with me working on my manuscripts and thesis, and for staying inside until your due date, after my defense, in September. I am looking forward to the next chapter in my life, being a mom. Brad and I love you so much already and we look forward to meeting you soon.

Table of Contents

Abstract	ii
Co-Authorship Statement.....	iv
Acknowledgments.....	vii
Table of Contents	x
List of Tables	xiv
List of Figures	xv
List of Schemes.....	xxii
List of Appendices	xxiii
List of Abbreviations and Symbols.....	xxiv
Chapter 1	1
1 Fundamentals of Electrogenerated Chemiluminescence (ECL)	1
1.1 Introduction.....	1
1.2 Ion Annihilation Pathway	1
1.3 Co-reactant Pathway	5
1.4 ECL Instrumentation.....	7
1.5 Scope of Thesis	10
1.6 References.....	11
Chapter 2.....	13
2 Electrogenerated Chemluminescence of Triazole-Modified Deoxycytidine Analogues in N,N-Dimethylformamide.....	13
2.1 Introduction.....	13
2.2 Experimental Section	16
2.3 Results and Discussion	20
2.3.1 Electrochemistry and its Correlation to Electronic Structures.....	20

2.3.2	ECL via Annihilation Mechanisms.....	26
2.3.3	ECL via Co-reactant Mechanisms	28
2.3.4	ECL Spectroscopy	31
2.4	Conclusions.....	33
2.5	References.....	34
Chapter 3.....		37
3	Synthesis, Structure, Electrochemistry, and Electrochemiluminescence of Thienyltriazoles.....	37
3.1	Introduction.....	37
3.2	Experimental Section	38
3.3	Results and Discussion	44
3.4	Conclusions.....	60
3.5	References.....	61
Chapter 4.....		64
4	Electrochemiluminescence of Iridium(III) Complexes.....	64
4.1	Bright Electrochemiluminescence of Iridium(III) Complexes	64
4.1.1	Introduction.....	64
4.1.2	Experimental Section	65
4.1.3	Results and Discussion	67
4.1.4	Conclusions.....	73
4.1.5	References.....	74
4.2	Correlating Electronic Structures to Electrochemiluminescence of Cationic Ir Complexes.....	76
4.2.1	Introduction.....	76
4.2.2	Experimental Section	77
4.2.3	Results and Discussion	78
4.2.4	Conclusions.....	84

4.2.5	References.....	84
Chapter 5.....		87
5	Mechanistic Insight into Electrochemiluminescence of Iridium(III) Complexes via Spooling Spectroscopy.....	87
5.1	Strongly Blue Luminescent Cationic Iridium(III) Complexes with an Electron-Rich Ancillary Ligand: Evaluation of Their Optoelectronic and Electrochemiluminescence Properties	87
5.1.1	Introduction.....	87
5.1.2	Experimental Section.....	89
5.1.3	Results and Discussion	92
5.1.4	Conclusions.....	100
5.1.5	References.....	101
5.2	Self-Enhanced Electrochemiluminescence of an Iridium(III) Complex: Mechanistic Insight.....	105
5.2.1	Introduction.....	105
5.2.2	Experimental Section.....	106
5.2.3	Results and Discussion	108
5.2.4	Conclusions.....	114
5.2.5	References.....	115
5.3	Electrochemiluminescence of Heterometallic Ruthenium(II)-Iridium(III) Soft Salts.....	118
5.3.1	Introduction.....	118
5.3.2	Experimental Section.....	119
5.3.3	Results and Discussion	122
5.3.4	Conclusions.....	131
5.3.5	References.....	131
Chapter 6.....		134
6	Sensitive Detection of Au ₂₅ Clusters by Electrochemiluminescence	134

6.1 Interrogating Near-Infrared Electrogenerated Chemiluminescence of Au ₂₅ (SC ₂ H ₄ Ph) ₁₈ ⁺ Clusters	134
6.1.1 Introduction.....	134
6.1.2 Experimental Section	135
6.1.3 Results and Discussion	137
6.1.4 Conclusions.....	144
6.1.5 References.....	144
6.2 Spooling ECL Spectroscopy of Au ₂₅ L ₁₈ ⁰ in the presence of BPO.....	148
6.2.1 Introduction.....	148
6.2.2 Experimental Section	148
6.2.3 Results and Discussion	150
6.2.4 Conclusions.....	157
6.2.5 References.....	158
Chapter 7.....	159
7 Dual Electrochemiluminescence of BDY-PbS Nanoparticles	159
7.1 Introduction.....	159
7.2 Experimental Section	160
7.3 Results and Discussion	162
7.4 Conclusions.....	172
7.5 References.....	172
Chapter 8.....	174
8 Concluding Remarks and Future Work	174
Appendices.....	176
Curriculum Vitae	266

List of Tables

Table 2.1. Electrochemical (from DPV) and quantum chemistry calculation data of compounds 2.1-1.4.....	25
Table 2.2. ECL data of compounds 2.1-2.4 in annihilation and co-reactant systems.....	28
Table 3.1. Redox Peak Potentials and Energy Levels of HOMOs and LUMOs.	49
Table 3.2. Absorption and Photoluminescence Spectroscopic Data of 3.1-3.4.....	51
Table 3.3. ECL Spectroscopic Data of 3.1-3.4.	55
Table 4.1. ECL efficiencies from annihilation and co-reactant studies and their corresponding ECL spectra.....	69
Table 5.1. Electrochemical and ECL data for 5.1-5.6.	93

List of Figures

Figure 1.1. Structure of 9,10-diphenylanthracene, DPA.	3
Figure 1.2. Structure of tris(2,2'-bipyridine)ruthenium(II), [Ru(bpy) ₃] ²⁺	4
Figure 1.3. Structure of benzoyl peroxide, BPO.....	5
Figure 1.4. Structure of tri- <i>n</i> -propyl amine, TPrA.....	6
Figure 1.5. CV or ECL setup for experiment with the electrochemical cell placed in the PMT detector, a sample CV (in red) with ECL-voltage curve (in green) is shown on the computer screen.	8
Figure 1.6. ECL spectrum or spooling setup, with the electrochemical cell in the spectrometer with the visible or NIR CCD camera, a sample ECL spooling spectra is shown on the computer screen.	10
Figure 2.1. Cyclic voltammograms of 2.1 (solid lines) in DMF containing 0.1 M TBAP as supporting electrolyte, and blank solution (dotted lines), with the initial scan from 0.000 to 2.169 V (anodic scan), and initial scan from 0.000 to -1.889 V (cathodic scan), with a scan rate of 0.1 V/s.....	20
Figure 2.2. Ball-and-stick representation of 2.1. Except for OH and NH ₂ protons, H-atoms are omitted for clarity. Carbon atoms are in grey, sulfur in yellow, nitrogen in blue, and oxygen in red. The final solution was submitted to the IUCR CIF checking program and had some Alert level A's or B's associated with the lack of complete data, however the general structure can be observed for 2.1.	21
Figure 2.3. Differential pulse voltammograms of 2.1 (solid lines) in DMF containing 0.1 M TBAP as supporting electrolyte, and blank solution (dotted lines), with the initial scan from 0.000 to 2.118 V (top, anodic scan), and initial scan from 0.000 to -1.929 V (bottom, cathodic scan) and their reverse scans.	22

Figure 2.4. Cyclic voltammogram (red) and ECL-voltage curve (green) of 2.1 scanned at 0.1 V/s with the initial potential at 0.000 to 2.069 V then scanned to -1.889 V and back to 0.000 V.....	23
Figure 2.5. Cyclic voltammogram (red) and ECL-voltage curve (green) of 2.1 with 5.0×10^{-3} M BPO scanned at 0.1 V/s, with the initial scan from 0.000 to -2.278 V and back to 0.000 V.	29
Figure 2.6. ECL spectra of 2.1-2.4 in DMF containing 5.0×10^{-3} M BPO and 0.1 M TBAP as supporting electrolyte and pulsing between potential ranges from (a) 0.000 to -2.278 V, t = 60 s for 2.1, (b) 0.000 to -2.452 V, t = 60 s for 2.2, (c) 0.000 to -2.517 V, t = 60 s for 2.3, and (d) 0.000 to -2.126 V, t = 60 s for 2.4. ECL intensities were normalized by their respective peak heights.	31
Figure 3.1. ORTEP representations of (a) 3.1, (b) 3.2, (c) 3.4 (30% probability ellipsoids, H-atoms removed for clarity, expect -OH protons) with rings approximately parallel to the page.	46
Figure 3.2. Cyclic voltammogram (red) and electrochemiluminescence-voltage curve (green) of 3.1 with a scan rate of 0.1 V/s and a potential range between 2.740 and -2.358 V.....	47
Figure 3.3. Differential pulse voltammogram and representations of the calculated HOMO and LUMO of (a) BiTTM (3.1) from 2.810 to -2.289 V, (b) TTM (3.2) from 2.683 to -1.976 V, (c) BiTTP (3.3) from 2.626 to -2.174 V, and (d) TTP (3.4) from 1.975 to -1.772 V, in ACN containing 0.1 M TBAP as supporting electrolyte with a scan rate of 0.1 V/s. Gaussian-09 (B3LYP/6-31+G*) was used for calculations of 3.1-3.4 in Hartree/Particle at T=289.15 K, P = 1 Atm.	50
Figure 3.4. Cyclic voltammogram (red) and ECL-voltage curve (green) of (a) BiTTM (3.1) from 0.000 to -1.989 V, (b) TTM (3.2) from 0.000 to -2.145 V, (c) BiTTP (3.3) from and 0.000 to -2.074 V, and (d) TTP (3.4) from 0.000 to -2.021 V, in ACN containing 5.0×10^{-3} M BPO and 0.1 M TBAP as supporting electrolyte with a scan rate of 0.1 V/s.	57
Figure 3.5. ECL spectra of 3.1-3.4 in ACN containing 5.0×10^{-3} M BPO and 0.1 M TBAP as supporting electrolyte, pulsing for t = 60 s between potential ranges from (a) 0.000 to -1.989	

V for 3.1, (b) 0.000 to -2.145 V for 3.2, (c) 0.000 to -2.074V for 3.3, and (d) 0.000 to -2.021 V for 3.4. ECL intensities were normalized by their respective peak heights.....	58
Figure 4.1. Cyclic voltammograms (dotted lines) overlaid with the ECL-voltage curves (solid lines) of compounds a) 4.1, b) 4.2, c) 4.3, and d) 4.4, in the annihilation path.	68
Figure 4.2. Normalized ECL spectra of a) 4.1, b) 4.2, c) 4.3, and d) 4.4, <i>via</i> annihilation (solid line) and co-reactant (dotted line) paths.	71
Figure 4.3. Cyclic voltammograms obtained in ACN with overlaid ECL-voltage curves for a) 4.5, b) 4.6, c) 4.7, and d) 4.8. The scan rate was at 0.1 V/s.....	78
Figure 4.4. Accumulated ECL spectra of a) 4.5, b) 4.6, c) 4.7, and d) 4.8, during two full cycles of the potential scanning, respectively. The scan rate was at 0.1 V/s.....	80
Figure 4.5. a) Voltage pulsing between -1.92 V and 1.56 V (blue) applied to the working electrode immersed in a solution of 4.5, corresponding current (red) and photocurrent (green), b) ECL spectrum after the pulsing process as in a), for 30 s (purple), curve-fit wave (black), and the average fitted spectrum (blue).	82
Figure 4.6. Spooling spectra of 4.8, acquired during a voltage scan between -1.73 V and 1.84 V at scan rate of 0.1 V/s for 130 s. Insets illustrate ECL evolution (blue) and devolution (black).	83
Figure 5.1. CVs (red) with ECL-voltage curves (green) overlaid of a) 5.1, b) 5.2, c) 5.3, d) 5.4, e) 5.5, and f) 5.6, first oxidation and reduction potential profile with a scan rate of 0.1 V/s.	92
Figure 5.2. a) CV of 5.4 with ECL-voltage curve overlaid with a potential profile ranging between -2.34 to 2.44 V, b) ECL spooling spectra of 5.4 during first potential scanning cycle in the range of -2.34 to 2.44 V and at a scan rate of 0.1 V/s (each spectrum was acquired with a time interval of 1 s), showing evolution of three wavelengths: i) initial ECL onset, 535 nm at 1.24 V (pink), ii) 582 nm at 1.94 V (purple), iii) 610 nm at 2.44 V (green), and showing devolution of one wavelength: iv) 610 nm at 2.34 V. The inset displays ECL onset with a peak wavelength of 574 nm at -2.14 V (orange) in the second potential scanning cycle.....	95

Figure 5.3. a) CV of 5.6 with ECL-voltage curve overlaid with a potential profile ranging between -2.00 to 2.30 V, b) ECL spooling spectra of 5.6 during first potential scanning cycle in the range of -2.00 to 2.30 V and at a scan rate of 0.1 V/s (each spectrum was acquired with a time interval of 1 s), showing evolution of four wavelengths: i) initial ECL onset, 528 nm at 1.20 V (orange), ii) 559 nm at 1.80 V (green), iii) 576 nm at 1.90 V (pink), iv) 605 nm at 2.20 V (dark blue), and showing devolution of three wavelength: iv) 605 nm at 2.30 V (light blue), v) 581 nm at 1.90 V (red), and vi) 550 nm at 1.70 V (dark grey). The inset displays ECL onset with a peak wavelength of 505 nm at -1.70 V (purple) in the second potential scanning cycle. 99

Figure 5.4. Cyclic voltammograms (dotted) overlaid with corresponding ECL-voltage curves (solid) in acetonitrile of a) 0.6 mM 5.2 with the applied potential ranges between -2.10 and 1.60 V (red) and between -2.10 to 2.43 V (green) vs. a saturated calomel electrode (SCE), and b), of 0.6 mM 5.7 with the applied potential ranges between -1.80 and 2.60 V (blue) vs. SCE. The scan rate was at 0.1 V/s. The vertical dashed lines show the potentials used for estimation of the ECL efficiencies of 5.2. 110

Figure 5.5. Selected ECL spooling spectra of 0.6 mM 5.2 in acetonitrile when the applied potential was scanned between -2.10 and 2.42 V for two cycles at a scan rate of 0.1 V/s, see Figure S5.3 in Appendix IV for the two complete cycles. Each ECL spectrum was acquired for 1 s and two scanning cycles took 145 s. a) Perspective view from zoomed-in ECL spooling spectra of the 1st cycle of potential scanning. Three emissions from different excited specials are color-coded, with apparent peak positions centered at b) 543 nm (pink), c) 566 nm (purple), and d) 588 nm (green). e) ECL devolution is illustrated by the spectra in (deep blue). Three excited states were deconvoluted to peak wavelengths at 543, 608, and 651 nm, respectively, which were generated in annihilation and co-reactant (the two dma groups on the bpy ligand) paths. 111

Figure 5.6. CVs of a) [Ru]Cl₂ (in black), b) TBA[Ir] (in pink), c) [Ir][Ru][Ir] (in purple), and d) 1:2 [Ru]Cl₂:TBA[Ir] mixture (in blue) in potential ranges between their 1st reduction and 1st oxidation, along with the corresponding ECL-voltage curves in red (a), blue (b), green (c), and orange (d), respectively. Scan rate was at 0.1 V/s. First cycle is shown, and arrows

indicate the scan direction. ECL spectra are displayed for e) [Ru]Cl₂, f) TBA[Ir], g) [Ir][Ru][Ir], and h) 1:2 [Ru]Cl₂:TBA[Ir] mixture..... 123

Figure 5.7. a) CV (in purple) with ECL-voltage curve overlaid (in green) of [Ir][Ru][Ir]; b) CV (in pink) with ECL-voltage curve overlaid (in orange) of 1:2 [Ru]Cl₂:TBA[Ir] mixture solution. Both are shown with an extended potential window. The scan rate was 0.1 V/s. . 125

Figure 5.8. Spooling ECL spectra of [Ir][Ru][Ir] soft salt, first cycle shown, with an extended potential window between 1.43 V and -2.83 V, t = 165 s for two cycles. Left inset shows the onset ECL spectra while the right inset illustrates the fitting of ECL spectra to one peak at 634 nm when the potential was 0.95 V. The applied voltage interval for the ECL spectra is 100 mV..... 127

Figure 5.9. CV (in purple) overlaid with ECL-voltage curve (in green) of [Ir][Ru][Ir] soft salt with 0.02 M TPrA co-reactant, between 0.00 V to 1.52 V, scan rate was 0.1 V/s, first cycle shown. 128

Figure 5.10. ECL spooling spectra of [Ir][Ru][Ir] soft salt with 0.02 M TPrA coreactant between 0.00 V to 1.52 V, applied voltage interval for the ECL spectra is 100 mV. Insets show ECL evolution (in pink) and devolution (in purple)..... 130

Figure 6.1. a) Differential pulse voltammograms of 0.67 mg/mL Au₂₅⁺ clusters in 1:1 benzene:acetonitrile solution, with 0.1 M tetra-*n*-butylammonium perchlorate as supporting electrolyte. b) cyclic voltammogram and ECL-voltage curve for a Au₂₅¹⁺ cluster solution containing with 5 mM benzoyl peroxide. 137

Figure 6.2. a) Spooled ECL spectra of Au₂₅⁺ clusters with BPO during one cycle of the applied potential from 0.04 to -1.86 V then back to 0.04 V. Each spectrum was acquired for 1 s using an iDUS NIR CCD camera cooled to -75 °C. b) A typical accumulated ECL spectrum of the same co-reactant solution collected over 80 s, two cycles of potential scanning between 0.04 to -1.86 V at a scan rate of 0.1 V/s. 141

Figure 6.3. Photoluminescence of a Au₂₅⁻ 1:1 benzene/acetonitrile solution using an iDus 401 CCD camera between 633 and 1200 nm upon excitation at 633 nm..... 142

Figure 6.4. Typical annihilation ECL-voltage curve of 0.1mM Au ₂₅ ⁰ in benzene:acetonitrile mixture containing 0.1 M TBAP, scan rate: 0.1 V/s. Inset: accumulated spectrum, T = 300 s, in the course of ECL experiment recorded with a NIR CCD camera.....	150
Figure 6.5. CV (in red) with ECL voltage-curve (in green) between 0.50 and -1.75 V of Au ₂₅ ⁰ with 0.005 M BPO in ACN:Bz (1:1) with 0.1 M TBAP supporting electrolyte, scan rate of 0.1 V/s.....	152
Figure 6.6. a) ECL spooling of Au ₂₅ ⁰ with 0.005 M BPO in ACN:Bz (1:1) with 0.1 M TBAP supporting electrolyte, scan rate of 0.1 V/s, between 0.50 and -1.75 V for 90 s, spectra at b) - 0.80 V, c) -1.10 V, d) -1.30 V, e) -1.50 V, these spectra were curve-fitted to 871 nm (black) and 960 nm (pink), the average fit is shown in purple.....	153
Figure 6.7. Accumulated spectrum between 0.50 and -1.75 V for 90 s of Au ₂₅ ⁰ with 0.005 M BPO in ACN:Bz (1:1) with 0.1 M TBAP supporting electrolyte, scan rate of 0.1 V/s. Curve-fitted to one peak at 920 nm.....	154
Figure 6.8. CV (in red) with ECL voltage-curve (in green) between 0.57 and -2.08 V of Au ₂₅ ⁰ with 0.050 M BPO in ACN:Bz (1:1) with 0.1 M TBAP supporting electrolyte, scan rate of 0.1 V/s.....	155
Figure 6.9. ECL spooling of Au ₂₅ ⁰ with 0.050 M BPO in ACN:Bz (1:1) with 0.1 M TBAP supporting electrolyte, scan rate of 0.1 V/s, between 0.57 and -2.08 V for 106 s, spectra at b) -0.90 V, c) -1.50 V, d) -1.80 V, e) -2.00 V, these spectra were curve-fitted to 871 nm (black) and 960 nm (pink), the average fit is shown in red.....	156
Figure 6.10. Accumulated spectrum between 0.57 and -2.08 V for 106 s of Au ₂₅ ⁰ with 0.050 M BPO in ACN:Bz (1:1) with 0.1 M TBAP supporting electrolyte, scan rate of 0.1 V/s. Curve-fitted to one peak at 859 nm.....	157
Figure 7.1. CV (in red) with ECL-voltage curve (in green) of BDY-PbS NPs in DCM with TPABF ₆ as supporting electrolyte with a potential range of -1.60 V to 0.74 V, for one complete cycle, at a scan rate of 0.1 V/s.....	162

Figure 7.2. DPV of BDY-PbS NPs in DCM with TPABF ₆ as supporting electrolyte with a potential range of -1.60 V to 0.74 V, forward direction (in blue) and reverse direction (in green).	163
Figure 7.3. Pulsing of BDY-PbS NPs in DCM with TPABF ₆ as supporting electrolyte, current show in red, applied potential shown in blue, and photocurrent shown in green.....	164
Figure 7.4. ECL visible spectrum of BDY-PbS NPs from pulsing between -1.60 V to 0.74 V for 15 s, visible CCD camera cooled to -55 °C, centered at 850 nm, T = 15 s.....	165
Figure 7.5. CV (in red) with ECL-voltage curve (in green) of BDY-PbS NPs in DCM with TPABF ₆ as supporting electrolyte with 0.02 M TPrA, in a potential range of 0.00 V to 1.58 V, for one complete cycle, at a scan rate of 0.1 V/s.	167
Figure 7.6. ECL NIR spectrum of BDY-PbS NPs with 0.02 M TPrA from scanning between 0.00 V to 1.58 V, at a scan rate of 0.1 V/s, NIR CCD camera cooled to -75 °C, centered at 800 nm, T = 82 s.	167
Figure 7.7. ECL NIR spooling of BDY-PbS NPs with 0.02 M TPrA, a) two cycles shown, between 0.00 V to 1.58 V, T = 82 s, at a scan rate of 0.1 V/s, b) evolution of 733 nm and 1028 nm from ECL onset at 0.38 V, first cycle shown, c) increase in 733 nm peak and decrease in 1028 nm peak (the point at which the 1028 nm started to decrease shown in green), first cycle shown.	168
Figure 7.8. CV (in red) with ECL-voltage curve (in green) of OA-PbS NPs in DCM with TPABF ₆ as supporting electrolyte with 0.02 M TPrA, in a potential range of 0.00 V to 1.58 V, for one complete cycle, with a scan rate of 0.1 V/s.	171
Figure 7.9. ECL spectra of OA-PbS NPs with 0.02 M TPrA from scanning between 0.00 V to 1.58 V, at a scan rate of 0.1 V/s, a) accumulated spectrum, b) spooling spectrum side profile, one cycle shown, NIR CCD camera cooled to -75 °C, centered at 800 nm, T = 80 s.	172

List of Schemes

Scheme 1.1. Schematic diagram showing the general principles of ECL with singlet excited state emission, $^1R^*$, where $R = \text{DPA}$	3
Scheme 1.2. Schematic diagram showing the general principles of ECL with triplet excited state emission, $^3R^*$, where $R = [\text{Ru}(\text{bpy})_3]^{2+}$	4
Scheme 2.1. Molecular structures of compounds 2.1-2.4.....	15
Scheme 3.1. General procedure for the synthesis of thienyltriazoles, 3.1 and 3.2, <i>via</i> Cu(I) catalyzed Huisgen 1,3-dipolar cycloaddition.....	45
Scheme 3.2. General procedure for the synthesis of thienyltriazoles, 3.3 and 3.4, <i>via</i> Cu(I) catalyzed Huisgen 1,3-dipolar cycloaddition.....	45
Scheme 4.1. Ir complexes 4.1-4.4 in study.....	65
Scheme 4.2. Structures of Ir complexes 4.1-4.8	77
Scheme 5.1. Ir complexes in study, 5.1-5.6.....	89
Scheme 5.2. Iridium(III) complexes $[(\text{dFphtl})_2\text{Ir}(\text{dmabpy})]\text{PF}_6$, 5.2, and $[(\text{dFphtl})_2\text{Ir}(\text{bpy})]\text{PF}_6$, 5.7.....	108
Scheme 7.1. BODIPY dye core structure	159

List of Appendices

Appendix I. Chapter 2: Electrogenated Chemluminescence of Triazole-Modified Deoxycytidine Analogues in N,N-Dimethylformamide	176
Appendix II. Chapter 3: Synthesis, Structure, Electrochemistry, and Electrochemiluminescence of Thienyltriazoles	183
Appendix III. Chapter 4: Electrochemiluminescence of Iridium(III) Complexes	227
Appendix IV. Chapter 5: Mechanistic Insight into Electrochemiluminescence of Iridium(III) Complexes <i>via</i> Spooling Spectroscopy.....	235
Appendix V. Chapter 6: Sensitive Detection of Au ₂₅ Clusters by Electrochemiluminescence	251

List of Abbreviations and Symbols

Abbreviation	Definition
Abs	Absorbance
ACN	Acetonitrile
alt	Aryltriazoles
A.U.	Arbitrary Unit
BDY	BODIPY dye
BiTTM	[1-(2,2'-Bithien-4-yl)-1H-1,2,3-triazol-4-yl]methanol
BiTTP	2-[1-(2,2'-Bithien-4-yl)-1H-1,2,3-triazol-4-yl]phenol
BODIPY	Boron-dipyrromethene
BPO	Benzoyl Peroxide
bpy	2,2'-Bipyridine
Bn	Benzyl group
Calcd	Calculated
CCD	Charge-coupled Device
CDCl ₃	Deuterated Chloroform
CE	Counter Electrode
CL	Chemiluminescence
CV	Cyclic Voltammetry or Cyclic Voltammogram
dC	Deoxycytidine

DCM	Dichloromethane
dFMepy	2-(2,4-Difluorophenyl)-5-methyl-pyridinato
dFphtl	2,4-Difluorophenyltriazole
DFT	Density functional theory
dma	Dimethylamino
dmabpy	4,4'-Bis(<i>N,N</i> -dimethylamino)-2,2'-bipyridine
DMF	<i>N,N</i> -Dimethylformamide
DMSO	Dimethyl sulfoxide
DMSO- <i>d</i> ₆	Deuterated Dimethyl sulfoxide
DNA	Deoxyribonucleic Acid
DPA	9,10-Diphenylanthracene
DPV	Differential Pulse Voltammetry or Differential Pulse Voltammogram
dsDNA	Double-stranded DNA
dtBubpy	4,4'-Di- <i>tert</i> -butyl-2,2'-bipyridine
ECL	Electrogenerated Chemiluminescence or Electrochemiluminescence
Em	Emission
ESI	Electron Spray Ionization
ET	Electron Transfer
EtOH	Ethanol
Ex	Excitation

Fc	Ferrocene
Fc ⁺	Ferrocenium Cation
HOMO	Highest Occupied Molecular Orbital
HRMS	High Resolution Mass Spectrometry
Ir(ppy) ₃	Tri(phenylpyridine)iridium(III)
LC	Ligand-centered
LEECs	Light-emitting Electrochemical Cells
LLCT	Ligand-to-ligand Charge Transfer
LUMO	Lowest Unoccupied Molecular Orbital
LRMS	Low Resolution Mass Spectrometry
MeOH	Methanol
MLCT	Metal-to-ligand Charge Transfer
MO	Molecular Orbital
MS	Mass Spectrometry
NC	Nanocrystal
NHE	Normal Hydrogen Electrode
NMR	Nuclear Magnetic Resonance
NP	Nanoparticle
OLED	Organic Light-emitting Device
ORTEP	Oak Ridge Thermal Ellipsoid Plot

PF ₆	Hexafluorophosphate
phtl	Phenyltriazole
[(phtl) ₂ Ir(bpy)] ⁺	Iridium(III)bis[1'-phenyl-1,2,3-triazolato-N,C ^{2'}]-2,2'bipyridine-hexafluorophosphate
PL	Photoluminescence
PMT	Photomultiplier Tube
ppy	2-Phenylpyridinato
ppyH	2-Phenylpyridine
QE	ECL Quantum Efficiencies
QRE	Quasi-reference Electrode
RE	Quasi-reference Electrode
[Ru(bpy) ₃] ²⁺	Tris(2,2'-bipyridine)ruthenium (II)
SCE	Saturated Calomel Electrode
SNPs	Single Nucleotide Polymorphisms
ssDNA	Single-Stranded DNA
TBA	Tetra- <i>n</i> -butylammonium
TBAP	Tetra- <i>n</i> -butylammonium Perchlorate
TBAPF ₆	Tetrabutylammonium Hexafluorophosphate
<i>t</i> -Bu	<i>Tert</i> -butyl
ThdC	2'-Deoxy-5-(1-(thiophen-3-yl)-1H-1,2,3-triazol-4-yl)cytidine
THF	Tetrahydrofuran

TOF	Time of Flight
TPrA	Tri- <i>n</i> -propylamine
TTA	Triplet-triplet Annihilation
TTM	[1-(3-Thienyl)-1H-1,2,3-triazol-4-yl]methanol
TTP	2-[1-(3-Thienyl)-1H-1,2,3-triazol-4-yl]phenol
UV	Ultraviolet
Vis	Visible
WE	Working Electrode

Symbol	Definition
A	Amperes or Amps
avg	Average
d	Doublet
dd	Doublet of Doublets
<i>D</i>	Diffusion Coefficient (cm ² /s)
<i>E</i>	Voltage (V)
<i>E</i> [°]	Standard Potential (V)
<i>E</i> ^{o'}	Formal Potential (V)
<i>E</i> _{ox} ^{o'}	Formal Oxidation Potential (V)
<i>E</i> _{red} ^{o'}	Formal Reduction Potential (V)

$E_{1/2}$	Half-wave Potential (V)
$\Delta E^{\circ'}$	Formal Potential Separation
ΔE_p	Peak Potential Separation
ΔE_{redox}	Electrochemical Gap (eV)
E_p	Peak Potential (V)
$E_{p,a}$	Anodic Peak Potential (V)
$E_{p,c}$	Cathodic Peak Potential (V)
Eq.	Equation
Eqs.	Equations
E_s	Singlet State Energy (eV)
E_t	Triplet State Energy (eV)
<i>et al.</i>	<i>et alii</i> (and others)
eV	Electronvolt
F	Faraday Constant (C)
$\Delta G^{\circ}_{\text{ann}}$	Gibbs Free Energy Change
h	Planck Constant (Js)
h	Hour(s)
Hz	Hertz
$h\nu$	Light (nm)
$\Delta H^{\circ}_{\text{ann}}$	Enthalpy Change of Ion Annihilation (eV)

i	Current (A)
i_p	Anodic Peak Current (A)
i_c	Cathodic Peak Current (A)
IR	Infrared
J	Coupling Constant (Hz)
m	Multiplet
M	Molar
mA	Milliamp
Me	Methyl
min	Minute(s)
mg	Milligrams
MHz	Megahertz
mL	Milliliter
mmol	Millimole
mol	Mole
mp	Melting point
ⁿ BuLi	<i>Normal</i> Butyllithium
n	Number of Electrons Transferred
nA	Nanoamp
ppm	Parts Per Million

Q	Charge (C)
R	ECL Emitter or Luminophore
$R^{\bullet-}$	Radical Anion of R
$R^{\bullet+}$	Radical Cation of R
R^*	Excited State of R
$^1R^*$	Excited Singlet State of R
$^3R^*$	Excited Triplet State of R
$(RR)^*$	Excimer or Excited Dimer
rt	Room Temperature
s	Singlet
ΔS°	Entropy Change
t	Triplet
t	Time (s)
T	Temperature ($^\circ\text{C}$)
Φ	Efficiency
Φ_{ECL}	ECL Efficiency or Quantum Efficiency of ECL
$\{^1\text{H}\}$	Proton Decoupled
$^\circ$	Degrees
$^\circ\text{C}$	Degrees Celsius
\AA	Angstrom

λ	Wavelength (nm)
λ_{em}	Wavelength for Emission (nm)
λ_{ex}	Wavelength for Excitation (nm)
λ_{max}	Maximum Wavelength (nm)
δ	Chemical Shift (ppm)
ν	(1) Frequency of Light (s^{-1}) (2) Scan Rate (V/s)
$\tilde{\nu}$	Wavenumbers (cm^{-1})
μ	Micro
μA	Microamp
μm	Micromolar
μM	Micrometer

Chapter 1

1 Fundamentals of Electrogenerated Chemiluminescence (ECL)

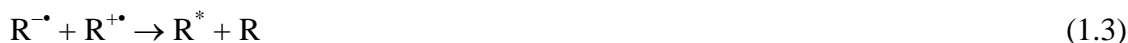
1.1 Introduction

Electrogenerated chemiluminescence or electrochemiluminescence, ECL, is a process where a species is electrochemically oxidized and reduced to generate radical cations and anions in solution.¹⁻⁵ Through electron transfer, the radicals will generate excited state species and ground state species. The excited species will relax back to its ground state, emitting light. As stated by Bard, the basic requirements for efficient annihilation ECL to occur are: 1) stable radical ions of the precursor molecules in the electrolyte of interest; 2) good photoluminescence efficiency of a product of the electron transfer reaction; and 3) sufficient energy in the electron transfer reaction to produce the excited state.¹ Usually when this criteria is met, ECL will be observed, however the efficiency often depends upon details of reaction kinetics. There are two main pathways to generate ECL, ion annihilation or co-reactant reactions. Hercules, Bard *et al.*, and Visco *et al.* reported on the first ECL studies in the 1960s.⁶⁻⁸ ECL is now a powerful analytical technique that produces light in the vicinity of the electrode, pairing electrochemical and spectroscopic methods. All of these are used in a wide variety of applications including biomolecular labeling, immunoassays, DNA analyses, detecting analytes, and organic light-emitting diodes.^{2,4,5,9-14}

1.2 Ion Annihilation Pathway

ECL can be generated by ion annihilation, shown in Eqs. 1.1 through 1.4.¹ Here, an ECL luminophore, R, can be electrochemically oxidized and reduced at the surface of an electrode to generate stable radical cations and anions. Potential scan directions are alternatively changed. For instance, if the applied potential is scanned to negative potential first, the radical anion, $R^{\bullet-}$, of a luminophore, Eq. 1.1, can be generated by scanning the applied potential negative. Upon the potential scanned in the reverse

direction, to positive potential, the luminophore is oxidized, generating its radical cation, $R^{\bullet+}$, Eq. 1.2. The radicals will generate an excited state species via electron transfer, Eq. 1.3, and emit light, Eq. 1.4.



In order to have direct population of the singlet excited state, the energy, $-\Delta H^{\circ}_{\text{ann}}$, must be larger than the energy, E_s , required to produce the lowest excited singlet state, ${}^1R^*$, from the ground state of R. The total free energy of annihilation can be calculated as defined in Eq. 1.5 to 1.7.^{1,15} The energy, $-\Delta H^{\circ}_{\text{ann}}$, can be calculated, Eq. 1.6, using the electrode potentials from Eqs. 1.1 and 1.2, with correction for entropy effects, $T\Delta S^{\circ}$, ~ 0.16 eV.

$$-\Delta H^{\circ}_{\text{ann}} = -\Delta G^{\circ}_{\text{ann}} - T\Delta S^{\circ} \approx \Delta E^{\circ} - 0.16 \text{ eV} \quad (1.5)$$

$$-\Delta H^{\circ}_{\text{ann}} = E_p(R/R^{\bullet+}) - E_p(R/R^{\bullet-}) - 0.16 \text{ eV} \quad (1.6)$$

$$-\Delta H^{\circ}_{\text{ann}} \geq E_s \quad (1.7)$$

If it is possible to directly generate the excited singlet state, ${}^1R^*$, the system is referred to as an energy-sufficient system, S-route, Eq. 1.3a. However, if the energy, $-\Delta H^{\circ}_{\text{ann}}$, is smaller than E_s , singlet state energy, but larger than the triplet state energy, E_t , the triplet state, ${}^3R^*$, can be formed via the T-route, Eq. 1.3b. Then the excited singlet state, ${}^1R^*$, by triplet-triplet annihilation (TTA), Eq. 1.8, can be generated.

S-route



T-route

Two common compounds used in calculating relative ECL efficiencies are 9,10-diphenylanthracene, DPA, Figure 1.1, and tris(2,2'-bipyridine)ruthenium(II), $[\text{Ru}(\text{bpy})_3]^{2+}$, Figure 1.2. DPA is a good example of an energy-sufficient system, S-route, Scheme 1.1.⁷ Whereas, $[\text{Ru}(\text{bpy})_3]^{2+}$ is sufficient to populate the emitting triplet state, Scheme 1.2, however it does not follow the T-route.¹⁶

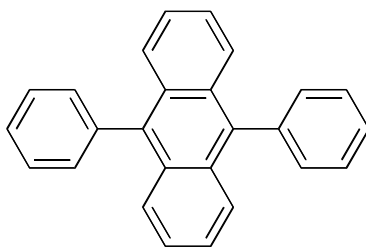
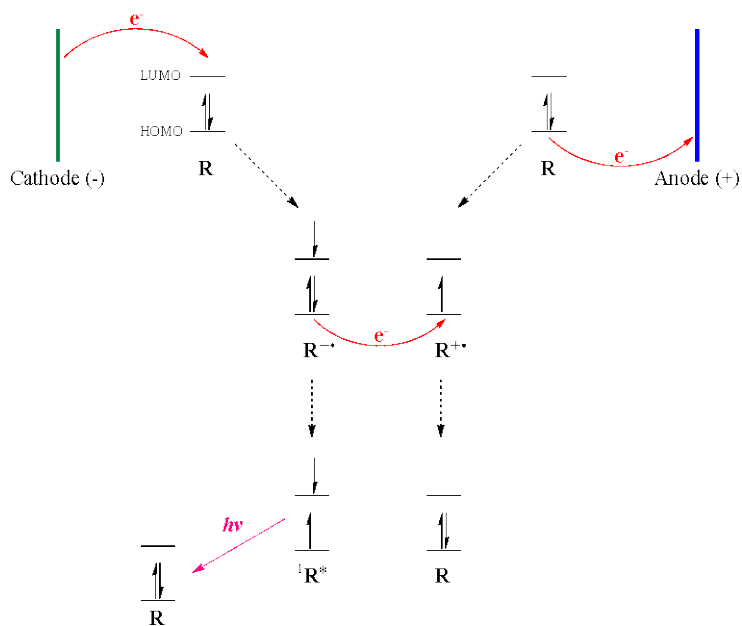
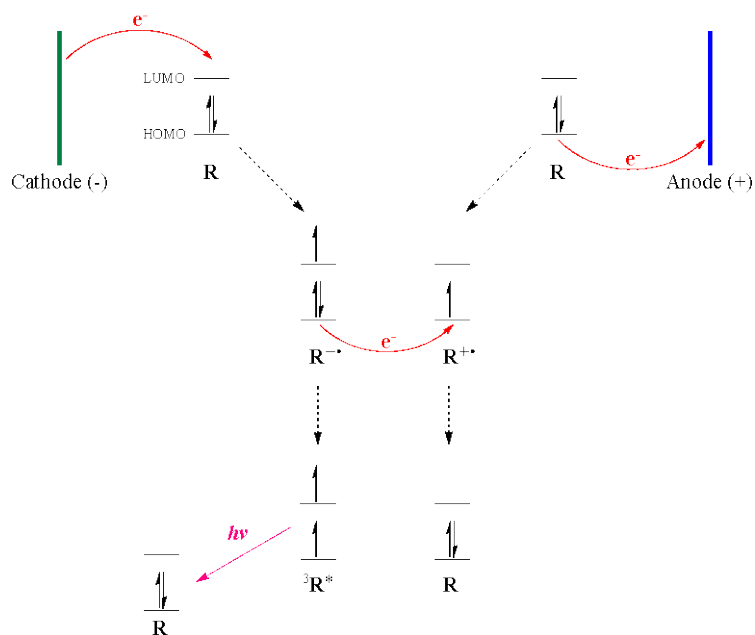


Figure 1.1. Structure of 9,10-diphenylanthracene, DPA.



Scheme 1.1. Schematic diagram showing the general principles of ECL with singlet excited state emission, ${}^1R^*$, where R = DPA



Scheme 1.2. Schematic diagram showing the general principles of ECL with triplet excited state emission, ${}^3R^*$, where $R = [Ru(bpy)_3]^{2+}$

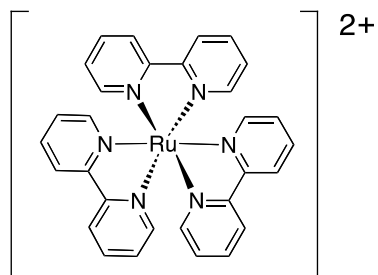
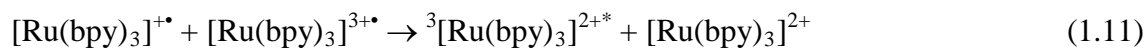


Figure 1.2. Structure of tris(2,2'-bipyridine)ruthenium(II), $[Ru(bpy)_3]^{2+}$.



In addition to generating singlet and triplet excited states, ion annihilation can also lead to the direct formation of excimers, an electronically excited dimeric species. Eqs. 1.13 and 1.14.



Excimer formation is likely in ECL because of the close proximity of the radical ions in the contact radical ion pair.¹ Excimer ECL emission, $(RR)^*$, is usually characterized by a broad featureless emission red-shifted from the singlet emission of the molecule, R^* .¹ In addition, the molecules should be aligned so that there is significant π -orbital overlap.¹

1.3 Co-reactant Pathway

The addition of a co-reactant to generate ECL is beneficial when the radicals generated in solution are not stable or when the solvent has a narrow potential window in which the radicals cannot be generated. A co-reactant can produce a reactive intermediate, either a strong reducing or strong oxidizing agent, upon electrochemical oxidation or reduction, that reacts with the reduced or oxidized ECL luminophore to generate the excited species.² If annihilation only produces weak ECL, the addition of a co-reactant may enhance the ECL intensity of the compound of interest.

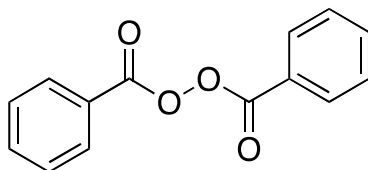


Figure 1.3. Structure of benzoyl peroxide, BPO.

Benzoyl peroxide, BPO, Figure 1.3, is a good co-reactant for reductive-oxidation ECL, where BPO is easily reduced, $BPO^{\bullet-}$, Eq. 1.15, then rapidly decomposes, generating a strong oxidizing species, benzoate radical, $C_6H_5CO_2^{\bullet}$, Eq. 1.16, that can

react with the ECL luminophore, R, to generate the radical cation of the ECL luminophore species, Eq. 1.17.



Then the ECL luminophore will be reduced to produce its radical anion, $\text{R}^{\bullet-}$, Eq. 1.1, and can react with the radical cation, $\text{R}^{\bullet+}$, formed in Eq. 1.17 to generate the excited species, R^* , Eq. 1.3.

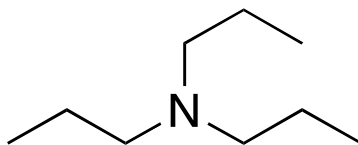
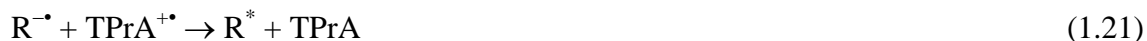


Figure 1.4. Structure of tri-*n*-propyl amine, TPrA.

Another common co-reactant is tri-*n*-propyl amine, TPrA, Figure 1.4, an excellent co-reactant for oxidative-reduction ECL. Using TPrA, the excited state species can be produced by three main routes.^{17,18} First, TPrA is oxidized to its radical cation, $\text{TPrA}^{\bullet+}$, Eq. 1.18, then deprotonates to generate the radical, a strong reducing species, TPrA^{\bullet} , Eq. 1.19. For the first mechanism, the radical, TPrA^{\bullet} , donates an electron to the ECL luminophore, R, generating the radical anion, $\text{R}^{\bullet-}$, Eq. 1.20. The radical cation of TPrA, $\text{TPrA}^{\bullet+}$, a sufficiently stable intermediate, can then remove an electron from the luminophore's radical anion species, $\text{R}^{\bullet-}$, generating the excited state species, R^* , Eq. 1.21, that will emit light, Eq. 1.4.





The second mechanism involves the oxidation of TPrA to TPrA^{•+}, Eq. 1.19, reacting with the oxidized luminophore, R^{•+}, Eq. 1.2, to generate the excited state species, R^{*}, Eq. 1.22, that will emit light, Eq. 1.4. The third mechanism follows Eq. 1.20 from the first proposed mechanism that generates the radical anion of the luminophore, R^{•-}, that reacts with its radical cation, R^{•+}, Eq. 1.2, to generate the excited state species similar to ion annihilation route, Eq. 1.3, and emit light, Eq. 1.4.



The third mechanism involves the TPrA[•] radical, Eq. 1.19, and the bulk species, R, to generate the radical anion, R^{•-}, Eq. 1.23. The radical anion will transfer an electron to the radical cation and generate the excited state species, Eq. 1.3, which will emit light, Eq. 1.4.



1.4 ECL Instrumentation

The electrochemical cell consists of a 2 mm Pt disc inlaid in a glass tube working electrode (WE), a coiled Pt wire counter electrode (CE), and either a coiled Ag wire or coiled Pt wire quasi reference electrode (RE). The supporting electrolyte contained 0.1 M TBAP, tetrabutylammonium perchlorate, or 0.1 M TBAPF₆, tetrabutylammonium hexafluorophosphate. The anhydrous solvents used were either DMF, *N,N*-dimethylformamide, or ACN, acetonitrile, or 1:1 ratio of benzene:acetonitrile, or DCM, dichloromethane, with a volume of 3 mL. The electrochemical cell was assembled in a glove box to minimize oxygen and water content. For co-reactant studies, benzoyl peroxide (BPO) or tri-*n*-propylamine (TPrA) were used.

For all experiments, the electrochemical workstation was used.¹⁹ Two setups were used: the first for voltammetry and ECL-voltage experiments, Figure 1.5, and the second, for accumulated ECL spectra and for spooling ECL spectra, Figure 1.6.

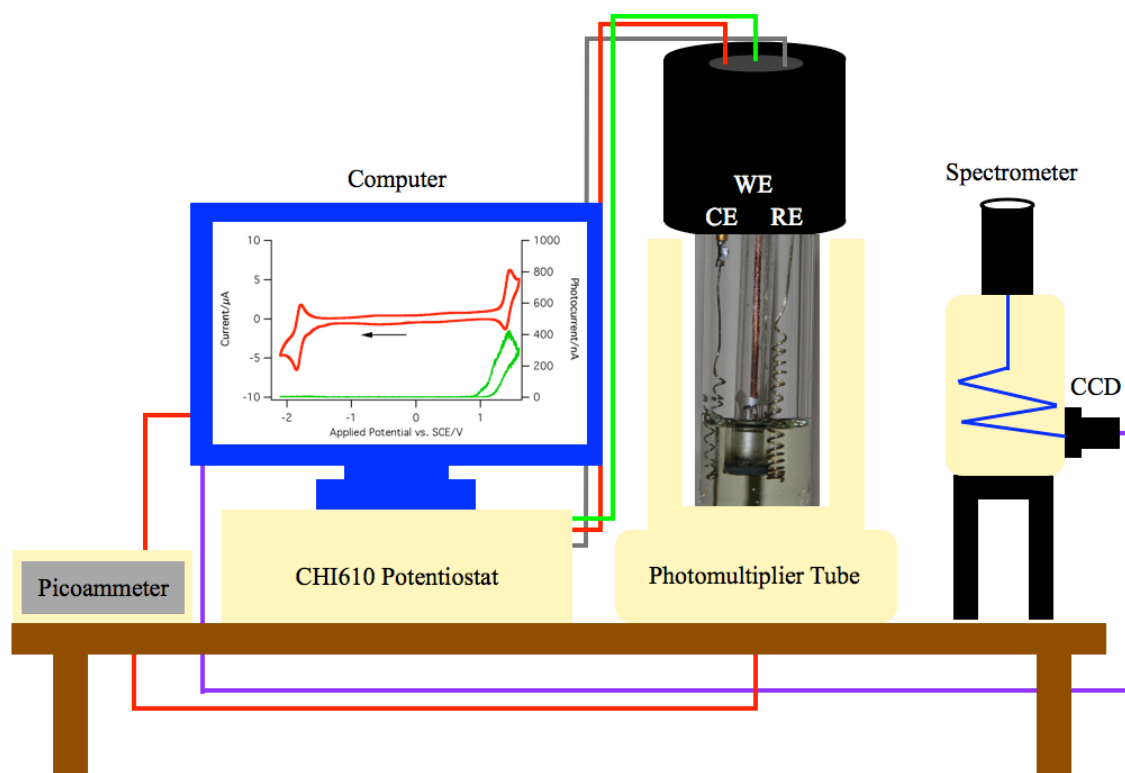


Figure 1.5. CV or ECL setup for experiment with the electrochemical cell placed in the PMT detector, a sample CV (in red) with ECL-voltage curve (in green) is shown on the computer screen.

Cyclic voltammetry (CV) and differential pulse voltammetry (DPV) experiments were conducted on a CHI 610A electrochemical analyzer (CH Instruments, Austin, TX). Potentials (V) were calibrated using an internal standard Fc/Fc^+ redox couple after each experiment, and are reported *vs.* a standard electrode.

The ECL was collected by the photomultiplier tube (PMT) under the flat Pyrex window at the bottom of the cell which was measured as a photocurrent, and transformed to a voltage signal using a picoammeter/voltage source (Keithley 6487, Cleveland, OH).¹⁹ The potential, current signals from the electrochemical workstation, and the photocurrent signal from the picoammeter were sent simultaneously through a DAQ board (DAQ 6052E, National Instruments, Austin, TX) to a computer. The data acquisition system

was controlled from a custom-made LabVIEW program (ECL_PMT610a.vi, National Instruments, Austin, TX). The photosensitivity on the picoammeter was set manually in order to avoid the saturation.

ECL pulsing experiments were conducted by using a potentiostat (Model AFCBPI, Pine Instrument Co., Grove City and PA), an EG&G PAR 175 Universal Programmer (Princeton Applied Research, Trenton, NJ), and the PMT with the picoammeter in the similar manner.¹⁹ The assembly was able to perform the pulsing experiments without a delay in a relative fast time pace. The data acquisition for the current, potential and ECL signals was carried out using another homemade LabVIEW program (ECL_PAR610a.vi).

The visible region ECL spectra were obtained by replacing the PMT with a spectrometer (Cornerstone 260, Newport, Canada) attached to a CCD camera (Model DV420-BV, Andor Technology, Belfast, UK).^{19,20} The camera was cooled to -55 °C prior to use, and controlled by a computer for operation and data acquisition. The intensities versus wavelengths (spectra) were recorded by Andor Technology program. The NIR region ECL spectra were recorded by Andor Technology program.²¹ Similar to the CV experiments, the samples were scanned between their redox potentials. When the ECL is in the NIR region, ECL spectroscopy was conducted on an Acton 2300i spectrograph with a grating of 50 l/mm blazed at 600 nm, and an Andor iDUS CCD camera, Model DU401-BR-DD-352. The camera was cooled to -75 °C prior to use.

Spooling ECL spectroscopy was developed during this thesis work. Spooling ECL experiments were conducted using the same setup described above along with the spooling function in the Andor software, Figure 1.6. Basically, one ECL spectrum was taken in a time interval of 1 s during the potential scanning. The following parameters were employed in the Andor Technology program under the kinetic parameters option tab: exposure time = 1 s, number of accumulations = 1, kinetic series length = T (where T = time that matches with the potential scan time for two complete cycles), kinetic cycle time = 1, and the spectrometer was centered at 850 nm, with the camera cooled to -55 °C (for visible CCD camera) and -75 °C (for NIR CCD camera). Simultaneously, the CHI

610A electrochemical analyzer and the Andor Technology program were run and the CV and spooling spectra were collected.

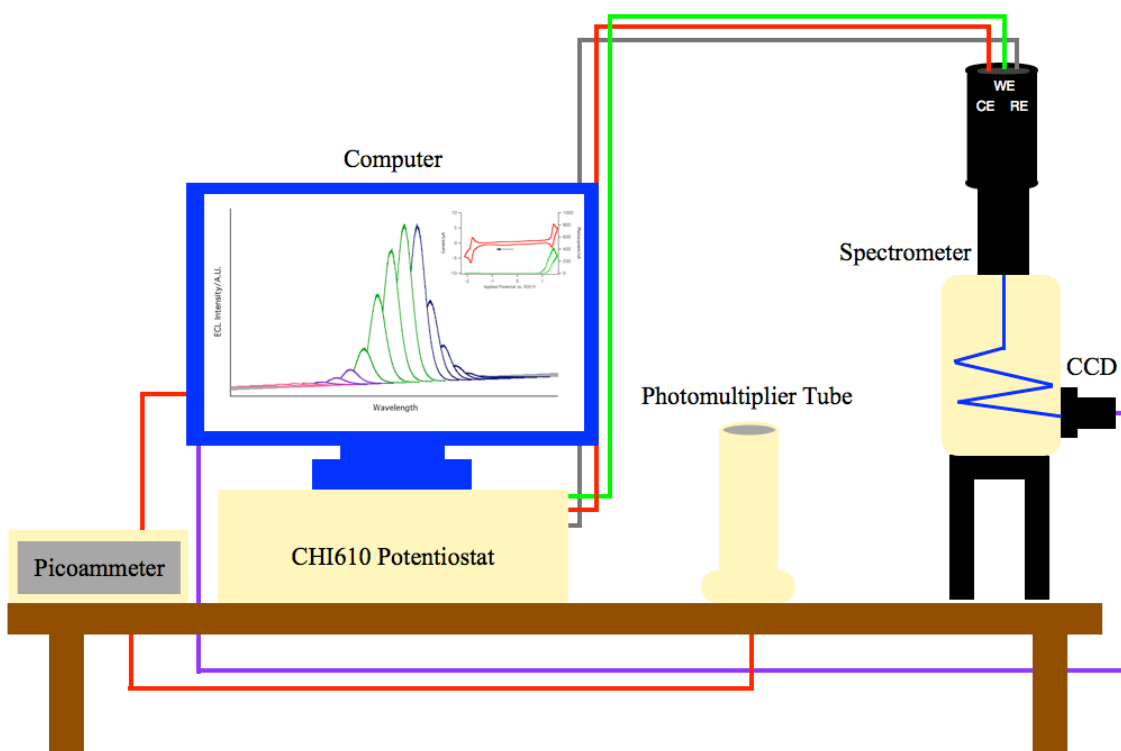


Figure 1.6. ECL spectrum or spooling setup, with the electrochemical cell in the spectrometer with the visible or NIR CCD camera, a sample ECL spooling spectra is shown on the computer screen.

1.5 Scope of Thesis

The use of ECL in biological, medicinal, and electrical applications is continuing to rise, however, there is a need to continue to study and learn the fundamental processes and the complex mechanisms of ECL generation for new metal complexes, clusters, nanoparticles or quantum dots, polymers, modified nucleosides or DNA, and other ECL active molecules. The work presented in this thesis aims at addressing the complex mechanism that generates ECL in the visible and NIR spectral regions. This will be accomplished by studying the electrochemistry and ECL of modified deoxycytidine

nucleosides in Chapter 2, synthesizing and analyzing thienyltriazoles in Chapter 3, correlating electronic structures to ECL, evaluating their ECL properties, determining a self-enhanced co-reactant mechanism, and electronic communication between soft salts of iridium(III) metal complexes in Chapters 4 and 5, studying the NIR ECL emission of Au₂₅ clusters in Chapter 6 and dual ECL emissions of BDY-PbS nanoparticles in Chapter 7. These chapters will include a comprehensive study on the redox chemistry, ECL generation *via* annihilation and co-reactant paths, ECL spectroscopy and a newly developed spooling ECL spectroscopy to further understand ECL generation mechanisms. A collective summary of the projects will be given in Chapter 8.

1.6 References

- (1) *Electrogenerated Chemiluminescence*; Bard, A. J., Ed.; Marcel Dekker: New York, 2004.
- (2) Miao, W. *Chem. Rev.* **2008**, *108*, 2506.
- (3) Bard, A. J.; Ding, Z.; Myung, N. *Struct. Bond* **2005**, *118*, 1.
- (4) Richter, M. M. *Chem. Rev.* **2004**, *104*, 3003.
- (5) Hu, L.; Xu, G. *Chem. Soc. Rev.* **2010**, *39*, 3275.
- (6) Hercules, D. M. *Science* **1964**, *145*, 808.
- (7) Visco, R. E.; Chandross, E. A. *J. Am. Chem. Soc.* **1964**, *86*, 5350.
- (8) Santhanam, K. S. V.; Bard, A. J. *J. Am. Chem. Soc.* **1965**, *87*, 139.
- (9) Pyati, R.; Richter, M. M. *Annu. Rep. Prog. Chem., Sect. C* **2007**, *103*, 12.
- (10) Kulmala, S.; Suomi, J. *Anal. Chim. Acta* **2003**, *500*, 21.
- (11) Fährnich, K. A.; Pravda, M.; Guilbault, G. G. *Talanta* **2001**, *54*, 531.
- (12) Knight, A. W. *Trends in Anal. Chem.* **1999**, *18*, 47.
- (13) Laser, D.; Bard, A. J. *J. Electrochem. Soc.* **1975**, *122*, 632.
- (14) Krishnan, S.; Hvastkovs, E. G.; Bajrami, B.; Choudhary, D.; Schenkman, J. B.; Rusling, J. F. *Anal. Chem.* **2008**, *80*, 5279.

- (15) Faulkner, L. R.; Tachikawa, H.; Bard, A. J. *J. Am. Chem. Soc.* **1972**, *94*, 691.
- (16) Tokel, N. E.; Bard, A. J. *J. Am. Chem. Soc.* **1972**, *94*, 2862.
- (17) Miao, W.; Choi, J.-P.; Bard, A. J. *J. Am. Chem. Soc.* **2002**, *124*, 14478.
- (18) Lai, R. Y.; Bard, A. J. *J. Phys. Chem. A* **2003**, *107*, 3335.
- (19) Booker, C.; Wang, X.; Haroun, S.; Zhou, J.; Jennings, M.; Pagenkopf, B. L.; Ding, Z. *Angew. Chem. Int. Ed.* **2008**, *47*, 7731.
- (20) Swanick, K. N.; Ladouceur, S.; Zysman-Colman, E.; Ding, Z. *Angew. Chem. Int. Ed.* **2012**, *51*, 11079.
- (21) Swanick, K. N.; Hesari, M.; Workentin, M. S.; Ding, Z. *J. Am. Chem. Soc.* **2012**, *134*, 15205.

Chapter 2

2 Electrogenenerated Chemluminescence of Triazole-Modified Deoxycytidine Analogues in N,N-Dimethylformamide[†]

2.1 Introduction

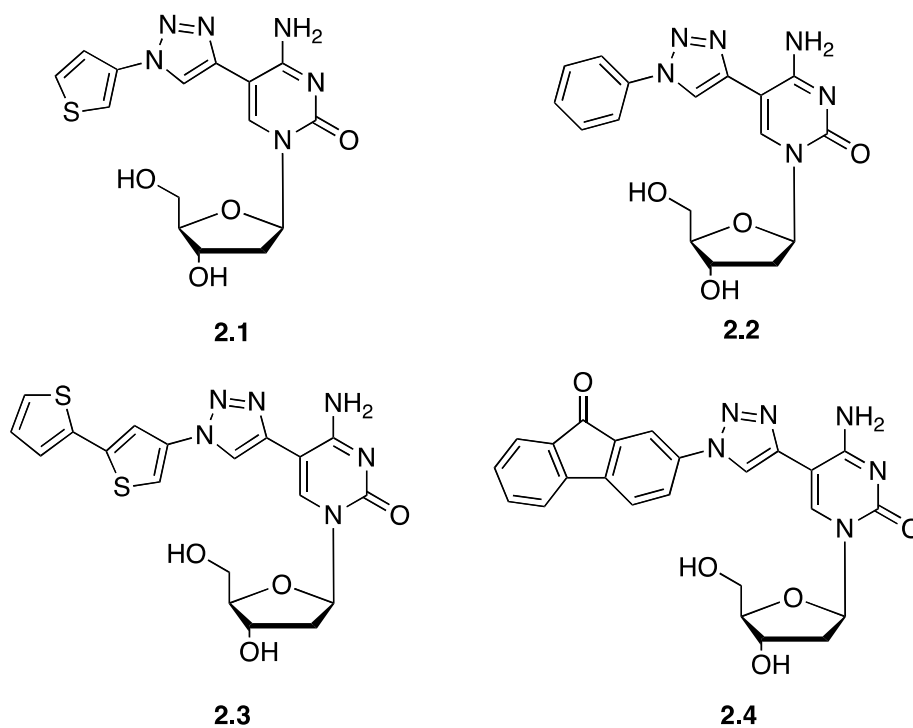
Electrogenenerated chemiluminescence or electrochemiluminescence (ECL) is the process in which radicals are electrochemically generated in solution and react through electron transfer to form excited states that emit light.¹ In the 1960s, Hercules, Bard et al., and Visco et al. reported on the first ECL studies.²⁻⁴ Since then, ECL has become a powerful analytical technique⁵⁻¹⁴ in immunoassay, food and water testing, trace metal determination, and biomolecule detection. Two main ECL systems are used: annihilation and co-reactant ECL.¹ Annihilation ECL is observed when a luminophore species in solution is scanned to its first oxidation and reduction potentials at an electrode. The excited species are formed from the generation of a radical cation and radical anion of the species in the vicinity of the electrode. The emission of light results from the excited state species. An alternative to annihilation ECL is a co-reactant system, which is performed with one directional potential scanning at an electrode in a solution containing the luminophore species and an added co-reactant reagent such as benzoyl peroxide, BPO.^{15,16} Radicals are generated from the luminophore, and intermediates from BPO that will decompose to produce powerful oxidizing species and react with the reduced luminophore. This generates an excited species, which upon decay emits light.

ECL applications in the detection and diagnostics of deoxyribonucleic acid (DNA) involve electrochemistry and spectroscopy, and have many distinct advantages over other spectroscopy-based detection systems¹¹ such as a lack of scattered light interference and the use of electrochemistry-based sensors¹⁷ which offer high sensitivity.

[†] This work is published in Kalen N. Swanick, David W. Dodd, Jacquelyn T. Price, Allison L. Brazeau, Nathan D. Jones, Robert H.E. Hudson, and Zhifeng Ding, *Phys. Chem. Chem. Phys.*, **2011**, *13*, 17405-17412. Reproduced by permission of The Royal Society of Chemistry (RSC). See Appendix I.

In fact, a common practice to detect DNA *via* ECL is to immobilize luminophore-labelled DNA double or single strands at an electrode,^{18,19} which can be measured with the emitted light upon redox reactions of the luminophore along with a co-reactant in the solution. The immobilized single strands can be employed to recognize complementary strands followed by ECL detection.^{19,20} Modified nucleosides could find potential applications as luminescent probes incorporated into single-stranded deoxyribonucleic acid (ssDNA) for sequence interrogation using ECL methods.^{20,21} Single nucleotide polymorphisms (SNPs) are single-base variations in the genetic code that occur about once every 1000 bases along the 3-billion base pair human genome.²² The ability to detect SNPs is of prime importance as mutations can be directly responsible for, or make one more susceptible to diseases such as asthma, diabetes, atherosclerosis, schizophrenia, and various cancers.²² Fluorescent modified nucleosides, when in the context of an oligomer, are potential candidates for the detection of nucleic acids with single nucleobase variations.²³⁻²⁸

Modifications of nucleosides in nucleic acid chemistry are well established.²⁹⁻³¹ However, there have been a few reports on modified deoxycytidine (dC) nucleosides,³²⁻³⁵ although the ECL behaviour of tris(2,2'-bipyridine)ruthenium (II) $[\text{Ru}(\text{bpy})_3]^{2+}$ has been widely studied since the 1970s.³⁶ In the above context, $[\text{Ru}(\text{bpy})_3]^{2+}$ can be attached to a target ssDNA as an ECL label then hybridize with its complementary strand of ssDNA immobilized on the surface of an electrode to measure the ECL response of the double-stranded DNA (dsDNA). Our objective was to create a metal-free DNA sensor based on dC in combination with ECL for the detection of SNPs.



Scheme 2.1. Molecular structures of compounds **2.1-2.4**

Our group previously synthesized triazole-modified deoxycytidine nucleosides, **2.1-2.4** (Scheme 2.1)^{37,38} These compounds are easy to prepare, and are potential candidates for use as metal-free ECL labels that can be incorporated into ssDNA for the detection of SNPs. The modified nucleosides contain four different aromatic groups, **2.1-2.4**, which have been appended to dC as desirable targets for potential uses in nucleic acid chemistry. Compound **2.2** has been reported previously although characterization data were lacking.³²

Here we report the electrochemical behaviour of these triazole-containing dC nucleosides, **2.1-2.4**, employing cyclic voltammetry (CV) and differential pulse voltammetry (DPV). ECL of these four compounds were also investigated *via* annihilation by scanning between the first oxidation and reduction potentials, and co-reactant mechanisms by adding BPO and scanning the potential in the cathodic region. The majority of DNA-based biosensors have used uracil for studies.^{39,40} At the time of writing, there have been no reports of ECL of any modified dC nucleosides in literature.

2.2 Experimental Section

Chemicals. Commercial products and chemical reagents were used as received. 9,10-Diphenylanthracene (DPA, 97%), benzoyl peroxide (BPO, reagent grade, $\geq 98\%$) and ferrocene (Fc, 98%) were purchased from Aldrich (Mississauga, ON). The supporting electrolyte, tetra-*n*-butylammonium perchlorate (TBAP, electrochemical grade) was purchased from Fluka. All solutions were prepared using anhydrous *N,N*-dimethylformamide (DMF, 99.8%) in a Sure/SealTM bottle, bought from Aldrich, that was immediately transferred into an N₂-filled drybox prior to use.

Synthesis. The synthesis of compounds **2.1-2.4** Scheme 2.1 was published elsewhere.³⁸ In brief, these compounds were obtained by performing a click reaction, using the Huisgen 1,3-dipolar cycloaddition reaction which is the premier example of a click reaction between alkynes and azides.^{41,42} The selective 1,4-disubstituted products of the click reaction were obtained by using a copper (I) catalysts.^{43,44} Compounds **2.1-2.4** were synthesized by reacting 5-ethynyldeoxycytidine with one of the four corresponding aryl azides in the presence of a Cu(I) catalyst, generated from CuSO₄ and sodium ascorbate, in a 1:1 THF-H₂O solution. The crude products of **2.1-2.4** were purified using column chromatography and characterized by ¹H and ¹³C{¹H} NMR spectroscopies and HRMS.³⁸ The purified triazole-containing compounds were then used for CV, DPV and ECL analysis.

Electrochemical Preparation. CV, DPV, and ECL experiments were conducted using a 2 mm diameter Pt disc inlaid in a glass sheath as the working electrode (WE), a coiled Pt wire as the counter electrode (CE), and a coiled Ag wire as the quasi reference electrode (RE). Prior to an experiment, the electrochemical cell was rinsed with acetone and deionized water, then immersed in 5 % KOH in isopropanol for 4 h. The cell was rinsed with copious amounts of deionized water, immersed in 1 % HCl for 4 h, and finally thoroughly rinsed with ultrapure water. The cell was dried at 120 °C for 12 h, and then cooled to room temperature.

The CE and RE were rinsed with acetone and ultrapure water then sonicated in DMF for 15 min, in ethanol for 5 min, and finally in ultrapure water for 5 min before being thoroughly rinsed again with ultrapure water. The electrodes were then dried at 120 °C for 5 min then left to cool to room temperature.

The WE was polished with a felt polishing pad using a 1.0 μm alumina suspension in ultrapure water (Milli-Q, Millipore) for 5 min followed by a 0.05 μm alumina suspension in ultrapure water to obtain a mirror surface and finally washed with copious amounts of ultrapure water (Buehler Ltd., Lake Bluff, IL). Then the WE electrode was electrochemically polished by cycling in 0.1 M aqueous H_2SO_4 solution for 400 segments between the potentials of 1.400 and -0.600 V at 0.5 V/s to obtain a clean and more reproducible Pt surface.⁴⁵ The oxidation and reduction of H_2SO_4 produces an ordered structure of polycrystalline Pt surfaces.⁴⁶ The electrodes were then washed repeatedly with ultrapure water, then dried with a stream of Ar gas over the Pt disc area and left to dry for 12 h at room temperature.

All solutions for electrochemical and ECL experiments were prepared in the electrochemical cell placed inside an N_2 -filled drybox that possessed little oxygen and moisture. The solutions of **2.1-2.4** in concentration range between 2.0×10^{-3} and 2.7×10^{-3} M in anhydrous DMF (Sure/SealTM bottle from Aldrich) containing 0.1 M TBAP as supporting electrolyte. For co-reactant systems, 5.0×10^{-3} M BPO was added to each solution of **2.1-2.4**. The electrodes were immersed in the solution and connected by copper wire inserted through the air-tight Teflon cap. The assembly was moved out of the drybox to perform electrochemistry and ECL experiments. After completion of each experiment, the electrochemical potential window was calibrated using Fc as the internal standard. The redox potential of Fc/Fc^+ was taken as 0.470 V vs. NHE.⁴⁷

Electrochemical Instrumentation. The CV was conducted on a CHI 610A electrochemical analyzer (CH Instruments, Austin, TX). The experimental parameters for CVs are listed here: 0.000 V initial potential in experimental scale, positive or negative initial scan polarity, 0.1 V/s scan rate, 4 sweep segments, 0.001 V sample interval, 2 s

quiet time, $1.5 \times 10^{-5} \text{ AV}^{-1}$ sensitivity. The potential range depended on the particular compound.

Four DPVs were taken for each compound on the CHI 610A, two for anodic scans (forward and reverse scans in the experimental potential scale between 0.000 V and upper limit potential value of the compound obtained from CV experiments) and two for cathodic scans (forward and reverse scans in the experimental potential scale between 0.000 V and low limit potential value of the compound obtained from CV experiments). The experimental parameters for DPVs are as following: 0.004 V increments, 0.05 V amplitude, 0.5 s pulse width, 0.0167 s sampling width, 0.2 s pulse period, 2 s quiet time, $1.5 \times 10^{-5} \text{ AV}^{-1}$ sensitivity.⁴⁵

ECL Instrumentation. The ECL cell was specifically designed to have a flat Pyrex window at the bottom for detection generated light from the WE and was sealed with a Teflon cap with a rubber O-ring for CV, DPV, and ECL measurements. The ECL data along with CV data were obtained using the CHI 610A coupled with a photomultiplier tube (PMT, R928, Hamamatsu, Japan) held at -750 V with a high voltage power supply. The ECL collected by the PMT under the flat Pyrex window at the bottom of the cell was measured as a photocurrent, and transformed to a voltage signal, using a picoammeter/voltage source (Keithley 6487, Cleveland, OH). The potential, current signals from the electrochemical workstation, and the photocurrent signal from the picoammeter were sent simultaneously through a DAQ board (DAQ 6052E, National Instruments, Austin, TX) in a computer. The data acquisition system was controlled from a custom-made LabVIEW program (ECL_PMT610a.vi, National Instruments, Austin, TX). The photosensitivity on the picoammeter was set manually in order to avoid the saturation.

ECL pulsing experiments were conducted by using a potentiostat (Model AFCBPI, Pine Instrument Co., Grove City and PA), an EG&G PAR 175 Universal Programmer (Princeton Applied Research, Trenton, NJ), and the PMT with the picoammeter in the similar manner. The assembly was able to perform the pulsing experiments without a delay in a relative fast time pace. The data acquisition for the

current, potential and ECL signals was carried out using another homemade LabVIEW program (ECL_PAR610a.vi). For co-reactant systems, the applied potential was pulsed at the WE in the cathodic region (in the experimental potential scale between 0 and low limit potential value for the compound reduction as obtained from CV experiments) with a pulse width of 0.1 s or 10 Hz.

The ECL spectra were obtained by replacing the PMT with a spectrometer (Cornerstone 260, Newport, Canada) attached to a CCD camera (Model DV420-BV, Andor Technology, Belfast, UK). The camera was cooled to -55 °C prior to use, and controlled by a computer for operation and data acquisition. The intensities versus wavelengths (spectra) were recorded by Andor Technology program. Similar to the pulsing experiments, the samples were pulsed at 10 Hz within each compound's potential window. The exposure time of the spectra was set to 60 s for both the annihilation and co-reactant systems. Vertical lines/spikes observed in the spectra were from cosmic rays from the CCD camera.

ECL Efficiency Calculations. ECL quantum efficiencies (QE) were calculated relative to DPA (the reported relative ECL efficiency, Φ_{ECL} , of DPA was taken 100 % or 1.0 in DMF)^{48,49} by integrating both the ECL intensity and current value versus time for each compound, as described in Eq. 2.1^{10,50,51},

$$\Phi_x = 100 \times \left(\frac{\int_a^b ECL dt}{\int_a^b Current dt} \right)_x \bigg/ \left(\frac{\int_a^b ECL dt}{\int_a^b Current dt} \right)_{st} \quad (2.1)$$

where x stands for the compound (**2.1-2.4**), a and b represents the integral time range, and st represents DPA.

2.3 Results and Discussion

2.3.1 Electrochemistry and its Correlation to Electronic Structures

The electrochemical behaviours of compounds **2.1-2.4** were studied in order to determine the oxidation and reduction potentials. Figure 2.1 shows the CVs of **2.1** in DMF solution containing 0.1 M TBAP as supporting electrolyte and the blank DMF solution containing 0.1 M TBAP at a scan rate of 0.1 V/s within potential ranges between 0.000 and 2.169, and between 0.000 and -1.889 V, respectively. When the potential was scanned initially from 0.000 to 2.169 V, compound **2.1** underwent the first oxidation at a peak potential of 1.858 V followed by a continuous rise in current in the potential scan until 2.169 V. There was no cathodic peak when the applied potential was scanned back, indicating the irreversibility of the electrochemical oxidation reaction. The radical cations might undergo further chemical reactions (EC mechanism).

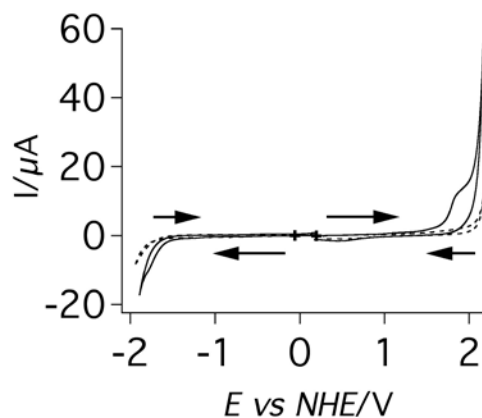


Figure 2.1. Cyclic voltammograms of **2.1** (solid lines) in DMF containing 0.1 M TBAP as supporting electrolyte, and blank solution (dotted lines), with the initial scan from 0.000 to 2.169 V (anodic scan), and initial scan from 0.000 to -1.889 V (cathodic scan), with a scan rate of 0.1 V/s.

The HOMO orbital revealed by the density function theory calculation is a linear combination of p_z atomic orbitals of S, C, N and O atoms in the thiophene, triazole and deoxycytidine rings³⁸. The electron withdrawn from compound **2.1** upon oxidation was delocalized in the molecule because of the co-planer structure determined by X-ray crystallography, Figure 2.2.

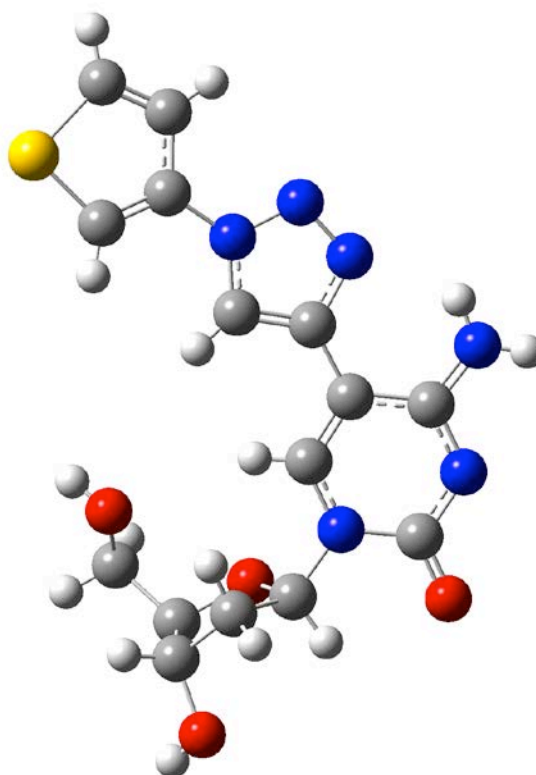


Figure 2.2. Ball-and-stick representation of **2.1**. Except for OH and NH₂ protons, H-atoms are omitted for clarity. Carbon atoms are in grey, sulfur in yellow, nitrogen in blue, and oxygen in red. The final solution was submitted to the IUCR CIF checking program and had some Alert level A's or B's associated with the lack of complete data, however the general structure can be observed for **2.1**.

Note that the crystal structure is our best estimation since it did not pass cif file checking (see details in Appendix I). Similarly, compound **2.1** demonstrated an irreversible reduction peak at -1.835 V when the applied potential was scanned from 0.000 V to cathodic region. Based on the DFT calculation, the LUMO orbital was mostly

contributed from p_z atomic orbitals of S, C and N atoms in the thiophene and triazole. Especially, dimerization would probably happen on the thiophene ring. It should be noted that some small multiple oxidation and reduction peaks were observed in consecutive cycling of the applied potential, due to the electrochemical reactivity of the intermediates from the EC reaction mechanisms (see more detail in the ECL section).

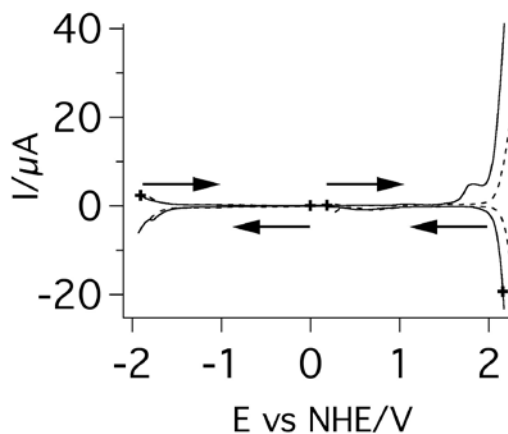


Figure 2.3. Differential pulse voltammograms of **2.1** (solid lines) in DMF containing 0.1 M TBAP as supporting electrolyte, and blank solution (dotted lines), with the initial scan from 0.000 to 2.118 V (top, anodic scan), and initial scan from 0.000 to -1.929 V (bottom, cathodic scan) and their reverse scans.

Typical DPVs of compound **2.1** conducted in the similar manner as in CVs in Figure 2.1, are illustrated in Figure 2.3, where the first irreversible oxidation and reduction peaks of **2.1** are well displayed. Again, isolating the anodic and cathodic DPVs avoids any additional redox peaks as seen in Figure 2.4. This agrees well with the observation from CVs because of the electrochemical reactivity of the intermediates. The formal potentials ($E^{0'}$) of **2.1** can be determined from DPVs by Eq. 2.2^{52,53}:

$$E^{0'} = E_{\max} + \Delta E/2 \quad (2.2)$$

where E_{\max} represents the peak potential in the DPV and ΔE represents the pulse height, 50 mV.

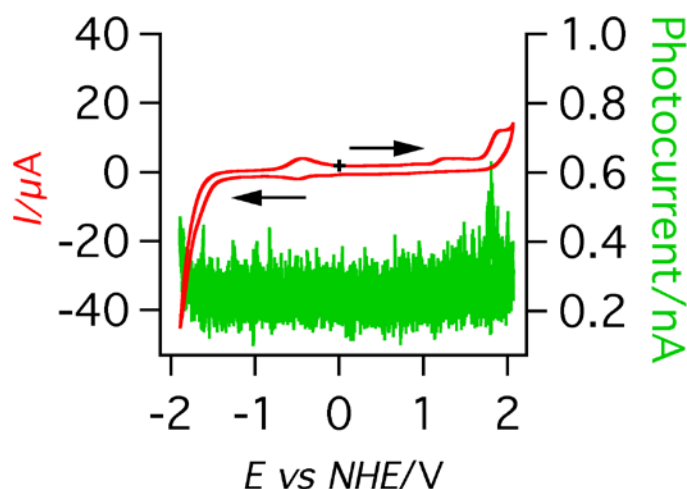


Figure 2.4. Cyclic voltammogram (red) and ECL-voltage curve (green) of **2.1** scanned at 0.1 V/s with the initial potential at 0.000 to 2.069 V then scanned to -1.889 V and back to 0.000 V.

The oxidation peak at 1.826 V in the anodic scan and reduction peak at -1.785 V in the cathodic scan were more visible, Figure 2.3, than in CV, Figure 2.1, since DPV suppresses the background signal and enhances sensitivity.⁴⁵

The electrochemical behaviours of compounds **2.2-2.4** were also characterized using CV and DPV, from which it can be concluded that compounds **2.2-2.4** undergo irreversible oxidation and reduction reactions, and their radical cations and anions are not stable.

All the electrochemical data have been summarized in Table 2.1. The electrochemical gaps, which are the potential difference between the formal potentials of the first reduction and oxidation, match well with their corresponding HOMO-LUMO energy gaps. The excited state gap taken from the PL emission wavelength from Table 2.2 shows similar energy values as the experimental energy values in Table 2.1.

From Table 2.1, there was a general trend of decreasing oxidation potential with increasing conjugation. The addition of a second thiophene ring in **2.3** decreases the oxidation potential from 1.851 V, in **2.1**, to 1.488 V in **2.3**. This trend, however, was not

apparent in the reduction potentials of **2.1-2.4**. Noticeably, Compound **2.4** underwent up to 4 reduction reactions as summarized in Table 2.1. Nevertheless, the trend of smaller electrochemical gaps, as seen in CV and DPV, with increasing conjugation was observed from our experimental data and from previous DFT quantum chemistry calculations our group has reported.³⁸ Here, the HOMO-LUMO gap decreases in **2.3**, 3.94 eV, relative to **2.1**, 4.15 eV, having greater delocalization of the π electrons due to increased conjugation in the aromatic system, Table 2.1.

Table 2.1. Electrochemical (from DPV) and quantum chemistry calculation data of compounds **2.1-1.4**.

	$E_{p,a}$ oxidation/V ^a	$E_{p,c}$ reduction/V ^a	$E^{0'}$ oxidation/V ^a	$E^{0'}$ reduction/V ^a	Electrochemical gap/eV	Theoretical HOMO/eV ^c	Theoretical LUMO/eV ^c	Theoretical HOMO-LUMO gap/eV
2.1	1.826	-1.785	1.851	-1.810	3.66	-5.90	-1.74	4.15 ^b
2.2	1.268	-2.081/ -2.449	1.293	-2.106/ -2.474	3.40	-5.88	-1.70	4.18 ^c
2.3	1.463	-1.948	1.488	-1.973	3.46	-5.90	-1.96	3.94 ^c
2.4	0.765/1.365	-1.310/ -1.550/ -1.806/ -2.480	0.790/1.390	-1.335/ -1.575/ -1.831/ -2.505	2.13	-5.93	-3.02	2.92 ^c

^aIn V vs. NHE at 0.1 V/s scan rate.

^bEnergy value obtained from previously reported data, DFT/B3LYP/6-31G* calculations.³⁸

^cEnergies obtained from DFT/B3LYP/6-31G* calculations.

For compounds **2.1** and **2.2**, the gaps, of 4.15 eV and 4.18 eV, were larger due to smaller conjugated systems. Synthesizing compounds with an additional thiophene ring, **2.3**, and extended aromatic system, **2.4**, the HOMO-LUMO gaps for these conjugated systems decreased to 3.94 eV for **2.3** and 2.92 eV for **2.4**. These values followed a similar trend as the experimental HOMO-LUMO gaps from the oxidation and reduction potentials of **2.1-2.4** as seen in Table 2.1. The gap observed in **2.2** from experimental data was smaller, 3.40 eV, than **2.1**, 3.66 eV, this may be due the slightly out-of-plane aromatic system of **2.1** compared to in-plane system of **2.2**. However, the HOMO-LUMO gap calculations were calculated from a solid-state representation of each compound, whereas, the redox, ECL and spectral data were obtained from solutions of these compounds. We must take into consideration the free rotation of the compounds in solution. Here, we would expect variations in the data as seen in the differences between the theoretical and experimental data.

2.3.2 ECL via Annihilation Mechanisms

Figure 2.4 shows the CV overlaid with the ECL-voltage curve of **2.1** that were run simultaneously in the potential range between its first oxidation and reduction peaks. During these continuous scans, we observed additional bumps/peaks in the middle of the potential window. These peaks were not from the neutral compound as demonstrated in Figure 2.1: when the applied potential was scanned separately for oxidation and reduction peaks, these additional peaks were not present. In addition, there were neither cathodic peak for oxidation and nor anodic peak for reduction in CVs, Figure 2.1. This is evidence that both radicals were not stable. Cations underwent chemical reactions to generate reduction-active species while radical anion generated redox-active species. However, we cannot determine which are the species.

At both positive and negative potential limits, weak ECL was observed. A slightly stronger emission of light was observed in the positive potential region. The radical cations appear to be more stable than the radical anions for **2.1**, as stronger ECL was detected in the region of positive potential, Figure 2.4. The weak ECL was expected since both radical cations and anions were not stable as observed from the irreversibility of its

electrochemical behaviours. The ECL given off from **2.1**, written as ThdC, was proposed *via* annihilation of radical cations, ThdC^{•+}, with radical anions, ThdC^{•-}, generated electrochemically, Eqs. 2.3 and 2.4.



An excited species, ThdC^{*}, and a ground-state species, ThdC, of **2.1**, are the products of the annihilation as seen in Eq. 2.5. The excited species then relaxes to its ground state, ThdC, as seen in Eq. 2.6 and emits light.



Figure 2.4 also shows that ECL can only be detected after one complete cycle of the potential sweep. In practice, two cycles or four segments of the potential sweep were conducted for each compound.

Compound **2.2** displayed similar ECL emission to that from compound **2.1**, and demonstrated stronger ECL intensity in the anodic region than in the cathodic region. For **2.3**, ECL emission was observed in the region of negative potential and **2.4** did not show a significant increase in positive or negative potential regions. Nevertheless, weak ECL was generated through annihilation mechanisms from compounds **2.3-2.4**, because of the irreversible redox reactions, resulting in unstable radical ions. The ECL efficiencies were determined as the photons emitted per redox event relative to the standard, DPA, as expressed in Eq. 2.1.⁵⁰ These ECL efficiencies, Table 2.2, were low relative to the standard, which were in a range between 0.40 to 0.52 % for **2.1**, 0.39 to 0.41 % for **2.2**, and 0.71 to 1.08 % for **2.3**. Compound **2.4** had the smallest ECL efficiency, ranging between 0.10 to 0.24 %.

Table 2.2. ECL data of compounds **2.1-2.4** in annihilation and co-reactant systems.

	Annihilation		Co-reactant		PL	Shifts ^b
	Scanning QE ^a /%	Scanning QE ^a /%	Pulsing QE ^a /%	λ_{\max} /nm	λ_{\max} /nm	λ_{\max} (ECL)- λ_{\max} (PL)/nm
2.1	0.40-0.52	0.33-1.48	0.71	515	375	140
2.2	0.39-0.41	0.73-0.86	0.20	395/577	380	15/197
2.3	0.71-1.08	0.24-0.39	0.25	588	380	208
2.4	0.10-0.24	0.54-2.33	1.87	556	385	171

^aECL quantum efficiencies (QE) measured in DMF relative to DPA ($\Phi_{\text{ECL}} = 100\%$ or 1.0 in DMF)^{48,49}.

^bThe shifts represent the difference between the ECL (in DMF) and PL (in EtOH)³⁸ emission wavelengths. Only small shifts (<5 nm) in PL emission maxima were observed when varying the solvent composition from EtOH to DMF.

2.3.3 ECL via Co-reactant Mechanisms

Figure 2.5 shows the CV overlaid with the simultaneous ECL-voltage curve of **2.1** containing BPO. The applied potential was only needed to scan in the cathodic region. In this way the short-life radical anions, ThdC^{•-}, generated can immediately react with their counterparts.^{54,1} Sometimes the radical cations can be generated directly from the co-reactant.

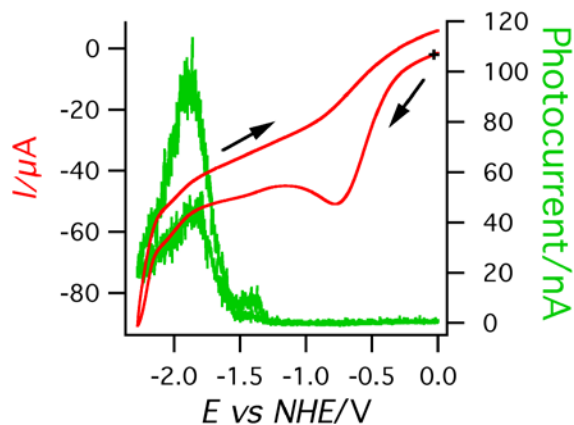
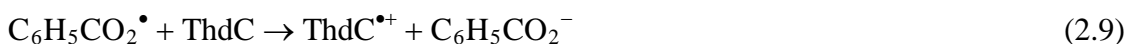


Figure 2.5. Cyclic voltammogram (red) and ECL-voltage curve (green) of **2.1** with 5.0×10^{-3} M BPO scanned at 0.1 V/s, with the initial scan from 0.000 to -2.278 V and back to 0.000 V.

It was discovered that ECL was enhanced when 5.0×10^{-3} M BPO was added to the solutions of **2.1-2.4**. The proposed ECL co-reactant mechanism for **2.1** begins when a negative potential is applied to the system, initially at 0.000 V, as seen in Figure 2.5 for compound **2.1**. Upon scanning to more negative potential, BPO is first reduced to its radical anion, $\text{BPO}^{\bullet-}$, at -0.780 V, Eq. 2.7. The radical anion, $\text{BPO}^{\bullet-}$, immediately decomposes to form a strong oxidizing intermediate radical, $\text{C}_6\text{H}_5\text{CO}_2^{\bullet}$, and $\text{C}_6\text{H}_5\text{CO}_2^-$, Eq. 2.8. This intermediate radical, $\text{C}_6\text{H}_5\text{CO}_2^{\bullet}$, reacts with **2.1** and generates the radical cation of **2.1**, $\text{ThdC}^{\bullet+}$, Eq. 2.9.



With the applied potential scanned to more negative potential, the radical anion of **2.1**, $\text{ThdC}^{\bullet-}$, was generated at -1.835 V, Eq. 2.4. The radical cation, $\text{ThdC}^{\bullet+}$, combines with the radical anion, $\text{ThdC}^{\bullet-}$, and generates an excited species, ThdC^* , of **2.1**, as stated

previously with the annihilation mechanism Eqs. 2.5 and 2.6, which relaxes down to its ground state, ThdC, and light is emitted.

An increase in photocurrent as shown in Figure 2.5 was observed when scanning to negative potential. The use of BPO contributes to the enhanced ECL intensities of **2.1-2.4** relative to the intensities observed in annihilation studies.

It is important to note that there was a relatively weak ECL peak in Figure 2.5 that was observed right after the BPO reduction potential, -0.780 V, but even before the reduction of compound **2.1**. In fact, the ThdC^{•+} generated through Eqs. 2.7 to 2.9 can react with BPO^{•-}, Eq. 2.10 to produce the excited species, ThdC^{*}:



Compounds **2.2-2.4**, in the same co-reactant system, displayed higher intensities of ECL than in annihilation systems relative to DPA as seen in Table 2.2. ECL was observed in all compounds after the reduction of BPO, following the same mechanism, Eq. 2.10.

The intensity of ECL varied from **2.1-2.4**. Compounds **2.1** and **2.4** displayed the highest ECL intensities with photocurrents around 100 nA for **2.1** and 180 nA for **2.4**. The efficiencies for these compounds were in a range between 0.33 to 1.48 % for **2.1** and 0.54 to 2.33 % for **2.4**. Compounds **2.2** and **2.3** had lower ECL intensities, relative to **2.1** and **2.4**, with photocurrents around 85 nA for **2.2** and 30 nA for **2.3**. The efficiencies were in a range between 0.73 to 0.86 % for **2.2** and 0.24 to 0.39 % for **2.3**.

ECL was enhanced when the applied potential was pulsed in the cathodic region between 0.000 V and low limit potential value for the compound reduction as obtained from CV experiments with a pulse width of 0.1 s. Instead of slowly scanning the potential from 0.000 V to -2.278 V in Figure 2.5, the working electrode was pulsed quickly between these potential values and an increase in intensity of ECL was observed. The efficiencies for these compounds were 0.71 % for **2.1**, 0.20 % for **2.2**, 0.25 % for **2.3**, and 1.87 % for **2.4**. Pulsing generates radical cations and anions in a faster alternative pace

and reduces the decay of the unstable radicals, leading to greater occasions for the cations and anions to meet, react, and emit light.

2.3.4 ECL Spectroscopy

Figure 2.6 shows the co-reactant ECL spectra of **2.1-2.4** with BPO during the pulsing of the applied potential in the cathodic regions (till the reduction of the compounds). The spectrum for **2.1** in the co-reactant system was fitted to one peak centered at 515 nm, Figure 2.6a (see spectra with curve-fitting, Figure S2.1, in Appendix D). The peak at 515 nm was red-shifted relative to that in PL by 140 nm. The long wavelength ECL can be assigned to emission from excimers.³⁸

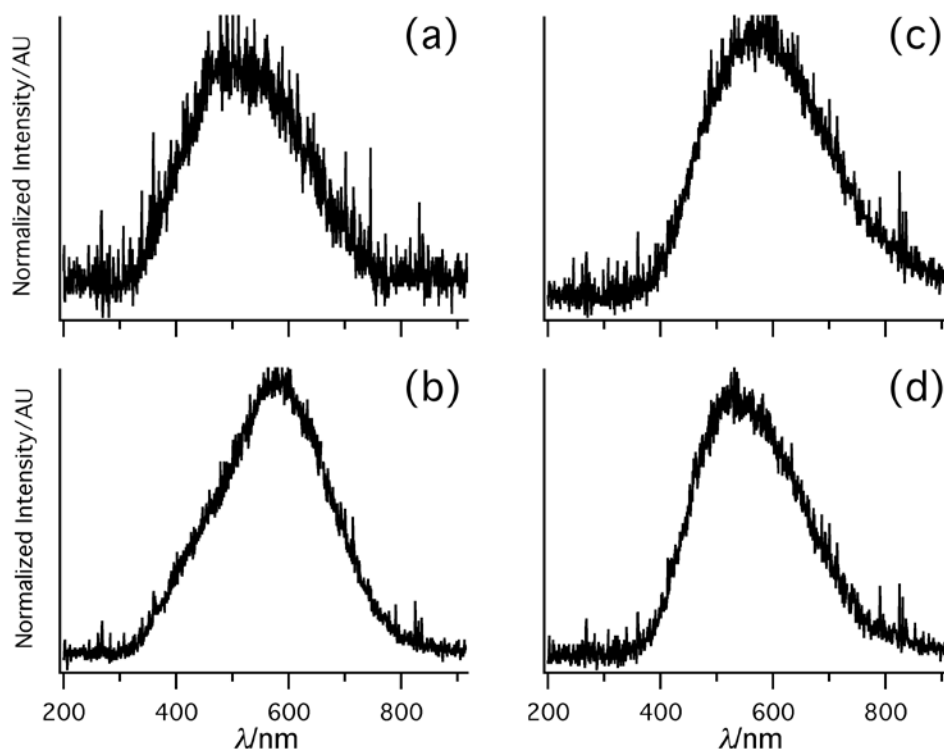


Figure 2.6. ECL spectra of **2.1-2.4** in DMF containing 5.0×10^{-3} M BPO and 0.1 M TBAP as supporting electrolyte and pulsing between potential ranges from (a) 0.000 to -2.278 V, $t = 60$ s for **2.1**, (b) 0.000 to -2.452 V, $t = 60$ s for **2.2**, (c) 0.000 to -2.517 V, $t = 60$ s for **2.3**, and (d) 0.000 to -2.126 V, $t = 60$ s for **2.4**. ECL intensities were normalized by their respective peak heights.

Excimers are excited states of dimers that can be observed in ECL of organic compounds.^{15,16} The formation of excimers might result from dimerization of the radical anion and cation or stacking of the monomer in the excited state with a monomer in the ground state due to the π conjugation of the modified nucleobase.⁵⁰ A possible mechanism for excimer growth in ECL for **2.1** is shown in Eqs. 2.11 to 2.13.⁵⁵ ThdC* can react with the ground state species ThdC to form an excimer as seen in Eq. 2.11. Another possible route for excimer formation involves the radical cation and anion species to form the excimer, (ThdC)₂^{*}, Eq. 2.12. The excimer can then relax down to its ground state and emit light, Eq. 2.13. For compound **2.1**, both the two routes are possible:



The energy of the resulting excited species, (ThdC)₂^{*}, was lower than that of the reactants and relaxes down to the ground state, ThdC, and a longer wavelength than the monomer will be observed, similar to the spectrum of **2.2**, Figure 2.6b. For **2.2**, the spectrum showed two peaks, one at 395 nm and the second broad band at 577 nm. The peaks were red-shifted by 15 and 197 nm with respect to the PL peak seen at 380 nm. From Eqs. 2.5 and 2.6, and Eqs. 2.9 to 2.13, we observed excited monomer and excimer formation from the two given pathways. It appears that as conjugation increases in the modified nucleosides, ECL emission becomes more red-shifted. Compound **2.3**, Figure 2.6c, showed one maximum at 588 nm and displayed the most significant red-shift of 208 nm relative to the PL peak at 380 nm. Furthermore, the maximum wavelength of compound **2.4**, Figure 2.6d, was at 556 nm, red-shifted to PL by 171 nm respectively. The growth in excimer formation was more easily observed with **2.2**, Figure 2.6b, and the most red-shifted compounds were **2.2**, **2.3** and **2.4**. We can conclude that compounds **2.1-2.4** can easily form excimers, however there was a combination of monomer and excimer present in ECL system **2.2** by pulsing the electrode potential.

The crystal structures of **2.1**, Figure 2.2, and **2.2**³⁸ illustrate the coplanar shape of the conjugated aromatic ring systems for these four compounds, allowing the π electrons to delocalize over the aromatic ring systems and therefore lowering the band gap between the HOMO and LUMO. This enhances the effective conjugation length and consequently causes emission peak to red-shift relative to the photoluminescence (PL) peaks as previously reported.³⁸

2.4 Conclusions

We have determined the redox potentials and calculated the ECL efficiencies of a series of modified triazolyldeoxycytidine nucleosides, **2.1-2.4**. With increasing conjugation in the luminophore, we observed a decrease in the separation between first oxidation and reduction peaks of the compounds. The annihilation ECL efficiencies were weak relative to DPA, ranging from 0.40 to 0.52 % for **2.1**, 0.39 to 0.41 % for **2.2**, 0.71 to 1.08 % for **2.3**, and 0.10 to 0.24 % for **2.4**. The efficiencies increased in the co-reactant systems with ECL efficiencies ranging from 0.33 to 1.48 % for **2.1**, 0.73 to 0.86 % for **2.2**, 0.24 to 0.39 % for **2.3**, and 0.54 to 2.33 % for **2.4**. The ECL spectra were red-shifted relative to the corresponding PL spectra previously reported with wavelengths ranging from 515 nm for **2.1**, 395 and 577 nm for **2.2**, 588 nm for **2.3**, and 556 nm for **2.4**. The generation of excimers in **2.1-2.4**, with the monomer still present in **2.2**, was observed in the ECL systems studied. The radical anions and cations generated in solution follow two pathways, *via* electron transfer, and combination of electron transfer and dimerization, forming excited species and excimers. Incorporating these modified nucleosides into ssDNA, and hybridizing the modified ssDNA with a complimentary ssDNA or a single-base mis-matched ssDNA may allow for an ECL readout which could give information on the nature of the mismatch, thereby leading to an effective means of SNP typing. ECL is a fast, cost effective technique that requires low quantity and is highly selective, sensitive, and tunable with our electrochemical instrumentation and detection systems. Using ECL detection with these modified nucleosides is in progress towards SNP typing of genes pertinent to various human genetic disorders.

2.5 References

- (1) Bard, A. J. *Electrogenerated Chemiluminescence*; Marcel Dekker, Inc.: New York, **2004**.
- (2) Hercules, D. M. *Science* **1964**, *145*, 808.
- (3) Visco, R. E.; Chandross, E. A. *J. Am. Chem. Soc.* **1964**, *86*, 5350.
- (4) Santhanam, K. S. V.; Bard, A. J. *J. Am. Chem. Soc.* **1965**, *87*, 139.
- (5) Pyati, R.; Richter, M. M. *Annu. Rep. Prog. Chem., Sect. C* **2007**, *103*, 12.
- (6) Richter, M. M. *Chem. Rev.* **2004**, *104*, 3003.
- (7) Kulmala, S.; Suomi, J. *Anal. Chim. Acta* **2003**, *500*, 21.
- (8) Fähnrich, K. A.; Pravda, M.; Guilbault, G. G. *Talanta* **2001**, *54*, 531.
- (9) Knight, A. W. *Trends in Anal. Chem.* **1999**, *18*, 47.
- (10) Laser, D.; Bard, A. J. *J. Electrochem. Soc.* **1975**, *122*, 632.
- (11) Miao, W. *Chem. Rev.* **2008**, *108*, 2506.
- (12) Hu, L.; Xu, G. *Chem. Soc. Rev.* **2010**, *39*, 3275.
- (13) Krishnan, S.; Hvastkovs, E. G.; Bajrami, B.; Choudhary, D.; Schenkman, J. B.; Rusling, J. F. *Anal. Chem.* **2008**, *80*, 5279.
- (14) Rusling, J. F.; Hvastkovs, E. G.; Hull, D. O.; Schenkman, J. B. *Chem. Commun.* **2008**, *2*, 141.
- (15) Lai, R. Y.; Fleming, J. J.; Merner, B. L.; Vermeij, R. J.; Bodwell, G. J.; Bard, A. J. *J. Phys. Chem. A* **2004**, *108*, 376.
- (16) Choi, J.-P.; Wong, K.-T.; Chen, Y.-M.; Yu, J.-K.; Chou, P.-T.; Bard, A. J. *J. Phys. Chem. B* **2003**, *107*, 14407.
- (17) Drummond, T. G.; Hill, M. G.; Barton, J. K. *Nat. Biotechnol.* **2003**, *21*, 1192.
- (18) Xu, X.; Bard, A. J. *J. Am. Chem. Soc.* **1995**, *117*, 2627.
- (19) Marquette, C. A.; Blum, L. J. *Anal. Bioanal. Chem.* **2008**, *390*, 155.
- (20) Miao, W.; Bard, A. J. *Anal. Chem.* **2003**, *75*, 5825.
- (21) Furukawa, K.; Abe, H.; Wang, J.; Uda, M.; Koshino, H.; Tsuneda, S.; Ito, Y. *Org. Biomol. Chem.* **2009**, *7*, 671.

- (22) Pinnisi, E. *Science* **1998**, *281*, 1787.
- (23) Tyagi, S.; Bratu, D. P.; Kramer, F. R. *Nat. Biotechnol.* **1998**, *16*, 49.
- (24) Silverman, A. P.; Kool, E. T. *Chem. Rev.* **2006**, *106*, 3775.
- (25) Li, X.; Liu, D. R. *Angew. Chem. Int. Ed.* **2004**, *43*, 4848.
- (26) Tyagi, S.; Kramer, F. R. *Nat. Biotechnol.* **1996**, *14*, 303.
- (27) Okamoto, A.; Tanaka, K.; Fukuta, T.; Saito, I. *J. Am. Chem. Soc.* **2003**, *125*, 9296.
- (28) Okamoto, A.; Tanaka, K.; Fukuta, T.; Saito, I. *ChemBioChem* **2004**, *5*, 958.
- (29) Zhang, J.; Sun, X. J.; Smith, K. M.; Visser, F.; Carpenter, P.; Barron, G.; Peng, Y. S.; Robins, M. J.; Baldwin, S. A.; Young, J. D.; Cass, C. E. *Biochemistry* **2006**, *45*, 1087.
- (30) Liu, L. F.; Li, Y. F.; Liotta, D.; Lutz, S. *Nucleic Acids Res.* **2009**, *37*, 4472.
- (31) Secrist, J. A.; Barrio, J. R.; Leonard, N. J. *Science* **1972**, *175*, 646.
- (32) Andersen, N. K.; Spáčilová, L.; Jennings, M. D.; Kočalka, P.; Jensen, F.; Nielsen, P. In *Joint Symposium of the 18th International Roundtable on Nucleosides, Nucleotides and Nucleic Acids and the 35th International Symposium on Nucleic Acids Chemistry*; No. 52 ed. Kyoto, Japan, **2008**, p 149.
- (33) Hassan, M. E. *Nucleosides & Nucleotides* **1991**, *10*, 1277.
- (34) Peters, D.; Hörnfeldt, A.-B.; Gronowitz, S.; Johansson, N. G. *Nucleosides & Nucleotides* **1992**, *11*, 1151.
- (35) Mizuta, M.; Banba, J.-I.; Kanamori, T.; Tawarada, R.; Ohkubo, A.; Sekine, M.; Seio, K. *J. Am. Chem. Soc.* **2008**, *130*, 9622.
- (36) Tokel-Takvoryan, N. E.; Hemingway, R. E.; Bard, A. J. *J. Am. Chem. Soc.* **1973**, *95*, 6582.
- (37) Swanick, K. N.; Dodd, D. W.; Hudson, R. H. E.; Ding, Z.; Jones, N. D. In *19th QOMSBQC Toronto, Canada*, **2008**, p 40.
- (38) Dodd, D. W.; Swanick, K. N.; Price, J. T.; Brazeau, A. L.; Ferguson, M. J.; Jones, N. D.; Hudson, R. H. E. *Org. Biomol. Chem.* **2010**, *8*, 663.
- (39) Kočalka, P.; Andersen, N. K.; Jensen, F.; Nielsen, P. *ChemBioChem* **2007**, *8*, 2106.

- (40) Munshi, V.; Lu, M.; Felock, P.; Barnard, R. J. O.; Hazuda, D. J.; Millers, M. D.; Lai, M.-T. *Anal. Biochem.* **2008**, *374*, 121.
- (41) Kolb, H. C.; Finn, M. G.; Sharpless, K. B. *Angew. Chem. Int. Ed.* **2001**, *40*, 2004.
- (42) Kolb, H. C.; Sharpless, K. B. *Drug Discov. Today* **2003**, *8*, 1128.
- (43) Wu, P.; Folkin, V. V. *Aldrichimica Acta* **2007**, *40*, 7.
- (44) Wu, P.; Feldman, A. K.; Nugent, A. K.; Hawker, C. J.; Scheel, A.; Voit, B.; Pyun, J.; Fréchet, J. M. J.; Sharpless, K. B.; Folkin, V. V. *Angew. Chem. Int. Ed.* **2004**, *43*, 3928.
- (45) Bard, A. J.; Ding, Z.; Myung, N. In *Structure & Bonding*; Springer Berlin/Heidelberg: **2005**; Vol. 118, p 1.
- (46) Cerviño, R. M.; Triaca, W. E.; Arvia, A. J. *J. Electroanal. Chem.* **1985**, *182*, 51.
- (47) Haram, S. K.; Quinn, B. M.; Bard, A. J. *J. Am. Chem. Soc.* **2001**, *123*, 8860.
- (48) Omer, K. M.; Ku, S.-Y.; Wong, K.-T.; Bard, A. J. *Angew Chem Int Edit* **2009**, *48*, 9300.
- (49) Bezman, R.; Faulkner, L. R. *J. Am. Chem. Soc.* **1972**, *94*, 6317.
- (50) Booker, C.; Wang, X.; Haroun, S.; Zhou, J.; Jennings, M.; Pagenkopf, B. L.; Ding, Z. *Angew. Chem. Int. Ed.* **2008**, *47*, 7731.
- (51) Wallace, W. L.; Bard, A. J. *J. Phys. Chem.* **1979**, *83*, 1350.
- (52) Bard, A. J.; Faulkner, L. R. *Electrochemical methods, fundamentals and applications*; 2nd ed.; John Wiley & Sons Inc.: New York, **2001**.
- (53) Girault, H. H. In *Presses Polytechnique et Universitaires Romandes* Laussane, Switzerland, **2001**.
- (54) Ding, Z.; Quinn, B. M.; Haram, S. K.; Pell, L. E.; Korgel, B. A.; Bard, A. J. *Science* **2002**, *296*, 1293.
- (55) Prieto, I.; Teetsov, J.; Fox, M. A.; Vanden Bout, D. A.; Bard, A. J. *J. Phys. Chem. A* **2001**, *105*, 520.

Chapter 3

3 Synthesis, Structure, Electrochemistry, and Electrochemiluminescence of Thienyltriazoles[†]

3.1 Introduction

Currently there has been increasing interest in materials for electrochemiluminescent sensors and organic light-emitting diodes, OLEDs, for applications in television and lighting technology.¹ Organic luminescence is also a promising technology for the fabrication of flat panel displays.² The design of new luminophores has been driven by the requirement for RGB full colour displays and white light illumination applications.³⁻⁷ The emission colour tuning in Alq₃, tris(8-hydroxyquinolino)aluminum, analogues has been investigated with extended conjugated chromophores,⁸ and by modifying the N-O containing compounds by the addition of electron-withdrawing, EWG, or electron-donating groups, EDG.^{3,8-10} Our group has studied the behaviour of some triazole-modified deoxycytidine analogues in previous work.¹¹

In this report we synthesized and studied the spectroscopic properties and electrochemistry of four potential blue-emitting thienyltriazoles with N in the thienyltriazole ring and O in a methoxy or phenol group attached to the triazole acting as possible coordination atoms to form metal complexes. Our attention has been focused on designing modified thienyltriazoles to tune deep-blue fluorescence using “click chemistry”.¹²⁻¹⁵ The modulation of our thienyltriazoles is based on the reaction of azidothiophenes with terminal alkynes with a hydroxyl group to form a triazole ring, thus creating a fluorescent multi-conjugated ring system with a hydroxyl group. Varying the conjugation in the thiophene ring system or adding a phenyl substituent between the

[†] This work is reprinted with permission from Kalen N. Swanick, Jacquelyn T. Price, Nathan D. Jones, and Zhifeng Ding, *J. Org. Chem.*, **2012**, *77*, 5646-5655. Copyright **2012** American Chemical Society (ACS). See Appendix II.

thiophene-triazole backbone and the hydroxyl group might potentially modulate the ECL efficiencies before complexation with metals. Click chemistry with simple small molecules, allows us to achieve the desired blue emission from the thiophene-triazoles (our first stage) while the hydroxyl group along with the triazole afford us potential N-O containing metal complex emitters (our second stage). In this context, four thienyltriazoles, **3.1-3.4**, have been synthesized in this study as seen in Scheme 3.1 and Scheme 3.2. Note that our thienyltriazoles are blue luminescent.

Electrochemiluminescence or electrogenerated chemiluminescence, ECL, generates luminescence in solution¹⁶, while electroluminescent devices, generate luminescence in the solid state. ECL involves light emission that is produced by an energetic electron transfer reaction between electrochemically generated radicals in the vicinity of an electrode.¹⁷ Two general methods for producing ECL are “annihilation” and “co-reactant” reactions.¹⁷ In annihilation systems, radical cations and anions are generated in solution and light emission results when they combine. Co-reactant studies are useful when a system does not give stable radical cations or anions. Co-reactant intermediates are either strong reducing agents in oxidative-reduction ECL or strong oxidizing agents in reductive-oxidation ECL.¹⁷ Benzoyl peroxide (BPO) is a common co-reactant and produces a strong oxidizing agent when reduced; this has been selected for the purpose of our studies.¹⁷ Previously, we have studied the ECL of iridium(III) complexes containing aryltriazoles that emitted blue light.¹⁸ We wanted to investigate if the prepared thienyltriazole ligands were electrochemiluminescent. Here, we report the electrochemical properties of **3.1-3.4** in Table 3.1, and the ECL spectra and corresponding ECL efficiencies, from annihilation and co-reactant pathways, in Table 3.3. Furthermore, using ECL to detect light is of importance for possible applications in biosensors, OLED displays, optoelectronics, microelectronics and bioanalytical chemistry.^{1,3,19-26}

3.2 Experimental Section

General Methods. For synthesis and characterization, all reagents were purchased from commercial sources and used as supplied unless otherwise indicated. All

experiments were conducted in air unless otherwise noted. Reactions that were carried out under an atmosphere of Ar were conducted using standard Schlenk techniques. Thin-layer chromatography was performed using 250 μm silica gel glass-backed plates and visualized by UV light. Flash column chromatography was performed using SiliaFlash P60, 40-63 μm (D50) 60 \AA , silica gel. All solvent mixtures were reported as volume ratios. Melting points were obtained using a Fisher-John melting point apparatus and reported uncorrected. The ^1H and $^{13}\text{C}\{^1\text{H}\}$ NMR data were recorded on a 400 MHz spectrometer at room temperature. The δ values, reported in ppm, were referenced as follows for ^1H (400.085 MHz) CDCl_3 (7.26 ppm); $\text{DMSO-}d_6$ (2.49 ppm); CD_3OD (3.31 ppm), and for $^{13}\text{C}\{^1\text{H}\}$ (100.602 MHz) CDCl_3 (77.16 ppm) and $\text{DMSO-}d_6$ (39.52 ppm). Data for the ^1H NMR spectra were reported as follows: chemical shift (δ), multiplicity, integration, assignment, and coupling constant(s). All coupling constants were reported in Hertz (Hz) and the spin multiplicities were indicated as follows: singlet (s), doublet (d), doublet of doublets (dd), triplet (t), and multiplet (m). High resolution mass spectrometry (HRMS) data were collected using electron spray (ESI) time-of-flight technique.

General Procedure for the Synthesis of Thienyltriazoles, 3.1-3.4, via Cu(I) Catalyzed Huisgen 1,3-Dipolar Cycloaddition. The following compounds were synthesized based on previous literature: 3-azidothiophene²⁶, 4-azido-2,2'-bithiophene²⁶, and 2-ethynylphenol²⁷. Compounds **3.1-3.4** were made by reacting either 2-propargyl alcohol, Scheme 3.1, or 2-ethynylphenol, Scheme 3.2, with one of the two corresponding thienylazides in the presence of a Cu(I) catalyst, from CuSO_4 and sodium ascorbate, in a 1:1 *t*-butanol: H_2O solution. The isolated products, **3.1-3.4**, were isolated then purified for electrochemical and spectroscopic analyses and for X-ray crystallography, **3.1**, **3.2**, and **3.4**, see Appendix II for NMR peak assignments.

Synthesis of [1-(2,2'-bithien-4-yl)-1H-1,2,3-triazol-4-yl]methanol (3.1, BiTTM). To a solution of 4-azido-2,2'-bithiophene (0.80 g, 3.8 mmol), 2-propargyl alcohol (0.22 g, 3.8 mmol) and *t*-butanol- H_2O (1:1, 6 mL), CuSO_4 (0.098 g, 0.62 mmol) was added at room temperature and stirred for 5 min. Sodium ascorbate (0.038 g, 0.19 mmol) was then added. The solution was initially yellow and the reaction mixture was stirred overnight at 35 $^\circ\text{C}$. After 16 h, the solution was yellow-brown. The product was

extracted with ethylacetate (3 × 10 mL) and washed with H₂O (3 × 10 mL). The combined organic phase, brown, was washed with ethylacetate (10 mL) and Brine (10 mL), dried (MgSO₄) and concentrated under vacuum to afford 0.82 g (81% yield) of **3.1**, light brown powder, mp 140-143 °C. HRMS: calcd for C₁₁H₉N₃OS₂ ([M]) 263.0187, found 263.0186.

Synthesis of [1-(3-thienyl)-1H-1,2,3-triazol-4-yl]methanol (3.2, TTM). To a solution of 3-azidothiophene (0.064 g, 0.51 mmol), 2-propargyl alcohol (0.037 g, 0.66 mmol) and *t*-butanol-H₂O (1:1, 2mL), CuSO₄ (0.017 g, 0.11 mmol) was added at room temperature and stirred for 5 min. Sodium ascorbate (0.007 g, 0.03 mmol) was then added. The solution was initially yellow and the reaction mixture was stirred overnight at 35 °C. After 16 h, the solution was yellow-brown. The product was extracted with ethylacetate (3 × 10 mL) and washed with H₂O (3 × 10 mL). The combined organic phase, yellow, was washed with ethylacetate (10 mL) and Brine (10 mL), dried (MgSO₄) and concentrated under vacuum. The product was dissolved in ethyl acetate and methanol. Hexanes was added to the solution then left for recrystallization over a period of 5 days. This afforded 0.089 g (96% yield) of **3.2**, golden crystals, mp 127-130 °C. HRMS: calcd for C₇H₇N₃OS ([M]) 181.0310, found 181.0308.

Synthesis of 2-[1-(2,2'-bithien-4-yl)-1H-1,2,3-triazol-4-yl]phenol (3.3, BiTTP). To a solution of 4-azido-2,2'-bithiophene (0.33 g, 1.6 mmol), 2-ethynylphenol (0.19 g, 1.6 mmol) and *t*-butanol-H₂O (1:1, 12 mL), CuSO₄ (0.041 g, 0.25 mmol) was added at room temperature and stirred for 5 min. Sodium ascorbate (0.016 g, 0.079 mmol) was then added. The solution was initially yellow and the reaction mixture was stirred overnight at 35 °C. After 72 h, the solution was yellow-brown. The product was extracted with ethylacetate (3 × 10 mL) and washed with H₂O (3 × 10 mL). The combined organic phase, brown, was washed with ethylacetate (10 mL) and Brine (10 mL), dried (MgSO₄) and concentrated under vacuum. The product was dissolved in MeOH (10 mL) then concentrated under vacuum to afford 0.42 g (81% yield) of **3.3**, light brown powder, mp 180-184 °C. HRMS: calcd for C₁₆H₁₁N₃OS₂ ([M]) 325.0344, found 325.0336.

Synthesis of 2-[1-(3-thienyl)-1H-1,2,3-triazol-4-yl]phenol (3.4, TTP). To a solution of 3-azidothiophene (0.28 g, 2.28 mmol), 2-ethynylphenol (0.27 g, 2.28 mmol) and *t*-butanol-H₂O (1:1, 10mL), CuSO₄ (0.058 g, 0.36 mmol) was added at room temperature and stirred for 5 min. Sodium ascorbate (0.023 g, 0.11 mmol) was then added. The solution was initially yellow. After stirring at 35 °C for 18 h, the solution turned brown-green with a precipitate. The product was extracted with ethylacetate (3 × 10 mL) and washed with H₂O (3 × 10 mL). The combined organic phase, brown solution, was washed with ethylacetate (10 mL) and Brine (10 mL), dried (MgSO₄) and concentrated under vacuum to afford 0.46 g (84% yield) of **3.4**, light brown powder, mp 170-176 °C. HRMS: calcd for C₁₂H₉N₃OS ([M]) 243.0466, found 243.0462.

Infrared Measurements. Infrared spectroscopy measurements were recorded using a Fourier transform infrared spectrometer; samples were run between KBr plates. The wavenumbers, $\tilde{\nu}$ values, were reported in cm⁻¹; peak intensities were given as follows: strong (s), medium (m) and weak (w).

UV-Visible and Photoluminescence Measurements. UV-visible absorption (Abs) and photoluminescence (PL) spectra were recorded over the range of 200-800 nm using a fluorimeter with a xenon flash lamp and PMT detector (190-680 nm) interfaced to a computer workstation. Quartz cuvettes were used using a 1 cm path length cell at 25 °C. Spectroscopic grade methanol (MeOH) was used as received.

CV and ECL Measurements. For electrochemical studies, 9,10-diphenylanthracene (DPA, 97%), benzoyl peroxide (BPO, reagent grade, ≥ 98%), ferrocene (Fc, 98%), and supporting electrolyte, tetra-*n*-butylammonium perchlorate (TBAP, electrochemical grade) were used as received. All solutions were prepared using anhydrous acetonitrile (ACN, 99.8%) in a Sure Seal bottle, that was immediately transferred into an N₂-filled drybox prior to use.

Electrochemical Preparation. Cyclic voltammetry (CV), differential pulse voltammetry (DPV), and electrogenerated chemiluminescence (ECL) experiments were conducted using a 2 mm diameter Pt disc inlaid in a glass sheath as the working electrode

(WE), a coiled Pt wire as the counter electrode (CE), and a coiled Ag wire as the quasi reference electrode (RE), respectively. Prior to each experiment, the WE was polished with a felt polishing pad using 1.0 μm , 0.3 μm and 0.05 μm alumina suspension for 5 min each to obtain a mirror surface then washed with copious amounts of deionized water. The WE was then electrochemically polished using a 0.1 M aqueous solution of H_2SO_4 by scanning 400 times between the potentials of 1.400 and -0.600 V at a scan rate of 0.5 V/s for a cleaner, more reproducible Pt surface.²² Finally, the WE was rinsed with deionized water then dried under a stream of Ar gas at room temperature. The CE and RE were rinsed with acetone, sonicated in acetone for 15 min, and then thoroughly rinsed with deionized water. The electrodes were dried at 100 °C for 5 min then left to cool to room temperature. The electrochemical cell was rinsed with acetone and deionized water, then immersed in a base bath of 5% KOH in isopropanol for 4 h, rinsed with deionized water, immersed in an acid bath of 1% HCl for 4 h, then thoroughly rinsed with deionized water. The cell was dried at 100 °C overnight then cooled to room temperature. All solutions for electrochemical experiments were prepared in a glass electrochemical cell inside an N_2 -filled drybox. The solutions of **3.1-3.4** ranged in concentration from 2.0-2.7 $\times 10^{-3}$ M in ACN containing 0.1 M TBAP, the supporting electrolyte. For co-reactant systems, 5.0 $\times 10^{-3}$ M BPO was added to each solution of **3.1-3.4**. These experiments were performed outside of the drybox. The electrodes were immersed in solution and connected by copper wire inserted through the cap. After completion of each experiment, the cell potential obtained was calibrated using Fc as the internal standard. The potentials were normalized to NHE using Fc/Fc⁺. The redox potential of Fc/Fc⁺ in ACN was taken as 0.400 V vs. NHE.^{28,29}

Electrochemical Instrumentation. CV is a technique that is used to measure the current during the process of linearly changing the potential between two limits on the working electrode at a given scan rate.²² For all CV experiments, the potential windows range from 2.810 to -2.290 V for annihilation systems and from 0.000 and -2.150 V for co-reactant systems. The experimental parameters for CVs were as followed: 0.000 V initial potential, positive or negative initial scan polarity, 0.1 V/s scan rate, 4 sweep segments, 0.001 V sample interval, 2 s quiet time, 1-5 $\times 10^{-5}$ AV^{-1} sensitivity. In DPV

experiments, the differential current is taken as the current at the end of the pulse minus the current seen just prior to the pulse as the applied potential advances from one pulse to the next pulse.³⁰ For the purposes of our experiments, four DPVs were taken for each compound, two for anodic scans (0.000 to 2.810 V and 2.810 to 0.000 V) and two for cathodic scans (-2.290 to 0.000 V and 0.000 to -2.290 V) respectively. The experimental parameters for DPVs were as followed: 0.004 V increments, 0.05 V amplitude, 0.5 s pulse width, 0.0167 s sampling width, 0.2 s pulse period, 2 s quiet time, $1.5 \times 10^{-5} \text{ AV}^{-1}$ sensitivity.

ECL instrumentation. The electrochemical cell had a flat Pyrex window at the bottom for detection generated from the WE and was sealed with a Teflon cap with a rubber O-ring for CV, DPV, and ECL measurements. The CV and ECL data were obtained using an electrochemical analyzer coupled with a photomultiplier tube (PMT) held at -750 V with a high voltage power supply. In the vicinity of the WE, ECL was generated and collected by the PMT under the flat Pyrex window at the bottom of the cell. The photocurrent from the PMT, which represents the ECL intensity, transformed this signal using a picoammeter/voltage source. The potential and current signals from the electrochemical workstation were sent through a data acquisition system (DAQ board) to the computer. The data acquisition system was controlled from a homemade LabVIEW program. The electrochemical cell was positioned inside the PMT to detect light emission for ECL pulsing experiments. The PMT was connected to the picoammeter/voltage source for signal conversion. A potentiostat was connected to an Universal Programmer. The data acquisition system was controlled from another homemade LabVIEW program. Current, potential and ECL signals were recorded simultaneously with the computer acquisition system. Pulsing the WE between the first oxidation and reduction peak potentials improved the ECL signals with a pulse width of 0.1 s or 10 Hz. The photosensitivity was set between 2 and 20 nA for annihilation systems and 200 nA for co-reactant systems. The ECL spectra were obtained using a spectrometer containing a charge-coupled device (CCD) camera that was cooled to -55 °C prior to use and connected to the computer. Similar to the pulsing experiments, the samples were pulsed between the first oxidation and reduction peak potentials, between

0.000 and -2.150 V, at 10 Hz. The exposure time of the spectra was set to 60 s for co-reactant systems. A program recorded the intensities. Vertical lines/spikes seen in the spectra were cosmic rays from the CCD spectrometer.

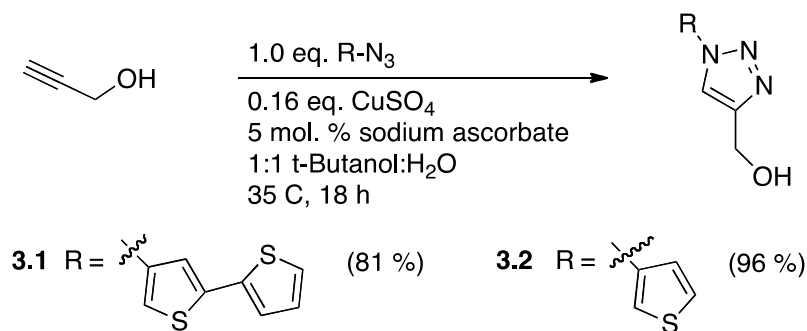
ECL calculations. ECL quantum efficiencies (QE) were calculated relative to DPA (reported absolute ECL efficiencies of DPA = 6.1 % in ACN)³¹ by integrating both the ECL intensity and current value for each compound relative to the DPA standard, see Eq. 2.1 in Chapter 2.

Theoretical Calculations. The ground state structures of **3.1-3.4** were optimized from the crystal structures, **3.1, 3.2, and 3.4**, by using density functional theory³² (DFT) with B3LYP/6-31+G* in Hartree/Particle at T=289.15 K, P=1 Atm. Frequency calculations were also executed at the same level of theory as the optimizations and the vibrational data confirmed that the structures were indeed true minima on the potential energy surface because there were no imaginary frequencies listed in the vibrational analysis. The crystal structure and optimized Cartesian coordinates of **3.1-3.4** have been given in Appendix II, S3.7 to S3.17.

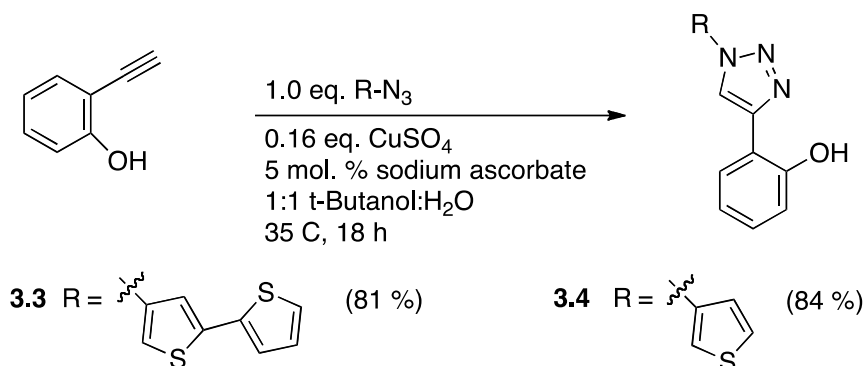
3.3 Results and Discussion

Synthesis of Thienyltriazoles. Our focus has been on synthesis of thiophene-based, luminescent molecules, using the copper alkyne-azide cycloaddition, CuAAC, approach (click chemistry),¹²⁻¹⁵ which chelate to Al and Zn for possible subsequent enhancement in fluorescence. The basic synthetic approach to our thienyltriazoles, **3.1-3.4**, has been outlined in Scheme 3.1 and Scheme 3.2. The triazole moiety links electron donor and acceptor units, leading to an inclusion of a luminescent emission *via* charge transfer processes. The precursors were readily available and were easily converted to **3.1-3.4** using published procedures. In fact, compounds **3.1-3.4** were prepared using the “click” reaction between 3-azidothiophene, or 4-azido-2,2'-bithiophene, with 2-progargyl alcohol or 2-ethynylphenol. The “click” reactions had mild reaction conditions, and required little product isolation and no chromatography. Stirring “click” reactions overnight at 35 °C resulted in high yields of **3.1-3.4** (81-96 %). Recrystallization

provided single crystals for **3.1**, **3.2**, and **3.4**, suitable for x-ray diffraction. The identity of **3.1-3.4** were confirmed by ^1H and $^{13}\text{C}\{^1\text{H}\}$ NMR spectra, LRMS, and HRMS.



Scheme 3.1. General procedure for the synthesis of thienyltriazoles, **3.1** and **3.2**, via Cu(I) catalyzed Huisgen 1,3-dipolar cycloaddition



Scheme 3.2. General procedure for the synthesis of thienyltriazoles, **3.3** and **3.4**, via Cu(I) catalyzed Huisgen 1,3-dipolar cycloaddition

Crystal structures. An ORTEP representation of **3.1** has been shown in Figure 3.1a. The solid state structure of **3.1** displays a high degree of planarity in the bithiophene ring system, with a torsion angle between the bithiophene rings, S(1)-C(1)-C(5)-C(6), of only 0.80°. There was twisting of the triazole ring system relative to the bithiophene ring system. A torsion angle of 41.42° around the ring junctions of C(8)-C(7)-N(1)-C(10) was observed between the triazole ring and its adjacent thiophene ring. In the solid state, molecules of **3.1** pack in a head-to-tail arrangement with their bithiophene ring systems approximately parallel and separated by a distance of 3.60 Å, between C(3) and C(6), Figure S3.1 in Appendix II. When looking at three crystallographically adjacent

molecules, there may be an H-bonding interaction between N(3) and the H-atom associated with O(1) a distance of 2.78 Å between the heavy atoms.

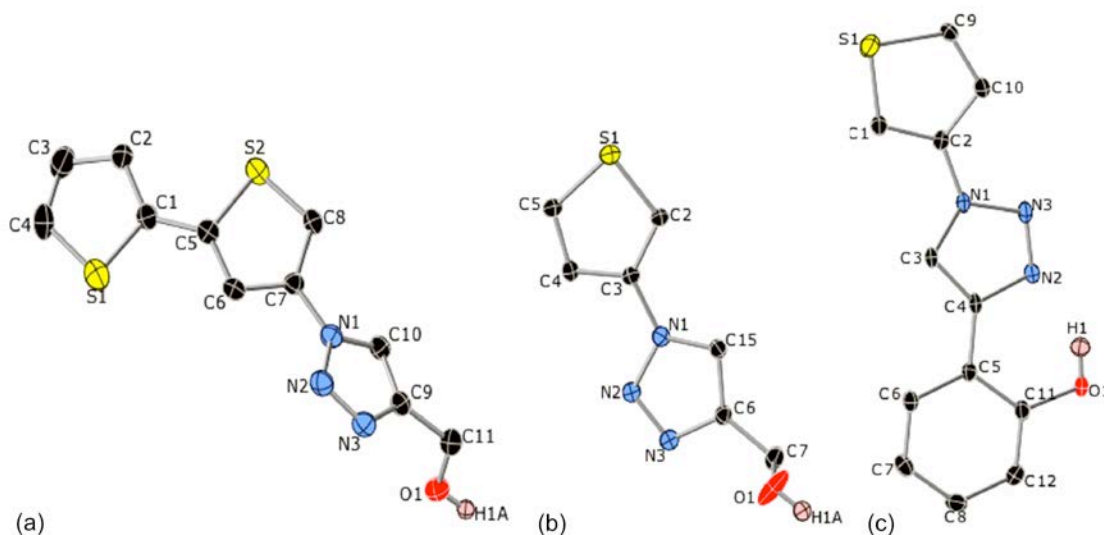


Figure 3.1. ORTEP representations of (a) **3.1**, (b) **3.2**, (c) **3.4** (30% probability ellipsoids, H-atoms removed for clarity, expect -OH protons) with rings approximately parallel to the page.

An ORTEP representation of **3.2** has been shown in Figure 3.1b. There was a high degree of planarity in the thiophene-triazole ring system of **3.2** with a small torsion angle of 4.10° between the two ring systems, C(3)-C(2)-N(1)-N(2). In the solid state, molecules of **3.2** pack in a head-to-tail arrangement with their ring systems approximately parallel and separated by a distance of 3.40 Å, between N(3) and C(15), Figure S3.2 in Appendix II. There may be an H-bonding interaction between N(3) and the H-atom associated with O(1) from adjacent molecules with a distance of 2.81 Å between the heavy atoms.

An ORTEP representation of **3.4** has been depicted in Figure 3.1c. The molecules of **3.4** display a high degree of planarity throughout the three ring systems. There was probably an intramolecular hydrogen bond between one of the triazole N-atoms and the phenol OH group: the N(2)-O(1) distance was 2.63 Å which was significantly less than the sum of the van der Waals radii of N and O (2.74 Å). The torsion angle between the thiophene and triazole rings C(1)-C(2)-N(1)-C(3) was 7.34° and the triazole and phenol

rings N(2)-C(4)-C(5)-C(11) was 1.80° . In the solid state, molecules of 4 π -stack with all three ring systems approximately parallel and separated by a distance of 3.31 Å, between N(2) and C(10), Figure S3.3 in Appendix II.

Electrochemistry and its correlation to crystal and electronic structures. The cyclic voltammogram (CV) of **3.1** is shown in Figure 3.2 in acetonitrile solution containing 0.1 M tetra-*n*-butylammonium perchlorate as supporting electrolyte. When the potential was scanned from 0.000 to 2.740 V, **3.1** underwent oxidation at a peak potential of 1.828 V, becoming a radical cation. The oxidation process was irreversible in the CV since there was no return peak in the reverse potential scan from 2.740 to 0.000 V. Upon scanning in negative potential range, **3.1** was reduced to a radical anion showing a cathodic peak at -2.092 V. The radical anions were not stable as well since there was no anodic wave in the reverse potential scan. It should be noted that new peaks appeared in the middle of the potential window after one cycle of the potential scan. This indicated that some chemical reactions from the generated radicals occurred after the electrochemical reactions, which agreed well with their stabilities illustrated by the CV in Figure 3.2.

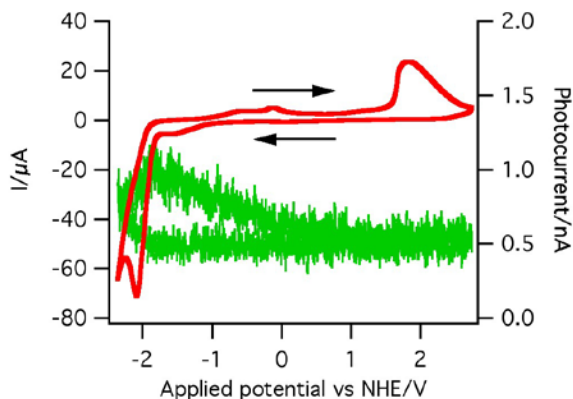


Figure 3.2. Cyclic voltammogram (red) and electrochemiluminescence-voltage curve (green) of **3.1** with a scan rate of 0.1 V/s and a potential range between 2.740 and -2.358 V.

In order to assess the redox property with less noise, differential pulse voltammetry (DPV) was used in the potential range of 2.810 and -2.289 V in the same supporting electrolyte, Figure 3.3. The formal potentials of **3.1** can be determined from Eq. 3.1^{30,33}, where E_{max} is the peak potential in the DPV and ΔE is the pulse height (50 mV), we have approximated the potentials using the equation for a reversible system.

$$E^{0'} = E_{\text{max}} + \frac{\Delta E}{2} \quad (3.1)$$

Upon scanning the potential from -2.289 to 2.810 V, a peak potential was observed at 1.894 V for the oxidation reaction, top solid wave in Figure 3.3a, which was close to the peak potential obtained by CV. The formal potential for the oxidation was calculated as 1.919 V, Table 3.1, from Eq. 3.1. DPV provides better visibility than the CV in Figure 3.2 and could easily access the formal oxidation potential. As demonstrated from the crystal structure, Figure 3.1a, the bithiophene ring plane has a torsion angle as large as 41.42° relative the triazole ring. This led to a decrease in the conjugation length, a low delocalization of the charge upon losing an electron and therefore a low stability of the generated radical cation. Furthermore, we observed that the HOMO electron density of **3.1**, inset in Figure 3.3a, was distributed mostly on the bithiophene chromophore and minor on the triazole ring using density functional theory (DFT). The electron density extended less as expected from our molecule design on this conjugated ring system.

Table 3.1. Redox Peak Potentials and Energy Levels of HOMOs and LUMOs.

	$E_{p,a}$ oxidation/V ^a	$E_{p,c}$ reduction/V ^a	$E_{ox}^{o'}/V^a$	$E_{red}^{o'}$ /V ^a	$\Delta E^{o'}/eV^b$	Theoretical Energy Gap/eV ^c
3.1	1.894	-1.905	1.919	-1.930	3.85	4.22
3.2	2.271	-1.524	2.296	-1.549	3.84	5.27
3.3	2.126	-1.906	2.151	-1.931	4.08	3.92
3.4	1.687	-1.460	1.712	-1.485	3.19	4.22

^aIn V vs. Ag/Ag⁺ at 0.1 V/s scan rate.

^bEnergies determined from DPV 1st oxidation and reduction peak potentials data ($\Delta E^{o'} = E_{ox}^{o'} - E_{red}^{o'}$).

^cEnergy gap values obtained from the DFT/B3LYP/6-31+G* calculations.

When the potential scanning direction was reversed, bottom solid wave in Figure 3.3a, a peak potential was observed at -1.905 V in the cathodic region, indicating the injection of an electron to the LUMO, reduction reaction with a calculated formal reduction potential of -1.930 V, Table 3.1. The LUMO electron density again was delocalized on the bithiophene ring, inset in Figure 3.3a.

A small cathodic peak was observed in the cathodic DPV scan, top curve in Figure 3.3a, representing the instability of the radical cation. At the beginning of the DPV scan, radical cations were generated in the vicinity of the electrode. Upon scanning more negative, these anions, if they were still there, were re-reduced to the neutral form. The lower peak current than that of the corresponding anodic peak in the anodic scan described well the irreversibility of the oxidation or the low stability of the radical cations. Similarly, a smaller anodic peak in the anodic DPV, top wave in Figure 3.3a,

than that of the corresponding cathodic peak, bottom curve in Figure 3.3a, illustrated the irreversibility of the reduction or the low stability of the radical anions.

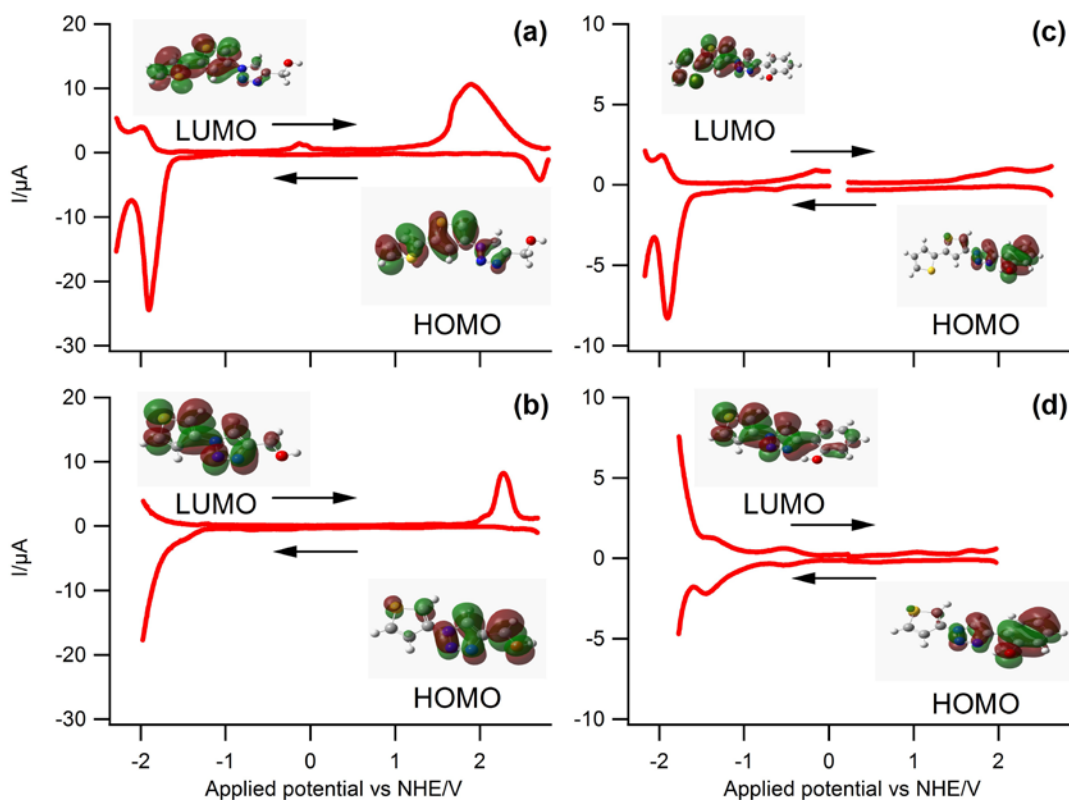


Figure 3.3. Differential pulse voltammogram and representations of the calculated HOMO and LUMO of (a) BiTTM (**3.1**) from 2.810 to -2.289 V, (b) TTM (**3.2**) from 2.683 to -1.976 V, (c) BiTTP (**3.3**) from 2.626 to -2.174 V, and (d) TTP (**3.4**) from 1.975 to -1.772 V, in ACN containing 0.1 M TBAP as supporting electrolyte with a scan rate of 0.1 V/s. Gaussian-09 (B3LYP/6-31+G*) was used for calculations of **3.1-3.4** in Hartree/Particle at T=289.15 K, P = 1 Atm.

The electron promotion from HOMO to LUMO was delocalized mainly on the bithiophene, which might cause an inefficient luminescent emission. The electrochemical gap determined from the first oxidation and reduction potentials ($\Delta E = E_{\text{ox}}^{0'} - E_{\text{red}}^{0'}$) read 3.85 eV in Table 3.1, which agrees very well with electronic energy gap values of 4.03 eV in MeOH and 3.91 eV in DMF determined from UV-visible spectra, Table 3.2, and Figures S3.4 to S3.5 in Appendix II. The energy gap between the excited state and the

ground state evaluated from the photoluminescence spectrum, Figure S3.6 in Appendix II, was 3.37 eV, Table 3.2, a value that was smaller than the electrochemical gap of 3.85 eV, Table 3.1. This implied a nonemissive relaxation from the electron promotion to the excited state.

Table 3.2. Absorption and Photoluminescence Spectroscopic Data of **3.1-3.4**.

	Absorption		Photoluminescence ^a			Stokes shift
	Abs λ_{\max}/nm	Abs/eV	Ex λ_{\max}/nm	Em λ_{\max}/nm	Em/eV ^d	$\lambda_{\max}(\text{PL})-$ $\lambda_{\max}(\text{Abs})/\text{nm}$
3.1	307 ^b /313 ^c	4.03/3.91	344	367	3.37	54
3.2	252 ^b	4.92	366	453	2.73	201
3.3	302 ^c	4.10	337	357	3.47	55
3.4	291 ^b	4.26	337	358	3.46	67

^aPL in MeOH.

^bAbs in MeOH.

^cAbs in DMF.

^dEnergies determined from PL data.

Table 3.1 summarizes the electrochemical data of the other three thienyltriazoles, where their formal oxidation and reduction potentials are listed. The DPV of **3.2-3.4**, Figure 3.3b to Figure 3.3d, shows irreversible oxidation and reduction processes in all cases, however, even though the processes were irreversible, the radical cations and anions were still generated in solution as seen in the increase in photocurrent in Figure 3.2. The irreversible processes lead to greater instability of the radical cations and anions,

meaning fewer radical combine in solution to generate the excited species and ultimately leading to weak ECL as a result. When the potential was scanned from -1.976 to 2.683 V in the electrolyte solution containing **3.2**, the radical cation was generated at a potential more positive than its formal potential for the oxidation reaction, 2.296 V, top solid wave in Figure 3.3b. The crystal structure showed a very good planarity and the HOMO electron density of **3.2** was delocalized on the thienyltriazole according to the DFT calculation, Figure 3.3b. However, **3.2** still showed a higher oxidation potential than **3.1**. This is because **3.1** might have a planar structure in solution and therefore a high degree of conjugation. Scanning from 2.683 to -1.976 V, **3.2** underwent reduction with a formal reduction potential of -1.549 V, generating a radical anion of **3.2**, bottom solid wave in Figure 3.3b. The electron density for the LUMO of **3.2** was well delocalized on the thiophene and triazole rings and partially on the hydroxyl group, Figure 3.3b, leading a facile electron injection and therefore a less negative formal potential, -1.549 V, than that of **3.1**, -1.930. The HOMO-LUMO gap of **3.2** from the DFT calculation read 5.27 eV, Table 3.1, and is much higher than the electrochemical gap, 3.84 eV, but is compatible with the electronic gap from the absorption spectrum, Table 3.2 and Figure S3.4 in Appendix II. The installation of the second thiophene ring in **3.1**, relative to **3.2**, shows a trend of increasing conjugation resulting in a decrease in energy between the HOMO and LUMO, from 5.27 eV in **3.2** to 4.22 eV in **3.1** from Table 3.1. When looking at the electrochemical behaviour of **3.2**, the electrochemical gap of 3.84 eV varied from its PL emission of 2.73 eV. This may be due to fast rotation between the thiophene and triazole rings, as seen in the disorder of the thiophene ring, in the crystal of **3.2**.

For compound **3.3**, the radical cation formed when the potential was scanned from -2.174 to 2.626 V with its formal oxidation potential of 2.151 V, top solid wave, Figure 3.3c. When the potential was scanned from 2.626 to -2.174 V, the radical anion was generated with its formal potential of -1.931 V, bottom solid wave in Figure 3.3c. From the HOMO in Figure 3.3c, the electron density of **3.3** resided mostly on the bithienyltriazole ring system. In the LUMO, the electron density was delocalized on the phenol and triazole rings, with very little contribution from the bithiophene chromophore. From Table 3.1, we observed a decrease in the theoretical energy gap with the installation of the phenol ring to the bithienyltriazole compound. The increase in conjugation in **3.3**

decreased the energy gap from 4.22 eV in **3.1** to 3.92 eV in **3.3**. For absorption, the energy was 4.10 eV, similar to the DFT energy of **3.3**, however there was no noticeable difference in energy between **3.1** and **3.3** for absorption. Compound **3.3** did not readily dissolve in MeOH, and was analyzed instead in DMF, Figure S3.5 in Appendix II. Only one band was observed for both **3.1** and **3.3** due to the solvent cutoff of DMF at approximately 270 nm. The addition of the bithiophene and phenol aromatic systems to compound **3.3** increases the absorption intensities and selectively tunes the wavelengths relative to **3.1** and **3.2**. The electrochemical gap of **3.3**, 4.08 eV, was compatible with the electronic gap but larger than its PL emission energy of 3.47 eV. This again implies that nonemissive relaxation from the electron promotion to excited state has occurred.

Lastly, compound **3.4** was scanned from -1.772 to 1.975 V, which generated the radical cation with its formal potential of 1.712 V, top solid wave in Figure 3.3d. From DFT, the HOMO electron density of **3.4** was delocalized on the entire compound, with the major contribution from the chromophore, very similar to that of **3.2**. The radical anion was formed when the potential was scanned from 1.975 to -1.772 V with its formal potential of -1.485 V, bottom solid wave, Figure 3.3d. The LUMO of **3.4** showed the electron density on the triazole and phenol rings. Comparing **3.2** with **3.4**, the theoretical energy gap of **3.4** was 4.22 eV, which was in good agreement with the absorption energy 4.26 eV, of **3.2**. From PL, the energy for **3.4** was 3.46 eV while the energy was 3.19 eV from the electrochemical gap of **3.4**. The decrease in energy between **3.2** and **3.4** was expected as we extended the conjugation in the compound. From DPV, we observed a decrease in the electrochemical gap of compound **3.2** of 3.84 eV to compound **3.4** of 3.19 eV. A decrease in energy was not observed between **3.1** and **3.3**, however this trend of decreasing energy with increased conjugation was seen between **3.1** and **3.2**.

ECL via annihilation. In Figure 3.2, the CV of **3.1** is overlaid with the ECL photocurrent-voltage curve recorded simultaneously. Weak light emission from the thienyltriazoles during potential scanning was observed. The proposed mechanism for the observed ECL in **3.1** can be seen in Eqs. 3.2 to 3.5 and follows the annihilation pathway. When scanning from zero to positive potential, the radical cation of **3.1** was generated.



The potential was then scanned from positive to negative region. This generated the radical anion of **3.1** as seen in Eq. 3.3.



Through this annihilation pathway, the radical cation and anion generates an excited species of **3.1** and a ground-state species of **3.1**, Eq. 3.4. The excited thienyltriazole species will return to its ground-state and emit light, Eq. 3.5, as observed in the ECL photocurrent in Figure 3.2.



The ECL light was detected in the negative potential region. The stability of the radicals can be determined due to where we observed light emission. The radical cations were more stable than the radical anions of this thienyltriazole compound because we only see ECL light after scanning from positive to negative potential. Compounds **3.2-3.4** demonstrated similar weak ECL emission.

Quantitatively, ECL efficiency can be calculated as the number of photons emitted per redox event relative to DPA.³⁴⁻³⁶ The ECL efficiencies were low, as seen in Table 3.1, however, the thienyltriazoles **3.1** and **3.3** displayed higher ECL efficiencies than **3.2** and **3.4** due to their extended π conjugation. The ECL efficiencies for compounds **3.1-3.4** were 0.11 % for **3.1**, 0.17 % for **3.2**, 0.50 % for **3.3**, and 1.11 % for **3.4**. CV of **3.1-3.4** shows irreversible processes indicating the poor radical stability.

Annihilation pulsing efficiencies were essentially zero, not efficient, because the radicals were not stable in solution as seen in the irreversible redox reactions, see Table 3.3. Since the compounds were not efficient through annihilation pulsing, the ECL spectrum for each compound was not obtained.

Table 3.3. ECL Spectroscopic Data of **3.1-3.4**.

	Annihilation		Co-reactant		λ_{\max}/nm	Shift ^b $\lambda_{\max}(\text{ECL})-$ $\lambda_{\max}(\text{Em})/\text{nm}$
	Scanning	Pulsing	Scanning	Pulsing		
	QE ^a /%	QE ^a /%	QE ^a /%	QE ^a /%		
3.1	0.11	0.00	0.50	0.40	544	185
3.2	0.17	0.00	0.16	0.01	554	91
3.3	0.50	0.00	0.35	0.08	546	189
3.4	1.11	0.01	0.40	0.02	422/576	84

^aECL quantum efficiencies (QE) measured in ACN relative to 9,10-diphenylanthracene, DPA, ($\Phi = 6.1\%$ in ACN)³¹.

^bThe shift represents the difference between the ECL and PL emission wavelengths in nm.

ECL via co-reactant. ECL was enhanced when BPO was added to the solutions of compounds **3.1-3.4** as observed in Figure 3.4. Adding a co-reactant to the solution was useful by generating ECL using a single potential step, one directional potential scanning at an electrode thus overcoming the limited potential window of the solvent, reducing the time delay for the meeting of radical anions and cations, and therefore enhancing the ECL light emission by generating radicals in solution.^{17,37}

The proposed mechanism for the observed ECL in **3.1**, Figure 3.4a, with BPO is stated in Eqs. 3.6 to 3.9 and follows the co-reactant pathway. When scanning from 0.000 V to more negative potential, BPO was first reduced to its radical anion, BPO^{•-}, at -0.760 V, as see in Eq. 3.6.



This radical rapidly decomposes to generate a strong oxidizing radical, $\text{C}_6\text{H}_5\text{CO}_2^\bullet$, Eq. 3.7.



In Eq. 3.8, the $\text{C}_6\text{H}_5\text{CO}_2^\bullet$ radical reacts with **3.1** and generate the radical cation of **3.1**, $\text{BiTTM}^{\bullet+}$.



Upon further reduction, the radical anion of **3.1** was observed at -1.883 V, Eq. 3.9.



The radical cation and anion of **3.1** combine and form the excited species of **3.1**, BiTTM^* , similar to Eq. 3.4 with the annihilation mechanism, and would eventually relax back down to its ground state and light would be emitted, Eq. 3.5.

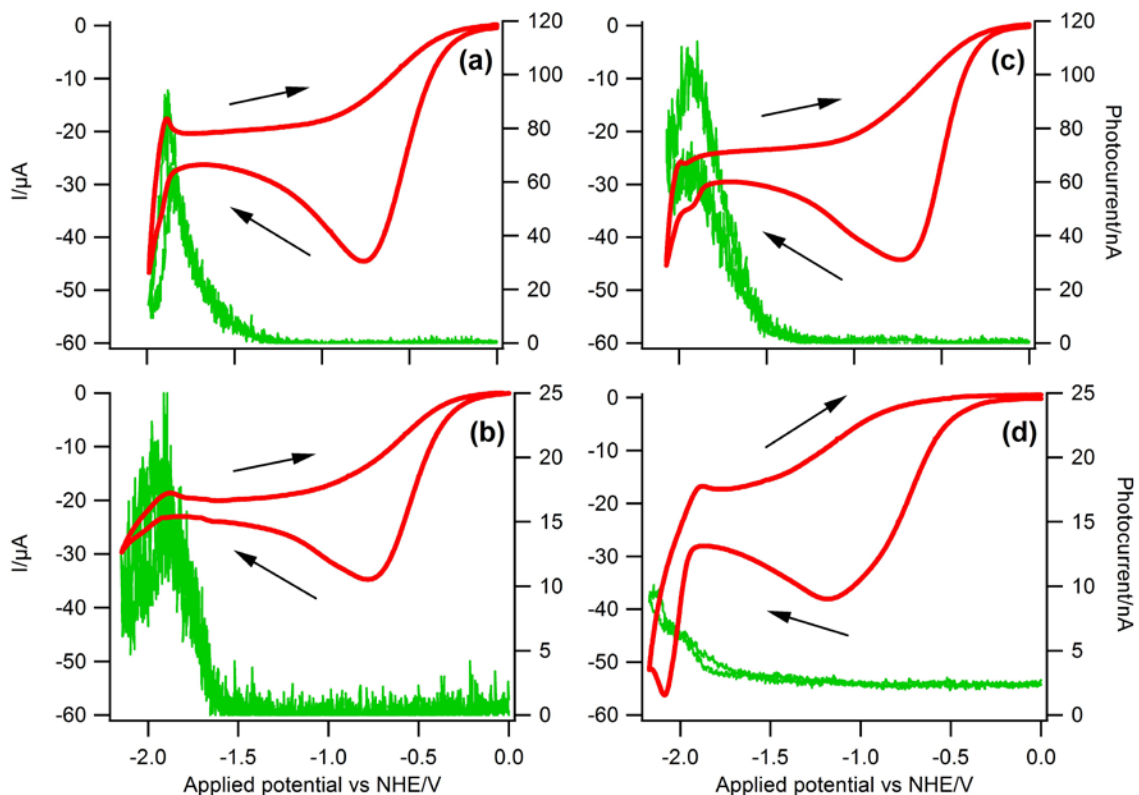


Figure 3.4. Cyclic voltammogram (red) and ECL-voltage curve (green) of (a) BiTTM (**3.1**) from 0.000 to -1.989 V, (b) TTM (**3.2**) from 0.000 to -2.145 V, (c) BiTTP (**3.3**) from and 0.000 to -2.074 V, and (d) TTP (**3.4**) from 0.000 to -2.021 V, in ACN containing 5.0×10^{-3} M BPO and 0.1 M TBAP as supporting electrolyte with a scan rate of 0.1 V/s.

A large increase in photocurrent in Figure 3.4a for **3.1**, approximately 90 nA, was observed using BPO. Comparing it to the photocurrent seen in annihilation, Figure 3.2, with approximately 3.1 nA, BPO significantly increased the amount of light detected. Compounds **3.2**, **3.3**, and **3.4** in the same co-reactant system showed increased intensities of photocurrent relative to that in the annihilation systems when extending the conjugation in the thienyltriazole ring system. ECL intensity generally increased with the addition of BPO to each system as seen in Table 3.3. Relative to the standard, DPA, a slight decrease in the efficiency appears. This was due to the fact that the efficiency of DPA was significantly higher with BPO relative to its efficiency without the co-reactant.

ECL was enhanced when using BPO and the efficiencies for compounds **3.1-3.4** were 0.50 % for **3.1**, 0.16 % for **3.2**, 0.35 % for **3.3**, and 0.40 % for **3.4**.

Pulsing experiments with co-reactant resulted in slightly higher efficiencies than in the annihilation mechanism as seen in Table 3.3. When BPO was added to the solutions, there was a small increase in efficiencies for **3.1** at 0.40 %, **3.2** at 0.01 %, **3.3** at 0.08 %, and **3.4** at 0.02 % because pulsing generates the radicals faster therefore reducing the decay of the unstable radicals.

Being able to detect photocurrent even with these very low efficiencies allowed our group to acquire the ECL spectra for compounds **3.1-3.4** as seen in Figure 3.5.

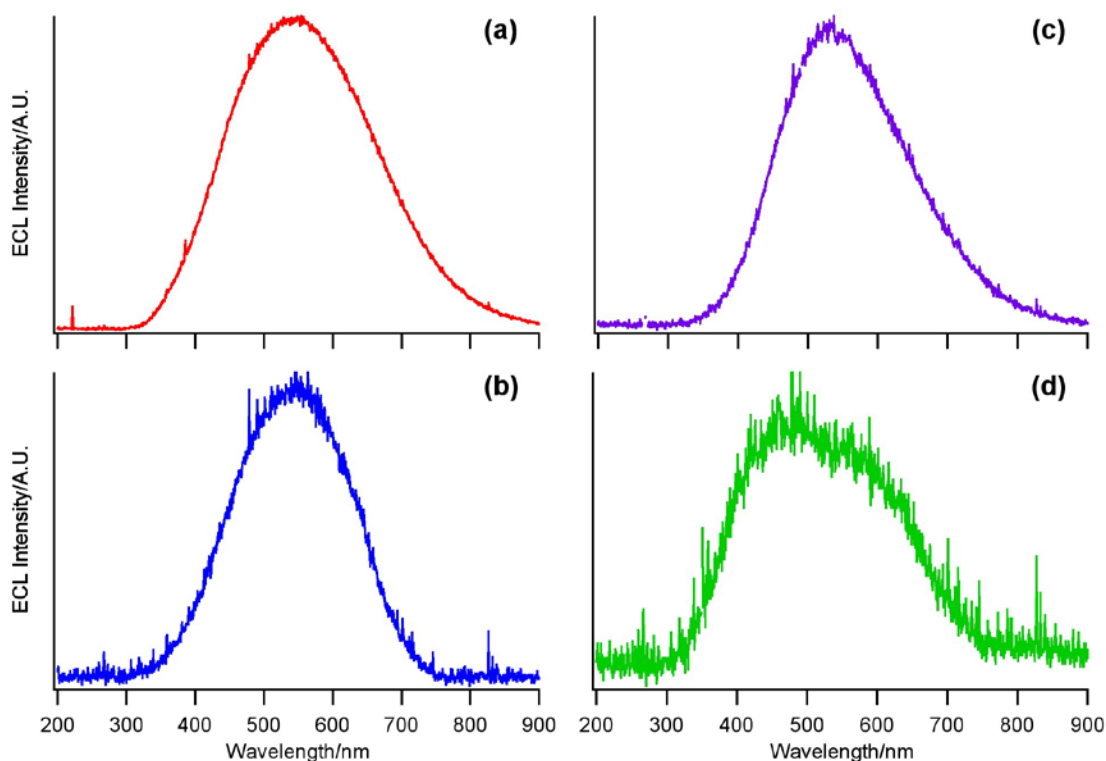


Figure 3.5. ECL spectra of **3.1-3.4** in ACN containing 5.0×10^{-3} M BPO and 0.1 M TBAP as supporting electrolyte, pulsing for $t = 60$ s between potential ranges from (a) 0.000 to -1.989 V for **3.1**, (b) 0.000 to -2.145 V for **3.2**, (c) 0.000 to -2.074V for **3.3**, and (d) 0.000 to -2.021 V for **3.4**. ECL intensities were normalized by their respective peak heights.

ECL spectra and their correlation to PL spectra. The ECL spectra of compounds **3.1-3.4** containing BPO were obtained, Figure 3.5, and their peak wavelengths are listed in Table 3.3. Pulsing between the potential ranges for each compound in the cathodic regions, thus reducing each compound, generated the excited species and the emission was acquired and recorded. The ECL spectra were red-shifted relative to the PL spectra as seen in Table 3.2. The ECL spectrum of **3.1** showed a maximum wavelength at 554 nm in ACN whereas its PL maximum was at 367 nm in MeOH. The difference of 185 nm could be due to the formation of excimers in solution during annihilation and co-reactant studies.

It was possible that excimers form in solution because they were excited states of dimers that can be observed in ECL of organic compounds.^{38,39} Excimers can form from dimerization of radical cations and anions or from stacking of the monomer in the ground state with one in the excited state due to the π conjugation of the compound.³⁴ When compound **3.1** was in solution with the excited species of **3.1**, BiTTM^* , an excimer of **3.1**, $(\text{BiTTM})_2^*$, Eq. 3.10, could be generated.



Another route would be the generation of the excimer of **3.1**, $(\text{BiTTM})_2^*$, when the radical cation and anion of **3.1** were in solution. Instead of generating an excited species of **3.1** and a ground state species of **3.1**, as seen in Eq. 3.4, it could form the excimer of **3.1**, $(\text{BiTTM})_2^*$, Eq. 3.11.



The excimer of **3.1**, $(\text{BiTTM})_2^*$, would relax down to its ground state and emit light as seen in Eq. 3.12.



Excimer formation would be an alternate route the results in light emission. By changing the substituents on the compounds, adding an additional thiophene ring or by adding a phenol ring, the PL and ECL co-reactant emissions were tuned based on the conjugated system. ECL peak wavelengths of **3.1** and **3.3** were the furthest red-shifted from their PL spectra. The ECL peak wavelength of **3.3** was observed at 546 nm with a red-shift of 189 nm relative to its PL peak wavelength. Compound **3.2** shows a red-shift of 91 nm and compound **3.4** demonstrates a red-shift of 84 nm. From Table 3.3, we can conclude that excimer formation was observed in each ECL system with BPO for all compounds studied when pulsing the electrode potential. The largest red-shift in wavelength was observed in **3.1** and **3.3**, the two compounds that had the bithiophene ring system. The addition of the phenol ring system to **3.4** changed the ECL excimer emission from 554 nm in **3.2** to 576 nm in **3.4**, thus, the extended conjugation in **3.4** increased the formation of excimers in solution for ECL measurements.

3.4 Conclusions

We synthesized four blue-emitting thienyltriazoles, **3.1-3.4**, that were characterized using ^1H and $^{13}\text{C}\{^1\text{H}\}$ NMR spectroscopy, high resolution mass spectrometry. Crystal structures of **3.1**, **3.2**, and **3.4** were determined by x-ray diffraction. While **3.1** showed a torsion angle of 41.42° between the bithiophene and triazole rings, **3.2** and **3.4** possessed greater planarity. All of the four compounds underwent irreversible redox reactions to generate electrochemically unstable radical anions and cations. Based on DFT calculations, the majority of electron density resided on the chromophore for the LUMOs of **3.1-3.4**, and mostly in the triazole hydroxyl/phenol ring systems for the HOMOs, with the exception of the HOMO of **3.1**, where the electron density was delocalized on the bithienyltriazole ring system. Electrochemical gaps determined from the differences between first formal reduction and oxidation reactions correlated well to HOMO-LUMO energy gaps obtained from UV-visible spectroscopy and the DFT calculations as well as energies of excited states measured from photoluminescence spectroscopy. They demonstrated a trend dependent on the conjugation length and planarity. ECL efficiencies for annihilation of electrogenerated radicals were determined to be 0.11 % for **3.1**, 0.17 % for **3.2**, 0.50 % for **3.3**, and 1.11 % for **3.4**, relative to that of

DPA. Upon addition of BPO as the co-reactant, ECL intensities were enhanced approximately 90 times for **3.1**, 20 times for **3.2**, 100 times for **3.3**, and 10 times for **3.4**, bearing efficiencies of 0.50 % for **3.1**, 0.16 % for **3.2**, 0.35 % for **3.3**, and 0.40 % for **3.4**, relative to DPA in the co-reactant system. The ECL spectra of **3.1-3.4** were acquired ranging from 544 nm for **3.1**, 554 nm for **3.2**, 546 nm for **3.3**, and 576 nm for **3.4**. The radicals electrogenerated in solution followed the dimerization and electron transfer pathways, leading to excimers. A red-shift was observed for all four compounds in the ECL spectra relative to the corresponding PL spectra. Monomer ECL emission was only observed for **3.4**. ECL is a valuable, quick, and cost-effective technique that requires little quantity of compound while being highly sensitive and selective.

3.5 References

- (1) Tang, C. W.; Van Slyke, S. A. *Appl. Phys. Lett.* **1987**, *51*, 913.
- (2) Shao, Y.; Qui, Y.; Hu, W.; Hong, X. *Adv. Mater. Opt. Electron.* **2000**, *10*, 285.
- (3) Liao, S.-H.; Shiu, J.-R.; Liu, S.-W.; Yeh, S.-J.; Chen, Y.-H.; Chen, C.-T.; Chow, T.-J.; Wu, C.-I. *J. Am. Chem. Soc.* **2009**, *131*, 763.
- (4) Kim, M. K.; Kwon, J.; Kwon, T. H.; Hong, J. I. *New J. Chem.* **2010**, *34*, 1317.
- (5) Ichikawa, M.; Mochizuki, S.; Jeon, H. G.; Hayashi, S.; Yokoyama, N.; Taniguchi, Y. *J. Mater. Chem.* **2011**, *21*, 11791.
- (6) Orselli, E.; Kottas, G. S.; Konradsson, A. E.; Coppo, P.; Frohlich, R.; Frtshlich, R.; De Cola, L.; van Dijken, A.; Buchel, M.; Borner, H. *Inorg. Chem.* **2007**, *46*, 11082.
- (7) Malinauskas, T.; Daskeviciene, M.; Kazlauskas, K.; Su, H. C.; Grazulevicius, J. V.; Jursenas, S.; Wu, C. C.; Getautis, V. *Tetrahedron* **2011**, *67*, 1852.
- (8) Pohl, R.; Anzenhacher, J., P. *Org. Lett.* **2003**, *5*, 2769.
- (9) Wang, S. *Coord. Chem. Rev.* **2001**, *215*, 79.
- (10) Chen, C. H.; Shi, J. *Coord. Chem. Rev.* **1998**, *171*, 161.
- (11) Swanick, K. N.; Dodd, D. W.; Price, J. T.; Brazeau, A. L.; Jones, N. D.; Hudson, R. H. E.; Ding, Z. *Phys. Chem. Chem. Phys.* **2011**, *13*, 17405.
- (12) Sharpless, K. B.; Kolb, H. C.; Finn, M. G. *Angew. Chem. Int. Ed.* **2001**, *40*, 2004.

- (13) Kolb, H. C.; Sharpless, K. B. *Drug Discov. Today* **2003**, *8*, 1128.
- (14) Wu, P.; Folkin, V. V. *Aldrichimica Acta* **2007**, *40*, 7.
- (15) Wu, P.; Feldman, A. K.; Nugent, A. K.; Hawker, C. J.; Scheel, A.; Voit, B.; Pyun, J.; Fréchet, J. M. J.; Sharpless, K. B.; Folkin, V. V. *Angew. Chem. Int. Ed.* **2004**, *43*, 3928.
- (16) Debad, J. D.; Morris, J. C.; Magnus, P.; Bard, A. J. *J. Org. Chem.* **1992**, *62*, 530.
- (17) Bard, A. J. *Electrogenerated Chemiluminescence*; Marcel Dekker, Inc.: New York, **2004**.
- (18) Swanick, K. N.; Ladouceur, S.; Zysman-Colman, E.; Ding, Z. *Chem. Commun.* **2012**, *48*, 3179.
- (19) Miao, W. *Chem. Rev.* **2008**, *108*, 2506.
- (20) Pyati, R.; Richter, M. M. *Annu. Rep. Prog. Chem., Sect. C* **2007**, *103*, 12.
- (21) Richter, M. M. *Chem. Rev.* **2004**, *104*, 3003.
- (22) Bard, A. J.; Ding, Z.; Myung, N. In *Structure & Bonding*; Springer Berlin/Heidelberg: **2005**; Vol. 118, p 1.
- (23) Zanarini, S.; Felici, M.; Valenti, G.; Marcaccio, M.; Prodi, L.; Bonacchi, S.; Contreras-Carballada, P.; Williams, R. M.; Feiters, M. C.; Nolte, R. J. M.; De Cola, L.; Paolucci, F. *Chem. Eur. J.* **2011**, *17*, 4640.
- (24) Chen, Z.; Wong, K. M.-C.; Kwok, E. C.-H.; Zhu, N.; Zu, Y.; Yam, V. W.-W. *Inorg. Chem.* **2011**, *50*, 2125.
- (25) Li, Y.; Qi, H.; Yang, J.; Zhang, C. *Microchim Acta* **2009**, *164*, 69.
- (26) Dodd, D. W.; Swanick, K. N.; Price, J. T.; Brazeau, A. L.; Ferguson, M. J.; Jones, N. D.; Hudson, R. H. E. *Org. Biomol. Chem.* **2010**, *8*, 663.
- (27) Acardi, A.; Cacchi, S.; Del Rosario, M.; Fabrizi, G.; Marinelli, F. *J. Org. Chem.* **1996**, *61*, 9280.
- (28) Gagné, R. R.; Koval, C. A.; Lisensy, G. C. *Inorg. Chem.* **1980**, *19*, 2854.
- (29) Koepp, H. M.; Wendt, H.; Strehlow, H. Z. *Elektrochem.* **1960**, *64*, 483.
- (30) Bard, A. J.; Faulkner, L. R. *Electrochemical methods, fundamentals and applications*; 2nd ed.; John Wiley & Sons Inc.: New York, **2001**.
- (31) Maness, K. M.; Bartelt, J. E.; Wightman, R. M. *J. Phys. Chem. A* **1994**, *98*, 3993.

- (32) Frisch, M. J.; Trucks, G. W.; Schlegel, H. B.; Scuseria, G. E.; Robb, M. A.; Cheeseman, J. R.; Scalmani, G.; Barone, V.; Mennucci, B.; Petersson, G. A.; Nakatsuji, H.; Caricato, M.; Li, X.; Hratchian, H. P.; Izmaylov, A. F.; Bloino, J.; Zheng, G.; Sonnenberg, J. L.; Hada, M.; Ehara, M.; Toyota, K.; Fukuda, R.; Hasegawa, J.; Ishida, M.; Nakajima, T.; Honda, Y.; Kitao, O.; Nakai, H.; Vreven, T.; J. A. Montgomery, J.; Peralta, J. E.; Ogliaro, F.; Bearpark, M.; Heyd, J. J.; Brothers, E.; Kudin, K. N.; Staroverov, V. N.; Keith, T.; Kobayashi, R.; Normand, J.; Raghavachari, K.; Rendell, A.; Burant, J. C.; Iyengar, S. S.; Tomasi, J.; Cossi, M.; Rega, N.; Millam, J. M.; Klene, M.; Knox, J. E.; Cross, J. B.; Bakken, V.; Adamo, C.; Jaramillo, J.; Gomperts, R.; Stratmann, R. E.; Yazyev, O.; Austin, A. J.; Cammi, R.; Pomelli, C.; Ochterski, J. W.; Martin, R. L.; Morokuma, K.; Zakrzewski, V. G.; Voth, G. A.; Salvador, P.; Dannenberg, J. J.; Dapprich, S.; Daniels, A. D.; Farkas, O.; Foresman, J. B.; Ortiz, J. V.; Cioslowski, J.; Fox, D. J. *Gaussian 09 (Revision B.01)*; Gaussian, Inc.: Wallingford, CT, **2010**.
- (33) Girault, H. H. *Electrochimie physique et analytique* Presses polytechniques et universitaires romandes: Laussane, **2001**.
- (34) Booker, C.; Wang, X.; Haroun, S.; Zhou, J.; Jennings, M.; Pagenkopf, B. L.; Ding, Z. *Angew. Chem. Int. Ed.* **2008**, *47*, 7731.
- (35) Wallace, W. L.; Bard, A. J. *J. Phys. Chem.* **1979**, *83*, 1350.
- (36) Laser, D.; Bard, A. J. *J. Electrochem. Soc.* **1975**, *122*, 632.
- (37) Ding, Z.; Quinn, B. M.; Haram, S. K.; Pell, L. E.; Korgel, B. A.; Bard, A. J. *Science* **2002**, *296*, 1293.
- (38) Lai, R. Y.; Fleming, J. J.; Merner, B. L.; Vermeij, R. J.; Bodwell, G. J.; Bard, A. J. *J. Phys. Chem. A* **2004**, *108*, 376.
- (39) Choi, J.-P.; Wong, K.-T.; Chen, Y.-M.; Yu, J.-K.; Chou, P.-T.; Bard, A. J. *J. Phys. Chem. B* **2003**, *107*, 14407.

Chapter 4

4 Electrochemiluminescence of Iridium(III) Complexes

4.1 Bright Electrochemiluminescence of Iridium(III)

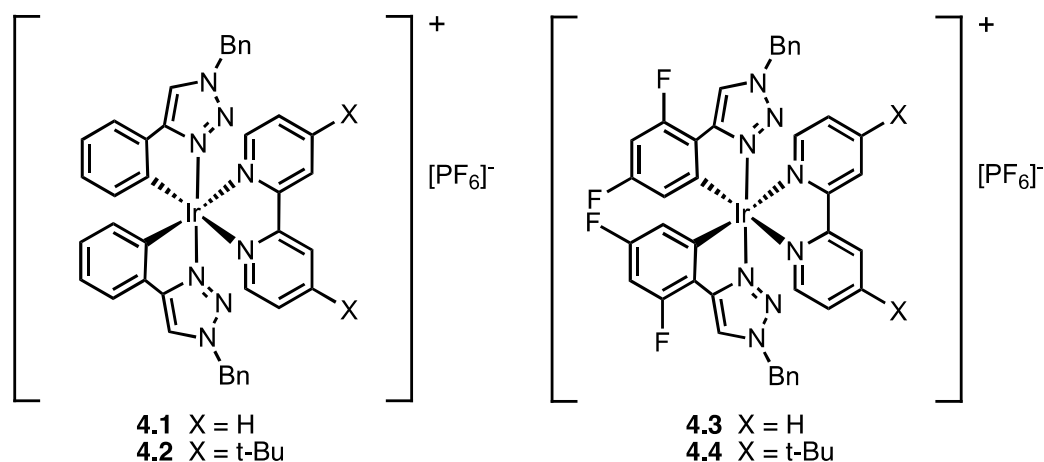
Complexes[†]

4.1.1 Introduction

An emissive excited molecule in electrochemiluminescence (ECL) is produced *via* electron transfer reactions between radical cations and anions electrogenerated in solution. ECL is therefore a powerful light-emitting technique, with wide potential applications in biology, medicine, organic light emission diodes, and other technologies.¹⁻⁶ One of the most widely investigated metal complexes, as luminophores, is $[\text{Ru}(\text{bpy})_3]^{2+}$, first reported by Tokel and Bard in 1972,⁷ which has good electrochemical reversibility, stability, and high ECL efficiency. Since then, many derivatives of $[\text{Ru}(\text{bpy})_3]^{2+}$ have been studied for ECL in biological applications.^{8,9} While neutral iridium(III) complexes have been shown to be ECL active in aqueous and organic media,¹⁰⁻¹⁶ and incorporated into electronic devices,¹⁷⁻¹⁹ ECL of charged iridium(III) complexes^{16,20,21} have recently shown promise in a myriad of applications.²²⁻²⁶ Only a few iridium(III) complexes have been reported as relatively efficient compounds, in reference to $[\text{Ru}(\text{bpy})_3]^{2+}$ and its analogs.^{10,11} Our research group has recently reported the synthesis and complete photophysical characterization of a series of highly luminescent iridium(III) complexes containing aryltriazole cyclometallating ligands.²⁷ In this communication we report the ECL mechanisms, ECL spectra, and high ECL efficiencies for four selected iridium(III) complexes, **4.1-4.4**, in acetonitrile that are promising ECL luminophores, Scheme 4.1. Please refer to Appendix III for general ECL procedures. For electrochemical workstation

[†] This work is published in Kalen N. Swanick, Sébastien Ladouceur, Eli Zysman-Colman, and Zhifeng Ding, *Chem. Commun.*, **2012**, 48, 3179-3181. Reproduced by permission of The Royal Society of Chemistry (RSC). See Appendix III.

and ECL setup information, please refer to our publications elsewhere.^{28,29} Figure 4.1 shows cyclic voltammograms (CVs) overlaid with the ECL-voltage curves of compounds **4.1-4.4**, in acetonitrile with 0.1 M TBAPF₆ as supporting electrolyte, in the potential range between their first oxidation and reduction, see Table S4.1 in Appendix III.²⁷



Scheme 4.1. Ir complexes **4.1-4.4** in study

4.1.2 Experimental Section

CV and ECL Measurements. For annihilation ECL studies, approximately 2 mg of compound, **4.1-4.4**, was added to a pyrex electrochemical cell with a flat Pyrex window at the bottom for detection of generated ECL, containing 0.1 M TBAPF₆ (tetrabutylammonium hexafluorophosphate) supporting electrolyte in anhydrous acetonitrile (3 mL) that was assembled in a dry box. For co-reactant studies, 5.0×10^{-3} M BPO was added to the annihilation solution and assembled in a dry box. A 2 mm diameter Pt disc inlaid in a glass sheath were used as the working electrode (WE), a coiled Pt wire as the counter electrode (CE), and a coiled Ag wire as the quasi reference electrode (RE), respectively. Routine cleaning procedures for the electrodes and cell were reported elsewhere.^{28,29} For detailed electrochemical workstation and ECL setup information, please refer to our previous publications.^{28,29}

Electrochemical Instrumentation. In brief, the cyclic voltammetry was conducted on a CHI 610A electrochemical analyzer (CH Instruments, Austin, TX). The

experimental parameters for cyclic voltammograms (CVs) are listed here: 0.00 V initial potential in experimental scale, positive or negative initial scan polarity, 0.1 V/s scan rate, 4 sweep segments, 0.001 V sample interval, 2 s quiet time, $1-5 \times 10^{-5} \text{ AV}^{-1}$ sensitivity. Potentials (V) were calibrated using an internal standard Fc/Fc⁺ redox couple (0.40 V in ACN)³⁰ after each experiment, and are reported *vs.* SCE standard electrode.

The ECL data along with CV data were obtained using the CHI 610A coupled with a photomultiplier tube (PMT, R928, Hamamatsu, Japan) held at -750 V with a high voltage power supply. The ECL collected by the PMT under the flat Pyrex window at the bottom of the cell was measured as a photocurrent, and transformed to a voltage signal, using a picoammeter/voltage source (Keithley 6487, Cleveland, OH). The potential, current signals from the electrochemical workstation, and the photocurrent signal from the picoammeter were sent simultaneously through a DAQ board (DAQ 6052E, National Instruments, Austin, TX) in a computer. The data acquisition system was controlled from a custom-made LabVIEW program (ECL_PMT610a.vi, National Instruments, Austin, TX). The photosensitivity on the picoammeter was set manually in order to avoid the saturation.

ECL pulsing experiments were conducted by using a potentiostat (Model AFCBPI, Pine Instrument Co., Grove City, PA), an EG&G PAR 175 Universal Programmer (Princeton Applied Research, Trenton, NJ), and the PMT with the picoammeter in the similar manner. The assembly was able to perform the pulsing experiments without a delay in a relative fast time pace. The data acquisition for the current, potential and ECL signals was carried out using another homemade LabVIEW program (ECL_PAR610a.vi). For co-reactant systems, the applied potential was pulsed at the WE in the cathodic region (in the experimental potential scale between 0 and low limit potential value for the compound reduction as obtained from CV experiments) with a pulse width of 0.1 s or 10 Hz.

The ECL spectra were obtained by replacing the PMT with a spectrometer (Cornerstone 260, Newport, Canada) attached to a CCD camera (Model DV420-BV, Andor Technology, Belfast, UK). The camera was cooled to -55 °C prior to use, and

controlled by a computer for operation and data acquisition. The intensities versus wavelengths (spectra) were recorded by Andor Technology program. Similar to the pulsing experiments, the samples were pulsed at 10 Hz within each compound's potential window.

ECL calculations. ECL quantum efficiencies (QE) were calculated relative to $[\text{Ru}(\text{bpy})_3](\text{PF}_6)_2$ taken as 100% in acetonitrile solution (absolute quantum ECL efficiency of $[\text{Ru}(\text{bpy})_3]^{2+}$ is 5.0 %^{31,32}) by integrating both the ECL intensity and current value versus time for each compound, see Eq. 2.1 in Chapter 2.

4.1.3 Results and Discussion

The four iridium(III) complexes studied were harder to oxidize and reduce than $[\text{Ru}(\text{bpy})_3](\text{PF}_6)_2$. The iridium(III) compounds underwent reversible reduction and quasi-reversible oxidation reactions leading to a strong light emission in the positive potential region, Figure 4.1. As a typical example of the four compounds, **4.1**, iridium(III)bis[1'-phenyl-1,2,3-triazolato-N,C^{2'}]-2,2'-bipyridine-hexafluorophosphate, $[(\text{phtl})_2\text{Ir}(\text{bpy})]^+$, was reduced to a radical anion, $(\text{phtl})_2\text{Ir}(\text{bpy})^\bullet$, and oxidized to a radical dication, $(\text{phtl})_2\text{Ir}(\text{bpy})^{2+\bullet}$, Eqs 4.1 to 4.2.

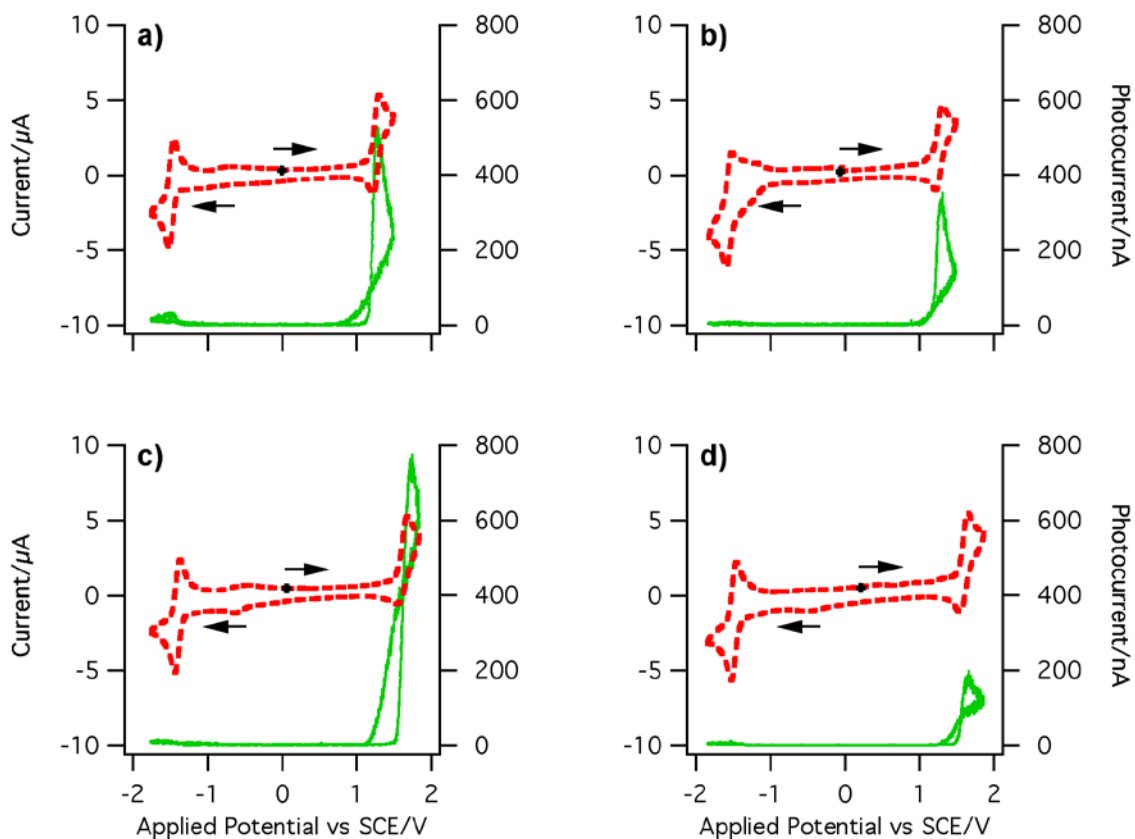
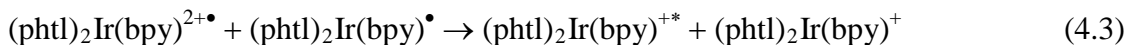


Figure 4.1. Cyclic voltammograms (dotted lines) overlaid with the ECL-voltage curves (solid lines) of compounds a) **4.1**, b) **4.2**, c) **4.3**, and d) **4.4**, in the annihilation path.

Since the former radical is more stable than the latter one, light was mostly detected in the anodic region where the two radicals met and reacted to give off light, Eqs. 4.3 to 4.4.



The ECL onset potentials in these annihilation systems were 1.11 V for **4.1**, 1.07 V for **4.2**, 1.15 V for **4.3**, and 1.47 V for **4.4**. Table 4.1 demonstrates the ECL efficiencies

determined as the photons emitted per redox event relative to the standard^{7,31,32}, [Ru(bpy)₃]²⁺. While **4.1** showed an ECL efficiency of 50 %, **4.2** demonstrated 32 %. This difference in ECL can be attributed to the *tert*-butyl (*t*-Bu) substituents on the bipyridine ligand to sterically inhibit the interactions between radicals. The addition of the fluorine substituents on the phenyltriazole ligands greatly enhanced the ECL efficiency to 85 %. However, the combination of the *t*-Bu substituents and the fluorine-substituted phenyltriazole in Ir complex **4.4**, greatly decreased the ECL efficiency to 17 %. ECL decreased when the applied potential was pulsed at 10 Hz between oxidation and reduction potentials for each compound. The faster pace pulsing led to ECL efficiency of 31 % for **4.1**, 14 % for **4.2**, 1 % for **4.3**, and 1 % for **4.4**. This indicates that time is necessary for the radicals to be generated in solution in order to form the excited species that emit light.

Table 4.1. ECL efficiencies from annihilation and co-reactant studies and their corresponding ECL spectra.

	Annihilation		Co-reactant		ECL
	Scanning/%	Pulsing/%	Scanning/%	Pulsing/%	λ /nm
4.1	50 (0.025)	31 (0.015)	5 (0.002)	53 (0.026)	606/587
4.2	32 (0.016)	14 (0.007)	17 (0.008)	177 (0.088)	576/579
4.3	85 (0.042)	1	103 (0.051)	499 (0.224)	522/504
4.4	17 (0.008)	1	70 (0.035)	350 (0.175)	510/503

^aEfficiencies are relative to [Ru(bpy)₃](PF₆)₂ taken as 100 % in acetonitrile solution (absolute quantum ECL efficiency of [Ru(bpy)₃]²⁺ is 5.0 %^{31,32}).

^bWavelength values acquired from annihilation/co-reactant ECL pulsing (for PL values please refer to our previous paper²⁷).

The diffusion coefficient values for **4.4** and $[\text{Ru}(\text{bpy})_3](\text{PF}_6)_2$ were determined³³ as $1.4 \times 10^{-5} \text{ cm}^2/\text{s}$ and $1.2 \times 10^{-5} \text{ cm}^2/\text{s}$, respectively (Figures S4.1 to S4.6 in Appendix III). While **4.1-4.4** are bright in ECL, the efficiencies are scan rate dependent. These compounds have similar diffusion coefficients but the scan rate dependence is very different from the standard. When comparing the efficiencies of **4.1-4.4** with the standard in pulsing and scanning modes, pulsing at 10 Hz is not favourable for **4.1-4.4** as seen in Table 4.1.

The ECL spectra of **4.1-4.4** are shown in Figure 4.2. When the applied potential is pulsed between the oxidation and reduction potentials of the compounds, the spectrum of each compound is collected using a CCD camera attached to a spectrograph. For **4.1**, the ECL spectrum showed one peak centered at 606 nm, Table 4.1, which corresponds well to the PL peak at 580 nm as stated in our previous report (Table S4.2 in Appendix III for PL data).²⁷ For **4.2**, one peak was observed, centered at 576 nm. Again, this matches well with the PL peak at 575 nm. The ECL spectra displayed one peak centered at 522 nm for **4.3** and 510 nm for **4.4**, which are consistent with the PL peaks of 514 nm for **4.3** and 498 nm for **4.4**. The addition of the fluorine and *t*-Bu substituents on the ligands decreased the emission wavelength by increasing the energy gap²⁷ between first oxidation and first reduction. ECL emission was strong enough for the naked eye to observe the light emission at the working electrode when pulsing between oxidation and reduction potentials for **4.3**. Please see paper for video of **4.3** being pulsed between 1.80 to -1.80 V.³⁴ In the darkroom, at the working electrode, we observed a bright yellow emission for **4.1** and **4.2**, and an intense green emission for **4.3** and **4.4**. We can confirm that the light observed electrochemically *via* ECL is the same light detected through PL using an external light source.

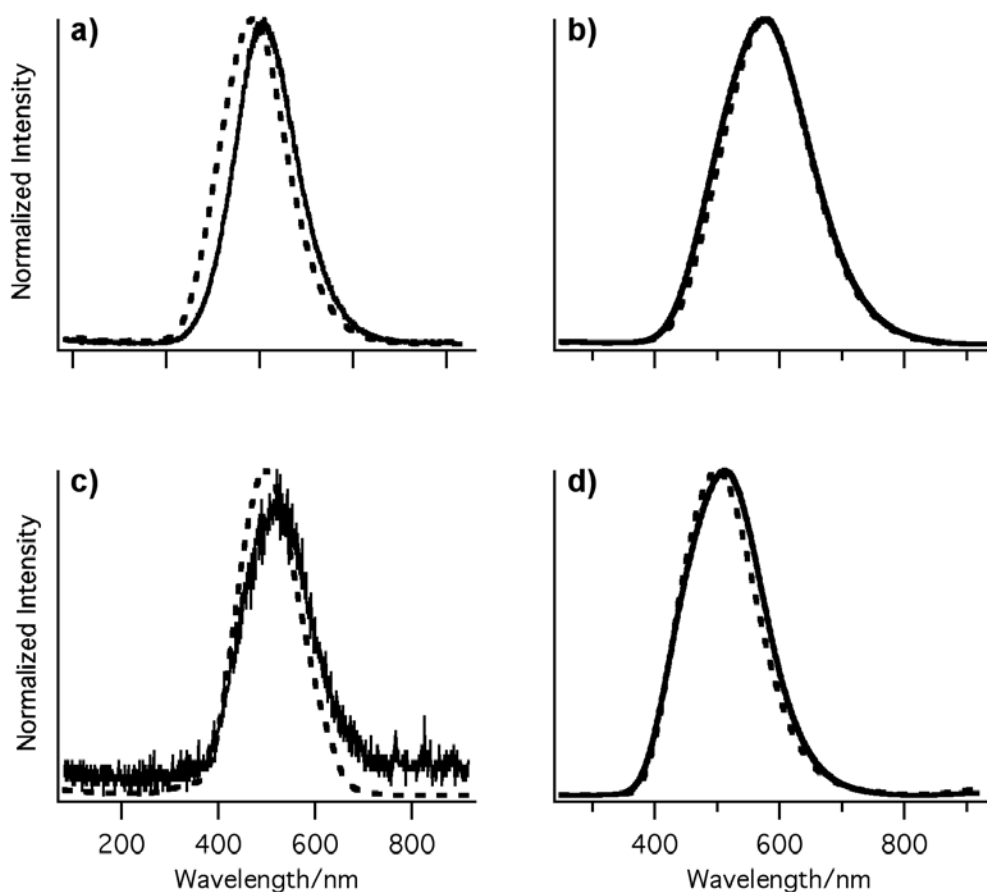


Figure 4.2. Normalized ECL spectra of a) **4.1**, b) **4.2**, c) **4.3**, and d) **4.4**, *via* annihilation (solid line) and co-reactant (dotted line) paths.

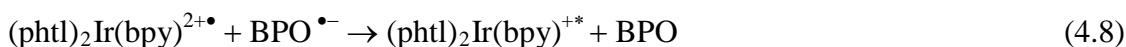
Using a co-reactant, a compound that can produce a strong oxidizing or reducing agent^{1,35} for ECL studies with a limiting cathodic or anodic potential window, ECL can be produced from the excited species generated by means of applied potentials in a single cathodic or anodic region. Common co-reactants for cathodic ECL include persulfate^{36,37}, oxygen³⁸, and benzoyl peroxide³⁵ (BPO, (C₆H₅CO)₂O₂). ECL-voltage curves of **4.1-4.4** *via* the co-reactant path with BPO are illustrated in Figure S4.7, in Appendix III, along with the simultaneously recorded CVs.

Limiting the potential to the cathodic region allows the short-lived BPO oxidized species to immediately react with the reduced species in solution to generate the excited molecules. ECL was found to be greatly enhanced when 5.0×10^{-3} M BPO was added to

the solutions of **4.1-4.4**. The ECL co-reactant mechanism follows the standard proposed mechanism as seen in Eqs. 4.5 to 4.7. Initially at 0.00 V, a negative potential is applied to the system. At -0.78 V, BPO is reduced to its radical anion, $\text{BPO}^{\bullet-}$, Eq. 4.5. The radical anion rapidly decomposes into a strong oxidizing intermediate radical, $\text{C}_6\text{H}_5\text{CO}_2^{\bullet}$, and $\text{C}_6\text{H}_5\text{CO}_2^-$, Eq. 4.6. The intermediate $\text{C}_6\text{H}_5\text{CO}_2^{\bullet}$ reacts with **4.1**, $(\text{phtl})_2\text{Ir}(\text{bpy})^+$, and generates the oxidized species, $(\text{phtl})_2\text{Ir}(\text{bpy})^{2+\bullet}$, Eq. 4.7.

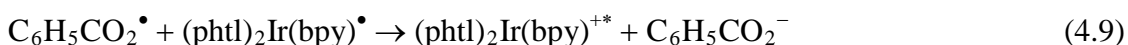


Upon scanning to more negative potential, **4.1** is reduced to $(\text{phtl})_2\text{Ir}(\text{bpy})^{\bullet}$, Eq. 4.2. Similar to the annihilation mechanism, the oxidized species of **4.1**, $(\text{phtl})_2\text{Ir}(\text{bpy})^{2+\bullet}$, and the reduced species of **4.1**, $(\text{phtl})_2\text{Ir}(\text{bpy})^{\bullet}$, generate the excited species of **4.1**, $(\text{phtl})_2\text{Ir}(\text{bpy})^{+*}$, Eq. 4.3. The excited species of **4.1**, $(\text{phtl})_2\text{Ir}(\text{bpy})^{+*}$, will relax back down to its ground-state, $(\text{phtl})_2\text{Ir}(\text{bpy})^+$, and light is emitted, Eq. 4.4. Furthermore, a relatively weak increase in ECL photocurrent, Figure S4.7 in Appendix III, was observed right after the BPO reduction potential, -0.78 V, but before the reduction of compounds **4.1-4.4**. The oxidized species of **4.1**, $(\text{phtl})_2\text{Ir}(\text{bpy})^{2+\bullet}$, generated through Eqs. 4.5 to 4.7, can react with $\text{BPO}^{\bullet-}$, Eq. 4.8, to produce the excited species of **4.1**, $(\text{phtl})_2\text{Ir}(\text{bpy})^{+*}$, that eventually emits light, Eq. 4.4. This ECL pathway, Eq. 4.8, was observed in **4.2-4.4** as well.



However, **4.1** displayed a large increase in photocurrent, 12 μA , Fig. S4.7 in Appendix III, following the typical route with BPO, Eqs. 4.5 to 4.7, compared to 500 nA from annihilation, Eqs. 4.1 to 4.4. For **4.2**, Figure S4.7 in Appendix III, an increase from 380 nA in annihilation to 40 μA of photocurrent with BPO was observed. The highest ECL intensity was observed from **4.3**, around 200 μA , and **4.4** had fairly strong ECL photocurrent of 140 μA . The ECL onset potentials with co-reactant were -1.36 V for **4.1**,

-1.01 V for **4.2**, -1.17 V for **4.3**, and -1.17 V for **4.4**. The ECL onset potential of each compound indicated that the compound initially used the pathway as seen in Eq. 4.8 because the initial photocurrent was detected before the reduction of the complex. However, upon reduction of the compound, the maximum amount of photocurrent was observed in Figure S4.7. As stated recently by Rosenthal *et al.*, the complete mechanism with BPO is complicated.³⁹ Another possible mechanism with BPO may involve the reduced species of **4.1**, reacting with the strong oxidizing intermediate radical, thus generating the excited species, Eq. 4.9, and emitting light.



Relative to $[\text{Ru}(\text{bpy})_3](\text{PF}_6)_2$, as seen in Table 4.1, compound **4.3** displayed high ECL efficiency around 103 %, and efficiencies of 5 % for **4.1**, 17 % for **4.2**, and 70 % for **4.4** were determined. Upon addition of BPO to **4.1-4.4**, the pulsing efficiencies were enhanced to 53 % for **4.1**, 177 % for **4.2**, 449 % for **4.3**, and 350 % for **4.4**.

The ECL spectra of **4.1-4.4** with BPO, Figure 4.2, were in agreement with the spectra from annihilation and PL, Table 4.1. Yellow emission was observed for **4.1** at 587 nm and **4.2** at 579 nm. Blue-green emission was detected for **4.3** at 504 nm and for **4.4** at 503 nm. We can conclude that monomer emission was observed based on agreement of PL and ECL spectra for **4.1-4.4**.

4.1.4 Conclusions

In summary, this ECL study determined that these iridium(III) complexes are bright ECL luminophores. ECL efficiency is enhanced, compared to $[\text{Ru}(\text{bpy})_3](\text{PF}_6)_2$, when BPO is used as a co-reactant. Complex **4.3** is an excellent candidate with an ECL efficiency more than 4 times higher than that of $[\text{Ru}(\text{bpy})_3]^{2+}$. The iridium(III) complexes containing aryltriazole cyclometallated ligands illustrate great promise in device applications due to their extremely bright ECL.

4.1.5 References

- (1) Bard, A. J. *Electrogenerated Chemiluminescence*; Marcel Dekker: New York, 2004.
- (2) Hu, L.; Xu, G. *Chem. Soc. Rev.* **2010**, *39*, 3275.
- (3) Miao, W. *Chem. Rev.* **2008**, *108*, 2506.
- (4) Pyati, R.; Richter, M. M. *Annu. Rep. Prog. Chem., Sect. C* **2007**, *103*, 12.
- (5) Richter, M. M. *Chem. Rev.* **2004**, *104*, 3003.
- (6) Chen, Z.; Wong, K. M.-C.; Au, V. K.-M.; Zu, Y.; Yam, V. W.-W. *Chem. Commun.* **2009**, 791.
- (7) Tokel, N. E.; Bard, A. J. *J. Am. Chem. Soc.* **1972**, *94*, 2862.
- (8) Li, M.-J.; Chen, Z.; Yam, V. W.-W.; Zu, Y. *ACS Nano.* **2008**, *2*, 905.
- (9) Li, M.-J.; Chen, Z.; Zhu, N.; Yam, V. W.-W.; Zu, Y. *Inorg. Chem.* **2008**, *47*, 1218.
- (10) Kapturkiewicz, A.; Angulo, G. *Dalton Trans.* **2003**, *20*, 3907.
- (11) Shin, I. S.; Kim, J. I.; Kwon, T. H.; Hong, J. I.; Lee, J. K.; Kim, H. *J. Phys. Chem. C* **2007**, *111*, 2280.
- (12) Ciana, L. D.; Zanarini, S.; Perciaccante, R.; Marzocchi, E.; Valenti, G. *J. Phys. Chem. C* **2010**, *114*, 3653.
- (13) Cole, C.; Muegge, B. D.; Richter, M. M. *Anal. Chem.* **2003**, *75*, 601.
- (14) Muegge, B. D.; Richter, M. M. *Anal. Chem.* **2004**, *76*, 73.
- (15) Zanarini, S.; Rampazzo, E.; Bonacchi, S.; Juris, R.; Marcaccio, M.; Montalti, M.; Paolucci, F.; Prodi, L. *J. Am. Chem. Soc.* **2009**, *131*, 14208.
- (16) Kim, J. I.; Shin, I.-S.; Kim, H.; Lee, J.-K. *J. Am. Chem. Soc.* **2005**, *127*, 1614.
- (17) Zhou, G.; Wong, W.-Y.; Yang, X. *Chem. Asian J.* **2011**, *6*, 1706.
- (18) Wong, W.-Y.; Ho, C.-L. *J. Mater. Chem.* **2009**, *19*, 4457.
- (19) Wong, W.-Y.; Ho, C.-L. *Coord. Chem. Rev.* **2009**, *253*, 1709.
- (20) Bandini, M.; Bianchi, M.; Valenti, G.; Piccinelli, F.; Paolucci, F.; Monari, M.; Umami-Ronchi, A.; Marcaccio, M. *Inorg. Chem.* **2010**, *49*, 1439.

- (21) Zanarini, S.; Felici, M.; Valenti, G.; Marcaccio, M.; Prodi, L.; Bonacchi, S.; Contreras-Carballada, P.; Williams, R. M.; Feiters, M. C.; Nolte, R. J. M.; De Cola, L.; Paolucci, F. *Chem. Eur. J.* **2011**, *17*, 4640.
- (22) Li, M.-J.; Jiao, P.; He, W.; Yi, C.; Li, C.-W.; Chen, X.; Chen, G.-N.; Yang, M. *Eur. J. Inorg. Chem.* **2011**, 197.
- (23) Liu, J.; Liu, Q.; Li, C.; Sun, L.; Li, F. *J. Am. Chem. Soc.* **2011**, *133*, 15276.
- (24) Wang, X.; Jia, J.; Huang, Z.; Zhou, M.; Fei, H. *Chem. Eur. J.* **2011**, *17*, 8028.
- (25) Lo, K. K.-W.; Li, S. P.-Y.; Zhang, K. Y. *New J. Chem.* **2011**, *35*, 265.
- (26) Wong, W.-Y.; Zhou, G.-J.; Yu, X.-M.; Kwok, H.-S.; Lin, Z. *Adv. Funct. Mater.* **2007**, *17*, 315.
- (27) Ladouceur, S.; Fortin, D.; Zysman-Colman, E. *Inorg. Chem.* **2011**, *50*, 11514.
- (28) Booker, C.; Wang, X.; Haroun, S.; Zhou, J.; Jennings, M.; Pagenkopf, B. L.; Ding, Z. *Angew. Chem. Int. Ed.* **2008**, *47*, 7731.
- (29) Swanick, K. N.; Dodd, D. W.; Price, J. T.; Brazeau, A. L.; Jones, N. D.; Hudson, R. H. E.; Ding, Z. *Phys. Chem. Chem. Phys.* **2011**, *13*, 17405.
- (30) Connelly, N. G.; Geiger, W. E. *Chem. Rev.* **1996**, *96*, 877.
- (31) McCord, P.; Bard, A. J. *J. Electroanal. Chem.* **1991**, *318*, 91.
- (32) Bartelt, J. E.; Drew, S. M.; Wightman, R. M. *J. Electrochem. Soc.* **1992**, *139*, 70.
- (33) Bard, A. J.; Faulkner, L. R. *Electrochemical methods, fundamentals and applications*; 2nd ed.; John Wiley & Sons Inc.: New York, **2001**.
- (34) Swanick, K. N.; Ladouceur, S.; Zysman-Colman, E.; Ding, Z. *Chem. Commun.* **2012**, *48*, 3179.
- (35) Choi, J.-P.; Wong, K.-T.; Chen, Y.-M.; Yu, J.-K.; Chou, P.-T.; Bard, A. J. *J. Phys. Chem. B* **2003**, *107*, 14407.
- (36) Ding, Z.; Quinn, B. M.; Haram, S. K.; Pell, L. E.; Korgel, B. A.; Bard, A. J. *Science* **2002**, *296*, 1293.
- (37) Hu, L.; Li, H.; Zhu, S.; Fan, L.; Shi, L.; Liu, X.; Xu, G. *Chem. Commun.* **2007**, *40*, 4146.
- (38) Cao, W.; Xu, G.; Zhang, Z.; Dong, S. *Chem. Commun.* **2002**, *14*, 1540.
- (39) Rosenthal, J.; Nepomnyashchii, A. B.; Kozhukh, J.; Bard, A. J.; Lippard, S. J. *J. Phys. Chem. C* **2011**, *115*, 17175.

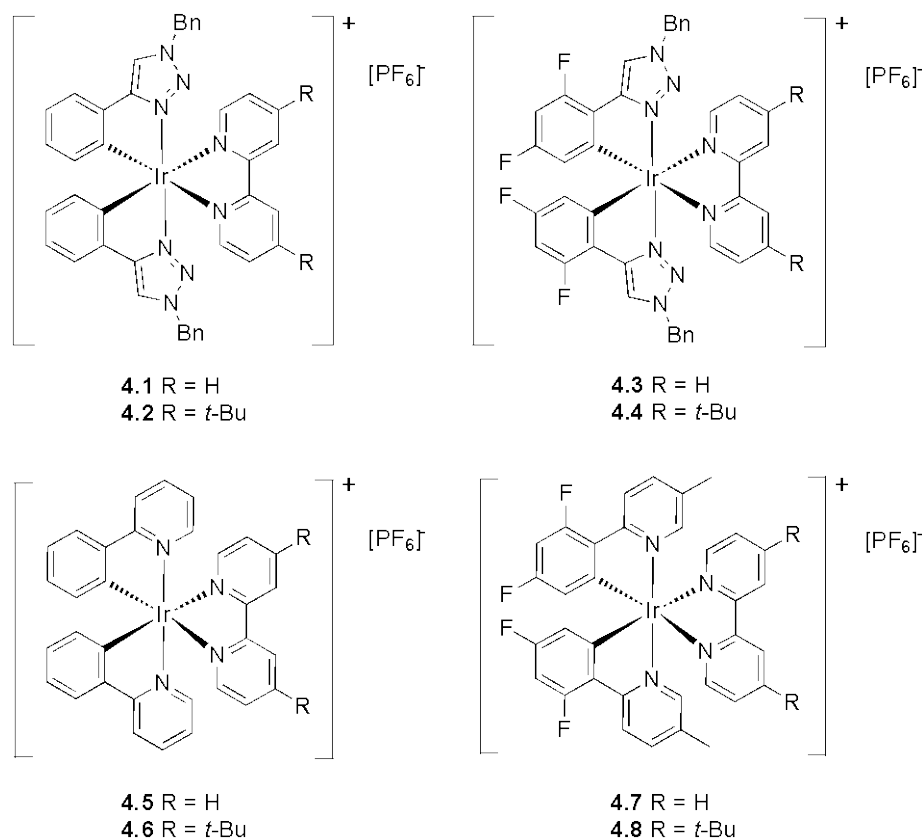
4.2 Correlating Electronic Structures to Electrochemiluminescence of Cationic Ir Complexes[†]

4.2.1 Introduction

While electroluminescence of *fac*-Ir(ppy)₃ (ppyH= 2-phenylpyridine) is up to 7%¹, electrochemiluminescence (ECL)² of this neutral species³ was reported as weak as 0.44%, even with tri-*n*-propylamine as a co-reactant⁴. Ionic liquids⁵ and polymers⁶⁻⁸ were added as electrode absorbates to enhance the light emission of *fac*-Ir(ppy)₃⁹ and its analogues. ECL of charged iridium(III) complexes has recently been explored by a few research groups including us¹⁰⁻¹³, showing great promise as bright ECL emitters. Understanding the structure-emission correlation should be a good strategy to design and prepare even brighter charged iridium(III) complexes.

Herein, we report our discovery on the structure-ECL relationship along with the structure-photoluminescence (PL) correlation of the following [(C[^]N)₂Ir(N[^]N)](PF₆) complexes containing two C[^]N ligands, either a 2-phenylpyridinato (ppy), **4.5-4.6**, or a 2-(2,4-difluorophenyl)-5-methyl-pyridinato (dFMeppy), **4.7-4.8**, and one N[^]N ligand, either 2,2'-bipyridine (bpy), **4.5** or **4.7**, or 4,4'-di-*tert*-butyl-2,2'-bipyridine (dtBubpy), **4.6** or **4.8**, Scheme 4.2.

[†] This work by Kalen N. Swanick, Sébastien Ladouceur, Eli Zysman-Colman, and Zhifeng Ding, **2013**, has been submitted.



Scheme 4.2. Structures of Ir complexes **4.1-4.8**

The correlations are extended to four other related heteroleptic cationic Ir complexes with phenyltriazole (phtl) or 2,4-difluorophenyltriazole (dFphtl) C[^]N ligands in combination with either bpy and dtBubpy, **4.1-4.4**,¹⁰ in Chapter 4.1. Spooling ECL spectroscopy was carried out to visualize the ECL evolution and devolution during the scanning of the applied potential.

4.2.2 Experimental Section

All chemicals were used as received. The syntheses of complexes **4.5-4.8** have been reported previously¹⁴. For ECL studies, ~2 mg of **4.5-4.8** were added to an electrochemical cell with a flat Pyrex window at the bottom for ECL detection, containing 0.1 M tetrabutylammonium hexafluorophosphate (TBAPF₆) supporting electrolyte in 3 mL anhydrous acetonitrile (ACN) that was assembled in a dry box. A 2 mm diameter Pt disc inlaid in a glass sheath was used as the working electrode (WE), a

coiled Pt wire as the counter electrode (CE), and a coiled Pt wire as the quasi reference electrode (RE), respectively. Ferrocene was used as the internal standard.¹⁰ Electrode and cell cleaning procedures¹⁵, details on CV and ECL experiments^{10,15,16}, and spooling ECL spectroscopy¹⁷ have been published elsewhere. $[\text{Ru}(\text{bpy})_3](\text{PF}_6)_2$ was used as an external standard for ECL efficiency with its absolute efficiency of 5.0 %¹⁸.

4.2.3 Results and Discussion

The ECL-voltage curves and cyclic voltammograms (CVs) for **4.5-4.8** are shown in Figure 4.3a-d, respectively. The accumulated ECL spectra, seen in Figure 4.4a-d, were collected during two full cycles of the potential scanning. Complex **4.5** underwent a quasi-reversible reduction reaction at a formal potential of -1.38 V vs. SCE, Eq. 4.10, and a quasi-reversible oxidation at 1.27 V, Eq. 4.11, with peak-to-peak separations of ~60 mV.

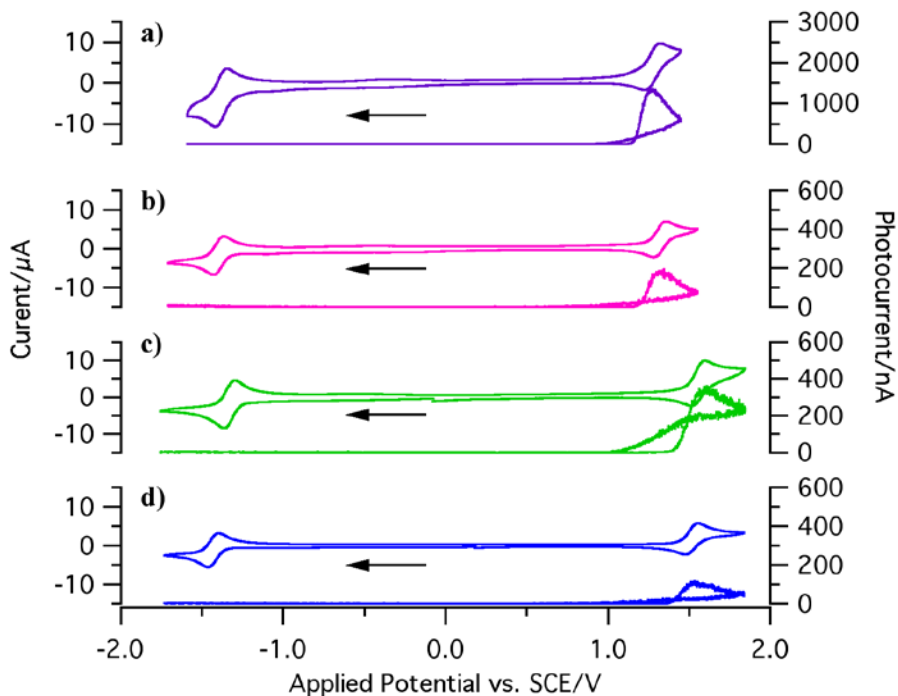
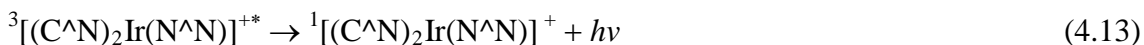
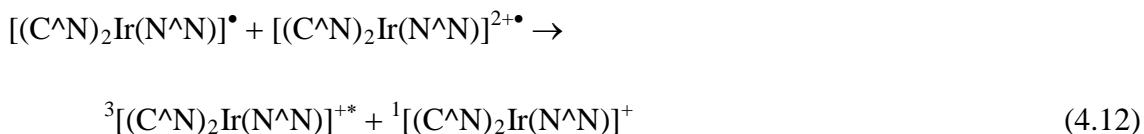
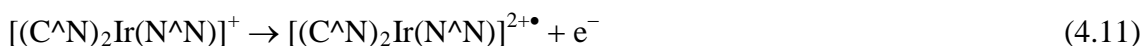
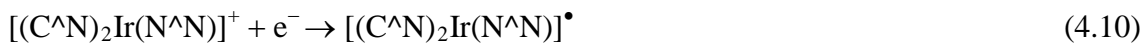


Figure 4.3. Cyclic voltammograms obtained in ACN with overlaid ECL-voltage curves for a) **4.5**, b) **4.6**, c) **4.7**, and d) **4.8**. The scan rate was at 0.1 V/s.

In the scanning process, the alternatively generated radicals $[(C^{\wedge}N)_2Ir(N^{\wedge}N)]^{\bullet}$ through the reduction, Eq. 4.10, and $[(C^{\wedge}N)_2Ir(N^{\wedge}N)]^{2+\bullet}$ via the oxidation, Eq. 4.11, met in the vicinity of the electrode to generate a triplet excited species, Eq. 4.12, which eventually emits light, Eq. 4.13, returning to its ground singlet state. For the metal chelates such as our Ir complexes, triplet-triplet annihilation¹⁹ mechanism to a singlet excited state for ECL of organic molecules might be absent since the observed ECL peak wavelengths in Figure 4.4 correlate to those of PL.



From Eq. 4.14²⁰⁻²², the enthalpy, $\Delta H^{\circ}_{\text{ann}}$, of the annihilation ECL process for **4.5** is 2.49 eV. Since the $-\Delta H^{\circ}_{\text{ann}}$ value is smaller than the optical HOMO-LUMO gap or singlet energy, E_s , 2.67 eV (464 nm)²³, Eq. 4.15, it is impossible for the electrogenerated excited state to be a singlet²⁴.

$$-\Delta H^{\circ}_{\text{ann}} = -\Delta G^{\circ}_{\text{ann}} - T\Delta S^{\circ} \approx \Delta E^{o'} - 0.16 \text{ eV} \quad (4.14)$$

$$-\Delta H^{\circ}_{\text{ann}} \geq E_s \quad (4.15)$$

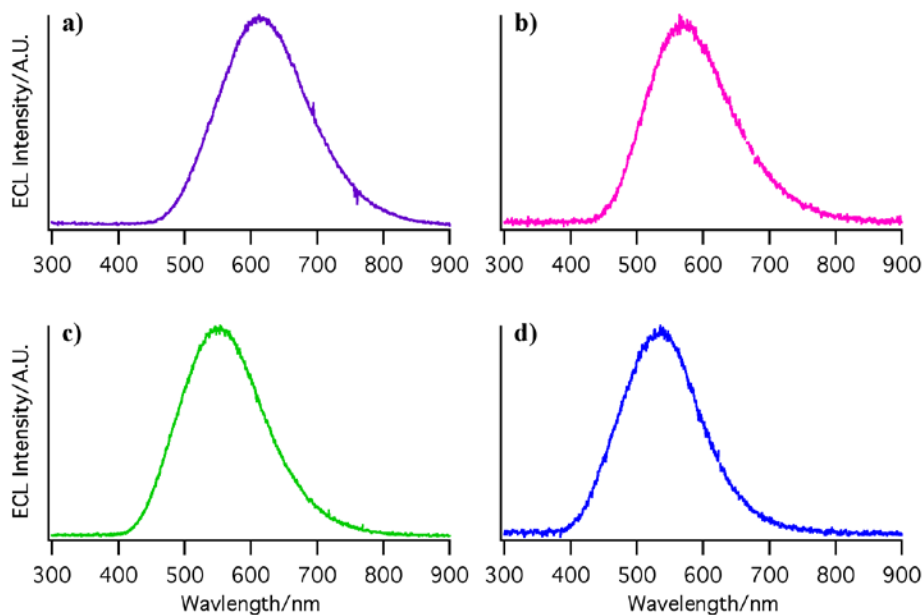


Figure 4.4. Accumulated ECL spectra of a) **4.5**, b) **4.6**, c) **4.7**, and d) **4.8**, during two full cycles of the potential scanning, respectively. The scan rate was at 0.1 V/s.

Instead, a triplet excited state, $^3[(C^{\wedge}N)_2Ir(N^{\wedge}N)]^{+*}$, must be produced directly, Eq. 12. This triplet state relaxes back to the singlet ground state, phosphorescing (see the ECL-voltage curve in Figure 4.3a similarly to the photoinduced phosphorescence¹⁴. The triplet was confirmed by the peak wavelength at 613 nm, 2.02 eV, in the ECL spectrum in the above annihilation path, Figure 4.4a, which matches very well with the PL peak wavelength at 602 nm, 2.06 eV. The ECL mechanism should be very similar to that of its counterpart, $[Ru(bpy)_3]^{2+}$.²⁵

For **4.6**, the reversibility of electrochemical behavior is very similar to that of **4.5**. ECL emission was also observed at the positive potential side, Figure 4.3b. The ECL peak wavelength, 576 nm/2.15 eV, Figure 4.4b, is very close to the PL emission, 591 nm/2.10 eV¹⁴. The ΔH°_{ann} is 2.55 eV, less than its E_s of 2.67 eV. This implies that the singlet excited state is not accessible for **4.6**, thus following the triplet route. The addition of the *tert*-butyl (*t*-Bu) substituents on the bpy ligand causes the increased separation between the oxidation and reduction potentials and thus a larger HOMO-LUMO gap¹⁴.

The addition of the two fluorine atoms and one methyl group on the C^N ligands in **4.7** contributes to further increasing the electrochemical gap to 2.89 eV¹⁴. The fluorine atoms on the structure of **4.7** have a significant impact on the wavelength emitted *via* ECL, 536 nm/2.31 eV, resulting in a 0.29 eV blue-shift from **4.5** to **4.7**. A similar trend was seen in the PL data¹⁴. Complex **4.7** has a $\Delta H^\circ_{\text{ann}}$ of 2.73 eV, which is smaller than the E_s of 2.82 eV, however, the difference is only 0.09 eV, so it is conceivable that direct population of the singlet excited state could be permitted, however it is sufficient to directly populate the emitting triplet excited state, as previously mentioned by Bard and Tokel²⁵.

Finally in **4.8**, the addition of the *t*-Bu substituents on the bpy ligand caused a slight blue-shift in ECL emission to 533 nm relative to **4.5-4.7**, and a larger electrochemical gap of 2.94 eV. The $\Delta H^\circ_{\text{ann}}$ of **4.8**, 2.78 eV, is smaller than the E_s , 2.82 eV with only a minute 0.04 eV difference. Similar to **4.7**, electrogenerating the singlet state in **4.8** may occur but the triplet state is nonetheless probably generated directly, following a similar mechanistic pathway to **4.5-4.7**.

The PL and ECL observation on **4.1-4.4** was reported by us¹⁰, see Chapter 4.1. The triplet excited species of **4.1** and **4.2** were probably generated directly in the ECL, based on Eqs. 4.14 and 4.15. However, in **4.3** and **4.4** the combination of the triazole moiety with the two fluorine atoms on the aryl group of the C^N ligands is responsible for a sufficiently large blue-shift in emission, thereby increasing the energy of the triplet state surface in these complexes, thus making it possible to reach directly the singlet excited state.

Complex **4.5** displayed the strongest ECL efficiency of the four complexes studied in this report. Here, a relative ECL efficiency of 90 % was obtained. Installing two *t*-Bu substituents on the bpy ligand in **4.6** resulted in a large decrease in efficiency to 16 %, despite an increase in PLQY¹⁴. With the two fluorine atoms installed on the ppy ligands, **4.7** showed a decrease in ECL efficiency, 41 %, relative to **4.5**, but higher than **4.6**. Furthermore, combining *t*-Bu substitution of the bpy with dFMeppy ligands, **4.8**, decreased the efficiency of the complex to 21 %. It can be seen that the role of the

substituents in both the triazole- and ppy-containing ligands studied are very important factors in tuning ECL emission. While trends in ECL emission energies mirror those observed in our previous photoluminescent studies, the only clear tendency with ECL efficiency is its marked decreases when *t*-Bu substituents are present on the complexes, opposite to their photoluminescence quantum yield. Compounds **4.1-4.4** showed similar substituent effect on the ECL efficiency, see Chapter 4.1.

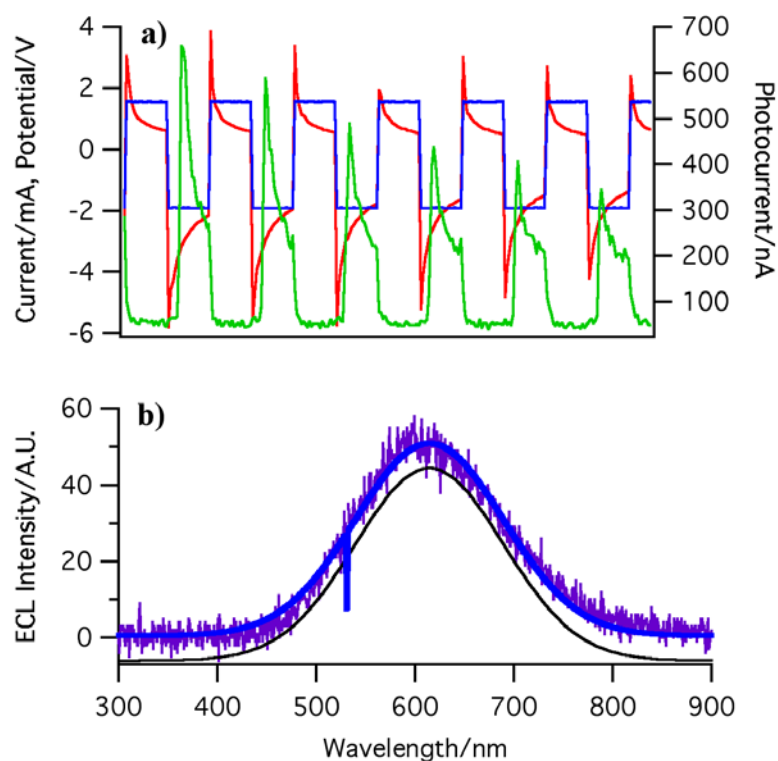


Figure 4.5. a) Voltage pulsing between -1.92 V and 1.56 V (blue) applied to the working electrode immersed in a solution of **4.5**, corresponding current (red) and photocurrent (green), b) ECL spectrum after the pulsing process as in a), for 30 s (purple), curve-fit wave (black), and the average fitted spectrum (blue).

When a voltage pulsing profile between -1.92 V and 1.56 V, first reduction and oxidation potentials, at 10 Hz was applied to the working electrode immersed in a solution of **4.5**, Figure 4.5a, a lower ECL intensity, 300-600 nA, was observed than that during scanning, 1400 nA, Figure 4.3a. This decrease in ECL can be attributed to the concentrations at which the radicals were generated in solution. Scanning at a rate of 0.1

V/s generated higher radical concentrations than pulsing at a frequency of 10 Hz, leading to higher ECL intensity. Other factors contributing to the decrease in photocurrent include the kinetics; the apparent slow reaction rate of the recombination of the two bulky radicals cannot match the faster pace of the reduction and oxidation processes of **4.5**, leading to a lower ECL efficiency. In order to reach the triplet state, more time may be necessary. The relative efficiencies from pulsing for all the four compounds are less than 0.028 %.

The ECL peak wavelength, 614 nm, in the above pulsing experiments, Figure 4.5b, reproduces that from scanning, 613 nm, Figure 4.4a. This shows how both methods result in the production of the same excited species in solution at the working electrode. Other compounds are similar in this aspect.

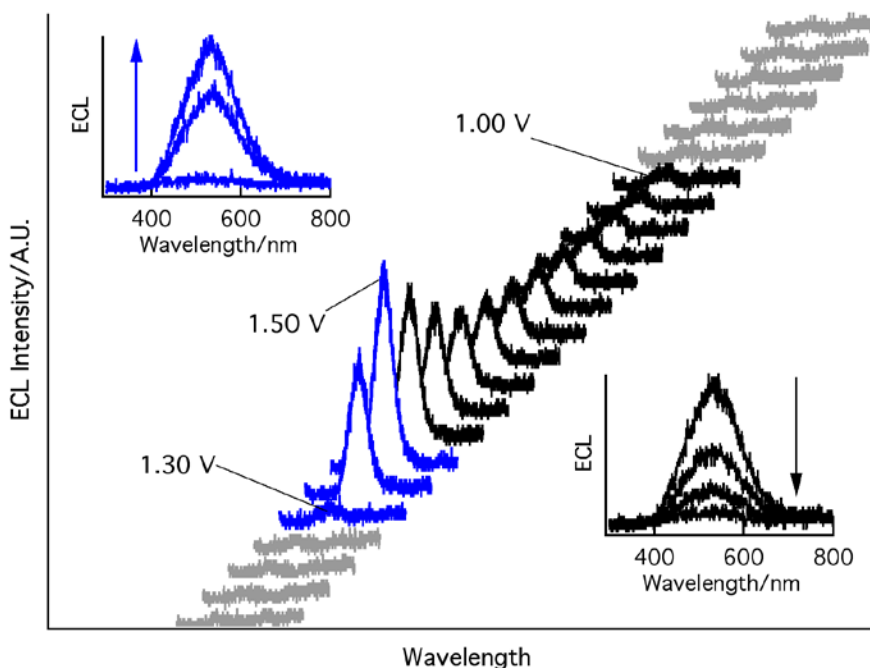


Figure 4.6. Spooling spectra of **4.8**, acquired during a voltage scan between -1.73 V and 1.84 V at scan rate of 0.1 V/s for 130 s. Insets illustrate ECL evolution (blue) and devolution (black).

We were able to record ECL spectra of **4.8** by our newly developed spooling ECL spectroscopy, Figure 4.6. This method tracks the development of the ECL signal with the applied potential. As the radicals of **4.8** were generated in solution, the radical annihilation yielded the triplet excited species of **4.8** that radioactively decayed through light emission, as shown in Figure 4.6. The inset spectra in blue in Figure 4.3 show the evolution of the peak at 533 nm, maximized at 1.50 V, and the inset spectra in black demonstrate the devolution of the peak when the potential scans back to 0.00 V. Only one excited species was generated in solution, with a λ_{em} at 533 nm. From Figure 4.6, the onset of ECL was observed at 1.30 V followed by a sharp increase in ECL (in blue) at 1.40 V. The devolution of this emission peak (at 533 nm in black) occurs from 1.60 V to 1.80 V and emission persists when scanning back to 1.00 V. At 0.90 V, ECL returned to the baseline (in grey). The spooling ECL spectra well reproduced the observations in the ECL-voltage curves as in Figure 4.3a to Figure 4.3d.

4.2.4 Conclusions

Complexes **4.5-4.8** are efficient in ECL emission. Generation of the excited triplet states appears to be advantageous, requiring less energy to produce higher ECL efficiencies. For all of the eight complexes, the installation of the fluorine and *t*-Bu substituents on the ligands increases the electrochemical gap thus promoting blue shifts in the ECL emission. However, the fluorine and *t*-Bu substituents on the ligands decrease the ECL intensity. Comparing complexes with the ppy and phtl C^N ligands, the ppy-containing complexes, **4.5-4.8**, show higher efficiencies than the phtl complexes, **4.1-4.4**, with the exception of **4.3**. This might be due to the generation of both triplet state and singlet state resulting in higher ECL efficiency. Highly ECL-efficient iridium complexes will find wide applications^{2,26}.

4.2.5 References

- (1) Richter, M. M. In *Electrogenerated Chemiluminescence*; Bard, A. J., Ed.; Marcel Dekker: New York, **2004**, p 301.

- (2) Miao, W. *Chem. Rev.* **2008**, *108*, 2506.
- (3) Vogler, A.; Kunkely, H. In *High-Energy Processes in Organometallic Chemistry*; American Chemical Society: **1987**; Vol. 333, p 155.
- (4) Bruce, D.; Richter, M. M. *Anal. Chem.* **2002**, *74*, 1340.
- (5) Roop, J.; Nothnagel, M.; Schnuriger, M.; Richter, M. M.; Baker, G. A. *J. Electroanal. Chem.* **2011**, *656*, 34.
- (6) Cole, C.; Muegge, B.; Richter, M. *Anal. Chem.* **2003**, *75*, 601.
- (7) Muegge, B. D.; Richter, M. M. *Anal. Chem.* **2004**, *76*, 73.
- (8) Muegge, B.; Richter, M. *Luminescence* **2005**, *20*, 76.
- (9) Kapturkiewicz, A.; Angulo, G. *Dalton Trans.* **2003**, 3907.
- (10) Swanick, K. N.; Ladouceur, S.; Zysman-Colman, E.; Ding, Z. *Chem. Commun.* **2012**, *48*, 3179.
- (11) Kim, J. I.; Shin, I.-S.; Kim, H.; Lee, J.-K. *J. Am. Chem. Soc.* **2005**, *127*, 1614.
- (12) Bandini, M.; Bianchi, M.; Valenti, G.; Piccinelli, F.; Paolucci, F.; Monari, M.; Umani-Ronchi, A.; Marcaccio, M. *Inorg. Chem.* **2010**, *49*, 1439.
- (13) Zanarini, S.; Felici, M.; Valenti, G.; Marcaccio, M.; Prodi, L.; Bonacchi, S.; Contreras-Carballada, P.; Williams, R. M.; Feiters, M. C.; Nolte, R. J. M.; De Cola, L.; Paolucci, F. *Chem. Eur. J.* **2011**, *17*, 4640.
- (14) Ladouceur, S.; Fortin, D.; Zysman-Colman, E. *Inorg. Chem.* **2011**, *50*, 11514.
- (15) Swanick, K. N.; Dodd, D. W.; Price, J. T.; Brazeau, A. L.; Jones, N. D.; Hudson, R. H. E.; Ding, Z. *Phys. Chem. Chem. Phys.* **2011**, *13*, 17405.
- (16) Swanick, K. N.; Price, J. T.; Jones, N. D.; Ding, Z. *J. Org. Chem.* **2012**, *77*, 5646.
- (17) Swanick, K. N.; Ladouceur, S.; Zysman-Colman, E.; Ding, Z. *Angew. Chem. Int. Ed.* **2012**, *51*, 11079.
- (18) McCord, P.; Bard, A. J. *J. Electroanal. Chem.* **1991**, *318*, 91.
- (19) Choi, J.-P.; Wong, K.-T.; Chen, Y.-M.; Yu, J.-K.; Chou, P.-T.; Bard, A. J. *J. Phys. Chem. B* **2003**, *107*, 14407.
- (20) Faulkner, L. R.; Bard, A. J. *Electroanalytical Chemistry*; Marcel Dekker: New York, **1977**; Vol. 10.
- (21) Faulkner, L. R.; Tachikawa, H.; Bard, A. J. *J. Am. Chem. Soc.* **1972**, *94*, 691.

- (22) Lai, R. Y.; Bard, A. J. *J. Phys. Chem. A* **2003**, *107*, 3335.
- (23) Fungo, F.; Wong, K.-T.; Ku, S.-Y.; Hung, Y.-Y.; Bard, A. J. *J. Phys. Chem. B* **2005**, *109*, 3984.
- (24) Lee, S. K.; Zu, Y.; Herrmann, A.; Geerts, Y.; Müllen, K.; Bard, A. J. *J. Am. Chem. Soc.* **1999**, *121*, 3513.
- (25) Tokel, N. E.; Bard, A. J. *J. Am. Chem. Soc.* **1972**, *94*, 2862.
- (26) Xu, L.; Li, Y.; Wu, S.; Liu, X.; Su, B. *Angew. Chem. Int. Ed.* **2012**, *51*, 8068.

Chapter 5

5 Mechanistic Insight into Electrochemiluminescence of Iridium(III) Complexes via Spooling Spectroscopy

5.1 Strongly Blue Luminescent Cationic Iridium(III) Complexes with an Electron-Rich Ancillary Ligand: Evaluation of Their Optoelectronic and Electrochemiluminescence Properties[†]

5.1.1 Introduction

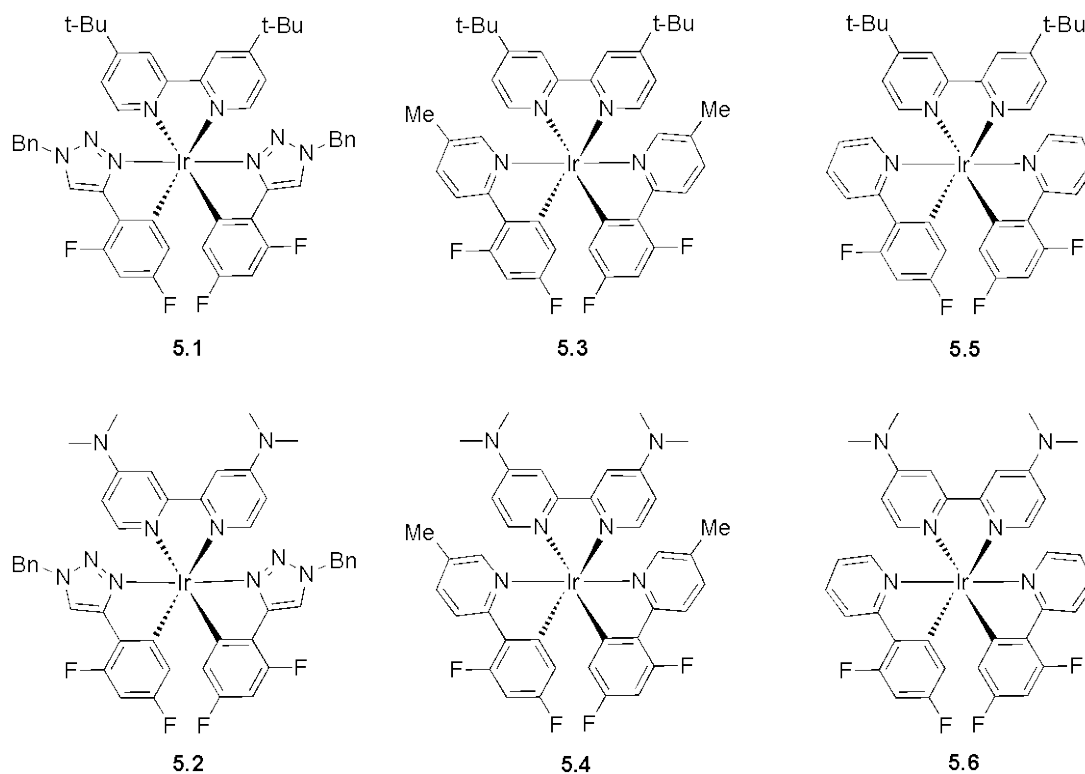
Cationic iridium(III) complexes have come to the fore as the emissive molecules of first choice in diverse solid and solution state applications such as light-emitting electrochemical cells (LEECs)¹⁻³ and biological and environmental probes^{4,5} owing to their attractive photophysical and physicochemical profile: high quantum efficiencies, large window of accessible excited state lifetimes, a HOMO-LUMO gap that is easily modulated and great thermal and chemical stabilities. In particular, the integration of readily soluble Ir complexes with electrogenerated chemiluminescence (ECL) techniques will produce increased sensitivity ECL-based assays compared to benchmark $[\text{Ru}(\text{bpy})_3]^{2+}$ derivatives with important implications for diverse biological and materials applications.^{6,7} Of late, there has been increased number of reports on ECL behavior in both aqueous and non-aqueous media using both neutral,⁸⁻²¹ charged^{12,21-29} mononuclear, oligonuclear^{30,31} and polymer-bound³² iridium(III) complexes. LEECs and ECL share a common mechanistic lineage in that the generation of light in both applications results from the recombination of holes (radical cations) and electrons (radical anions), which have been electrochemically generated, to form excitons radiatively relaxing back to the ground state.

[†] This work is published in Sébastien Ladouceur, Kalen N. Swanick, Shawn Gallagher-Duval, Zhifeng Ding and Eli Zysman-Colman, *Eur. J. Inorg. Chem.*, **2013**, accepted, DOI: 10.1002/ejic.201300849. See Appendix IV.

For most applications, including full-color lighting and visual displays, access to a blue emitter is a prerequisite and one that is phosphorescent is potentially advantageous. For instance, power consumption in organic light-emitting diodes (OLEDs) can be measurably improved with integrated phosphors compared to blue fluorophores.³³ Through judicious modification of the ligand sphere, iridium complexes phosphorescing from the red to sky-blue have been reported. However, still missing is a highly luminescent blue luminophore. To our knowledge, the “bluest” cationic iridium luminophores generally show structured ligand-centered (³LC) emission bands between 451-490 nm in either DCM or ACN solution, with photoluminescent quantum yields (Φ_{PL}) ranging from 3 to 54 %;³⁴⁻⁴⁴ cationic iridium complexes incorporating σ -donating phosphine ancillary ligands demonstrate Φ_{PL} as high as 80 %.^{42,45}

We,⁴⁶ and others,⁴⁷⁻⁵⁰ have recently reported the use of aryltriazoles (atl) as cyclometallating ligands (C[^]N) for cationic iridium complexes of the form [(C[^]N)₂Ir(L[^]L)]⁺, where L[^]L is a datively coordinating ligand such as 2,2'-bipyridine. We demonstrated that the replacement of a 2-phenylpyridine (ppy) C[^]N ligand by an atl resulted in a net blue shift (ca. 533 cm⁻¹) in the emission spectrum with an increase in quantum efficiency due in part to the presence of *N*-benzyl groups on the triazoles.⁴⁶ The bluest of the emitters reported in our initial study, **5.1**, Scheme 5.1, exhibited an emission λ_{max} of 499 nm in ACN solution at 298 K with $\Phi_{\text{PL}} = 80\%$, similar to a structurally related complex observed by De Cola and co-workers.⁴⁷ In addition, De Angelis and co-workers^{51,52} reported that the combined effects of electron-releasing substituents on the bipyridine ligand and of electron-withdrawing substituents on the phenylpyridine ligands can tune the emission to higher energy. Based on all above, we hypothesized that the substitution of the dtBubpy L[^]L ligand (dtBubpy: 4,4'-di-*t*-butyl-2,2'-bipyridine) of **5.1** with a more electron-donating dmabpy (dmabpy: 4,4'-bis(*N,N*-dimethylamino)-2,2'-bipyridine), as in **5.2**, would produce a desired further blue-shift. In order to assess the impact of the proposed structural modification on the photophysical behavior, we contrast **5.2** with benchmark complex **5.4**, a methylated analog to that reported in the literature, **5.6**, also known as N969.⁵² We further explore the impact of methylation at the 5-position on the pyridine ring of the C[^]N ligand through a comparison with between **5.3** and **5.5**

along with **5.4** and **5.6**, **5.3** being a green-blue emitter previously reported by Bolink and co-workers.⁵³ Herein, we report the solution state photophysical, electrochemical behavior at ambient temperature along with 77 K photophysical data for **5.2** and **5.4** and compare with benchmark complexes **5.1**, **5.3**, **5.5** and **5.6**, Scheme 5.1. We further evaluate in a rational manner the ECL properties for **5.2**, **5.4** and **5.6** in order to discern structure property relationships relevant to the development of ECL luminophores. DFT calculations were also used to rationalize the structure-property relationships observed experimentally in our optoelectronic studies.



Scheme 5.1. Ir complexes in study, **5.1-5.6**

5.1.2 Experimental Section

Electrochemistry and Electrogenerated Chemiluminescence Characterization.

For annihilation ECL studies, approximately 2 mg of compound, **5.1-5.6**, was added to a pyrex electrochemical cell with a flat Pyrex window at the bottom for detection of generated ECL. A 2 mm diameter Pt disc inlaid in a glass sheath were used

as the working electrode (WE), a coiled Pt wire as the counter electrode (CE), and a coiled Ag wire as the quasi reference electrode (RE), respectively. Routine cleaning procedures for the electrodes and cell were reported elsewhere.^{25,54,55} For detailed electrochemical workstation and ECL setup information, please refer to our previous publications.^{25,54,55} The cell contained 0.1 M tetrabutylammonium hexafluorophosphate (TBAPF₆) supporting electrolyte in anhydrous acetonitrile (3 mL) that was assembled in a dry box.

The cyclic voltammetry (CV) was conducted on a CHI 610A electrochemical analyzer (CH Instruments, Austin, TX). The experimental parameters for the cyclic voltammograms (CVs) are listed here: 0.00 V initial potential in experimental scale, positive or negative initial scan polarity, 0.1 V/s scan rate, 4 sweep segments, 0.001 V sample interval, 2 s quiet time, $1-5 \times 10^{-5}$ AV⁻¹ sensitivity. Potentials (V) were calibrated using an internal standard Fc/Fc⁺ redox couple after each experiment, and are reported vs. a SCE standard electrode (0.40 V in ACN).⁵⁶

The ECL data along with CV data were obtained using the CHI 610A coupled with a photomultiplier tube (PMT, R928, Hamamatsu, Japan) held at -750 V with a high voltage power supply. The ECL collected by the PMT under the flat Pyrex window at the bottom of the cell was measured as a photocurrent, and transformed to a voltage signal, using a picoammeter/voltage source (Keithley 6487, Cleveland, OH). The potential, current signals from the electrochemical workstation, and the photocurrent signal from the picoammeter were sent simultaneously through a DAQ board (DAQ 6052E, National Instruments, Austin, TX) in a computer. The data acquisition system was controlled from a custom-made LabVIEW program (ECL_PMT610a.vi, National Instruments, Austin, TX). The photosensitivity on the picoammeter was set manually in order to avoid the saturation.

The ECL spectra were obtained by replacing the PMT with a spectrometer (Cornerstone 260, Newport, Canada) attached to a CCD camera (Model DV420-BV, Andor Technology, Belfast, UK). The camera was cooled to -55 °C prior to use and

controlled by a computer for operation and data acquisition. The intensities versus wavelengths (spectra) were recorded by Andor Technology program.

For the spooling experiments, the same spectrometer and CCD camera were used and the following parameters were employed in the Andor Technology program under the kinetic parameters option tab: for **5.4**: exposure time = 1 s, number of accumulations = 1, kinetic series length = 175 s (matching with the potential scan time for two complete cycles), kinetic cycle time = 1, and the spectrometer was centered at 500 nm using the 121.6 l/mm grating, with the camera cooled to -55 °C. On the CHI 610A electrochemical analyzer, the initial potential was set to 0.00 V, high potential = 2.44 V, low potential = -2.34 V, sensitivity = $1 \times 10^{-5} \text{ AV}^{-1}$, initial scan polarity = negative, scan rate = 0.1 V/s sweep segments = 4, sample interval = 0.001 V, quiet time 2 s. Simultaneously, the CHI 610A electrochemical analyzer and the Andor Technology program were run and the CV and spooling spectra were collected; for **5.6**: exposure time = 1 s, number of accumulations = 1, kinetic series length = 155 s (matching with the potential scan time for two complete cycles), kinetic cycle time = 1, and the spectrometer was centered at 600 nm using the 121.6 l/mm grating, with the camera cooled to -55 °C. On the CHI 610A electrochemical analyzer, the initial potential was set to 0.00 V, high potential = 2.20 V, low potential = -2.00 V, sensitivity = $1 \times 10^{-5} \text{ AV}^{-1}$, initial scan polarity = negative, scan rate = 0.1 V/s sweep segments = 4, sample interval = 0.001 V, quiet time 2 s. Simultaneously, the CHI 610A electrochemical analyzer and the Andor Technology program were run and the CV and spooling spectra were collected.

ECL quantum efficiencies (QE) were calculated relative to $[\text{Ru}(\text{bpy})_3](\text{PF}_6)_2$ taken as 100 % in acetonitrile solution (absolute quantum ECL efficiency of $[\text{Ru}(\text{bpy})_3]^{2+}$ is 5.0 %^{57,58}) by integrating both the ECL intensity and current value versus time for each compound, see Eq. 2.1 in Chapter 2.

5.1.3 Results and Discussion

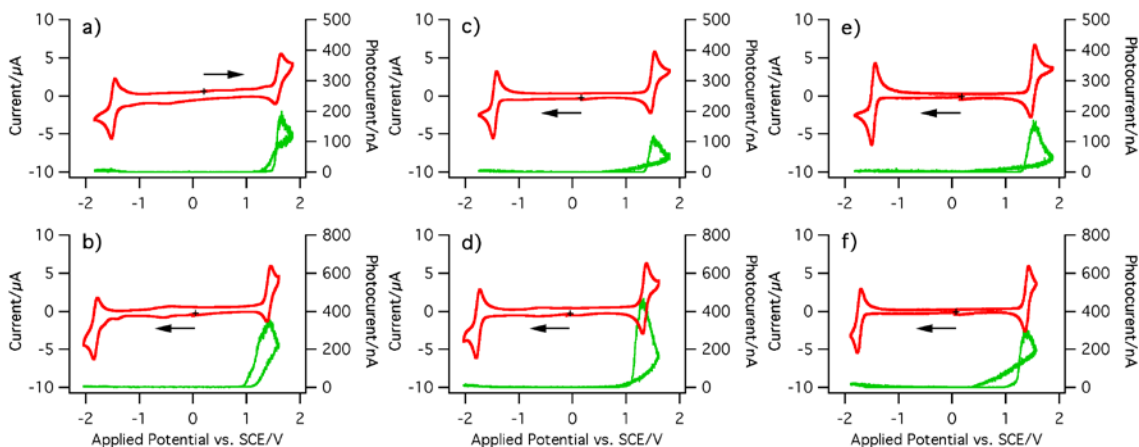


Figure 5.1. CVs (red) with ECL-voltage curves (green) overlaid of a) **5.1**, b) **5.2**, c) **5.3**, d) **5.4**, e) **5.5**, and f) **5.6**, first oxidation and reduction potential profile with a scan rate of 0.1 V/s.

The electrochemical properties were investigated by cyclic voltammetry in ACN and results are summarized in Table 5.1. All electrochemical processes are either quasi-reversible or reversible at a 0.1 V/s scan rate. The oxidation is assigned to a largely iridium-centered event wherein the potential is modulated by the nature of the C^N ligands while the reduction is localized on the N^N ancillary ligand (dtBubpy and dmabpy at ca. -1.46 and -1.78 V, respectively). For instance, **5.2** underwent a quasi-reversible oxidation at 1.42 V and a reversible reduction at -1.82 V, Figure 5.1. Both of these potentials are significantly cathodically shifted compared to those of **5.1** due to the presence of the strongly electron-donating dmabpy ligand.

Table 5.1. Electrochemical and ECL data for **5.1-5.6**.

	$E_{1/2,ox}$ (V) ^a [ΔE_p (mV)]	ΔE_{redox} (V)	$E_{1/2,red}$ (V) [ΔE_p (mV)]	Φ_{ECL} ^b (%)	ECL λ_{max} (nm)
5.1 ^c	1.61 (100)	3.10	-1.49 (67)	17	510
5.2 ^d	1.42 (72)	3.24	-1.82 (67)	32	536
5.3 ^e	1.51 (98)	2.94	-1.42 (74)	21	533
5.4	1.35 (70)	3.12	-1.77 (63)	32	510
5.5	1.50 (70)	2.97	-1.47 (62)	17	519
5.6	1.36 (62)	3.14	-1.78 (63)	38	527

^aMeasured in ACN (ca. 1.5 mM) with NBu₄PF₆ (ca. 0.1 M) as the supporting electrolyte at a scan rate of 0.1 V/s. Potentials (V) are calibrated using Fc/Fc⁺ and are reported vs. SCE.

^bAnnihilation ECL efficiencies are relative to [Ru(bpy)₃](PF₆)₂ taken as 100 % in ACN (Φ_{ECL} of [Ru(bpy)₃]²⁺ is 5.0 %) ^{59,60}.

^cECL data taken from ref ²⁵.

^dCV data taken from ref ⁶¹.

^eCV data taken from ref ⁴⁶.

The CV profiles for **5.4** and **5.6** are similar to that for **5.2** but shows reduced destabilization of both the oxidation and reduction reactions. We had previously shown that triazoles destabilize HOMO/LUMO orbitals compared to ppy-type analogs.⁴⁶ The combined effect of atl and dmabpy is a further 300 mV increase in the HOMO-LUMO gap for **5.2** compared to **5.3**. The electrochemical gap of 3.24 V for **5.2** is larger than that recently reported for [(dFppz)₂Ir(dmabpy)]PF₆ at 3.19 V.⁶² For further comparison, the first oxidation and reduction waves for previously reported **5.6** occur at 1.36 and -1.78 V,

respectively, correlating well with those measured for **5.4**. Thus, the inclusion of the methyl group does not appreciably affect the electrochemical gap.

ECL is light emission from excited states produced by electron transfer between radical anions and cations generated electrochemically in the vicinity of the working electrode during potential scanning/cycling along electrochemical measurements. Moderately strong ECL emissions from all the six complexes were observed during dynamic potential scanning, green curves in Figure 5.1, in the regions of first oxidation and reduction reactions. All the ECL-voltage curves show light emissions in the anodic regions, illustrating higher stability of radical anions than that of radical cations.

ECL annihilation efficiencies were evaluated when the applied potential was scanned between the first reduction and oxidation peak potentials, Table 5.1. Complexes **5.2** and **5.4** and **5.6** generated modestly high ECL signals compared to **5.1**²⁵ once the radical anions and radical cations combined to generate the excited species, Figure 5.1. In fact, each of **5.1**, **5.3** and **5.5** exhibited reduced ECL efficiencies, due to the presence of the two *t*-butyl groups on the bipyridine. The Φ_{ECL} , based on two cycles, for **5.4**, 32 % is identical to that of **5.2**, 32 %, while that of **5.6** shows higher ECL efficiency of 38 %. The electron-donating property does play an important role in ECL characteristics. Each of the complexes follows the same annihilation ECL mechanism as we previously determined for **5.1**,²⁵ where triplet excited species can be generated directly from the radicals without passing by the singlet excitons.

The ECL spectra are generally red-shifted with respect to the photoluminescent spectrum due to the higher concentrations required during ECL acquisition and are broad and unstructured, Table 5.1.⁶³ While a slight 337 cm⁻¹ red-shift in the unstructured ECL spectrum for **5.2** compared to **5.1** was observed, **5.4** gives a maximum $\lambda_{\text{ECL}} = 510$ nm, making it, to the best of our knowledge, amongst the bluest ECL-active phosphors known, Figure S5.1 in Appendix IV.²⁴

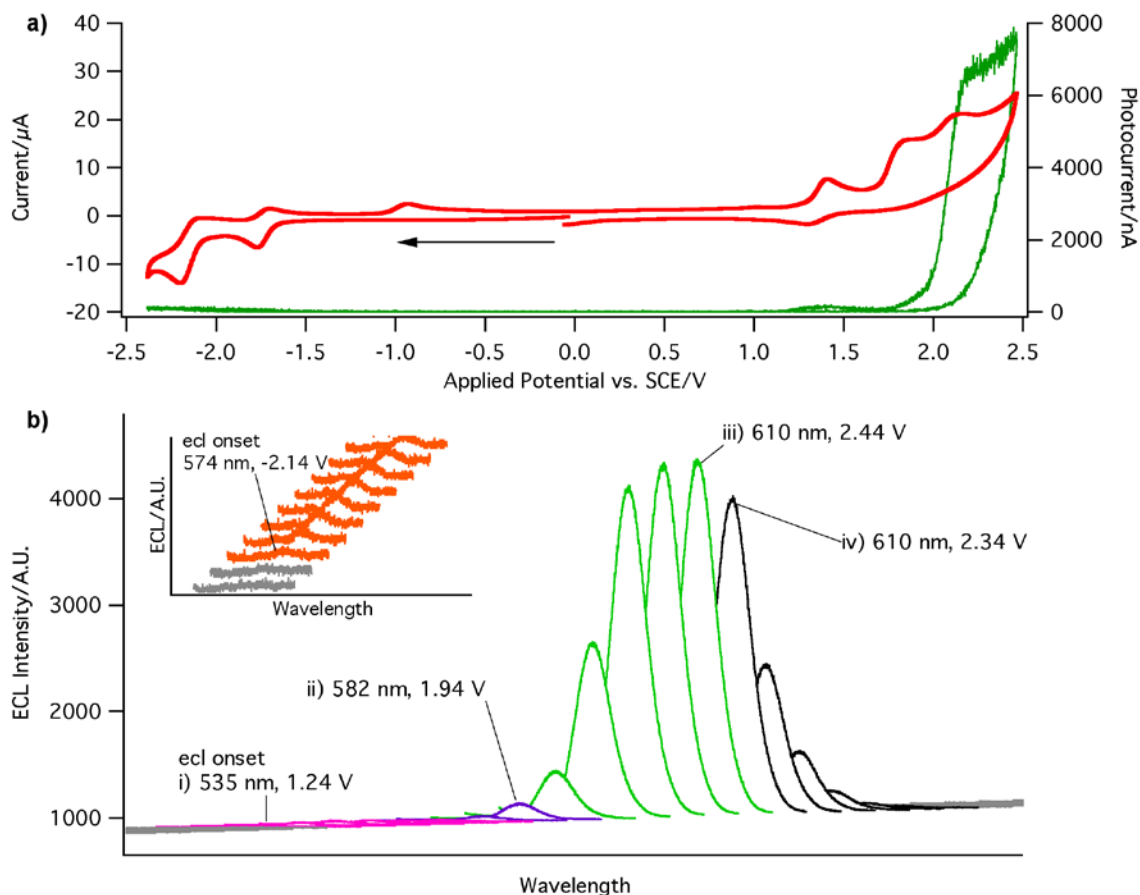


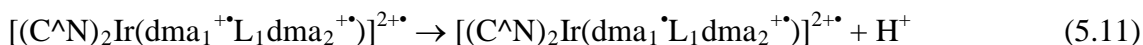
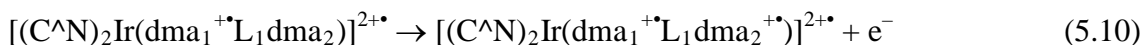
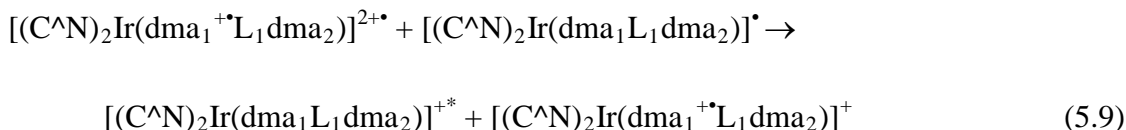
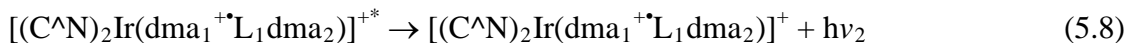
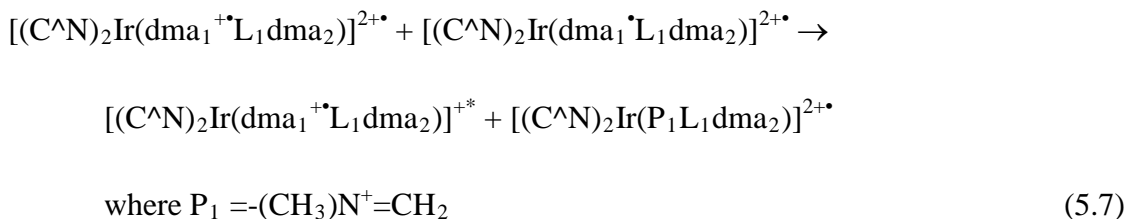
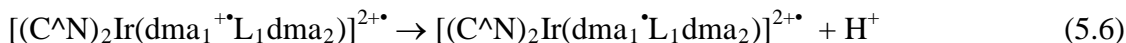
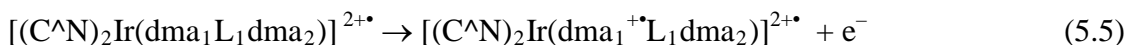
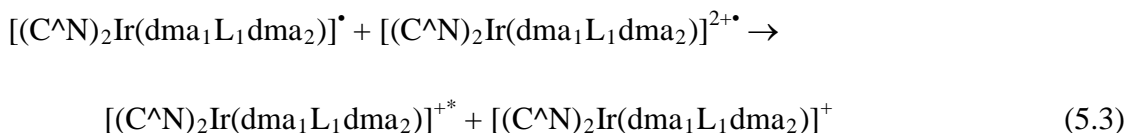
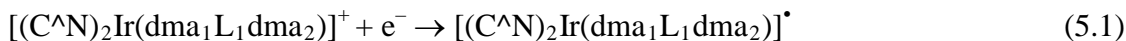
Figure 5.2. a) CV of **5.4** with ECL-voltage curve overlaid with a potential profile ranging between -2.34 to 2.44 V, b) ECL spooling spectra of **5.4** during first potential scanning cycle in the range of -2.34 to 2.44 V and at a scan rate of 0.1 V/s (each spectrum was acquired with a time interval of 1 s), showing evolution of three wavelengths: i) initial ECL onset, 535 nm at 1.24 V (pink), ii) 582 nm at 1.94 V (purple), iii) 610 nm at 2.44 V (green), and showing devolution of one wavelength: iv) 610 nm at 2.34 V. The inset displays ECL onset with a peak wavelength of 574 nm at -2.14 V (orange) in the second potential scanning cycle.

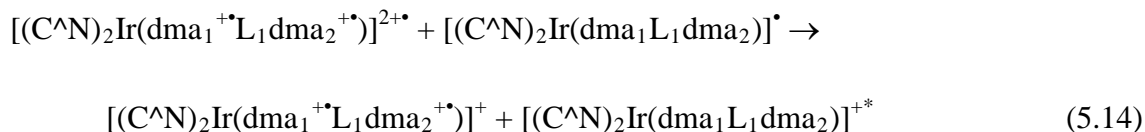
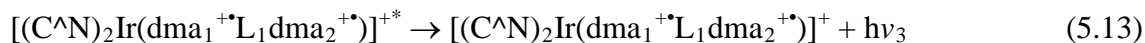
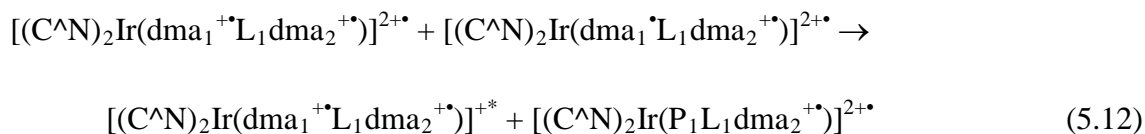
When the potential window was extended to include the second and third oxidations of **5.4**, Figure 5.2, and **5.6**, Figure 5.3, a large enhancement in ECL was observed. A similar trend was previously reported for **5.2**.⁶¹ Initially for **5.4**, the Ir center is oxidized and onset of ECL is observed at 1.24 V, reaching a maximum of approximately 110 nA of ECL at 1.44 V. Upon scanning to more positive potentials, the

two *N,N*-dimethylamino (dma) groups on the dmabpy ligand, were each oxidized over a range from 1.94 to 2.44 V. The oxidation of the dma substituents is similar to the tri-*n*-propylamine (TPrA) mechanism, however, this route is a self-coreactant pathway because the dma groups are part of the complex's design and not added to the solution as a typical co-reactant. When scanning to 1.94 V, ECL was increased to 580 nA because of the oxidation of the first dma group and ECL enhancement occurs through recruitment of the generated radicals *via* the self-coreactant pathway. Increasing the potential to 2.44 V results in the oxidation of the second dma substituent and results in a significant enhancement in ECL, 7880 nA. The ECL relative self-coreactant efficiencies, Φ_{ECL} , (based on one cycle), were higher when the potential window was extended and the dma substituents on the dmabpy ligand were both oxidized. There was increase in efficiency for **5.4**, 129 %, and an even more dramatic enhancement for **5.6**, 538 %. Notably, subtle changes in the structure of the complex, in this case the absence of the methyl group on the C^N ligands in **5.6**, confers a large increase in ECL efficiency. **5.6** has a similar relative efficiency to **5.2**, 550 %, however, the structure of the coordinating moiety of the C^N ligands differs between the pyridine in **5.6** and the *N*-benzyl triazole in **5.2**, thus making **5.2** more efficient.

In order to track the emission mechanisms with the extended potential window, ECL spooling spectra were collected at a time interval of 1 s with an applied potential scanning rate of 0.1 V/s for two complete cycles as in Figure 5.3a (the potential was scanned from 0.00 V to -2.34 V then to positive potential until 2.44 V, then back to 0.00 V). Figure 5.2b shows the ECL spectra for **5.4** collected for one complete potential scanning cycle. A weak emission at 535 nm was observed at 1.24 V. The emission was red-shifted to 582 nm at 1.94 V, which is caused by the change from an electron-donating dma group to an electron-withdrawing dma⁺ radical on the dmabpy ligand as we had previously concluded.⁶¹ The intensity of the emission continued to increase in intensity while simultaneously red-shifting to 610 nm during the course of potential scanning to 2.44 V. The emission intensity began to decrease as the potential moved from 2.44 V back towards 0.00 V until it returned to its baseline; however, the emission remained at 610 nm.

The above observations of the self-coreactant ECL routes can be summarized by the following four mechanisms involving the generation of an excited species with and without the dma groups acting like a TPrA-like self-coreactant. The C[^]N ligand is dFMeppy for **5.4**, and dFppy for **5.6**, and L₁ represents the bpy core of the ancillary ligand possessing two dma groups, dma₁ and dma₂, which together constitute the dmabpy ligand, Eqs. 5.1-5.14.





The structure of **5.4**, containing the methylated pyridine fragment within its C[^]N ligand, differs from **5.2**, itself containing the triazole within its C[^]N ligand; however, three emissions were observed in both cases when scanning the potential to their respective third oxidations, and ECL thus proceeds through similar mechanisms as previously reported. Here, for **5.4**, the three emissions were observed at 535 nm, Eq. 5.4, 582 nm, Eq. 5.8, and 610 nm, Eq. 5.13. Interestingly, when the potential was scanned towards negative potential in the second cycle, weak ECL emission was seen at -2.14 V, after the first reduction of **5.4**, which corresponds to a wavelength of 574 nm. This onset was due to the presence of small amount of radical cations generated in the first cycle. These radicals could react with the radical anion generated at -2.14 V, producing ECL at 574 nm.

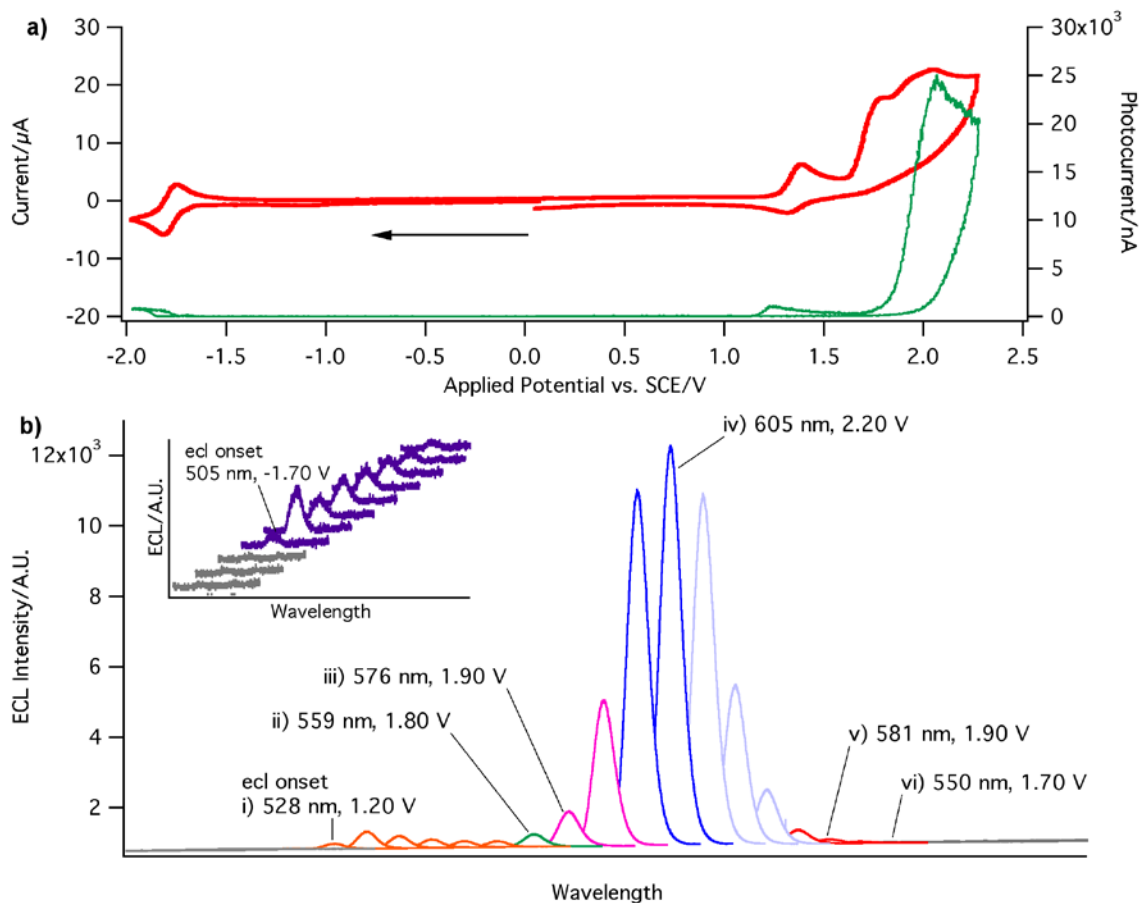


Figure 5.3. a) CV of **5.6** with ECL-voltage curve overlaid with a potential profile ranging between -2.00 to 2.30 V, b) ECL spooling spectra of **5.6** during first potential scanning cycle in the range of -2.00 to 2.30 V and at a scan rate of 0.1 V/s (each spectrum was acquired with a time interval of 1 s), showing evolution of four wavelengths: i) initial ECL onset, 528 nm at 1.20 V (orange), ii) 559 nm at 1.80 V (green), iii) 576 nm at 1.90 V (pink), iv) 605 nm at 2.20 V (dark blue), and showing devolution of three wavelength: iv) 605 nm at 2.30 V (light blue), v) 581 nm at 1.90 V (red), and vi) 550 nm at 1.70 V (dark grey). The inset displays ECL onset with a peak wavelength of 505 nm at -1.70 V (purple) in the second potential scanning cycle.

Structurally, **5.6** differs from **5.4** due to the removal of the methyl substituent on the pyridine unit of the C^N ligand. For **5.6**, an additional emission was observed compared to **5.4** when scanning to its third oxidation, Figure 5.3. The four emissions were seen at 528 nm, Eq. 5.4 *via* Eq. 5.3 or Eq. 5.9 or Eq. 5.14, 559 nm, 576 nm, Eq. 5.8,

and 605 nm, Eq. 5.13, *via* the spooled spectra, with a similar onset, as described with **5.4**. Likewise, when the potential was scanned from 0.00 V towards negative potential in the second cycle, at -1.70 V an additional ECL emission was observed at 505 nm. The emission at 576 nm, 1.90 V, may have been the result of simultaneous detection of the emission resulting from generation of excited species following the second oxidation of **5.6** at 1.80 V, 559 nm, and the third oxidation of **5.6** at 2.00 V, 605 nm. The intensity of the emission moving from 1.20 V to 2.20 V continued to increase along with concomitant red-shifting of the emission. When the ECL intensity began to decrease, the emission started to blue-shift back to 581 nm at 1.90 V and finally to 550 nm at 1.70 V. This shift in emission on the devolution, return scan, may be due to the dynamics in the vicinity of the electrode. It is important to note that scanning to the complexes first or second reductions did not change the peak wavelengths for the ECL emissions. Complexes **5.2**, **5.4**, and **5.6**, all show similar ECL emissions, even with different C^N ligands, however the ECL intensity differs dramatically between **5.4**, 8.0×10^3 nA, and **5.6**, 2.5×10^4 nA.

5.1.4 Conclusions

In summary, two new highly luminescent cationic blue-emitting iridium complexes, **5.2** and **5.4**, are reported and fully characterized. The redox behavior for the six complexes is similar in that each has a quasi-reversible oxidation and reversible reduction wave. The presence/absence of the methyl group does not alter the nature of the emission. Introduction of the dFphtl shifts the oxidation anodically but the reduction cathodically while the incorporation of the electron-donating NMe₂ group shifts both the oxidation and reduction cathodically, resulting in a large electrochemical gap of 3.24 V for **5.2** compared to 3.12 V for **5.4**. These complexes are ECL active under annihilation conditions, emitting sky-blue to blue-green light. Complexes bearing dtBubpy N^N ligands were less bright than their dmabpy congeners in the ECL spectra. Upon scanning out to 2.50 V, dramatic enhancement in the ECL emission was observed. The absence of the methyl group in **5.6** lead to an enhancement in the ECL signal of 538 % while for **5.4**, the ECL signal was only enhanced by 129 %. This study illustrates the inherent difficulties and challenges in designing i) highly efficient cationic blue emitters and the limitations in pushing the emission further to the blue using π -acceptor ancillary ligands;

ii) developing highly efficient ECL luminophores. We are nevertheless currently evaluating these luminophores both in the solid state for LEEC devices and in solution as ECL-based biological probes.

5.1.5 References

- (1) Slinker, J. D.; Rivnay, J.; Moskowitz, J. S.; Parker, J. B.; Bernhard, S.; Abruña, H. D.; Malliaras, G. G. *J. Mater. Chem.* **2007**, *17*, 2976.
- (2) Hu, T.; He, L.; Duan, L.; Qiu, Y. *J. Mater. Chem.* **2012**, *22*, 4206.
- (3) Ladouceur, S.; Zysman-Colman, E. *Eur. J. Inorg. Chem.* **2013**, ASAP, DOI: 10.1002/ejic.201300171.
- (4) Lo, K. K.-W.; Li, S. P.-Y.; Zhang, K. Y. *New J. Chem.* **2011**, *35*, 265.
- (5) Zhao, Q.; Li, F.; Huang, C. *Chem. Soc. Rev.* **2010**, *39*, 3007.
- (6) Hu, L.; Xu, G. *Chem. Soc. Rev.* **2010**, *39*, 3275.
- (7) Xu, L.; Li, Y.; Wu, S.; Liu, X.; Su, B. *Angew. Chem. Int. Ed.* **2012**, *51*, 8068.
- (8) Bruce, D.; Richter, M. M. *Anal. Chem.* **2002**, *74*, 1340.
- (9) Cole, C.; Muegge, B. D.; Richter, M. M. *Anal. Chem.* **2003**, *75*, 601.
- (10) Muegge, B. D.; Richter, M. M. *Anal. Chem.* **2003**, *76*, 73.
- (11) Zanarini, S.; Rampazzo, E.; Bonacchi, S.; Juris, R.; Marcaccio, M.; Montalti, M.; Paolucci, F.; Prodi, L. *J. Am. Chem. Soc.* **2009**, *131*, 14208.
- (12) Kim, J. I.; Shin, I.-S.; Kim, H.; Lee, J.-K. *J. Am. Chem. Soc.* **2005**, *127*, 1614.
- (13) Kapturkiewicz, A.; Angulo, G. *Dalton Trans.* **2003**, 3907.
- (14) Kapturkiewicz, A.; Nowacki, J.; Borowicz, P. *Electrochim. Acta* **2005**, *50*, 3395.
- (15) Kapturkiewicz, A.; Chen, T.-M.; Laskar, I. R.; Nowacki, J. *Electrochem. Commun.* **2004**, *6*, 827.
- (16) Li, C.; Lin, J.; Yang, X.; Wan, J. *J. Organomet. Chem.* **2011**, *696*, 2445.
- (17) Shin, I.-S.; Kim, J. I.; Kwon, T.-H.; Hong, J.-I.; Lee, J.-K.; Kim, H. *J. Phys. Chem. C* **2007**, *111*, 2280.
- (18) Shin, I.-S.; Yoon, S.; Kim, J. I.; Lee, J.-K.; Kim, T. H.; Kim, H. *Electrochim. Acta* **2011**, *56*, 6219.

- (19) Roop, J.; Nothnagel, M.; Schnuriger, M.; Richter, M. M.; Baker, G. A. *J. Electroanal. Chem.* **2011**, *656*, 34.
- (20) Shin, I.-S.; Kang, Y.-T.; Lee, J.-K.; Kim, H.; Kim, T. H.; Kim, J. S. *Analyst* **2011**, *136*, 2151.
- (21) Doeven, E. H.; Zammit, E. M.; Barbante, G. J.; Hogan, C. F.; Barnett, N. W.; Francis, P. S. *Angew. Chem. Int. Ed.* **2012**, *51*, 4354.
- (22) Bandini, M.; Bianchi, M.; Valenti, G.; Piccinelli, F.; Paolucci, F.; Monari, M.; Umani-Ronchi, A.; Marcaccio, M. *Inorg. Chem.* **2010**, *49*, 1439.
- (23) Lin, H.; Cinar, M. E.; Schmittel, M. *Dalton Trans.* **2010**, *39*, 5130.
- (24) Zanarini, S.; Felici, M.; Valenti, G.; Marcaccio, M.; Prodi, L.; Bonacchi, S.; Contreras-Carballada, P.; Williams, R. M.; Feiters, M. C.; Nolte, R. J. M.; De Cola, L.; Paolucci, F. *Chem. Eur. J.* **2011**, *17*, 4640.
- (25) Swanick, K. N.; Ladouceur, S.; Zysman-Colman, E.; Ding, Z. *Chem. Commun.* **2012**, *48*, 3179.
- (26) Li, M.-J.; Jiao, P.; Lin, M.; He, W.; Chen, G.-N.; Chen, X. *Analyst* **2011**, *136*, 205.
- (27) Li, C.; Lin, J.; Guo, Y.; Zhang, S. *Chem. Commun.* **2011**, *47*, 4442.
- (28) Kiran, R. V.; Hogan, C. F.; James, B. D.; Wilson, D. J. D. *Eur. J. Inorg. Chem.* **2011**, *31*, 4816.
- (29) Shu, Q.; Birlenbach, L.; Schmittel, M. *Inorg. Chem.* **2012**, *51*, 13123.
- (30) Schmittel, M.; Shu, Q.; Cinar, M. E. *Dalton Trans.* **2012**, *41*, 6064.
- (31) Schmittel, M.; Qinghai, S. *Chem. Commun.* **2012**, *48*, 2707.
- (32) Muegge, B. D.; Richter, M. M. *Luminescence* **2005**, *20*, 76.
- (33) Jeon, S. O.; Lee, J. Y. *J. Mater. Chem.* **2012**, *22*, 7239.
- (34) He, L.; Duan, L.; Qiao, J.; Wang, R.; Wei, P.; Wang, L.; Qiu, Y. *Adv. Funct. Mater.* **2008**, *18*, 2123.
- (35) He, L.; Qiao, J.; Duan, L.; Dong, G.; Zhang, D.; Wang, L.; Qiu, Y. *Adv. Funct. Mater.* **2009**, *19*, 2950.
- (36) Mydlak, M.; Bizzarri, C.; Hartmann, D.; Sarfert, W.; Schmid, G.; De Cola, L. *Adv. Funct. Mater.* **2010**, *20*, 1812.

- (37) He, L.; Duan, L.; Qiao, J.; Zhang, D.; Wang, L.; Qiu, Y. *Chem. Commun.* **2011**, 47, 6467.
- (38) Felici, M.; Contreras-Carballada, P.; Vida, Y.; Smits, J. M. M.; Nolte, R. J. M.; De Cola, L.; Williams, R. M.; Feiters, M. C. *Chem. Eur. J.* **2009**, 15, 13124.
- (39) He, L.; Duan, L.; Qiao, J.; Dong, G.; Wang, L.; Qiu, Y. *Chem. Mater.* **2010**, 22, 3535.
- (40) Tamayo, A. B.; Garon, S.; Sajoto, T.; Djurovich, P. I.; Tsyba, I. M.; Bau, R.; Thompson, M. E. *Inorg. Chem.* **2005**, 44, 8723.
- (41) Yang, C.-H.; Beltran, J.; Lemaur, V.; Cornil, J.; Hartmann, D.; Sarfert, W.; Fröhlich, R.; Bizzarri, C.; De Cola, L. *Inorg. Chem.* **2010**, 49, 9891.
- (42) Shik Chin, C.; Eum, M.-S.; Yi Kim, S.; Kim, C.; Kwon Kang, S. *Eur. J. Inorg. Chem.* **2007**, 2007, 372.
- (43) Chen, H.-F.; Hung, W.-Y.; Chen, S.-W.; Wang, T.-C.; Lin, S.-W.; Chou, S.-H.; Liao, C.-T.; Su, H.-C.; Pan, H.-A.; Chou, P.-T.; Liu, Y.-H.; Wong, K.-T. *Inorg. Chem.* **2012**, 51, 12114.
- (44) Meier, S. B.; Sarfert, W.; Junquera-Hernandez, J. M.; Delgado, M.; Tordera, D.; Orti, E.; Bolink, H. J.; Kessler, F.; Scopelliti, R.; Grätzel, M.; Nazeeruddin, M. K.; Baranoff, E. *J. Mater. Chem. C* **2013**, 1, 58.
- (45) Lowry, M. S.; Hudson, W. R.; Pascal Jr., R. A.; Bernhard, S. *J. Am. Chem. Soc.* **2004**, 126, 14129.
- (46) Ladouceur, S.; Fortin, D.; Zysman-Colman, E. *Inorg. Chem.* **2011**, 50, 11514.
- (47) Fernández-Hernández, J. M.; Yang, C.-H.; Beltrán, J. I.; Lemaur, V.; Polo, F.; Fröhlich, R.; Cornil, J.; De Cola, L. *J. Am. Chem. Soc.* **2011**, 133, 10543.
- (48) Felici, M.; Contreras-Carballada, P.; Smits, J. M. M.; Nolte, R. J. M.; Williams, R. M.; De Cola, L.; Feiters, M. C. *Molecules* **2010**, 15, 2039.
- (49) Liu, S.; Müller, P.; Takase, M. K.; Swager, T. M. *Inorg. Chem.* **2011**, 50, 7598.
- (50) Beyer, B.; Ulbricht, C.; Escudero, D.; Friebe, C.; Winter, A.; González, L.; Schubert, U. S. *Organometallics* **2009**, 28, 5478.
- (51) Nazeeruddin, M. K.; Wegh, R. T.; Zhou, Z.; Klein, C.; Wang, Q.; DeAngelis, F.; Fantacci, S.; Grätzel, M. *Inorg. Chem.* **2006**, 45, 9245.
- (52) De Angelis, F.; Fantacci, S.; Evans, N.; Klein, C.; Zakeeruddin, S. M.; Moser, J.-E.; Kalyanasundaram, K.; Bolink, H. J.; Grätzel, M.; Nazeeruddin, M. K. *Inorg. Chem.* **2007**, 46, 5989.

- (53) Bolink, H. J.; Coronado, E.; Costa, R. n. D.; Lardiés, N.; Ortì, E. *Inorg. Chem.* **2008**, *47*, 9149.
- (54) Booker, C.; Wang, X.; Haroun, S.; Zhou, J.; Jennings, M.; Pagenkopf, B. L.; Ding, Z. *Angew. Chem. Int. Ed.* **2008**, *47*, 7731.
- (55) Swanick, K. N.; Dodd, D. W.; Price, J. T.; Brazeau, A. L.; Jones, N. D.; Hudson, R. H. E.; Ding, Z. *Phys. Chem. Chem. Phys.* **2011**, *13*, 17405.
- (56) Connelly, N. G.; Geiger, W. E. *Chem. Rev.* **1996**, *96*, 877.
- (57) McCord, P.; Bard, A. J. *J. Electroanal. Chem.* **1991**, *318*, 91.
- (58) Bartelt, J. E.; Drew, S. M.; Wightman, R. M. *J. Electrochem. Soc.* **1992**, *139*, 70.
- (59) McCord, P.; Bard, A. J. *J. Electroanal. Chem.* **1991**, *318*, 91.
- (60) Bartelt, J. E.; Drew, S. M.; Wightman, R. M. *J. Electrochem. Soc.* **1992**, *139*, 70.
- (61) Swanick, K. N.; Ladouceur, S.; Zysman-Colman, E.; Ding, Z. *Angew. Chem. Int. Ed.* **2012**, *51*, 11079.
- (62) Baranoff, E.; Bolink, H. J.; Constable, E. C.; Delgado, M.; Haussinger, D.; Housecroft, C. E.; Nazeeruddin, M. K.; Neuburger, M.; Orti, E.; Schneider, G. E.; Tordera, D.; Walliser, R. M.; Zampese, J. A. *Dalton Trans.* **2013**, *42*, 1073.
- (63) Lai, R. Y.; Bard, A. J. *J. Phys. Chem. B* **2003**, *107*, 5036.

5.2 Self-Enhanced Electrochemiluminescence of an Iridium(III) Complex: Mechanistic Insight[†]

5.2.1 Introduction

Heteroleptic cationic iridium complexes have been used as alternative luminophores to neutral *ortho*-metallated iridium complexes (e.g., *fac*-Ir(ppy)₃, where ppyH is 2-phenylpyridine) for visual display applications.^{1,2} Single-layer devices known as light-emitting electrochemical cells (LEECs) can now be fabricated, which operate through ion diffusion to opposite electrodes thereby enhancing electronic charge injection at low operating voltages (the so-called electrodynamic model).³⁻⁸ We have synthesized several cationic iridium complexes of the form [(C[^]N)₂Ir(N[^]N)], where C[^]N is a cyclometallating ligand and N[^]N is a neutral diimine ancillary ligand,^{9,10} and explored their optoelectronic properties. We recently have discovered that iridium(III) complexes bearing aryltriazole C[^]N ligands exhibit bright electrochemiluminescence (or electrogenerated chemiluminescence, ECL), with which ECL efficiency is up to four times greater than that of [Ru(bpy)₃]²⁺ upon addition of benzoyl peroxide (BPO) as a co-reactant.¹¹ Development of such highly efficient and stable ECL emitters over a broad spectrum of wavelengths, as illustrated by the Bard group for other luminophores,¹²⁻¹⁵ has been anticipated for many years, and might find wide applications such as for DNA determination, immunoassay development.¹⁶⁻¹⁹

With the goal of obtaining bright true blue-light emitters, we recently investigated the photophysical and ECL properties of [(dFphtl)₂Ir(dmabpy)]⁺, **5.2**, [dFphtl = 1-benzyl-4-(2,4-difluorophenyl)-1*H*-1,2,3-triazole; dmabpy = 4,4'-(dimethylamino)-2,2'-bipyridine]; Scheme 5.2].²⁰ Though not apparent initially, during subsequent investigation of the ECL behavior of **5.2**, we realized that we could exploit the redox chemistry of the two dimethylamino (dma) groups on the bpy ligand of **5.2** and thus

[†] This work is published in Kalen N. Swanick, Sébastien Ladouceur, Eli Zysman-Colman, and Zhifeng Ding, *Angew. Chem. Int. Ed.*, **2012**, *51*, 11079-11082. Reproduced by permission of John Wiley and Sons. See Appendix IV.

enhance its ECL efficiency. This prediction was based on ECL studies using tri-*n*-propylamine (TPrA) as a co-reactant to enhance the ECL and efficiently generate light in organic solvents²¹⁻²⁶ though TPrA is the most efficient in generating light with luminophores in aqueous media.^{16,27-30}

The classic form of ECL involves electron transfer between electrochemically generated radical ions in solution to produce excited species that emit light.^{16,17} In recent years, the use of TPrA as a co-reactant has been found to be a sensitive technique for biological determinations.¹⁷ Herein, we report the electrochemistry and ECL of **5.2** in comparison with a structurally similar cationic Ir(III) complex, [(dFphtl)₂Ir(bpy)]⁺, **5.7**, (bpy = 2,2'-bipyridine). For the first time, ECL auto-enhancement was observed, with three excited states in the ECL emission of **5.2** deconvoluted by means of our recently developed ECL spooling technique. By contrast, **5.7** emitted ECL only at one peak wavelength with no enhancement in photocurrent. The ECL of **5.2** was discovered to be self-enhanced with the two dma groups acting as co-reactants. It is conceivable that **5.2** can be modified with anchoring groups that form bonds with lipid, nucleic acids and proteins for simplified and enhanced ECL detection in biological applications.

5.2.2 Experimental Section

CV and ECL Measurements. A 2 mm diameter Pt disc inlaid in a glass sheath was used as the working electrode (WE), a coiled Pt wire as the counter electrode (CE), and a coiled Ag wire as the quasi reference electrode (QRE). After each experiment, the electrochemical potential window was calibrated using ferrocene (FC) as the internal standard. The redox potential of the ferrocene/ferrocenium (Fc/Fc⁺) couple was taken as 0.424 V *vs.* SCE.³¹ Approximately 2 mg of an Ir complex was added to the electrochemical cell with a flat Pyrex window at the bottom for detection of generated ECL, containing 0.1 M TBAP (tetrabutylammonium perchlorate) supporting electrolyte in anhydrous acetonitrile (3.0 mL) that was assembled in a dry box.

CV Instrumentation. For detailed electrochemical workstation and ECL setup information, please refer to our previous publications.^{11,18,32} In brief, the cyclic voltammetry was conducted on a CHI 610A electrochemical analyzer (CH Instruments,

Austin, TX). The experimental parameters for cyclic voltammograms (CVs) are listed here: 0.00 V initial potential in experimental scale, positive or negative initial scan polarity, 0.1 V/s scan rate, 4 sweep segments, 0.001 V sample interval, 2 s quiet time, $1-5 \times 10^{-5} \text{ AV}^{-1}$ sensitivity.

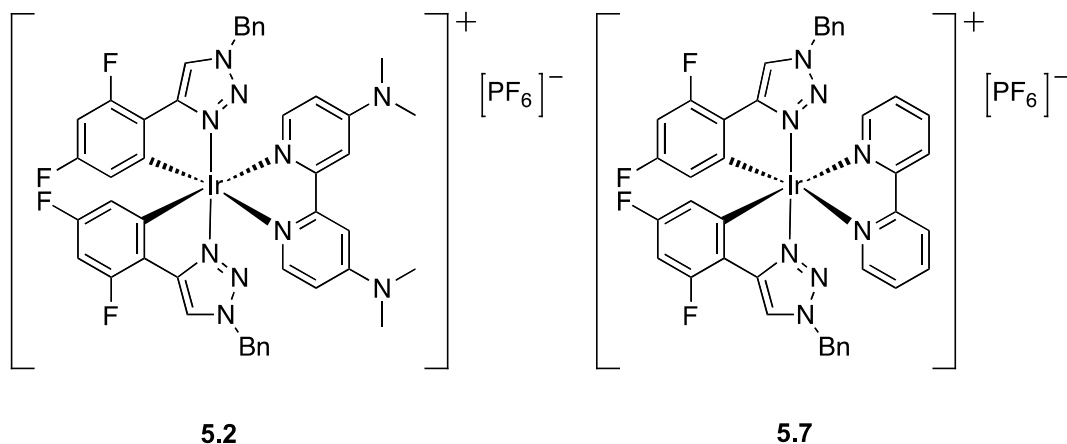
ECL Instrumentation. The ECL-voltage curves were obtained using the CHI 610A coupled with a photomultiplier tube (PMT, R928, Hamamatsu, Japan) held at -750 V with a high voltage power supply. The ECL collected by the PMT under the flat Pyrex window at the bottom of the cell was measured as a photocurrent, and transformed to a voltage signal, using a picoammeter/voltage source (Keithley 6487, Cleveland, OH). The potential, current signals from the electrochemical workstation, and the photocurrent signal from the picoammeter were sent simultaneously through a DAQ board (DAQ 6052E, National Instruments, Austin, TX) in a computer. The data acquisition system was controlled from a custom-made LabVIEW program (ECL_PMT610a.vi, National Instruments, Austin, TX). The photosensitivity on the picoammeter was set manually in order to avoid the saturation.

ECL Accumulated Spectra. The ECL spectra were obtained by replacing the PMT with a spectrometer (Cornerstone 260, Newport, Canada) attached to a CCD camera (Model DV420-BV, Andor Technology, Belfast, UK). The camera was cooled to $-55 \text{ }^{\circ}\text{C}$ prior to use, and controlled by a computer for operation and data acquisition. The intensities versus wavelengths (ECL spectra) were recorded by Andor Technology program. Similar to the CV experiments, the samples were scanned between their redox potentials.

ECL Spooling Spectroscopy. For the spooling experiments, the spectrometer and camera set was used and the following parameters were used for the Andor Technology program under the kinetic parameters option tab: exposure time = 1 s, number of accumulations = 1, kinetic series length = 80 s (matching with the potential scan time), kinetic cycle time = 1, and the spectrometer was centered at 600 nm using a 150 l/mm grating. On the CHI 610A electrochemical analyzer, the initial potential was set to 0.00 V, appropriate high and low potentials, sensitivity = $1-5 \times 10^{-5} \text{ AV}^{-1}$, initial scan polarity

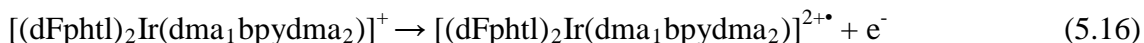
= negative, scan rate = 0.1 V/s, sweep segments = 4, sample interval = 0.001 V, quiet time 2 s. Simultaneously, the CHI 610A electrochemical analyzer and the Andor Technology program was run and collected the CV and spectra as seen in Figure S5.3, Appendix IV.

5.2.3 Results and Discussion



Scheme 5.2. Iridium(III) complexes $[(dFphtl)_2Ir(dmabpy)]PF_6$, **5.2**, and $[(dFphtl)_2Ir(bpy)]PF_6$, **5.7**

Complexes **5.2** and **5.7**, Scheme 5.2, similar in structure to other cationic iridium complexes that we have investigated,¹¹ show a very good ECL efficiency in acetonitrile (ACN) in the annihilation path when the applied potential was scanned in the range between their first oxidation and first reduction. The pair of cyclic voltammogram (CV) and ECL-voltage curves (in red) of **5.2** in Figure 5.4a demonstrated quasi-reversible reduction at -1.82 V, Eq. 5.15, and oxidation at 1.42 V, Eq. 5.16, versus a saturated calomel electrode (SCE):



where $[(dFphtl)_2Ir(dma_1bpydma_2)]^+$ represents **5.2**, with the dmabpy ligand now shown as two dma groups attached to bpy.

Complex **5.2** was found to have an ECL efficiency of 34 %, ECL-voltage in red, Figure 5.4a, relative to $[\text{Ru}(\text{bpy})_3]^{2+}$.^{11,18,32,33} Importantly, note that ECL was only detected after the oxidation reaction, illustrating a higher stability of $[(\text{dFphtl})_2\text{Ir}(\text{dma}_1\text{bpydma}_2)]^\bullet$ than that of $[(\text{dFphtl})_2\text{Ir}(\text{dma}_1\text{bpydma}_2)]^{2+}$. While the first reduction reaction was localized on the ancillary ligand,²⁰ the oxidation originated mainly from Ir as shown by the DFT calculations³⁴.

Upon scanning to higher positive voltages, we found that **5.2** underwent three further oxidation reactions with peak potentials at 1.75, 1.94 and 2.18 V, respectively, CV in green, Figure 5.4a. This can be clearly seen from differential pulsed voltammograms (DPVs) of **5.2**, Figure S5.2 in Appendix IV. Incredibly, the ECL efficiency in the apparent annihilation process was increased to 550 % of that of $[\text{Ru}(\text{bpy})_3]^{2+}$ when the positive potential was extended to 2.43 V. Light emission was enhanced 16 times. The ECL efficiency was estimated to be 200 % and 400 %, respectively, if the applied potential stopped right after the second oxidation (voltage at vertical purple dashed line, CV curve in green in Figure 5.4a or right after the third oxidation reaction (voltage at vertical black dashed line, CV curve in green in Figure 5.4a. The fourth oxidation reaction appeared not to enhance the ECL efficiency any further though the whole green ECL-voltage curve does give a higher ECL efficiency because of the annihilation reaction continuing in the diffusion layer.

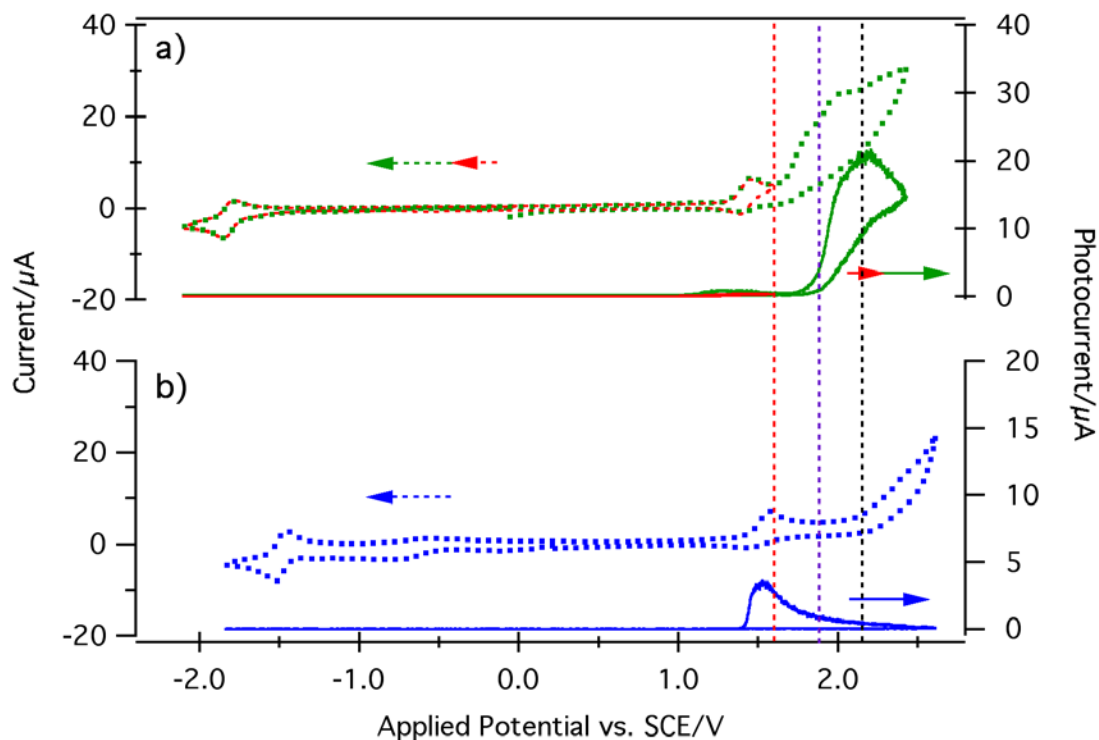


Figure 5.4. Cyclic voltammograms (dotted) overlaid with corresponding ECL-voltage curves (solid) in acetonitrile of a) 0.6 mM **5.2** with the applied potential ranges between -2.10 and 1.60 V (red) and between -2.10 to 2.43 V (green) vs. a saturated calomel electrode (SCE), and b), of 0.6 mM **5.7** with the applied potential ranges between -1.80 and 2.60 V (blue) vs. SCE. The scan rate was at 0.1 V/s. The vertical dashed lines show the potentials used for estimation of the ECL efficiencies of **5.2**.

In contrast, **5.7** did not show the second and third extra oxidation peaks after the similar increases in scan potentials beyond the first oxidation peak, Figure 5.4b; however, **5.7** underwent a second oxidation event at a potential shifted 800 mV anodically relative to the first oxidation event, a value similar to the potential difference between the first and fourth oxidation peaks of **5.2**. Through a comparison of the structures of the two complexes, it is plausible to assign the second and third oxidation waves to iterative oxidation events of the two dma substituents. The fourth oxidation wave probably originated from the oxidation of either the bpy moiety or the C^N ligand. Based on the DFT calculations, it is very likely that this oxidation is localized on the triazole ligand.

The observed ECL enhancement is then due to the presence of the dma substituents on the bpy ligand in **5.2**, each acting as a self-co-reactant. The mechanisms should be similar to the addition of TPrA to Ru complexes and other luminophores in ECL studies.^{16,21} Without any self-co-reactant present, the ECL for **5.7** decayed after the first oxidation, Figure 5.4b.

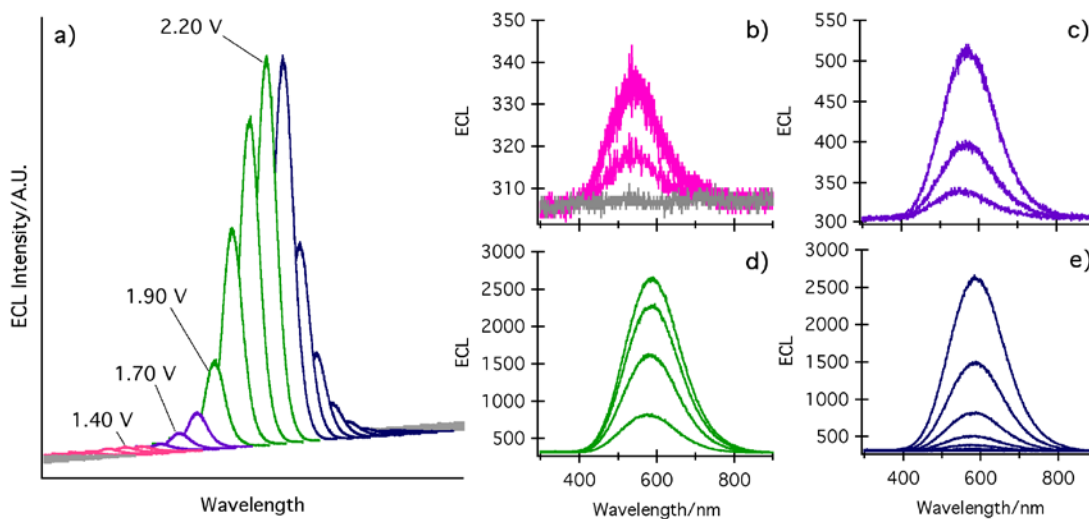
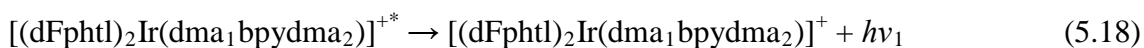
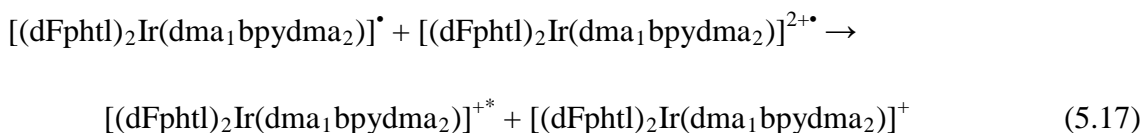


Figure 5.5. Selected ECL spooling spectra of 0.6 mM **5.2** in acetonitrile when the applied potential was scanned between -2.10 and 2.42 V for two cycles at a scan rate of 0.1 V/s, see Figure S5.3 in Appendix IV for the two complete cycles. Each ECL spectrum was acquired for 1 s and two scanning cycles took 145 s. a) Perspective view from zoomed-in ECL spooling spectra of the 1st cycle of potential scanning. Three emissions from different excited specials are color-coded, with apparent peak positions centered at b) 543 nm (pink), c) 566 nm (purple), and d) 588 nm (green). e) ECL devolution is illustrated by the spectra in (deep blue). Three excited states were deconvoluted to peak wavelengths at 543, 608, and 651 nm, respectively, which were generated in annihilation and co-reactant (the two dma groups on the bpy ligand) paths.

Figure 5.5a shows a magnified section of ECL spooling spectra of **5.2** acquired in the first cycle of the potential scanning between -2.10 and 2.42 V. Two cycle scans over 145 s at a scan rate of 0.1 V/s were conducted. Each ECL spectrum was acquired for 1 s. Please see Figure S5.3 in Appendix IV for the complete spooling spectra for two cycles.

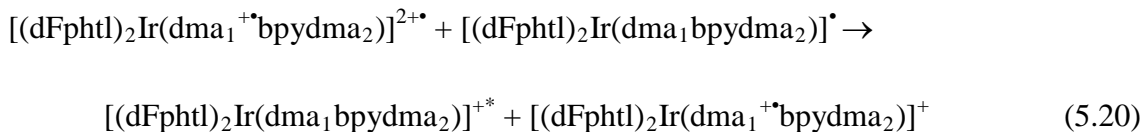
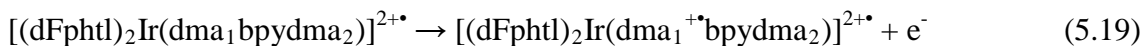
For the first cycle, the scan started at 0.00 V and went to -2.10 V before the scan direction was switched towards positive potential. The ECL spectrum at 1.20 V began to display a weak wave centered at 543 nm, which is close to the photoluminescence (PL) peak wavelength, 495 nm in ACN. The small discrepancy of the ECL and PL wavelengths is probably due to self-absorption given the higher concentrations used in ECL.³⁵ When the applied potential continued more positive, the ECL wave grew, Figure 5.5b, and reached a maximum at 1.40 V that is the same as the first maximum potential in the ECL-voltage curve, Figure 5.4a. ECL evolution, ECL spectra in pink, Figure 5.5b, in this potential range follows the annihilation mechanism shown in Eqs. 5.17 and 5.18:



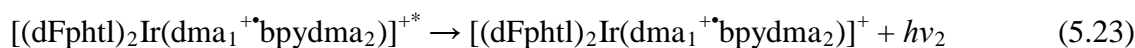
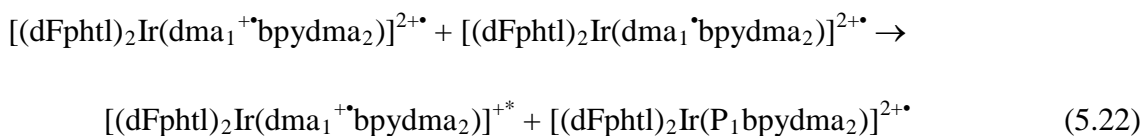
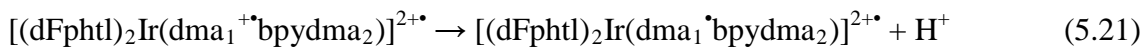
In the initial scanning from 0.00 to -2.10 V, $[(\text{dFphtl})_2\text{Ir}(\text{dma}_1\text{bpydma}_2)]^\bullet$ radicals were formed upon reduction right after -1.82 V, Eq. 5.15. The applied potential was swept towards positive potentials and $[(\text{dFphtl})_2\text{Ir}(\text{dma}_1\text{bpydma}_2)]^{2+\bullet}$ radical cations were generated with an onset potential of 1.20 V, Eq. 5.16. The two radicals combined in the vicinity of the electrode to yield the excited state species that is responsible for light emission upon relaxation to the ground state, Eqs. 5.17 and 5.18.

Upon further scanning to more positive potentials, the ECL spectrum showed an increase in intensity as depicted in the ECL-voltage curve, green curve in Figure 5.4a. More importantly, the apparent ECL peak wavelength was red-shifted as illustrated by the purple spectra in Figure 5.5a and Figure 5.5c. As described above for the cyclic voltammetry, the two dma groups on the bpy ligand can be oxidized consecutively. Immediately after the first oxidation localized on the Ir center, the first dma substituent began to lose one electron to generate $[(\text{dFphtl})_2\text{Ir}(\text{dma}_1^{+\bullet}\text{bpydma}_2)]^{2+\bullet}$, Eq. 5.19. The $[(\text{dFphtl})_2\text{Ir}(\text{dma}_1^{+\bullet}\text{bpydma}_2)]^{2+\bullet}$ species could react with the radical generated in the cathodic region, Eq. 5.15, to generate the same excited species as in the annihilation path,

$[(\text{dFphtl})_2\text{Ir}(\text{dma}_1\text{bpydma}_2)]^{+*}$, Eq. 5.20. The light emission would follow the same process as described by Eq. 5.18.



There is another pathway where the oxidized species generated in Eq. 5.19 might deprotonate once to produce $[(\text{dFphtl})_2\text{Ir}(\text{dma}_1^{\bullet}\text{bpydma}_2)]^{2+*}$, a strong reducing agent, Eq. 5.21. The radical would react with the oxidized complex already present in solution, to generate the second excited species $[(\text{dFphtl})_2\text{Ir}(\text{dma}_1^{+\bullet}\text{bpydma}_2)]^{+*}$, Eq. 5.22, where $P_1 = -(\text{CH}_3)\text{N}^+=\text{CH}_2$. This excited state could emit light at a different wavelength, $h\nu_2$, Eq. 5.23.



Based on this mechanistic proposal, the purple ECL spectra were deconvoluted and fitted to two peaks, fixed at 543 nm and the second being fitted to 608 nm, Figures S5.4a and S5.4b in Appendix IV. The red-shift of the second peak is due to the switch from electron-donating dma group to electron-withdrawing $\text{dma}^{+\bullet}$ radical on the bpy. As described initially by Nazeeruddin, De Angelis and Grätzel et al.,^{4,36} the presence of the dma-substituents on the bipyridine ligand act to significantly destabilize the lowest unoccupied molecular orbitals (LUMO), resulting in a large increase in the HOMO-LUMO gap (HOMO = highest occupied molecular orbital). It is conceivable that electron-withdrawing $\text{dma}^{+\bullet}$ would shrink the gap and produce a red-shifted ECL spectrum. Note that $\text{dma}^{+\bullet}$ radical is stabilized by delocalization of the charge throughout the entire bpy ligand.

The ECL peak intensity was further enhanced when the scan moved to more positive potential, green ECL spectra in Figure 5.5a and Figure 5.5d. This trend continued until 2.20 V. In this potential region, the second dma group on the dmabpy ligand can be oxidized, becoming a self-co-reactant like the first dma substituent and generating one additional excited species. The ECL process follows a similar co-reactant mechanism as with dma_1 , Eq. 5.22, involvement described above. However, now there is the generation of the third excited species, $[(\text{dFphtl})_2\text{Ir}(\text{dma}_1^{+\bullet}\text{bpydma}_2^{+\bullet})]^{+*}$, emitting at 651 nm, $h\nu_3$ given in Eq. 5.24:



The third ECL peak position was obtained in the same manner through a three-component deconvolution of the ECL spectra, green in Figure 5.5a and Figure 5.5d, with the first two curves now fixed at 543 and 608 nm, respectively, Figure S5.4c in Appendix IV.

Finally, as the potential continued to increase from 2.21 to 2.42 V then swept back to 0.00 V, a decrease in ECL intensity was observed with the apparent ECL maximum centered at 568 nm until no emission was observed in the ECL, Figure 5.5e. The flat spectra continued until the ECL progression of the second cycle reached around 1.20 V. The ECL spectra, black in Figure 5.5a and Figure 5.5e, were fitted by curves, Figure S5.5a-e in Appendix IV, showing that the three peaks all decreased in intensity as the potential moved first from 2.20 V to 2.42 V and then towards negative potentials.

Over the second cycle, we observed the evolution of the same three ECL peaks as those observed in the first cycle, 543, 608 and 651 nm, indicating a reproducible ECL behavior over subsequent potential scan cycles.

5.2.4 Conclusions

In summary, for the first time three different emissions were observed during an ECL process. By means of fitting curves, these three emissions in **5.2** were deconvoluted from the spooling ECL spectra to be 543, 608, and 651 nm, correlating to three ECL

mechanisms: the first being the typical annihilation route¹⁷ while the second and third involved a self-co-reactant route implicating the oxidation of dmabpy, similar to the TPrA co-reactant mechanism.^{17,21} By contrast, **5.7** only follows the annihilation route because of the absence of dma substituents on the bpy. The ECL efficiency for **5.2** increased from approximately 35 % (annihilation) to 200 % (after the second oxidation) to 400 % (after the third oxidation) and finally to 550 % (after the fourth oxidation). These ECL efficiencies are the highest reported for iridium complexes. Moreover, this dramatic increase in ECL is attributed to the unique architecture of the dmabpy ligand acting as a self-co-reactant in **5.2**. This may lead to an avenue for greatly simplifying ECL detection protocols with integrated co-reactant and luminophore in a single molecule, and drastically enhancing detection sensitivity up to 16 times.

5.2.5 References

- (1) Fernández-Hernández, J. M.; Yang, C.-H.; Beltrán, J. I.; Lemaur, V.; Polo, F.; Fröhlich, R.; Cornil, J.; De Cola, L. *J. Am. Chem. Soc.* **2011**, *133*, 10543.
- (2) Mauro, M.; Schuermann, K. C.; Prétôt, R.; Hafner, A.; Mercandelli, P.; Sironi, A.; De Cola, L. *Angew. Chem. Int. Ed.* **2010**, *49*, 1222.
- (3) Slinker, J. D.; Gorodetsky, A. A.; Lowry, M. S.; Wang, J.; Parker, S.; Rohl, R.; Bernhard, S.; Malliaras, G. G. *J. Am. Chem. Soc.* **2004**, *126*, 2763.
- (4) De Angelis, F.; Fantacci, S.; Evans, N.; Klein, C.; Zakeeruddin, S. M.; Moser, J.-E.; Kalyanasundaram, K.; Bolink, H. J.; Grätzel, M.; Nazeeruddin, M. K. *Inorg. Chem.* **2007**, *46*, 5989.
- (5) Costa, R. D.; Ortí, E.; Bolink, H. J.; Graber, S.; Schaffner, S.; Neuburger, M.; Housecroft, C. E.; Constable, E. C. *Adv. Funct. Mater.* **2009**, *19*, 3456.
- (6) Holder, E.; Langeveld, B. M. W.; Schubert, U. S. *Adv. Mater.* **2005**, *17*, 1109.
- (7) Hu, T.; He, L.; Duan, L.; Qiu, Y. *J. Mater. Chem.* **2012**, *22*, 4206.
- (8) Slinker, J. D.; Rivnay, J.; Moskowitz, J. S.; Parker, J. B.; Bernhard, S.; Abruna, H. D.; Malliaras, G. G. *J. Mater. Chem.* **2007**, *17*, 2976.
- (9) Ladouceur, S.; Fortin, D.; Zysman-Colman, E. *Inorg. Chem.* **2010**, *49*, 5625.
- (10) Ladouceur, S.; Fortin, D.; Zysman-Colman, E. *Inorg. Chem.* **2011**, *50*, 11514.

- (11) Swanick, K. N.; Ladouceur, S.; Zysman-Colman, E.; Ding, Z. *Chem. Commun.* **2012**, 48, 3179.
- (12) Nepomnyashchii, A. B.; Bard, A. J. *Acc. Chem. Res.* **2012**, 45, 1844.
- (13) Nepomnyashchii, A. B.; Ono, R. J.; Lyons, D. M.; Bielawski, C. W.; Sessler, J. L.; Bard, A. J. *Chem. Sci.* **2012**, 3, 2628.
- (14) Suk, J.; Omer, K. M.; Bura, T.; Ziessel, R.; Bard, A. J. *J. Phys. Chem. C* **2011**, 115, 15361.
- (15) Omer, K. M.; Ku, S.-Y.; Wong, K.-T.; Bard, A. J. *Angew. Chem. Int. Ed.* **2009**, 48, 9300.
- (16) Miao, W. *Chem. Rev.* **2008**, 108, 2506.
- (17) Bard, A. J. *Electrogenerated Chemiluminescence*; Marcel Dekker: New York, **2004**.
- (18) Swanick, K. N.; Dodd, D. W.; Price, J. T.; Brazeau, A. L.; Jones, N. D.; Hudson, R. H. E.; Ding, Z. *Phys. Chem. Chem. Phys.* **2011**, 13, 17405.
- (19) Xu, L.; Li, Y.; Wu, S.; Liu, X.; Su, B. *Angew. Chem. Int. Ed.* **2012**, 51, 8068.
- (20) Ladouceur, S.; Swanick, K. N.; Gallagher-Duval, S.; Ding, Z.; Zysman-Colman, E. *Eur. J. Inorg. Chem.* **2013**, DOI: 10.1002/ejic.201300849.
- (21) Lai, R. Y.; Bard, A. J. *J. Phys. Chem. A* **2003**, 107, 3335.
- (22) Lee, S. K.; Richter, M. M.; Streckowski, L.; Bard, A. J. *Anal. Chem.* **1997**, 69, 4126.
- (23) Miao, W.; Bard, A. J. *Anal. Chem.* **2004**, 76, 5379.
- (24) Miao, W.; Bard, A. J. *Anal. Chem.* **2004**, 76, 7109.
- (25) Richter, M. M.; Bard, A. J.; Kim, W.; Schmehl, R. H. *Anal. Chem.* **1998**, 70, 310.
- (26) Vinyard, D. J.; Richter, M. M. *Anal. Chem.* **2007**, 79, 6404.
- (27) Miao, W.; Choi, J.-P.; Bard, A. J. *J. Am. Chem. Soc.* **2002**, 124, 14478.
- (28) Kanoufi, F. d. r.; Zu, Y.; Bard, A. J. *J. Phys. Chem. B* **2000**, 105, 210.
- (29) Knight, A. W.; Greenway, G. M. *Analyst* **1996**, 121, 101R.
- (30) Zu, Y.; Bard, A. J. *Anal. Chem.* **2000**, 72, 3223.
- (31) Cao, W.; Zhang, X.; Bard, A. J. *J. Electroanal. Chem.* **2004**, 566, 409.

- (32) Booker, C.; Wang, X.; Haroun, S.; Zhou, J.; Jennings, M.; Pagenkopf, B. L.; Ding, Z. *Angew. Chem. Int. Ed.* **2008**, *47*, 7731.
- (33) Swanick, K. N.; Price, J. T.; Jones, N. D.; Ding, Z. *J. Org. Chem.* **2012**, *77*, 5646.
- (34) Swanick, K. N.; Ladouceur, S.; Zysman-Colman, E.; Ding, Z. *Angew. Chemie. Int. Ed.* **2012**, *51*, 11079.
- (35) Rashidnadi, S.; Hung, T. H.; Wong, K.-T.; Bard, A. J. *J. Am. Chem. Soc.* **2008**, *130*, 634.
- (36) Nazeeruddin, M. K.; Wegh, R. T.; Zhou, Z.; Klein, C.; Wang, Q.; De Angelis, F.; Fantacci, S.; Grätzel, M. *Inorg. Chem.* **2006**, *45*, 9245.

5.3 Electrochemiluminescence of Heterometallic Ruthenium(II)-Iridium(III) Soft Salts[†]

5.3.1 Introduction

Electrochemiluminescence (ECL) is an emerging sensitive tool for analyte detection and biological probes.¹⁻⁶ ECL is emitted through bimolecular recombination of radical cations and anions electrochemically generated in solution. Radical species can be generated from a single molecular emitter (annihilation mechanism) or through a bimolecular set of electrochemical and chemical reactions between the emitter and a suitable co-reactant (co-reactant mechanism). The seminal ECL system in fact is based on $[\text{Ru}(\text{bpy})_3]^{2+}$ /tri-*n*-propylamine (TPrA) co-reactant scheme (bpy = 2,2'-bipyridine).⁷⁻¹⁰ Most ECL studies involve single luminophores and thus a unique emission process. The search for high-efficiency ECL reagents that can emit over the entire visible spectrum is intense and much recent interest has focussed on neutral¹¹⁻¹⁵ and charged¹⁶⁻²⁰ iridium(III) mononuclear complexes to address these design challenges.

Based on the pioneering work by Richter and co-workers,^{21,22} Hogan *et al.* showed how mixtures of luminophores in the presence of TPrA could be addressed at different potentials and thus produce ECL systems with multiple emissive readouts.^{23,24} Independently, pursuing “lab-on-a-molecule”^{25,26} design, Schmittel *et al.* have investigated the ECL behavior of oligonuclear Ir(III)-Ru(II) and Ir(III)-Ru(II)-Ir(III) systems with TPrA wherein the metals are electronically isolated but covalently attached.²⁷ They demonstrated that in these systems different ECL and photoluminescent (PL) behavior exists and that multiple ECL emissions are possible through recombination of different radical cationic species with the co-reactant. We illustrated that multiple ECL signals could be obtained under self-co-reactant conditions from the same luminophore by generating species at different oxidation states.²⁰ Recently, Hogan *et al.* elegantly demonstrated electrochemically-controlled reversible switching between emission from

[†] This work by Kalen N. Swanick, Martina Sandroni, Zhifeng Ding and Eli Zysman-Colman, **2013**, has been submitted.

two separate luminophores within the same solution for independent emission detection.²⁴

Herein we report for the first time the electrochemistry and ECL of the heterometallic soft salt $[\text{Ru}(\text{dtbubpy})_3][\text{Ir}(\text{ppy})_2(\text{CN})_2]_2$, **[Ir][Ru][Ir]** that is a 2:1 stoichiometric mixture of complexes containing a cationic $[\text{Ru}(\text{dtbubpy})_3]$ and an anionic $[\text{Ir}(\text{ppy})_2(\text{CN})_2]$ with strong ion-pairing interaction,²⁸ under both annihilation and co-reactant conditions. The soft salt is composed of a red-emitting ruthenium(II) cation and a blue-emitting iridium(III) anion (dtbubpy = 4,4'-di-*t*-butyl-2,2'-bipyridine; ppyH = 2-phenylpyridine). We compare **[Ir][Ru][Ir]** with reference complexes $[\text{Ru}(\text{dtbubpy})_3]\text{Cl}_2$, **[Ru]Cl₂**, and TBA $[\text{Ir}(\text{ppy})_2(\text{CN})_2]$, **TBA[Ir]**, as well as their 1:2 mixture in solution (TBA = tetra-*n*-butylammonium). Surprisingly, the ECL signal of **[Ir][Ru][Ir]** reflects emission solely from the [Ru] moiety. ECL is probably generated from $[\text{Ir}]^\bullet$ and $[\text{Ru}]^{+\bullet}$ annihilation, which therefore reduce the energy required to emit light. A significant enhancement in ECL intensity was observed from the soft salt solution, which is further enhanced by adding TPrA as a co-reactant.

5.3.2 Experimental Section

Synthesis. TBA $[\text{Ir}(\text{ppy})_2(\text{CN})_2]$, **TBA[Ir]**,²⁹ and $[\text{Ru}(\text{dtbubpy})_3]\text{Cl}_2$, **[Ru]Cl₂**,³⁰ were synthesized according to previously reported procedures, and the spectroscopic and MS data matched those found in the literature. The synthesis of **[Ir][Ru][Ir]** was previously reported by us.³¹ X-ray quality crystals were obtained by vapour diffusion of *tert*-butylmethyl ether (TBME) in an acetonitrile solution of the salt. These were collected and used in the electrochemistry and ECL studies.

[Ir][Ru][Ir]: ¹H NMR (400 MHz, CD₃CN, 25 °C): 9.64 (dm, 4H, J = 5.9 Hz), 8.48 (d, 6H, J = 1.7 Hz), 7.95 (d, 4H, 8.0 Hz), 7.83 (m, 4H), 7.62 (dd, 4H, J = 8.0 Hz, J = 0.8 Hz), 7.55 (d, 6H, J = 6.0 Hz), 7.38 (dd, 6H, J = 6.0 Hz, J = 2.0 Hz), 7.21 (m, 4H), 7.78 (m, 4H), 6.68 (td, 4H, J = 7.4 Hz, J = 1.2 Hz), 6.19 (dm, 4H, J = 7.4 Hz), 1.38 (s, 54H) ppm. HR-MS (ESI⁺): Found m/z = 453.2447; calculated for (C₅₄H₇₂N₆Ru), [2]²⁺ m/z = 453.2433. HR-MS (ESI⁻): Found m/z = 553.0972; calculated for (C₂₄H₁₆IrN₄), [1]⁻ m/z = 553.0999.

Electrochemical preparation. Cyclic voltammetry (CV), and ECL experiments were conducted using a 2 mm diameter Pt disc inlaid in a glass sheath as the working electrode (WE), a coiled Pt wire as the counter electrode (CE), and a coiled Pt wire as the quasi reference electrode (RE). Electrode cleaning procedures have been previously reported elsewhere.³² All solutions for electrochemical and ECL experiments were prepared in the electrochemical cell placed inside an N₂-filled drybox that possessed little oxygen and moisture. The solutions of complexes studied had concentrations of approximately 5.0×10^{-4} M in anhydrous acetonitrile (Sure/Seal™ bottle from Aldrich, Mississauga, ON) containing 0.1 M TBAPF₆ as supporting electrolyte. The electrodes were immersed in the solution and connected by copper wire inserted through the air-tight Teflon cap. The assembly was moved out of the drybox to perform electrochemistry and ECL experiments. After completion of each experiment, the electrochemical potential window was calibrated using ferrocene (Fc) as the internal standard. The redox potential of Fc/Fc⁺ was taken as 0.40 V vs. SCE.³³

Electrochemical instrumentation. The CV was conducted on a CHI 610A electrochemical analyzer (CH Instruments, Austin, TX). The experimental parameters for CV are listed here: 0.000 V initial potential in experimental scale, positive or negative initial scan polarity, 0.1 V/s scan rate, 4 sweep segments, 0.001 V sample interval, 2 s quiet time, 1×10^{-5} AV⁻¹ sensitivity. The potential range was adjusted depending on the particular complex.

ECL instrumentation. The ECL cell was specifically designed to have a flat Pyrex window at the bottom for detection generated light from the WE and was sealed with an air-tight Teflon cap with a rubber O-ring for CV and ECL measurements. The ECL data along with CV data were obtained using the CHI 610A coupled with a photomultiplier tube (PMT, R928, Hamamatsu, Japan) held at -750 V with a high voltage power supply. The ECL collected by the PMT under the flat Pyrex window at the bottom of the cell was measured as a photocurrent, and transformed to a voltage signal, using a picoammeter/voltage source (Keithley 6487, Cleveland, OH). The potential, current signals from the electrochemical workstation, and the photocurrent signal from the picoammeter were sent simultaneously through a DAQ board (DAQ 6052E, National

Instruments, Austin, TX) in a computer. The data acquisition system was controlled from a custom-made LabVIEW program (ECL_PMT610a.vi, National Instruments, Austin, TX). The photosensitivity on the picoammeter was set manually in order to avoid the saturation.³²

The ECL spectra were obtained by replacing the PMT with a spectrometer (Cornerstone 260, Newport, Canada) attached to a CCD camera (Model DV420-BV, Andor Technology, Belfast, UK). The camera was cooled to -55 °C prior to use, and controlled by a computer for operation and data acquisition. The intensities versus wavelengths (spectra) were recorded by Andor Technology program. Similar to the CV experiments, the samples were scanned at 0.1 V/s, within each complex's potential window. The exposure time of the spectra was set to the amount of time for two complete scans. Vertical lines/spikes observed in the spectra were due to cosmic rays from the CCD camera.

For the spooling ECL spectroscopy, the same spectrometer and CCD camera were used and the following parameters were employed in the Andor Technology program under the kinetic parameters option tab: for **[Ir][Ru][Ir]**: exposure time = 1 s, number of accumulations = 1, kinetic series length = 165 s (matching with the potential scan time for two complete cycles), kinetic cycle time = 1, and the spectrometer was centered at 600 nm using the 121.6 l/mm grating, with the camera cooled to -55 °C. On the CHI 610A electrochemical analyzer, the initial potential was set to 0.00 V, high potential = 1.43 V, low potential = -2.83 V, sensitivity = $1 \times 10^{-5} \text{ AV}^{-1}$, initial scan polarity = negative, scan rate = 0.1 V/s sweep segments = 4, sample interval = 0.001 V, quiet time 2 s. Simultaneously, the CHI 610A electrochemical analyzer and the Andor Technology program were run and the CV and spooling ECL spectra were collected.

ECL efficiency calculations. ECL quantum efficiencies (QE) were calculated relative to $[\text{Ru}(\text{bpy})_3](\text{PF}_6)_2$ (the reported absolute ECL efficiency, Φ_{ECL} , of $[\text{Ru}(\text{bpy})_3]^{2+}$ is 0.05) by integrating both the ECL intensity and current value versus time for each compound, see Eq. 2.1 in Chapter 2.

5.3.3 Results and Discussion

The electrochemical properties of **[Ru]Cl₂**, **TBA[Ir]** and the soft salt **[Ir][Ru][Ir]** were assessed in acetonitrile, using TBAPF₆ as the supporting electrolyte. The data are gathered in Table S5.1 in Appendix IV, and the cyclic voltammograms (CVs) are shown in Figure 5.6, together with the corresponding ECL-voltage curves. Similar to **[Ru(bpy)₂]³⁺**,⁹ red-emitting **[Ru]Cl₂** exhibits a reversible oxidation at 1.11 V vs. SCE, corresponding to the Ru^{II/III} couple, and a reversible reduction at -1.45 V, attributed to electron injection into the LUMO mostly contributed from the dtbubpy ligands, Figure 5.6a. The chloride oxidation as that in the case of **[Ru(bpy)₃]Cl₂**⁹ was not observed in the potential window, indicating that **[Ru]Cl₂** is easier to be oxidized than Cl⁻. Green-emitting **TBA[Ir]** is characterized by an irreversible oxidation at 0.98 V and a reversible reduction at -2.32 V, displaying a much larger electrochemical gap (ΔE_{redox}) than **[Ru]Cl₂**, Figure 5.6b. The oxidation process is centered on iridium (t_{2g}) with significant contributions from the phenyl rings of the ppy ligands, while the reduction is mainly localized on the pyridyl rings. The electrochemical data for these reference compounds match those reported the literature.^{34,35}

The first reduction and oxidation of **[Ir][Ru][Ir]** show a superposition of partial features of the two reference complexes, Figure 5.6c. The reduction wave corresponds to that of **[Ru]²⁺**, Figure 5.6a. The oxidation centered on Ir is the first oxidation wave for the soft salt, an irreversible process identical to that of **TBA[Ir]**, Figure 5.6b. The ratio of the reduction current peak to the oxidation one is 1:2 corresponding to the stoichiometry of the salt.

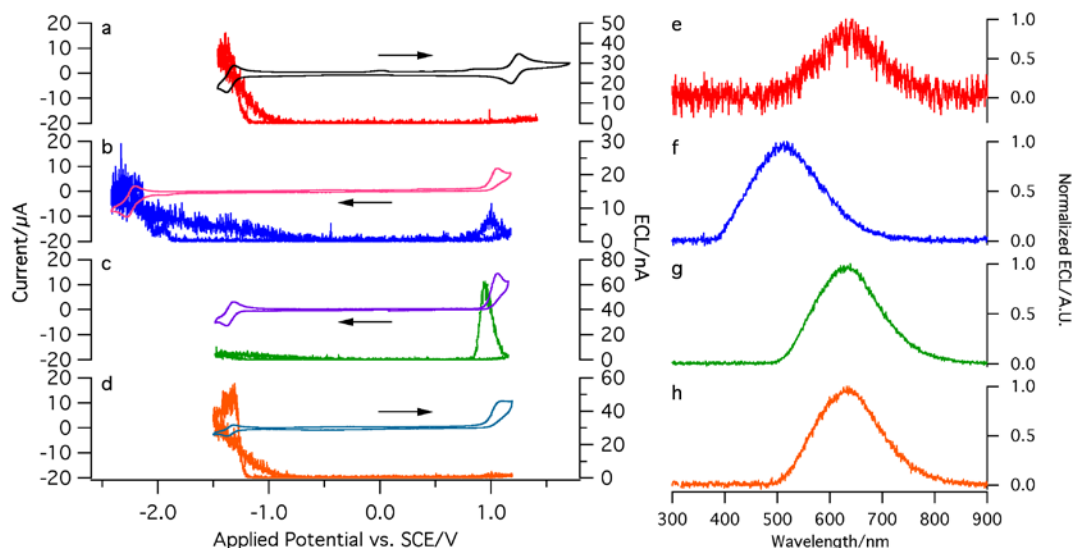
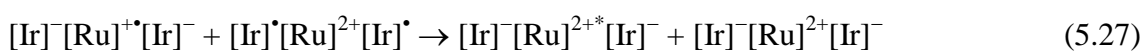


Figure 5.6. CVs of a) $[\text{Ru}]\text{Cl}_2$ (in black), b) $\text{TBA}[\text{Ir}]$ (in pink), c) $[\text{Ir}][\text{Ru}][\text{Ir}]$ (in purple), and d) 1:2 $[\text{Ru}]\text{Cl}_2:\text{TBA}[\text{Ir}]$ mixture (in blue) in potential ranges between their 1st reduction and 1st oxidation, along with the corresponding ECL-voltage curves in red (a), blue (b), green (c), and orange (d), respectively. Scan rate was at 0.1 V/s. First cycle is shown, and arrows indicate the scan direction. ECL spectra are displayed for e) $[\text{Ru}]\text{Cl}_2$, f) $\text{TBA}[\text{Ir}]$, g) $[\text{Ir}][\text{Ru}][\text{Ir}]$, and h) 1:2 $[\text{Ru}]\text{Cl}_2:\text{TBA}[\text{Ir}]$ mixture.

For ECL, typically the $[\text{Ru}]^{2+}$ and $[\text{Ir}]^-$ complexes produce ECL from their electrogenerated radicals $[\text{Ru}]^{+\bullet}$ and $[\text{Ru}]^{3+\bullet}$, Figure 5.6a, $[\text{Ir}]^{2-\bullet}$ and $[\text{Ir}]^\bullet$, Figure 5.6b, respectively. The stronger ECL signals in the cathodic region in Figure 5.6a and b for the reference complexes point to a greater stability for the $[\text{Ir}]^\bullet$ species of $\text{TBA}[\text{Ir}]$ and $[\text{Ru}]^{3+\bullet}$ species of $[\text{Ru}]\text{Cl}_2$, despite the greater reversibility observed for the $[\text{Ir}]^{2-\bullet}$ species of $\text{TBA}[\text{Ir}]$ and the $[\text{Ru}]^{+\bullet}$ species of $[\text{Ru}]\text{Cl}_2$. Very interestingly, due to communication between the $[\text{Ru}]^{2+}$ and $[\text{Ir}]^-$ ions in the soft salt, ECL was generated *via* the annihilation mechanism involving radicals from both complexes instead of from one species alone, Figure 5.6c, in a potential window from 1.16 to -1.48 V. Initially, $[\text{Ru}]^{2+}$ is reduced to its radical anion, $[\text{Ru}]^{+\bullet}$, at -1.36 V, Eq. 5.25, and $[\text{Ir}]^-$ is oxidized to its radical cation, $[\text{Ir}]^\bullet$, at 1.07 V, Eq. 5.26. The excited species $[\text{Ru}]^{2+\bullet}$ is generated, Eq. 5.27, *via* electron transfer from the HOMO of $[\text{Ru}]^{+\bullet}$ to the HOMO of $[\text{Ir}]^\bullet$, Scheme S5.1, Appendix IV. The $[\text{Ru}]^{2+\bullet}$ then emits light *via* relaxation to the ground state, Eq. 5.28. The $[\text{Ru}]^{+\bullet}$ was

stabilized while the $[\text{Ir}]^{\bullet}$ was destabilized in the soft salt, the radical cations appear to be less stable than the radical anions: ECL was generated mostly in the anodic region in contrast to that from the reference mononuclear complexes. The ECL intensity, corresponding to the photons generated, of the $[\text{Ir}][\text{Ru}][\text{Ir}]$ complex is 62 nA compared to 45 nA for $[\text{Ru}]\text{Cl}_2$, an increase of approximately 1.4 times.



The ECL efficiencies of $[\text{Ru}]\text{Cl}_2$ and $\text{TBA}[\text{Ir}]$ were 2.14 %, and 2.83 %, while the $[\text{Ir}][\text{Ru}][\text{Ir}]$ soft salt was determined to be 2.51 %. Thus, there was no significant ECL efficiency enhancement for the soft salt relative to the reference complexes in this potential region.

The ECL emission spectra were acquired during potential scanning for the three complexes, Figure 5.6e to Figure 5.6h. The heterometallic soft salt shows an ECL peak wavelength at 634 nm, Figure 5.6g, while mononuclear parent complexes display ECL peak wavelengths at 638 nm for $[\text{Ru}]\text{Cl}_2$, Figure 5.6e, and 517 nm for $\text{TBA}[\text{Ir}]$, Figure 5.6f. The ECL spectrum of $[\text{Ru}]\text{Cl}_2$ correlates well with the 298 K photoluminescence (PL) spectrum in acetonitrile solution, $\lambda_{\text{em}} = 630$ nm. By contrast, the ECL emission of $\text{TBA}[\text{Ir}]$ is red shifted with respect to the PL spectrum in acetonitrile, structured, with main λ_{em} peaks at 477 and 506 nm, which is due to the higher concentration required during the ECL experiments, internal filter effect (self-absorption) and instrument effects.³⁶ Finally, the ECL of $[\text{Ir}][\text{Ru}][\text{Ir}]$ is characterized by pure $[\text{Ru}]^{2+}$ emission, indicating that $[\text{Ru}]^{2+*}$ is the only excited species formed during the electrochemical process. These observations corroborate our proposed ECL mechanisms for the soft salt.

Electrochemistry and ECL of a solution containing 1:2 $[\text{Ru}]\text{Cl}_2:\text{TBA}[\text{Ir}]$ mixture of the reference complexes were also carried out in the same potential range as the soft

salt, Figure 5.6d. While the CVs of the soft salt and the mixture are similar, there is a large discrepancy in the ECL-voltage curves: the light emission of the mixture follows the same cathodic emission pattern as their reference complexes instead of anodic ECL found in the soft salt. As well, the maximum ECL intensity reached only 56 nA, Figure 5.6d, with a relative efficiency of 4.37 % compared to 62 nA for $[\text{Ir}][\text{Ru}][\text{Ir}]$, Figure 5.6c. The ECL peak wavelength of 635 nm for the mixture, Figure 5.6h, matches that of $[\text{Ir}][\text{Ru}][\text{Ir}]$, Figure 5.6g.

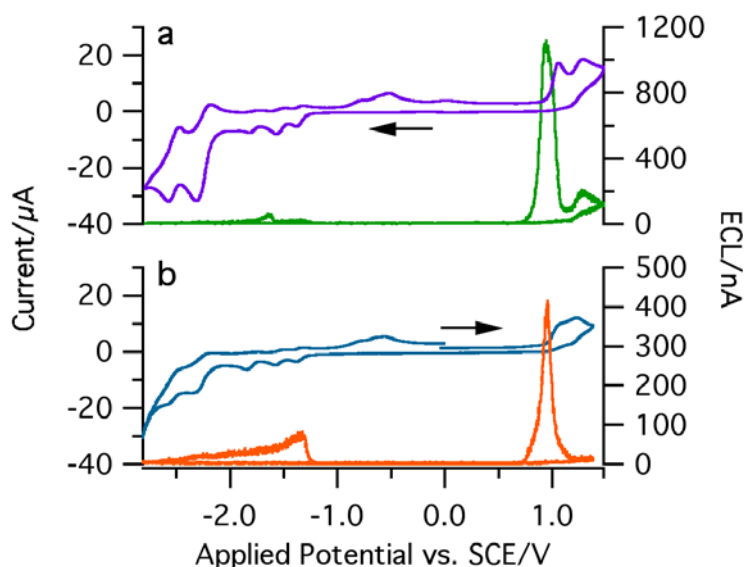
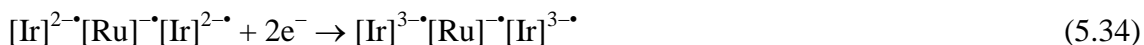


Figure 5.7. a) CV (in purple) with ECL-voltage curve overlaid (in green) of $[\text{Ir}][\text{Ru}][\text{Ir}]$; b) CV (in pink) with ECL-voltage curve overlaid (in orange) of 1:2 $[\text{Ru}]\text{Cl}_2:\text{TBA}[\text{Ir}]$ mixture solution. Both are shown with an extended potential window. The scan rate was 0.1 V/s.

Extending the potential more positive, Figure 5.7a, the soft salt undergoes a second irreversible oxidation, to generate $[\text{Ru}]^{3+}$, Eq. 5.29, centred on Ru at 1.48 V, which is very similar to that for the oxidation of $[\text{Ru}]^{2+}$ in $[\text{Ru}]\text{Cl}_2$, Figure 5.6a. The oxidation wave of the Ir moiety was not well resolved due to simultaneous oxidation of the two Ir moieties. However, the two consecutive oxidation current peak heights of the two Ir anions and the Ru cation demonstrate the 2:1 ratio corresponding to the stoichiometry of $[\text{Ir}][\text{Ru}][\text{Ir}]$. More interestingly, upon scanning to further negative

potentials, Figure 5.7a, additional reduction waves were observed. The second and third reduction peaks, Eqs. 5.30 and 5.31, possess similar current heights as the first, Eq. 5.25, which are attributed to further reduction reactions centered on the dtbubpy ligands on $[\text{Ru}]^{2+}$ by comparison with the literature data.³⁰

Scanning to further cathodic potentials reveals two successive reduction reactions of the ppy ligands on both $[\text{Ir}]^-$ anions. When $[\text{Ir}]^-$ was reduced to $[\text{Ir}]^{2-\bullet}$, Eq. 5.32, the electrochemical current was more than 4 times higher than that for the first reduction of the $[\text{Ru}]^{2+}$ moiety. The generated $[\text{Ir}]^{2-\bullet}$ moiety can reduce $[\text{Ru}]^{2+}$ in the bulk, to regenerate the $[\text{Ir}]^-$ species, Eq. 5.33, a catalytic effect. Furthermore, there is almost no such catalytic enhancement on the second reduction of the $[\text{Ir}]^-$ anions, Eq. 5.34.



The ECL-voltage curve in a potential window between 1.48 and -2.79 V in Figure 5.7a demonstrates a dramatic enhancement in ECL intensity in the annihilation path upon generation of $[\text{Ru}]^{2+\bullet}$. The strong ECL peak reached a maximum intensity of 1118 nA. The enhancement in ECL intensity increased approximately 18x in Figure 5.7a compared to Figure 5.6c. Here, the efficiency increased from 2.51 % to 7.21 %, an increase in efficiency of about 3x. It appears that only the $[\text{Ru}]^{2+\bullet}$ excited species in this situation can be generated, emitting light *via* pathways similar to that expressed by Eqs. 5.27 and 5.28.

In comparison, the CV of the 1:2 $[\text{Ru}]\text{Cl}_2:\text{TBA}[\text{Ir}]$ mixture solution, Figure 5.7b, in this potential range displays the sum of those for the two individual complexes, $[\text{Ru}]\text{Cl}_2$, Figure 5.6a, and $\text{TBA}[\text{Ir}]$, Figure 5.6b. There is no catalytic current enhancement in the CV, however ECL was now mostly generated in the anodic potential region compared to Figure 5.6d, where ECL was only generated in the cathodic region.

The potential window must be extended to greater positive potential in order to observe any enhancement with the mixed solution. The maximum ECL, upon oxidation of $[\text{Ir}]^-$, was enhanced much less than the soft salt, with an ECL intensity of 414 nA. The second ECL peak, as observed in the soft salt, around 1.28 V, Figure 5.7a, does not appear in the 1:2 $[\text{Ru}]\text{Cl}_2:\text{TBA}[\text{Ir}]$ mixed solution at the same potential. The relative efficiency of the mixed solution was 3.96 %, lower than the soft salt.

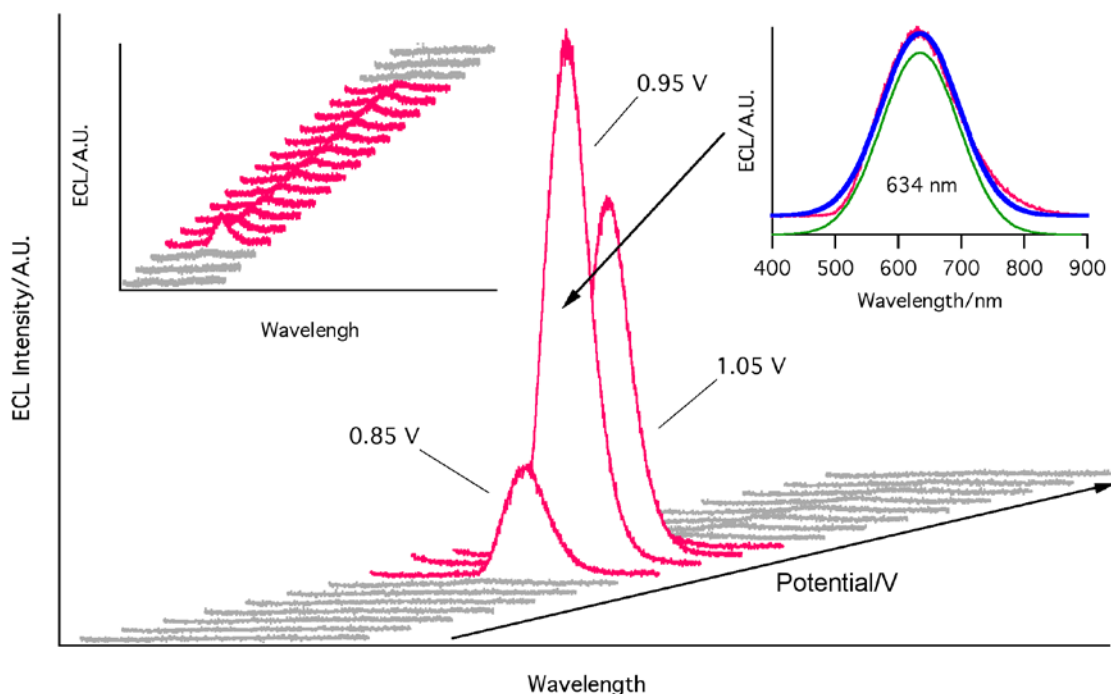


Figure 5.8. Spooling ECL spectra of $[\text{Ir}][\text{Ru}][\text{Ir}]$ soft salt, first cycle shown, with an extended potential window between 1.43 V and -2.83 V, $t = 165$ s for two cycles. Left inset shows the onset ECL spectra while the right inset illustrates the fitting of ECL spectra to one peak at 634 nm when the potential was 0.95 V. The applied voltage interval for the ECL spectra is 100 mV.

Spooling ECL spectra^{20,33} in the extended potential window were recorded for 165 s at an interval of 1 s, Figure 5.8, for one complete cycle, see Figure S5.7 in Appendix IV, for two complete cycles. Only one peak wavelength at 634 nm was observed during the ECL evolution and devolution. These spectra clearly exclude the possibility that $[\text{Ir}]^{-*}$ excited species was generated, and the second ECL peak in Figure 5.7a was also due to the generation of $[\text{Ru}]^{2+*}$. Furthermore, the ECL enhancement might be due to the increase concentration of $[\text{Ru}]^{+*}$ moiety caused by the catalytic electrochemical reaction observed in the CV in Figure 5.7, Eq. 5.33. Finally, spooling ECL spectra of the 1:2 $[\text{Ru}]\text{Cl}_2\text{:TBA}[\text{Ir}]$ mixture also shows the consistent ECL peak wavelength at 634 nm from $[\text{Ru}]^{2+*}$, Figure S5.8, Appendix IV. Again, the ECL intensity was weaker than that from the soft salt.

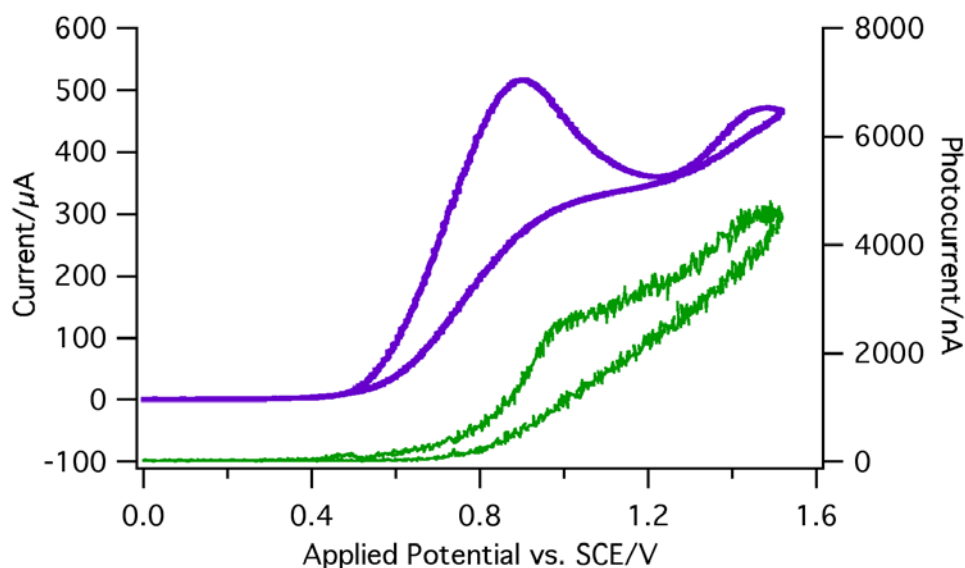


Figure 5.9. CV (in purple) overlaid with ECL-voltage curve (in green) of $[\text{Ir}][\text{Ru}][\text{Ir}]$ soft salt with 0.02 M TPrA co-reactant, between 0.00 V to 1.52 V, scan rate was 0.1 V/s, first cycle shown.

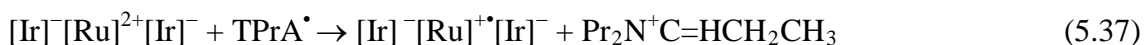
The soft salt solution containing 20 mM TPrA co-reactant was scanned anodically with a potential window between 0.00 V and 1.52 V, Figure 5.9. TPrA underwent oxidation reaction beginning at 0.48 V, at which the ECL onset was observed. ECL

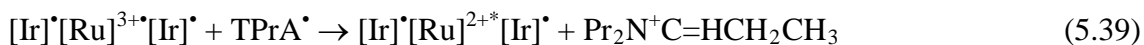
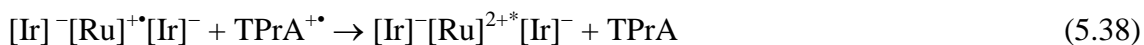
showed a maximum of 140 nA at this potential. In this potential region, neither complex moiety is yet oxidized.

The ECL generation followed the mechanism proposed for $[\text{Ru}(\text{bpy})_3]^{2+}/\text{TPrA}$ co-reactant system in the same situation reported by Miao *et al.*,⁸ involving the TPrA^{\bullet} cation radicals as the main driving force, Eqs. 5.35 and 5.36; i.e. TPrA was oxidized to $\text{TPrA}^{+\bullet}$, Eq. 5.35, then rapidly deprotonated to generate the TPrA^{\bullet} radical, Eq. 5.36. The TPrA^{\bullet} radical donated an electron to the LUMO of the $[\text{Ru}]^{2+}$ moiety, generating the $[\text{Ru}]^{+\bullet}$ species, Eq. 5.37. At this time, the $\text{TPrA}^{+\bullet}$ radical then removed an electron from the HOMO of $[\text{Ru}]^{+\bullet}$ moiety, Eq. 5.38. Thus, $[\text{Ru}]^{2+\bullet}$ is generated that will emit light when radiatively relaxing to the ground state, Eq. 5.28.

As the potential was scanned more positive, TPrA continued to oxidize and reached a peak at 0.90 V,³⁷ at which ECL intensity rose to a maximum of 1430 nA. ECL continued to increase from that point while the rising slope decreased. Here, TPrA in the vicinity of the electrode was depleted and therefore the TPrA^{\bullet} concentration decreased. While $[\text{Ir}]^-$ oxidation to $[\text{Ir}]^{\bullet}$ in the soft salt was initiated and reached a peak at 1.04 V, TPrA^{\bullet} , with a reduction potential of -1.70 V vs. SCE,³⁷ does not have a sufficiently negative potential to reduce $[\text{Ir}]^-$ to $[\text{Ir}]^{2-\bullet}$ with its reduction potential of -2.33 V, Figure 5.7a. Again, no $[\text{Ir}]^{\bullet}$ excited state should be generated.

Finally, once the $[\text{Ru}]^{2+}$ moiety was oxidized around 1.49 V, an enhancement of ECL intensity up to 4800 nA was observed. No reverse oxidation wave was observed, demonstrated by the instability of $\text{TPrA}^{+\bullet}$ due to a fast deprotonation process, as described by Lai and Bard.³⁷ The addition of TPrA as co-reactant to the $[\text{Ir}][\text{Ru}][\text{Ir}]$ soft salt enhanced the amount of ECL intensity ca. 4x compared to that in annihilation of the soft salt, from 1118 nA, Figure 5.7a, to 4800 nA, Figure 5.9.





Here, the $[\text{Ru}]^{2+}$ species is oxidized to generate $[\text{Ru}]^{3+}$, Eq. 5.27. The strong reducing agent, TPrA^{\bullet} , Eq. 5.34, donates an electron to the LUMO of the $[\text{Ru}]^{3+}$ species, Eq. 5.39. This generates the $[\text{Ru}]^{2+*}$ excited species that emits light. Although the intensity of ECL was 4x higher using TPrA as co-reactant compared to the intensity *via* annihilation. However, the relative ECL efficiency was determined to be 2.67 % compared to 7.21 % from annihilation scanning since the consumption of the electrons went even higher.

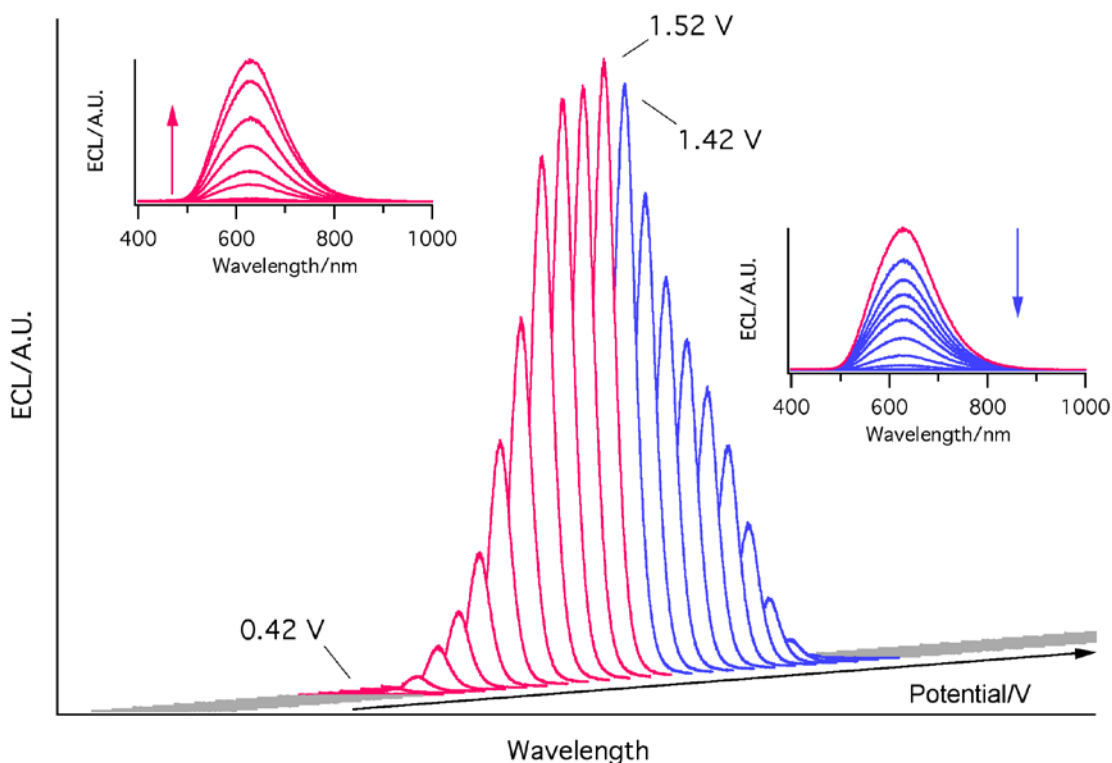


Figure 5.10. ECL spooling spectra of $[\text{Ir}][\text{Ru}][\text{Ir}]$ soft salt with 0.02 M TPrA coreactant between 0.00 V to 1.52 V, applied voltage interval for the ECL spectra is 100 mV. Insets show ECL evolution (in pink) and devolution (in purple).

Consistent with the above ECL experiments, no $[\text{Ir}]^*$ was observed from spooling ECL spectra, Figure 5.10, one complete cycle, see Figure S5.9 in Appendix IV for two complete cycles. The spooling spectra showed constant evolution and devolution of peak at 634 nm. This confirms that the $[\text{Ru}]^{2+*}$ excited species is the only species that emits light *via* annihilation or co-reactant studies.

5.3.4 Conclusions

We have shown the contributions from the $[\text{Ru}]^{2+}$ and $[\text{Ir}]^-$ moieties in the **[Ir][Ru][Ir]** soft salt to the ECL generation during electrochemical reactions. It is plausible that the two moieties in the soft salt can reduce the energy required to produce ECL in the annihilation path, from 2.56 and 3.30 eV for $[\text{Ru}]^{2+}$ and $[\text{Ir}]^-$, respectively, to 2.42 eV for the soft salt (Table S5.1 in Appendix IV). Spooling ECL spectroscopy has proven the light emission mechanisms. While the ECL peak wavelength in the annihilation path is consistent at 634 nm due to the $[\text{Ru}]^{2+*}$ excited species, ECL intensity is enhanced 18 times in an extended potential window. In the co-reactant route with TPrA, the ECL intensity was 4x larger than that in the annihilation path. Nevertheless, in both routes, no ECL signal was generated from $[\text{Ir}]^*$ moieties due to the electrocatalytic reduction of $[\text{Ru}]^{2+}$ by $[\text{Ir}]^{2-\bullet}$, and insufficient reduction power of TPrA \bullet to generate $[\text{Ir}]^{2-\bullet}$.

5.3.5 References

- (1) Bard, A. J. *Electrogenerated Chemiluminescence*; Marcel Dekker: New York, 2004.
- (2) Miao, W. *Chem. Rev.* **2008**, *108*, 2506.
- (3) Richter, M. M. *Chem. Rev.* **2004**, *104*, 3003.
- (4) Bard, A. J.; Ding, Z.; Myung, N. *Struct. Bond* **2005**, *118*, 1.
- (5) Ding, Z.; Quinn, B. M.; Haram, S. K.; Pell, L. E.; Korgel, B. A.; Bard, A. J. *Science* **2002**, *296*, 1293.
- (6) Hu, L.; Xu, G. *Chem. Soc. Rev.* **2010**, *39*, 3275.
- (7) Li, M.-J.; Chen, Z.; Yam, V. W.-W.; Zu, Y. *ACS Nano* **2008**, *2*, 905.
- (8) Miao, W.; Choi, J.-P.; Bard, A. J. *J. Am. Chem. Soc.* **2002**, *124*, 14478.

- (9) Tokel, N. E.; Bard, A. J. *J. Am. Chem. Soc.* **1972**, *94*, 2862.
- (10) Li, M.-J.; Chen, Z.; Zhu, N.; Yam, V. W.-W.; Zu, Y. *Inorg. Chem.* **2008**, *47*, 1218.
- (11) Shin, I.-S.; Kang, Y.-T.; Lee, J.-K.; Kim, H.; Kim, T. H.; Kim, J. S. *Analyst* **2011**, *136*, 2151.
- (12) Reid, E. F.; Burn, P. L.; Lo, S.-C.; Hogan, C. F. *Electrochim. Acta* **2013**, *100*, 72.
- (13) Shin, I.-S.; Yoon, S.; Kim, J. I.; Lee, J.-K.; Kim, T. H.; Kim, H. *Electrochim. Acta* **2011**, *56*, 6219.
- (14) Zhu, S.; Song, Q.; Zhang, S.; Ding, Y. *J. Mol. Struct.* **2013**, *1035*, 224.
- (15) Li, C.; Lin, J.; Yang, X.; Wan, J. *J. Organomet. Chem.* **2011**, *696*, 2445.
- (16) Kiran, R. V.; Hogan, C. F.; James, B. D.; Wilson, D. J. D. *Eur. J. Inorg. Chem.* **2011**, *2011*, 4816.
- (17) Zanarini, S.; Felici, M.; Valenti, G.; Marcaccio, M.; Prodi, L.; Bonacchi, S.; Contreras-Carballada, P.; Williams, R. M.; Feiters, M. C.; Nolte, R. J. M.; De Cola, L.; Paolucci, F. *Chem. Eur. J.* **2011**, *17*, 4640.
- (18) Li, C.; Lin, J.; Guo, Y.; Zhang, S. *Chem. Commun.* **2011**, *47*, 4442.
- (19) Swanick, K. N.; Ladouceur, S.; Zysman-Colman, E.; Ding, Z. *Chem. Commun.* **2012**, *48*, 3179.
- (20) Swanick, K. N.; Hesari, M.; Workentin, M. S.; Ding, Z. *J. Am. Chem. Soc.* **2012**, *134*, 15205.
- (21) Bruce, D.; Richter, M. M. *Anal. Chem.* **2002**, *74*, 1340.
- (22) Muegge, B. D.; Richter, M. M. *Anal. Chem.* **2003**, *76*, 73.
- (23) Doeven, E. H.; Zammit, E. M.; Barbante, G. J.; Hogan, C. F.; Barnett, N. W.; Francis, P. S. *Angew. Chem. Int. Ed.* **2012**, *51*, 4354.
- (24) Doeven, E. H.; Zammit, E. M.; Barbante, G. J.; Francis, P. S.; Barnett, N. W.; Hogan, C. F. *Chem. Sci.* **2013**, *4*, 977.
- (25) Schmittel, M.; Qinghai, S. *Chem. Commun.* **2012**, *48*, 2707.
- (26) Shu, Q.; Birlenbach, L.; Schmittel, M. *Inorg. Chem.* **2012**, *51*, 13123.
- (27) Schmittel, M.; Shu, Q.; Cinar, M. E. *Dalton Trans.* **2012**, *41*, 6064.

- (28) Mauro, M.; Schuermann, K. C.; Pretot, R.; Hafner, A.; Mercandelli, P.; Sironi, A.; De Cola, L. *Angew Chem Int Ed Engl* **2010**, *49*, 1222.
- (29) Nazeeruddin, M. K.; Humphry-Baker, R.; Berner, D.; Rivier, S.; Zuppiroli, L.; Graetzel, M. *J. Am. Chem. Soc.* **2003**, *125*, 8790.
- (30) Schwalbe, M.; Schäfer, B.; Görls, H.; Rau, S.; Tschierlei, S.; Schmitt, M.; Popp, J.; Vaughan, G.; Henry, W.; Vos, J. G. *Eur. J. Inorg. Chem.* **2008**, *21*, 3310.
- (31) Sandroni, M.; Zysman-Colman, E. *Inorg. Chem.* **2013**, submitted.
- (32) Swanick, K. N.; Price, J. T.; Jones, N. D.; Ding, Z. *J. Org. Chem.* **2012**, *77*, 5646.
- (33) Swanick, K. N.; Ladouceur, S.; Zysman-Colman, E.; Ding, Z. *Angew. Chem. Int. Ed.* **2012**, *51*, 11079.
- (34) Bernhard, S.; Barron, J. A.; Houston, P. L.; Abruña, H. D.; Ruglovsky, J. L.; Gao, X.; Malliaras, G. G. *J. Am. Chem. Soc.* **2002**, *124*, 13624.
- (35) Di Censo, D.; Fantacci, S.; De Angelis, F.; Klein, C.; Evans, N.; Kalyanasundaram, K.; Bolink, H. J.; Gratzel, M.; Nazeeruddin, M. K. *Inorg. Chem.* **2008**, *47*, 980.
- (36) Nepomnyashchii, A. B.; Pistner, A. J.; Bard, A. J.; Rosenthal, J. *J. Phys. Chem. C* **2013**, *117*, 5599.
- (37) Lai, R. Y.; Bard, A. J. *J. Phys. Chem. A* **2003**, *107*, 3335.

Chapter 6

6 Sensitive Detection of Au₂₅ Clusters by Electrochemiluminescence

6.1 Interrogating Near-Infrared Electrogenerated Chemiluminescence of Au₂₅(SC₂H₄Ph)₁₈⁺ Clusters[†]

6.1.1 Introduction

The optical properties of nanostructures such as silicon nanocrystals (NCs),¹ carbon quantum dots,²⁻⁴ and gold nanoparticles (NPs),⁵ are attractive to many researchers because of their potential applications.⁶⁻⁹ Among a variety of gold NPs, Au₂₅L₁₈ clusters have been the focus of recent investigations due to their molecule-like, 1.1 nm in diameter, behavior, monodispersed synthesis protocols,^{10,11} and unique optical,¹²⁻¹⁸ electrochemical,^{19,20} and structural portfolio.²¹⁻²³ A Au₂₅ cluster consists of an icosahedral Au₁₃ core and six semi-rings containing -Au-S-Au-S-.^{18,24,25} Murray et al.⁵ and Jin et al.^{26,27} have pioneered studies exploring the various properties of Au₂₅, for instance, observing the difference in photoluminescence (PL) by changing the combination of protecting ligands and electropositivity.²⁸ These studies show that the origins of the clusters' optical properties are dependent on the charge and protecting ligand's functionalities.²⁶ Zhu et al. and Chen et al. demonstrated that Au clusters protected by bovine serum albumin (BSA) can also be utilized in analytical detection methods based on spectroscopic properties of the Au-BSA cluster.^{29,30} Of the stable charged states of Au₂₅L₁₈^z (z = -1, 0 and +1), the -1 form is the most studied, although recent synthetic protocols have allowed the isolation and investigation of the 0 and +1 states. The different charged states induce various properties on the gold clusters that have been probed by ¹H NMR,^{31,32} PL,²⁶ and electron paramagnetic resonance spectroscopy.³³

[†] This work is reprinted with permission from Kalen N. Swanick, Mahdi Hesari, Mark S. Workentin and Zhifeng Ding, *J. Am. Chem. Soc.*, **2012**, *134*, 15205-15208. Copyright **2012** American Chemical Society (ACS). See Appendix V.

Electrogenerated chemiluminescence (ECL) is the process in which electrogenerated radicals form excited species emitting light without the need for an external light source.³⁴⁻³⁶ Advantages of ECL include simultaneous generation of radical cations and anions and the control of electrode potentials that drive light emission processes. ECL has great potential in biological applications such as detection in immunoassays, food and water testing, trace metal determination, sensors, and biomolecules.³⁴⁻³⁶ Our motivation is to explore ECL of various compounds^{3,4,37-39} towards applications in biosensors and bioanalytical chemistry.

Herein, we report the ECL of Au₂₅ in the near-infrared (NIR) region by means of spooling spectroscopy to gain insight into ECL mechanisms during potentiodynamic processes. Previously, ECL studies of Au₂₅ clusters have been conducted in aqueous solution and resulted in very weak ECL only in the visible region.^{29,30} Generating NIR-ECL light is especially important for bioimaging applications, but there are few reports on NIR-ECL^{40,41} and no reports on NIR-ECL of Au clusters. Furthermore, the fact that Au₂₅ clusters have at least three excited states corresponding to their oxidation states gives an unique opportunity to interrogate spectroelectrochemical properties correlating to their structures.^{31-33,42,43} For the first time, NIR-ECL of the Au₂₅ has been observed, and mechanisms for the NIR emission have been explored. The correlation of the Au₂₅⁺ structure, revealed by DFT calculation in literature, the electrochemistry, UV-visible and PL spectroscopy to the ECL emission processes is presented.

6.1.2 Experimental Section

A 2 mm diameter Pt disc inlaid in a glass sheath was used as the working electrode (WE), a coiled Pt wire as the counter electrode (CE), and a coiled Pt wire as the quasi reference electrode (QRE). Ag wire as the QRE was found to react with the Au clusters during electrochemistry processes. After each experiment, the electrochemical potential window was calibrated using ferrocene (Fc) as the internal standard. The redox potential of the ferrocene/ferrocenium (Fc/Fc⁺) couple was taken as 0.424 V vs. SCE.⁴⁴

For annihilation ECL studies, approximately 2 mg of Au₂₅(SC₂H₄Ph)₁₈⁺ clusters was added to the electrochemical cell with a flat Pyrex window at the bottom for

detection of generated ECL, containing 0.1 M TBAP, tetrabutylammonium perchlorate, Fluka, 99 %, supporting electrolyte in anhydrous acetonitrile, 1.5 mL, Sigma-Aldrich, 99.8 %, and anhydrous benzene, 1.5 mL, Sigma-Aldrich, 99.8 %, that was assembled in a glove box. For co-reactant studies, 5.0×10^{-3} M BPO, benzoyl peroxide, Sigma-Aldrich, Luperox® A98, 98 %, was added to the annihilation solution and assembled in a dry box.

For detailed electrochemical workstation and ECL setup information, please refer to our previous publications.³⁷⁻³⁹ In brief, the cyclic voltammetry was conducted on a CHI 610A electrochemical analyzer (CH Instruments, Austin, TX). The experimental parameters for cyclic voltammograms (CVs) are listed here: 0.00 V initial potential in experimental scale, positive or negative initial scan polarity, 0.1 V/s scan rate, 4 sweep segments, 0.001 V sample interval, 2 s quiet time, $1-5 \times 10^{-5}$ A/V sensitivity.

The ECL-voltage curves were obtained using the CHI 610A coupled with a photomultiplier tube, PMT, R928, Hamamatsu, Japan, held at -750 V with a high voltage power supply. The ECL collected by the PMT under the flat Pyrex window at the bottom of the cell was measured as a photocurrent, and transformed to a voltage signal, using a picoammeter/voltage source, Keithley 6487, Cleveland, OH. The potential, current signals from the electrochemical workstation, and the photocurrent signal from the picoammeter were sent simultaneously through a DAQ board, DAQ 6052E, National Instruments, Austin, TX, in a computer. The data acquisition system was controlled from a custom-made LabVIEW program, ECL_PMT610a.vi, National Instruments, Austin, TX. The photosensitivity on the picoammeter was set manually in order to avoid the saturation.

The intensities versus wavelengths, ECL spectra, were recorded by Andor Technology program. Similar to the CV experiments, the samples were scanned between their redox potentials. Since the ECL is in NIR region, ECL spectroscopy was conducted on an Acton 2300i spectrograph with two gratings, 50 l/mm blazed at 600 nm and 300 l/mm blazed at 700 nm, and an Andor iDUS CCD camera, Model DU401-BR-DD-352. Response curves of the two CCD cameras, red for BR-DD and green for BV, are shown in Figure S6.7 in Appendix V.

For the spooling experiments, the NIR set was used and the following parameters were employed for the Andor Technology program under the kinetic parameters option tab: exposure time = 1 s, number of accumulations = 1, kinetic series length = 80 s, matching with the potential scan time, kinetic cycle time = 1, and the spectrometer was centered at 700 nm using the 50 l/mm grating. On the CHI 610A electrochemical analyzer, the initial potential was set to 0.30 V, high potential = 0.30 V, low potential = -2.20 V, sensitivity = $1-5 \times 10^{-5}$ A/V, initial scan polarity = negative, scan rate = 0.1 V/s, sweep segments = 4, sample interval = 0.001 V, quiet time 2 s. Simultaneously, the CHI 610A electrochemical analyzer and the Andor Technology program was run and the CVs and spectra were collected as seen in Figure S6.8 in Appendix V.

6.1.3 Results and Discussion

$\text{Au}_{25}(\text{SC}_2\text{H}_4\text{Ph})_{18}^+\text{C}_6\text{F}_5\text{CO}_2^-$ clusters, referred to as Au_{25}^+ , were synthesized and purified utilizing established procedures reported by Maran et al., see Appendix V.^{31,45} The electrochemistry of dilute 0.67 mg/mL Au_{25}^+ cluster electrolyte solutions was investigated by cyclic voltammetry (CV) and differential pulse voltammetry (DPV), and representative traces are shown in Figure S6.12a,^{37,38} in Appendix V, and Figure 6.1a, respectively. DPV better displays the redox behavior at this low concentration of Au_{25}^+ , required for the ECL study, due to the suppression of the background current.

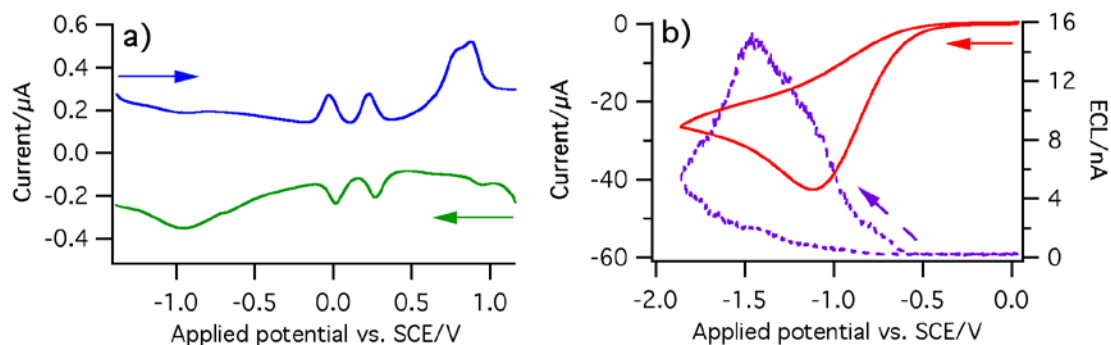
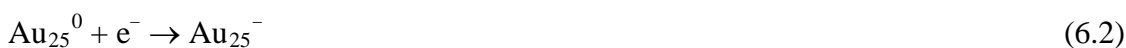


Figure 6.1. a) Differential pulse voltammograms of 0.67 mg/mL Au_{25}^+ clusters in 1:1 benzene:acetonitrile solution, with 0.1 M tetra-*n*-butylammonium perchlorate as

supporting electrolyte. b) cyclic voltammogram and ECL-voltage curve for a Au_{25}^{1+} cluster solution containing with 5 mM benzoyl peroxide.

During cathodic scanning, red curve, Figure 6.1a, of the applied potential, two quasi-reversible reduction waves are observed with half-wave potentials³⁵ of 0.24 and -0.008 V. These correspond to the Au_{25}^{+} clusters being reduced consecutively to Au_{25}^0 and then Au_{25}^{-} , Eqs. 6.1 and 6.2. The energy difference to convert Au_{25}^{+} to Au_{25}^{-} via the two successive electrons is 0.25 eV. Au_{25}^{-} displays similar CV and DPV with a similar energy value to remove two successive electrons.^{26,42} At more negative potentials there is a broad, irreversible reduction wave with an estimated half-wave potential of -0.99 V corresponding to the further reduction of Au_{25}^{-} to Au_{25}^{2-} , Eq. 6.3. This reduction injects an electron into the LUMO, making Au_{25}^{2-} less stable. The anodic scan, blue curve, Figure 6.1a, shows the two well-defined waves corresponding to the reverse of Eqs. 6.1 and 6.2 and, at potentials more positive than 0.51 V, two more irreversible reactions corresponding to the oxidation of Au_{25}^{+} to Au_{25}^{2+} and Au_{25}^{3+} , Eqs. 6.4 and 6.5. These half-wave potentials were roughly estimated to be 0.82 and 0.90 V, respectively. Note that the Au_{25}^{2+} is known to be unstable,⁴⁶ leading to a smaller current for the following oxidation.



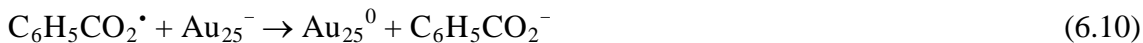
For Au_{25}^{+} the potential difference between the first oxidation, Eq. 6.4, and third reduction, Eq. 6.3, peaks gives an estimation on the HOMO-LUMO energy gap of 1.55 eV after charging correction.⁴² This is a very rough estimation because of the irreversibility of the reduction of Au_{25}^{-} to Au_{25}^{2-} , Eq. 6.3, and possible complexity of

side reactions like its analogues, Au₃₈ and Au₁₄₇ clusters, that shifts the peak potential of the third reduction from the true standard potential.^{47,48} This electrochemical energy gap corresponds well to the observed 1.53 eV optical absorption onset of Au₂₅⁺ in CH₂Cl₂, Figure S6.4 in Appendix V, and is close to that, 1.48 eV, calculated by DFT for Au₂₅⁻, which has paired electrons in all of the three HOMOs.⁴⁹

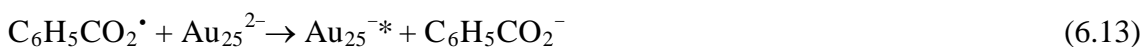
The ECL of the solution above was measured upon continuous alternative electrochemical oxidation and reduction between the potentials defined by Eqs. 6.3 and 6.4. The Au₂₅⁺ solution exhibited very weak ECL *via* this annihilation path,^{35-38,50} Figure S6.12b, where electrogenerated Au₂₅²⁺ and Au₂₅²⁻ react, and Au₂₅^{-*} excited state is produced, emitting light upon relaxation to the ground state, Eqs. 6.6 and 6.7. It is found that Au₂₅²⁻ is more stable than Au₂₅²⁺ since ECL can only be observed in the anodic potential region. No ECL spectrum was obtained due to low intensity caused by the instability of the dication and dianion.⁴⁶



Figure 6.1b presents a CV trace along with the corresponding ECL-voltage curve of a Au₂₅⁺ solution with 5 mM benzoyl peroxide (BPO, (C₆H₅CO)₂O₂), a common cathodic ECL co-reactant.^{36,51-53} ECL has an onset potential of -0.56 V, at which BPO was reduced to BPO^{-•}, Eq. 6.8,^{37,38,51,52} and the Au₂₅⁺ underwent a two-step reduction reaction to Au₂₅⁻ as in Eqs. 6.1 and 6.2. In the diffusion layer containing the above two species, a strong oxidizing intermediate radical C₆H₅CO₂[•] was generated *via* decomposition of BPO^{-•}, Eq. 6.9, which accepts one electron from Au₂₅⁻ and transformed it to Au₂₅⁰, Eq. 6.10. The Au₂₅^{-*} excited state was generated by transferring one electron from BPO^{-•} to the LUMO of Au₂₅⁰, Eq. 6.11,³⁸ which emitted light upon relaxation to the ground state, Eq. 6.7. The ECL-voltage curve shows a slight maximum at -0.79 V. This ECL mechanism is very similar to that of a molecular luminophore with BPO as a co-reactant prior to reducing the luminophore.³⁸



The ECL intensity in the BPO co-reactant system increased dramatically when the applied potential was scanned to more negative potentials. As described above, Au_{25}^{2-} is the dominant species in the vicinity of the electrode biased more negative than -0.98 V. Au_{25}^{-*} was generated in this potential region by the reaction of Au_{25}^{2-} either with Au_{25}^0 , Eq. 6.12, or $\text{C}_6\text{H}_5\text{CO}_2^{\bullet}$ in the diffusion layer, Eq. 6.13, or with Au_{25}^+ in the bulk solution, Eq. 6.14. ECL intensity reached the highest at -1.45 V.



The strong oxidizing intermediate radical, $\text{C}_6\text{H}_5\text{CO}_2^{\bullet}$, may persist in solution long enough to combine with the reduced forms of the clusters, also generating the excited species in solution. While the BPO co-reactant systems is complicated,⁵³ the presence of the multiple oxidation states of the cluster adds even more complexity and additional ECL mechanisms can be proposed based on the possible combinations. It is noteworthy that no ECL was observed in a BPO solution containing no Au_{25}^0 , Figure S6.13 in Appendix V, in the same potential window.

The increased ECL intensity using a co-reactant allowed the acquisition of ECL spectra. Figure 6.2a presents ECL spectra acquired on solutions containing Au_{25}^+ clusters with BPO with a time interval of 1 s during potentiodynamic scanning from 0.04 to -1.86 V and back to 0.04 V. Figure S6.8a shows the voltammogram at a scan rate of 0.1 V/s during this spectroelectrochemical measurement, which is very similar to that in Figure

6.1b. The spectroelectrochemistry was carried out by means of our newly developed spooling spectroscopy for ECL. Briefly, the ECL cell was placed into a holder attached to an Acton spectrograph with an Andor NIR CCD camera cooled to $-75\text{ }^{\circ}\text{C}$, and ECL processes were driven by the potential scanning at 0.1 V/s in the range between 0.04 and -1.86 V , with a spectrum recorded every 100 mV , which is equivalent to 1 s .

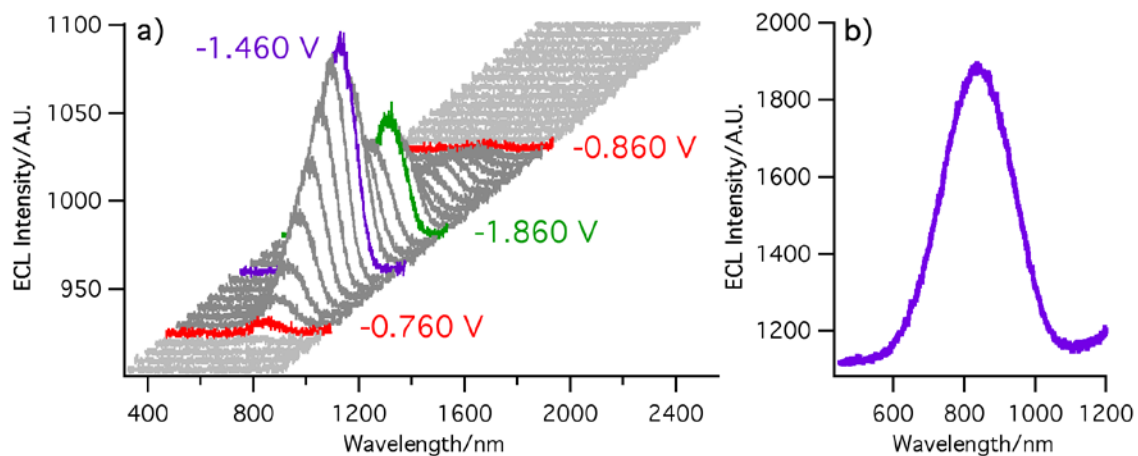


Figure 6.2. a) Spooled ECL spectra of Au_{25}^{+} clusters with BPO during one cycle of the applied potential from 0.04 to -1.86 V then back to 0.04 V . Each spectrum was acquired for 1 s using an iDUS NIR CCD camera cooled to $-75\text{ }^{\circ}\text{C}$. b) A typical accumulated ECL spectrum of the same co-reactant solution collected over 80 s , two cycles of potential scanning between 0.04 to -1.86 V at a scan rate of 0.1 V/s .

The spectra in Figure 6.2a track the evolution and devolution of the ECL emission and gives insight into the ECL mechanisms. As was observed in the ECL-voltage curve shown in Figure 6.1b, a pronounced ECL spectrum, Figure 6.2a, red spectrum, was obtained at -0.76 V on the forward scan. The peak wavelength was determined to be 893 nm , 1.39 eV , very close to the HOMO-LUMO energy gap of Au_{25}^{+} estimated above by electrochemistry and UV-visible spectroscopy and calculated for Au_{25}^{-} by DFT.⁴⁹ The ECL intensity increased as the potential was made more negative up to -1.46 V , while the ECL peak wavelength remained constant at 893 nm , purple in Figure 6.2a. As the applied potential becomes even more negative, the ECL peak

intensity decreased due to the concentration depletion of the clusters as well as BPO. This is illustrated in Figure 6.2a between the -1.46 V, purple spectrum, and -1.86 V, green spectrum. On the reverse potential scan from -1.86 to 0.04 V, the ECL spectra devolve. Because the ECL peak wavelength remains constant at 893 nm throughout the potential window, this is indicative of only one excited state being involved. This is further exemplified in Figure S9 where the spectra over two potential cycles are shown and the ECL peak wavelength remains the same. The above observations support very well the proposed ECL mechanisms as expressed by Eqs. 6.6 to 6.12 and agree with the ECL-voltage curve in Figure 6.1b. Furthermore, an ECL spectrum accumulated for 80 s was also collected by scanning the potential between 0.04 to -1.86 V at a scan rate of 0.1 V/s. The acquired spectrum displays a maximum wavelength of 893 nm as well, Figure 6.2b, which confirms that only one excited state is involved in the ECL process.

It is informative to compare the ECL spectra, Figure 6.2, with PL spectra measured on a solution of Au_{25}^- , Figure 6.3, in order to confirm the identity of the excited state involved in the ECL processes. The PL spectra were measured on the same spectrograph and CCD camera set used for the ECL measurements to exclude any ambiguities about the PL spectrum of the clusters measured previously on different instruments/detectors.^{26,27,28} Our confocal setup covers the entire spectral range, 630-1180 nm, of interest and a peak response quantum efficiency of 95 % at 800 nm, see Appendix V for the instrument specification.

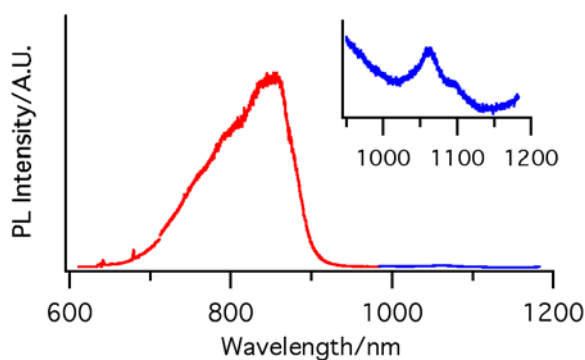


Figure 6.3. Photoluminescence of a Au_{25}^- 1:1 benzene/acetonitrile solution using an iDus 401 CCD camera between 633 and 1200 nm upon excitation at 633 nm.

Figure 6.3 depicts a typical PL spectrum of the Au_{25}^- cluster solution, showing two luminescence shoulders at 719, 1.72 eV, and 820 nm, 1.51 eV, as reported by the Jin group^{26,27} and similar to the Au cluster investigated by El-Sayed and Whetten.⁵⁴ Also observed was a strong peak at 857 nm, 1.45 eV, as well as a weak one at 1080 nm, 1.15 eV, inset in Figure 6.3, as described by the Murray group.²⁸ The only difference between our results and those reported earlier is in the intensity pattern due to differences in the detector response efficiencies in the different setups being compared, Figure S6.9 to S6.11 in Appendix V. The most interesting luminescence peak is the strongest one at 857 nm, which can be assigned to the excited-state luminescence emission with energy higher than that from a relaxed excited state across the HOMO-LUMO gap at 1.34 eV.⁵⁴ The other two shoulders may be the excited states populated from the electron promotion from HOMO-1 to LUMO or HOMO to LUMO+1. The weak luminescence peak can be assigned to semi-ring states, namely phosphorescence emission due to the transition from a triplet excited state to the ground state, as in the case of Au clusters, reported by Morran and Murray with femtosecond spectroscopy¹⁵ and by the Murray group NIR PL spectroscopy,^{42,54}

Our spooling Au_{25}^+ ECL spectra clearly identify the excited state in the whole ECL process to be Au_{25}^{*-} across the HOMO-LUMO gap, giving an emission peaked at 893 nm, 1.39 eV. This agrees very well with our elucidated ECL mechanisms above. From a thermodynamics point of view, the excited state in ECL was generated directly from radical reactions without the nonradioactive relaxation of excited states in PL processes. Our ECL and PL emission are in agreement with the observations from PL spectra of Au_{25}^- solution. Based on the atomic contributions to the HOMOs that are essentially superatom *p* orbitals and LUMOs that comprise mainly *d* orbitals from the DFT calculation⁴⁹ and magnetic circular dichroism spectroscopy,⁴³ the ECL emission observed is likely due to the radioactive electronic relaxation from the LUMOs to HOMOs.

The above observation on ECL of Au_{25} clusters is very different from that on ECL of silicon NCs, which depended more sensitively on surface chemistry and the presence of rich surface states,¹ as previously reported by Ding et al. While thiophenolate

ligands having more electron-withdrawing substituents enhance the PL of semi-ring states in Au_{25}^- clusters,²⁸ ECL is favored in the electronic relaxation across the HOMO-LUMO gap. This is probably due to the activity of the cluster icosahedral Au_{13} core incompletely covered by protecting ligand complexes or six staple-shaped motifs (-S-Au-S-Au-S-).^{33,55} It is plausible that semi-ring state emission observed in PL plays a minor role in ECL, possibly because its intensity is not as high as that of surface states in larger NCs.

6.1.4 Conclusions

In summary, this work unambiguously demonstrates that NIR-ECL of Au_{25} can be observed in annihilation of electrogenerated Au_{25}^{2+} and Au_{25}^{2-} species and enhanced in the path of co-reactant system with BPO. The light emission was explicitly elucidated as being due to the electronic relaxation of the Au_{25}^{-*} excited state to the ground state across HOMO-LUMO gap by means of electrochemistry, PL spectroscopy, and our newly developed spooling spectroscopy during the ECL evolution and devolution.

6.1.5 References

- (1) Ding, Z.; Quinn, B. M.; Haram, S. K.; Pell, L. E.; Korgel, B. A.; Bard, A. J. *Science* **2002**, *296*, 1293.
- (2) Bourlinos, A. B.; Zbořil, R.; Petr, J.; Bakandritsos, A.; Krysmann, M.; Giannelis, E. P. *Chem. Mater.* **2011**, *24*, 6.
- (3) Zhou, J.; Booker, C.; Li, R.; Zhou, X.; Sham, T.-K.; Sun, X.; Ding, Z. *J. Am. Chem. Soc.* **2007**, *129*, 744.
- (4) Zhou, J.; Booker, C.; Li, R.; Sun, X.; Sham, T.-K.; Ding, Z. *Chem. Phys. Lett.* **2010**, *493*, 296.
- (5) Wang, G.; Huang, T.; Murray, R. W.; Menard, L.; Nuzzo, R. G. *J. Am. Chem. Soc.* **2005**, *127*, 812.
- (6) Wu, Z.; Wang, M.; Yang, J.; Zheng, X.; Cai, W.; Meng, G.; Qian, H.; Wang, H.; Jin, R. *Small* **2012**, *8*, 2028.
- (7) Ghosh Chaudhuri, R.; Paria, S. *Chem. Rev.* **2012**, *112*, 2373.
- (8) Lu, Y.; Chen, W. *Chem. Soc. Rev.* **2012**, *41*, 3594.

- (9) Murray, R. W. *Chem. Rev.* **2008**, *108*, 2688.
- (10) Wu, Z.; Suhan, J.; Jin, R. *J. Mater. Chem.* **2009**, *19*, 622.
- (11) Dharmaratne, A. C.; Krick, T.; Dass, A. *J. Am. Chem. Soc.* **2009**, *131*, 13604.
- (12) Devadas, M. S.; Kim, J.; Sinn, E.; Lee, D.; Goodson, T.; Ramakrishna, G. *J. Phys. Chem. C* **2010**, *114*, 22417.
- (13) Sakanaga, I.; Inada, M.; Saitoh, T.; Kawasaki, H.; Iwasaki, Y.; Yamada, T.; Umezumi, I.; Sugimura, A. *Appl. Phys. Express* **2011**, *4*, 095001/1.
- (14) Devadas, M. S.; Bairu, S.; Qian, H.; Sinn, E.; Jin, R.; Ramakrishna, G. *J. Phys. Chem. Lett.* **2011**, *2*, 2752.
- (15) Miller, S. A.; Womick, J. M.; Parker, J. F.; Murray, R. W.; Moran, A. M. *J. Phys. Chem. C* **2009**, *113*, 9440.
- (16) Qian, H.; Y. Sfeir, M.; Jin, R. *J. Phys. Chem. C* **2010**, *114*, 19935.
- (17) Parker, J. F.; Fields-Zinna, C. A.; Murray, R. W. *Acc. Chem. Res.* **2010**, *43*, 1289.
- (18) Zhu, M.; Aikens, C. M.; Hollander, F. J.; Schatz, G. C.; Jin, R. *J. Am. Chem. Soc.* **2008**, *130*, 5883.
- (19) Garcia-Raya, D.; Madueno, R.; Blazquez, M.; Pineda, T. *J. Phys. Chem. C* **2009**, *113*, 8756.
- (20) Kumar, S. S.; Kwak, K.; Lee, D. *Electroanalysis* **2011**, *23*, 2116.
- (21) MacDonald, M. A.; Chevrier, D. M.; Zhang, P.; Qian, H.; Jin, R. *J. Phys. Chem. C* **2011**, *115*, 15282.
- (22) Perera, N. V.; Isley, W.; Maran, F.; Gascon, J. A. *J. Phys. Chem. C* **2010**, *114*, 16043.
- (23) Akola, J.; Kacprzak, K. A.; Lopez-Acevedo, O.; Walter, M.; Gronbeck, H.; Hakkinen, H. *J. Phys. Chem. C* **2010**, *114*, 15986.
- (24) Zhu, M.; Eckenhoff, W. T.; Pintauer, T.; Jin, R. *J. Phys. Chem. C* **2008**, *112*, 14221.
- (25) Heaven, M. W.; Dass, A.; White, P. S.; Holt, K. M.; Murray, R. W. *J. Am. Chem. Soc.* **2008**, *130*, 3754.
- (26) Wu, Z.; Jin, R. *Nano Lett.* **2010**, *10*, 2568.
- (27) Qian, H.; Zhu, M.; Wu, Z.; Jin, R. *Acc. Chem. Res.* **2012**, DOI: 10.1021/ar200331z.

- (28) Wang, G.; Guo, R.; Kalyuzhny, G.; Choi, J.-P.; Murray, R. W. *J. Phys. Chem. B* **2006**, *110*, 20282.
- (29) Fang, Y.-M.; Song, J.; Li, J.; Wang, Y.-W.; Yang, H.-H.; Sun, J.-J.; Chen, G.-N. *Chem. Commun.* **2011**, *47*, 2369.
- (30) Li, L.; Liu, H.; Shen, Y.; Zhang, J.; Zhu, J.-J. *Anal. Chem.* **2011**, *83*, 661.
- (31) Venzo, A.; Antonello, S.; Gascon, J. A.; Guryanov, I.; Leapman, R. D.; Perera, N. V.; Sousa, A.; Zamuner, M.; Zanella, A.; Maran, F. *Anal. Chem.* **2011**, *83*, 6355.
- (32) Liu, Z.; Zhu, M.; Meng, X.; Xu, G.; Jin, R. *J. Phys. Chem. Lett.* **2011**, *2*, 2104.
- (33) Zhu, M.; Aikens, C. M.; Hendrich, M. P.; Gupta, R.; Qian, H.; Schatz, G. C.; Jin, R. *J. Am. Chem. Soc.* **2009**, *131*, 2490.
- (34) Miao, W. *Chem. Rev.* **2008**, *108*, 2506.
- (35) Bard, A. J.; Faulkner, L. R. *Electrochemical Methods, Fundamentals and Applications*; 2nd ed.; Wiley: New York, **2001**.
- (36) Bard, A. J. *Electrogenerated Chemiluminescence*; Marcel Dekker: New York, **2004**.
- (37) Swanick, K. N.; Dodd, D. W.; Price, J. T.; Brazeau, A. L.; Jones, N. D.; Hudson, R. H. E.; Ding, Z. *Phys. Chem. Chem. Phys.* **2011**, *13*, 17405.
- (38) Swanick, K. N.; Ladouceur, S.; Zysman-Colman, E.; Ding, Z. *Chem. Commun.* **2012**, *48*, 3179.
- (39) Booker, C.; Wang, X.; Haroun, S.; Zhou, J.; Jennings, M.; Pagenkopf, B. L.; Ding, Z. *Angew. Chem. Int. Ed.* **2008**, *47*, 7731.
- (40) Liang, G.; Shen, L.; Zou, G.; Zhang, X. *Chem. Eur. J.* **2011**, *17*, 10213.
- (41) Lee, S. K.; Richter, M. M.; Streckowski, L.; Bard, A. J. *Anal. Chem.* **1997**, *69*, 4126.
- (42) Lee, D.; Donkers, R. L.; Wang, G.; Harper, A. S.; Murray, R. W. *J. Am. Chem. Soc.* **2004**, *126*, 6193.
- (43) Yao, H. *J. Phys. Chem. Lett.* **2012**, *3*, 1701.
- (44) Cao, W.; Zhang, X.; Bard, A. J. *J. Electroanal. Chem.* **2004**, *566*, 409.
- (45) Antonello, S.; Hesari, M.; Polo, F.; Maran, F. *Nanoscale* **2012**, *4*, 5333.
- (46) Antonello, S.; Holm, A. H.; Instuli, E.; Maran, F. *J. Am. Chem. Soc.* **2007**, *129*, 9836.

- (47) Quinn, B. M.; Kontturi, K. *J. Am. Chem. Soc.* **2004**, *126*, 7168.
- (48) Toikkanen, O.; Ruiz, V.; Ronnholm, G.; Kalkkinen, N.; Liljeroth, P.; Quinn, B. M. *J. Am. Chem. Soc.* **2008**, *130*, 11049.
- (49) Aikens, C. M. *J. Phys. Chem. C* **2008**, *112*, 19797.
- (50) Bard, A. J.; Faulkner, L. R. In *Electroanalytical Chemistry*; Bard, A. J., Ed.; Dekker: New York, **1977**; Vol. 10, p 1.
- (51) Choi, J.-P.; Wong, K.-T.; Chen, Y.-M.; Yu, J.-K.; Chou, P.-T.; Bard, A. J. *J. Phys. Chem. B* **2003**, *107*, 14407.
- (52) Lai, R. Y.; Fleming, J. J.; Merner, B. L.; Vermeij, R. J.; Bodwell, G. J.; Bard, A. J. *J. Phys. Chem. A* **2004**, *108*, 376.
- (53) Rosenthal, J.; Nepomnyashchii, A. B.; Kozhukh, J.; Bard, A. J.; Lippard, S. J. *J. Phys. Chem. C* **2011**, *115*, 17175.
- (54) Link, S.; Beeby, A.; FitzGerald, S.; El-Sayed, M. A.; Schaaff, T. G.; Whetten, R. L. *J. Phys. Chem. B* **2002**, *106*, 3410.
- (55) Akola, J.; Walter, M.; Whetten, R. L.; Häkkinen, H.; Grönbeck, H. *J. Am. Chem. Soc.* **2008**, *130*, 3756.

6.2 Spooling ECL Spectroscopy of $\text{Au}_{25}\text{L}_{18}^0$ in the presence of BPO

6.2.1 Introduction

The Au_{25}^0 , has one singly-occupied electron in one of the three semi-degenerated HOMO orbitals.³ While we have reported that $\text{Au}_{25}(\text{SC}_2\text{H}_4\text{Ph})_{18}^+$ cluster is a strong NIR-ECL emitter¹, see Chapter 6.1, its counterpart, $\text{Au}_{25}(\text{SC}_2\text{H}_4\text{Ph})_{18}^0$, Au_{25}^0 is anticipated to form several excited states based on its electronic configuration. Benzoyl peroxide (BPO) is a popular co-reactant in organic solvents. We employed benzoyl peroxide (BPO)¹ as a co-reactant which is suitable to react with electrogenerated precursors of Au clusters, even in a small potential window, in the course of electrochemical oxidative and reductive processes². Au_{25}^0 then eventually gains or losses electron(s) at the HOMO or LUMO orbitals^{4,5}. Thus, in the course of the ECL process it would be interesting to elucidate and control light generation of the Au_{25}^0 clusters in the presence of BPO, as a strong oxidizing agent. The HOMO-LUMO energy gap in Au_{25} can be correlated to the energy difference between the excited and ground states tend to near-IR emission. In this section, the focus will be on the Au_{25}^0 clusters containing two concentrations of BPO as the co-reactant.

6.2.2 Experimental Section

All experiments were conducted using a 2 mm diameter Pt disc inlaid in a glass tube as the working electrode (WE). The counter electrode (CE) consisted of a coiled Pt wire and the quasi reference electrode (RE) was another coiled Pt wire. After every experiment, the electrochemical potential window was calibrated using ferrocene (Fc) as the internal standard, having a redox potential of the ferrocene/ferrocenium (Fc/Fc^+) couple taken as 0.424 V vs. SCE.⁶

Annihilation ECL studies contained approximately 2 mg of Au_{25}^0 clusters and 0.1 M TBAP, tetrabutylammonium perchlorate, supporting electrolyte to the electrochemical cell with 1.5 mL anhydrous acetonitrile, and anhydrous 1.5 mL benzene, that was

assembled in a glove box. 5.0×10^{-3} M BPO, benzoyl peroxide, was added to the electrochemical cell for co-reactant ECL studies and assembled in a glove box.

Please refer to our previous publications for detailed electrochemical workstation and ECL setup information.^{1,7,8} In brief, the cyclic voltammetry was conducted on a CHI 610A electrochemical analyzer (CH Instruments, Austin, TX). The experimental parameters for cyclic voltammograms (CVs) are listed here: 0.00 V initial potential in experimental scale, positive or negative initial scan polarity, 0.1 V/s scan rate, 4 sweep segments, 0.001 V sample interval, 2 s quiet time, $1-5 \times 10^{-5}$ A/V sensitivity (for annihilation studies) and 1×10^{-5} to 1×10^{-4} A/V sensitivity (for co-reactant studies).

The ECL spectra, intensities versus wavelengths, were recorded by the Andor Technology program. The samples were scanned between their redox potentials, similar to the CV experiments. ECL spectroscopy was conducted on an Acton 2300i spectrograph with two gratings, 50 l/mm blazed at 600 nm and 300 l/mm blazed at 700 nm, and an Andor iDUS CCD camera, Model DU401-BR-DD-352 because the ECL is in NIR region.

For the spooling experiments, the NIR set was used and the following parameters were employed for the Andor Technology program under the kinetic parameters option tab: a) for 0.005 M BPO concentration of Au250: exposure time = 1 s, number of accumulations = 1, kinetic series length = 80 s, matching with the potential scan time, kinetic cycle time = 1, and the spectrometer was centered at 700 nm using the 50 l/mm grating. On the CHI 610A electrochemical analyzer, the initial potential was set to -0.22 V, high potential = 0.15 V, low potential = -2.10 V, sensitivity = 1×10^{-5} A/V, initial scan polarity = negative, scan rate = 0.1 V/s, sweep segments = 4, sample interval = 0.001 V, quiet time 2 s. Simultaneously, the CHI 610A electrochemical analyzer and the Andor Technology program was run and the CVs and spectra were collected. b) for 0.05 M BPO concentration of Au250: exposure time = 1 s, number of accumulations = 1, kinetic series length = 80 s, matching with the potential scan time, kinetic cycle time = 1, and the spectrometer was centered at 700 nm using the 50 l/mm grating. On the CHI 610A electrochemical analyzer, the initial potential was set to -0.22 V, high potential =

0.15 V, low potential = -2.50 V, sensitivity = 1×10^{-4} A/V, initial scan polarity = negative, scan rate = 0.1 V/s, sweep segments = 4, sample interval = 0.001 V, quiet time 2 s. Simultaneously, the CHI 610A electrochemical analyzer and the Andor Technology program was run and the CVs and spectra were collected.

6.2.3 Results and Discussion

ECL via Annihilation. Au_{25}^0 clusters were synthesized, purified and characterized following room temperature monodispersed synthesis procedure^{4,9}. The electrochemistry of 0.1 mM Au_{25}^0 in benzene:acetonitrile (1:1), containing 0.1 M TBAP reveals four distinct peaks, Figure 6.4.

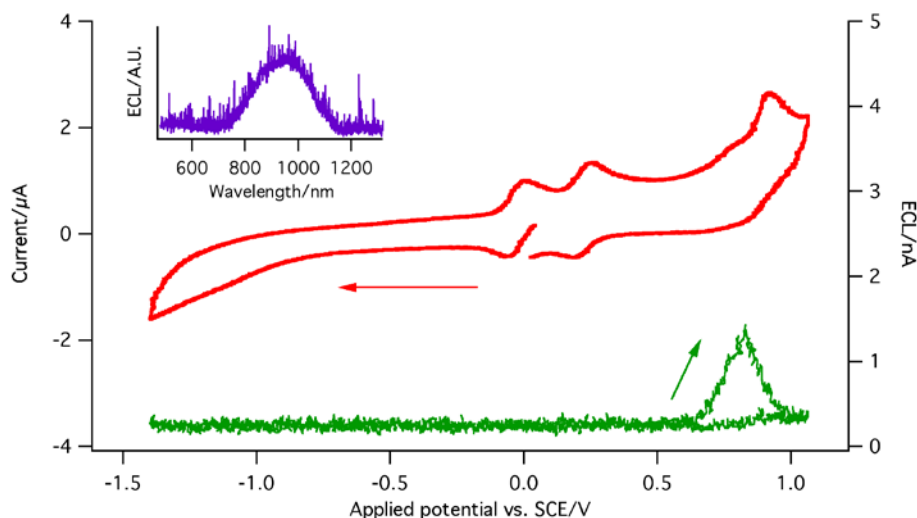


Figure 6.4. Typical annihilation ECL-voltage curve of 0.1mM Au_{25}^0 in benzene:acetonitrile mixture containing 0.1 M TBAP, scan rate: 0.1 V/s. Inset: accumulated spectrum, $T = 300$ s, in the course of ECL experiment recorded with a NIR CCD camera.

In a typical cyclic voltammogram (CV), the applied potential was initiated from 0.05 V at which a zero current was obtained indicating no oxidation or reduction process occurred^{4,10}. On scanning the potential to the negative, Au_{25}^0 gains one electron and forms Au_{25}^- at -0.04 V, Eq. 6.18, which is further reduced at -1.15 V to form Au_{25}^{2-} , Eq. 6.19. When scanning the potential to positive, Au_{25}^0 losses one electron and forms Au_{25}^+

at 0.18 V, Eq. 6.15, which is further oxidized at 0.89 V to form Au_{25}^{2+} , Eq. 6.16. The peak current height is suggested that at close potential further oxidation can happen to form Au_{25}^{3+} , Eq. 6.17.



ECL of Au_{25}^+ in the annihilation path, scanning potential between highest, Au_{25}^{2+} , and lowest, Au_{25}^{2-} , charge states, was observed during the potential scanning between $\text{Au}_{25}^{2-}/\text{Au}_{25}^{2+}$ redox peaks, Eqs. 6.16 and 6.18. The above electrochemistry agrees well with that by Maran et al.⁴

Figure 6.4 displays an ECL-voltage curve of Au_{25}^0 and its corresponding ECL spectra in the course of annihilation. The onset of the ECL-voltage curve reveals light emission at 0.57 V at which the Au_{25}^+ starts to oxidize to Au_{25}^{2+} , Eq. 6.16. The electrogenerated Au_{25}^{2+} reacts with Au_{25}^{2-} , which presents in the double layer in the course of scanning, acting as a reducing agent in the vicinity of the working electrode. An electron transfer happens from a HUMO orbital of Au_{25}^{2-} to one of the HUMO orbitals of Au_{25}^{2+} resulting in the formation of the excited state, Au_{25}^{-*} , Eq. 6.20. The excited will relax back to its ground state and emit light, $h\nu_1$, at 940 nm, Eq. 6.21.



ECL via Co-reactant Route. Generation of ECL Au_{25}^0 clusters using BPO as the co-reactant⁴ was also performed., Figure 6.5. The concentration of BPO was varied, 5 mM and 50 mM, to study radical concentration effect on the Au_{25}^0 ECL. First 5 mM

BPO was used, Figure 6.5. Initially, the potential was scanned towards negative potential, reducing Au_{25}^0 to Au_{25}^- , Eq. 6.18, and BPO was reduced at -1.12 V vs. SCE to its radical anion, $\text{BPO}^{\bullet-}$, Eq. 6.22. The $\text{BPO}^{\bullet-}$ radical then rapidly decomposed and generated the benzoate radical, $\text{C}_6\text{H}_5\text{CO}_2^{\bullet}$, Eq. 6.23, a strong oxidizing species, and benzoate anion, $\text{C}_6\text{H}_5\text{CO}_2^-$.

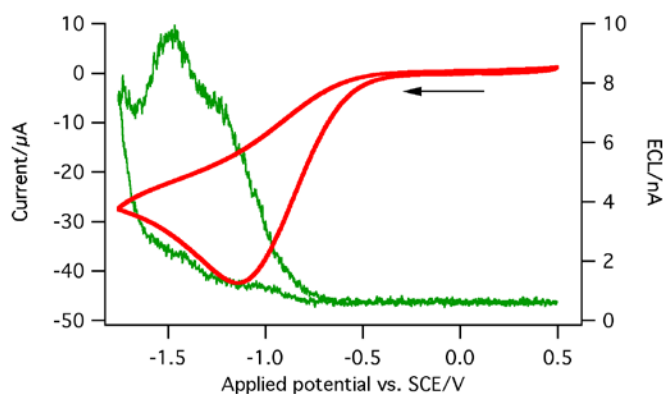
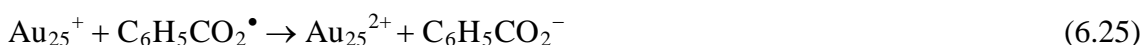


Figure 6.5. CV (in red) with ECL voltage-curve (in green) between 0.50 and -1.75 V of Au_{25}^0 with 0.005 M BPO in ACN:Bz (1:1) with 0.1 M TBAP supporting electrolyte, scan rate of 0.1 V/s.

The initial onset of ECL occurred at -0.80 V, Figure 6.6. Here, Au_{25}^0 was reduced to Au_{25}^- . From the bulk solution, the benzoate radical can oxidize Au_{25}^0 to Au_{25}^+ , Eq. 6.24, and once more to Au_{25}^{2+} , Eq. 6.25. Then the $\text{BPO}^{\bullet-}$ radical can donate an electron to Au_{25}^{2+} and generate the Au_{25}^{+*} excited state species, Eq. 6.26. The Au_{25}^{+*} will relax back to its ground state and emit at 880 nm, $h\nu_2$, Figure 6.6b, Eq. 6.27, a different wavelength and mechanism than in annihilation, Eq. 6.21.



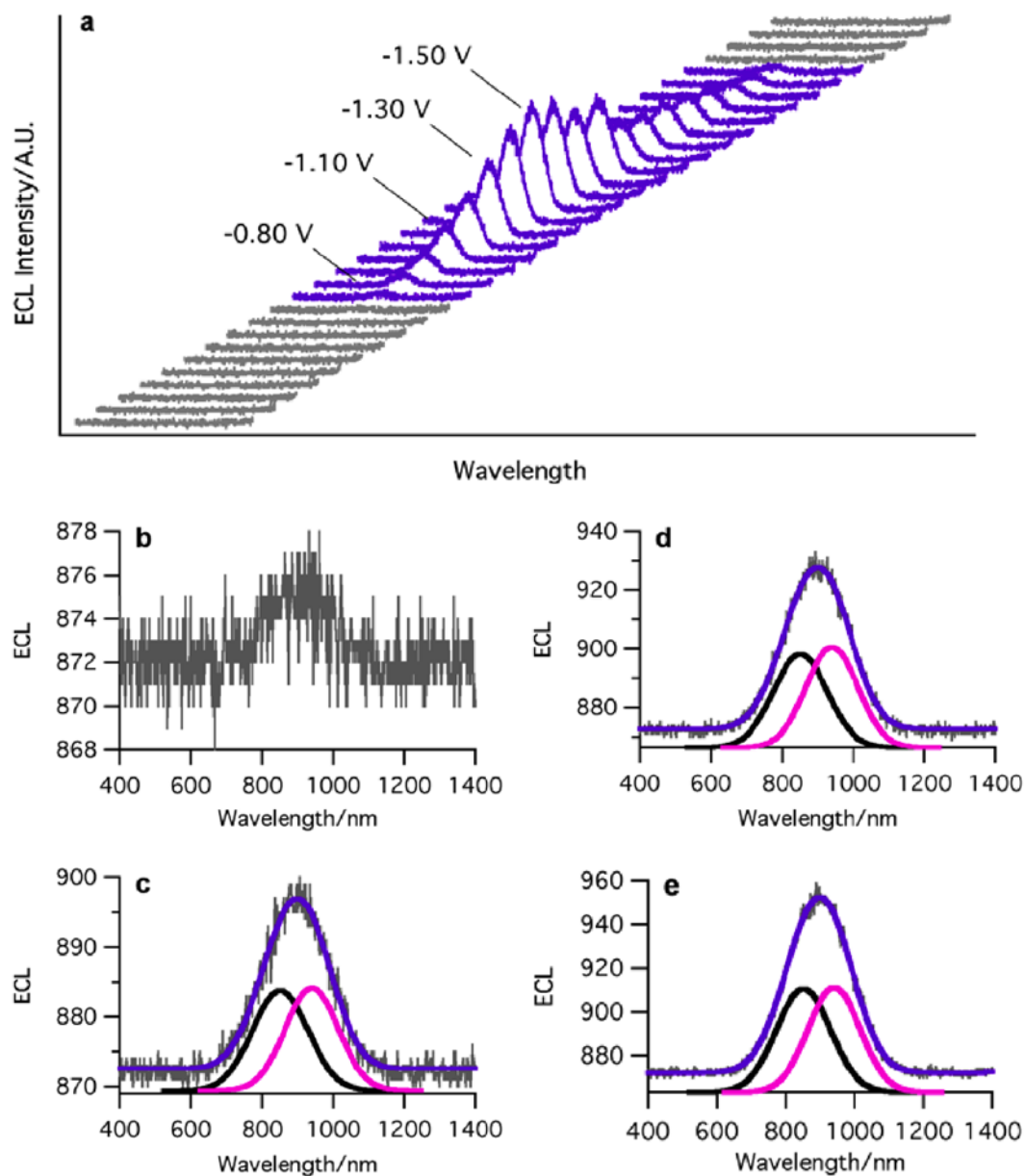


Figure 6.6. a) ECL spooling of Au_{25}^0 with 0.005 M BPO in ACN:Bz (1:1) with 0.1 M TBAP supporting electrolyte, scan rate of 0.1 V/s, between 0.50 and -1.75 V for 90 s, spectra at b) -0.80 V, c) -1.10 V, d) -1.30 V, e) -1.50 V, these spectra were curve-fitted to 871 nm (black) and 960 nm (pink), the average fit is shown in purple.

Scanning more negative to -1.75 V, increased the amount of ECL observed, as seen in the accumulated spectrum when the potential was cycled between 0.50 V and -1.75 V for 90 s, Figure 6.7. When the potential reached -1.50 V, it generated the greatest ECL intensity. Initially it appears that one excited species was generated at 920 nm, Figure 6.7, however from our new spooling technique, Figure 6.6, we were able to curve-fit each spectra recorded to observe the evolution of two different excited species, fixed at 871 nm and 960 nm.

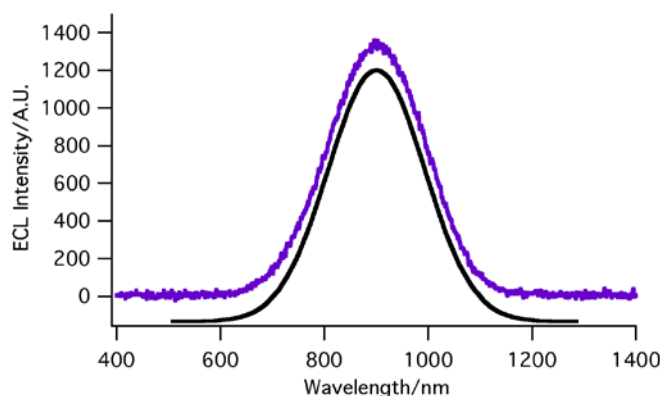
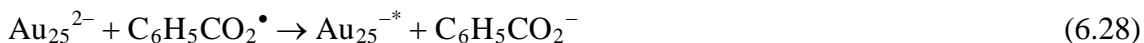


Figure 6.7. Accumulated spectrum between 0.50 and -1.75 V for 90 s of Au_{25}^0 with 0.005 M BPO in ACN:Bz (1:1) with 0.1 M TBAP supporting electrolyte, scan rate of 0.1 V/s. Curve-fitted to one peak at 920 nm.

At -1.50 V Au_{25}^- begins to reduce to Au_{25}^{2-} , Eq. 6.19. The Au_{25}^{2-} will react with $\text{C}_6\text{H}_5\text{CO}_2^\bullet$ to generate Au_{25}^{-*} excited species, Eq. 6.28, with an emission, $h\nu_1$, Eq. 6.21, at 960 nm, Figure 6.6e.



By curve-fitting the ECL peaks, it was discovered that the two ECL mechanisms were competing with each other, depending on the applied potential. Light emission at 880 nm follows Eq. 6.26 at less negative potential with low $\text{C}_6\text{H}_5\text{CO}_2^\bullet$, while ECL at 960 nm dominates at highly negative potential at which Au_{25}^{2-} generates the Au_{25}^{-*} excited species, Eq. 6.28.

When increasing the concentration of BPO to 50 mM, Figure 6.8, the potential, was initially at 0.20 V then scanned negative, with the initial onset of ECL observed at -0.90 V, Figure 6.9b. Here, the Au_{25}^0 species from the bulk reacts with much higher $\text{C}_6\text{H}_5\text{CO}_2^\bullet$ to generate the oxidized species Au_{25}^+ , Eq. 6.24, and $\text{C}_6\text{H}_5\text{CO}_2^\bullet$ can generate the Au_{25}^{2+} species, Eq. 6.25 as previously mentioned. An electron transfer between the $\text{BPO}^{\bullet-}$ radical and Au_{25}^{2+} species generates the Au_{25}^{+*} excited species, Eq. 6.26. The Au_{25}^{+*} excited species emits light at approximately 880 nm, Eq. 6.27, Figure 6.9b.

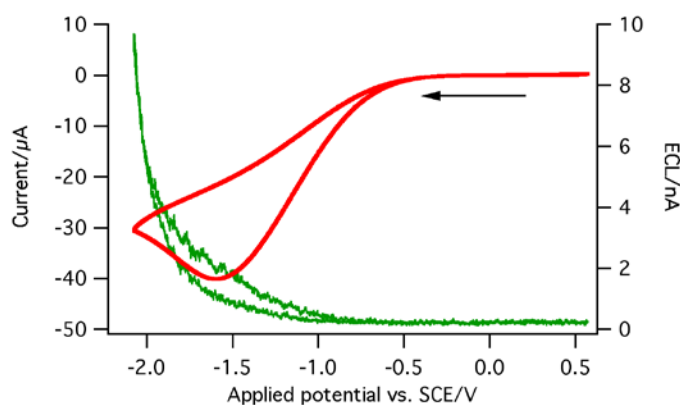


Figure 6.8. CV (in red) with ECL voltage-curve (in green) between 0.57 and -2.08 V of Au_{25}^0 with 0.050 M BPO in ACN:Bz (1:1) with 0.1 M TBAP supporting electrolyte, scan rate of 0.1 V/s.

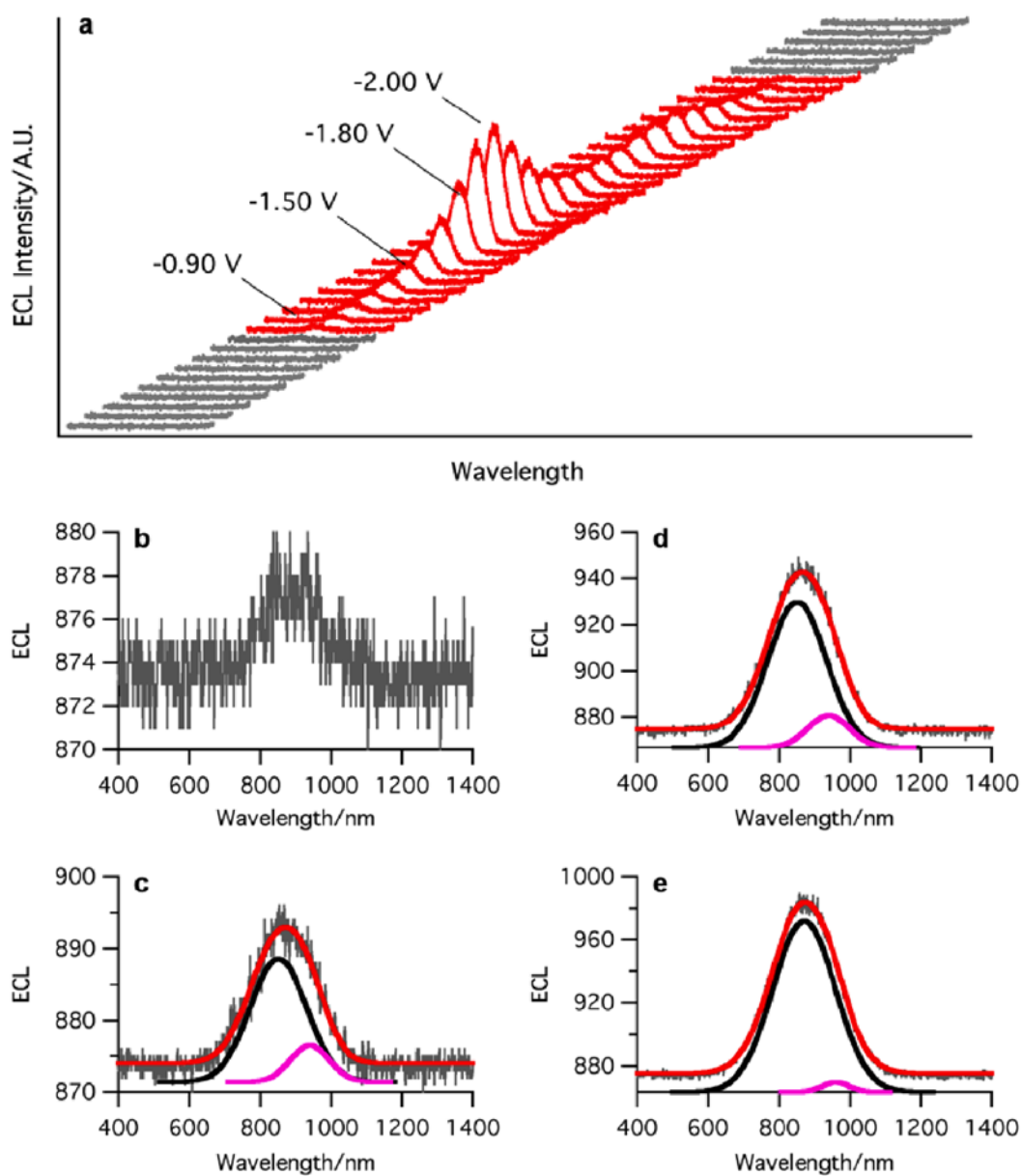


Figure 6.9. ECL spooling of Au_{25}^0 with 0.050 M BPO in ACN:Bz (1:1) with 0.1 M TBAP supporting electrolyte, scan rate of 0.1 V/s, between 0.57 and -2.08 V for 106 s, spectra at b) -0.90 V, c) -1.50 V, d) -1.80 V, e) -2.00 V, these spectra were curve-fitted to 871 nm (black) and 960 nm (pink), the average fit is shown in red.

Accumulating the spectrum between 0.57 and -2.08 V for 106 s, resulted in an ECL maximum at 859 nm, Figure 6.10. From the spooling data, Figure 6.9, we curve-fit these spectra to two peaks and saw the growth of the 871 nm peak when the concentration of BPO increased to 50 mM while the peak at 960 nm changes in intensity.

The mechanism for ECL generation follows the same co-reactant pathways as the 5 mM case, Eqs. 6.26 and 6.28. With a higher concentration of BPO in solution, a greater amount of $\text{C}_6\text{H}_5\text{CO}_2^\bullet$ was generated, Eq. 6.23, the Au_{25}^{+*} generation dominates even at the working electrode biased at a very negative potential, Eq. 6.26. This lead to the increase in its ECL intensity in the fitted spectra, Figure 6.9c-e.

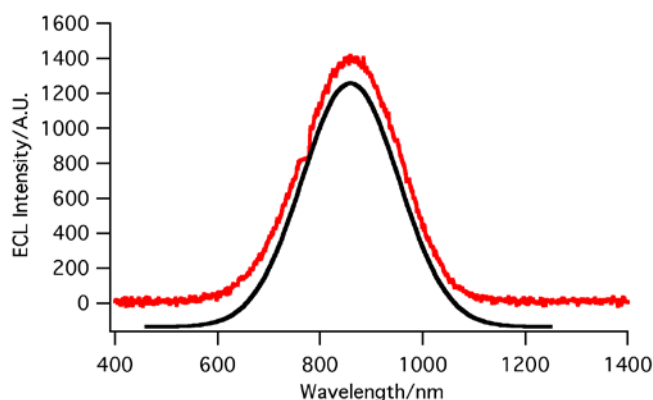


Figure 6.10. Accumulated spectrum between 0.57 and -2.08 V for 106 s of Au_{25}^0 with 0.050 M BPO in ACN:Bz (1:1) with 0.1 M TBAP supporting electrolyte, scan rate of 0.1 V/s. Curve-fitted to one peak at 859 nm.

6.2.4 Conclusions

The increase in BPO concentration caused a growth in the strongly oxidizing $\text{C}_6\text{H}_5\text{CO}_2^\bullet$ radicals leading to the generation of the majority of ECL through Au_{25}^{+*} , Eq. 6.26, while at low BPO concentration, both excited state generation reactions expressed by Eq. 6.28, for Au_{25}^{-*} , and Eq. 6.26, for Au_{25}^{+*} , contributed to ECL emission. It is important to highlight that multiple pathways are possible to obtain the ECL emissions at 960 nm from the Au_{25}^{-*} and 871 nm from the Au_{25}^{+*} , in low or high BPO concentrations.

It is plausible to switch ECL generation routes, Au_{25}^{+*} excited species and Au_{25}^{-*} excited species, and therefore ECL wavelengths by controlling the BPO concentration.

6.2.5 References

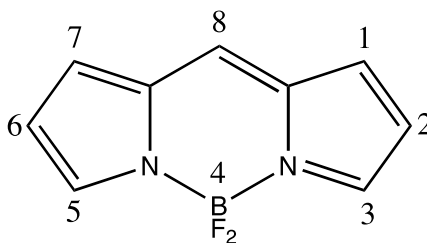
- (1) Swanick, K. N.; Hesari, M.; Workentin, M. S.; Ding, Z. *J. Am. Chem. Soc.* **2012**, *134*, 15205.
- (2) Bard, A. J. F., L.R.; *Electrochemical Methods; Fundamental and Applications*; 2nd ed.; John Wiley & Sons: New York, **2001**.
- (3) Tofanelli, M. A.; Ackerson, C. J. *J. Am. Chem. Soc.* **2012**, *134*, 16937.
- (4) Antonello, S.; Hesari, M.; Polo, F.; Maran, F. *Nanoscale* **2012**, *4*, 5333.
- (5) Liu, Z.; Zhu, M.; Meng, X.; Xu, G.; Jin, R. *J. Phys. Chem. Lett.* **2011**, *2*, 2104.
- (6) Cao, W.; Zhang, X.; Bard, A. J. *J. Electroanal. Chem.* **2004**, *566*, 409.
- (7) Booker, C.; Wang, X.; Haroun, S.; Zhou, J.; Jennings, M.; Pagenkopf, B. L.; Ding, Z. *Angew. Chem. Int. Ed.* **2008**, *47*, 7731.
- (8) Swanick, K. N.; Dodd, D. W.; Price, J. T.; Brazeau, A. L.; Jones, N. D.; Hudson, R. H. E.; Ding, Z. *Phys. Chem. Chem. Phys.* **2011**, *13*, 17405.
- (9) Dharmaratne, A. C.; Krick, T.; Dass, A. *J. Am. Chem. Soc.* **2009**, *131*, 13604.
- (10) Lee, D.; Donkers, R. L.; Wang, G.; Harper, A. S.; Murray, R. W. *J. Am. Chem. Soc.* **2004**, *126*, 6193.

Chapter 7

7 Dual Electrochemiluminescence of BDY-PbS Nanoparticles

7.1 Introduction

PbS nanoparticles (NPs) are infrared (IR) emitting materials that can be used in optical fibre communications and for in vivo bio-imaging and can be tuned by varying their shape, size and surface ligand.^{1,2} Their common capping ligands include oleic acid (OA) however the electrochemiluminescence (ECL) of PbS NPs in this format is weak. This is because OA ligands do not have any electronic communication with the PbS NPs.^{1,2} Trioctylphosphine (TOP) has been employed by Sun *et al.* which displayed an increase in the ECL signal dramatically. 4,4-Difluoro-4-bora-3a,4a-diaza-*s*-indacene (BODIPY) dyes have a sharp fluorescence peak and high quantum yields. BODIPY dyes were discovered in 1968 by Treibs and Kreuzer³ and show emission in the visible region and have been frequently used as dye sensitizers, probes and labels for biomolecules.⁴⁻⁷



Scheme 7.1. BODIPY dye core structure

The ECL of boron-dipyrromethene (BDY) dyes have been studied extensively by Bard *et al.*,⁸⁻¹⁴ and also by Forster *et al.*¹⁵ These dyes show good redox stability, and are efficient, tunable ECL emitters.⁹ Lu *et al.* have reported the synthesis and photophysical properties of new BDY-capped PbS NPs that display dual photoluminescence (PL) emission, in the visible and near-infrared (NIR) regions.² The BDY surface ligand is expected to communicate electronically with the PbS NPs and potentially enhance their

performance in optoelectronic devices.² In this study, we investigated the ECL emission of these BDY-PbS NPs, to see if the two moieties would emit in the visible and NIR region. Our new spooling ECL spectroscopy can determine the mechanism for ECL emission. Also, we were interested in observing any electronic communication between this new BDY ligand and the PbS NPs. To the best of our knowledge, this is the first ECL report of BDY-PbS NPs.

7.2 Experimental Section

For annihilation ECL studies, approximately 1 mg of compound was added to a pyrex electrochemical cell with a flat Pyrex window at the bottom for detection of generated ECL, which contained 0.1 M tetrabutylammonium hexafluorophosphate (TBAPF₆) supporting electrolyte in anhydrous dichloromethane (DCM, 3 mL). A 2 mm diameter Pt disc inlaid in a glass sheath were used as the working electrode (WE), a coiled Pt wire as the counter electrode (CE), and a coiled Ag wire as the quasi reference electrode (RE), respectively. Routine cleaning procedures for the electrodes and cell were reported elsewhere.¹⁶ For detailed electrochemical workstation and ECL setup information, please refer to our previous publications.^{16,17} The cell was assembled in a dry box.

The cyclic voltammetry (CV) was conducted on a CHI 610A electrochemical analyzer (CH Instruments, Austin, TX). The experimental parameters for the cyclic voltammograms (CVs) are listed here: 0.00 V initial potential in experimental scale, positive or negative initial scan polarity, 0.1 V/s scan rate, 4 sweep segments, 0.001 V sample interval, 2 s quiet time, $1 \times 10^{-6} \text{ AV}^{-1}$ sensitivity (for annihilation studies) and $1 \times 10^{-4} \text{ AV}^{-1}$ sensitivity (for co-reactant studies). Potentials (V) were calibrated using an internal standard Fc/Fc⁺ redox couple after each experiment, and are reported vs. a SCE standard electrode (0.342 V in ACN).^{18,19}

ECL and CV data were obtained using the CHI 610A coupled with a photomultiplier tube (PMT, R928, Hamamatsu, Japan) held at -750 V with a high voltage power supply. The ECL collected by the PMT under the flat Pyrex window at the bottom

of the cell was measured as a photocurrent, and transformed to a voltage signal, using a picoammeter/voltage source (Keithley 6487, Cleveland, OH). The potential, current signals from the electrochemical workstation, and the photocurrent signal from the picoammeter were sent simultaneously through a DAQ board (DAQ 6052E, National Instruments, Austin, TX) in a computer. The data acquisition system was controlled from a custom-made LabVIEW program (ECL_PMT610a.vi, National Instruments, Austin, TX). The photosensitivity on the picoammeter was set manually in order to avoid the saturation.

The ECL spectra were obtained by replacing the PMT with a spectrometer (Cornerstone 260, Newport, Canada) attached to a visible region CCD camera (Model DV420-BV, Andor Technology, Belfast, UK). The camera was cooled to $-55\text{ }^{\circ}\text{C}$ prior to use and controlled by a computer for operation and data acquisition. The intensities versus wavelengths (spectra) were recorded by Andor Technology program.

Since the ECL is in NIR region, ECL spectroscopy was conducted on an Acton 2300i spectrograph with a grating of 50 l/mm blazed at 600 nm, attached with an Andor iDUS CCD camera, Model DU401-BR-DD-352 and accumulated over the time that matches with the potential scan time for two complete cycles.

Spooling ECL experiments were conducted using the same setup along with the spooling function in the Andor software. Basically, one ECL spectrum was taken in a time interval of 1 s during the potential scanning. The following parameters were employed in the Andor Technology program under the kinetic parameters option tab: exposure time = 1 s, number of accumulations = 1, kinetic series length = T (where T = time that matches with the potential scan time for two complete cycles), kinetic cycle time = 1, and the spectrometer was centered at 800 nm, with the camera cooled to $-75\text{ }^{\circ}\text{C}$. On the CHI 610A electrochemical analyzer, the initial potential was set to 0.00 V, high potential = 1.90 V, low potential = 0.00 V, sensitivity = $1 \times 10^{-4}\text{ AV}^{-1}$, initial scan polarity = positive, scan rate = 0.1 V/s, sweep segments = 4, sample interval = 0.001 V, and quiet time 2 s. Simultaneously, the CHI 610A electrochemical analyzer and the Andor Technology program were run, and the CV and spooling spectra were collected.

7.3 Results and Discussion

Electrochemistry. Figure 7.1 shows a cyclic voltammogram (CV) of a dark blue BDY-PbS NP solution (red curve). Initially the potential was scanned from 0.00 V towards -1.60 V. A cathodic wave was observed with a peak potential of -1.41 V, which represents the reduction of the BDY portion of the NPs to $\text{BDY}^{\bullet-}$, Eq. 7.1. When reversing the scan from -1.60 V towards positive potential, a return wave was seen at -1.28 V. Upon scanning more positive, an anodic wave showed a peak potential of 0.55 V, displaying the oxidation of BDY to $\text{BDY}^{\bullet+}$, Eq. 7.2. Once the applied potential reached 0.74 V, the potential was scanned towards 0.00 V and a return wave peaked at 0.46 V was seen. According to the literature¹³, the HOMO and LUMO were contributed by the atoms on the conjugated system of the BDY ligand, which undergo redox reactions.

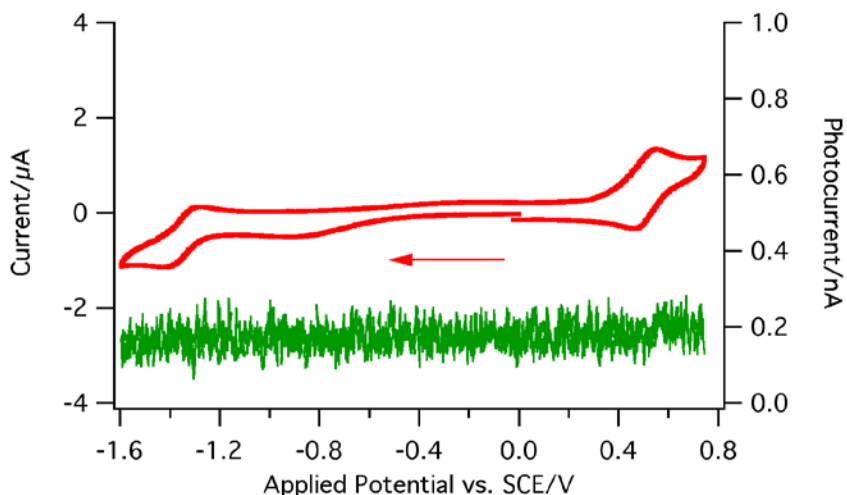


Figure 7.1. CV (in red) with ECL-voltage curve (in green) of BDY-PbS NPs in DCM with TPABF_6 as supporting electrolyte with a potential range of -1.60 V to 0.74 V, for one complete cycle, at a scan rate of 0.1 V/s.

Figure 7.2 demonstrates DPVs. When scanning from -1.60 V to 0.74 V, in blue, two peaks were observed at -1.37 V and at 0.49 V. Upon scanning the reverse direction from 0.74 V to -1.60 V (in green), the DPV showed two peaks at 0.54 V and -1.32 V. These peaks correspond to the $\text{BDY}^{+\bullet}$ and $\text{BDY}^{-\bullet}$ radicals, Eqs. 1 and 2. The peaks are consistent with the peaks observed in the CV. Bard et al. have reported redox potentials of BODIPY dyes having a small separation between first oxidation and first reduction, ranging from 2.0 to 2.4 V.¹³ The BDY-PbS NPs' first oxidation and first reduction have a separation of 1.96 V, Figure 7.1, close to the reported values for these BODIPY dyes. According to Bard et al. the second oxidation and reduction peaks are much further away, since we wanted a limited potential window for light emission, the potential window only included the first oxidation and reduction of the BDY-PbS NPs. The redox chemistry for the PbS portion of the NPs proved to be difficult to observe during CV experiments. The redox chemistry of the PbS might be outside of the potential window. There is also a possibility that due to the 10:1 ratio² of BDY:PbS in the NPs, the electrochemical current maybe be so small for the PbS, it could not be observed during the CV experiments. Another possibility is that the BDY may have capped the PbS very well at the surface therefore the electrochemistry of the PbS was not seen.

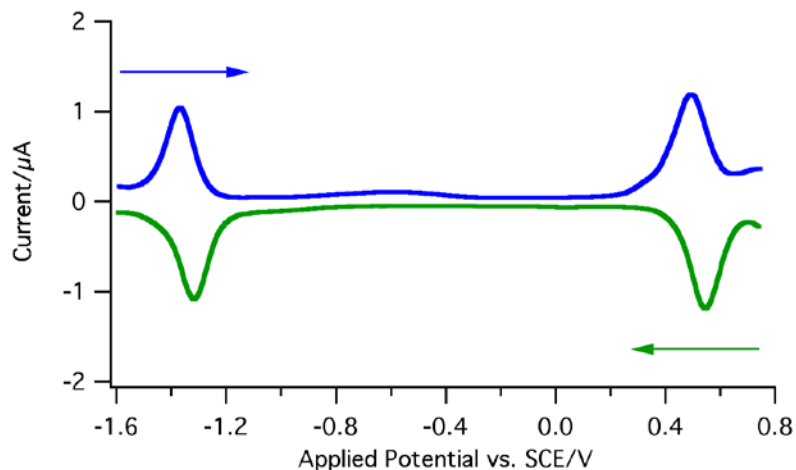


Figure 7.2. DPV of BDY-PbS NPs in DCM with TPABF_6 as supporting electrolyte with a potential range of -1.60 V to 0.74 V, forward direction (in blue) and reverse direction (in green).

ECL *via* Annihilation. When scanning between the NPs' first oxidation and first reduction no photocurrent (ECL) was observed, Figure 7.1. The solution was pulsed between its first oxidation and first reduction potentials, medium ECL emission was observed, Figure 7.3. The photocurrent produced was between 114 nA and 188 nA for several pulse cycles. During pulsing experiments, a change in solution colour was observed. Initially, the solution was dark blue. Then after pulsing it changed to a burgundy colour with some precipitate. Formation of a precipitate would cause a decrease in the amount of ECL produced, in addition to blocking the light from entering the photomultiplier tube (PMT).

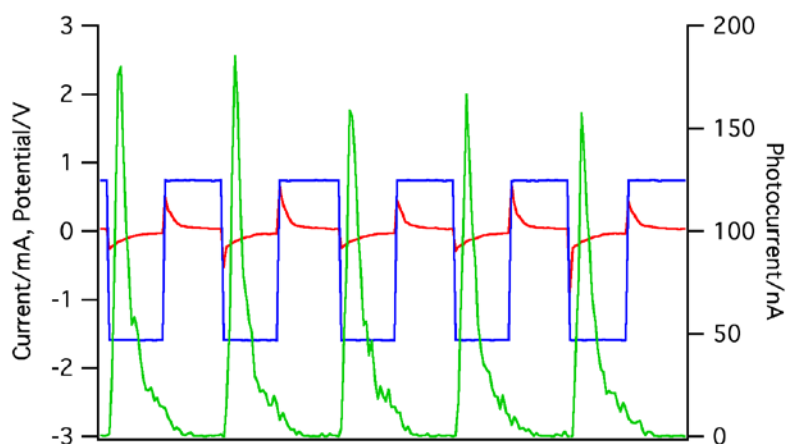


Figure 7.3. Pulsing of BDY-PbS NPs in DCM with TPABF₆ as supporting electrolyte, current show in red, applied potential shown in blue, and photocurrent shown in green.

When pulsing the solution between -1.60 V to 0.74 V, ECL was generated as seen in the green photocurrent in Figure 7.3. Here, the radical cation appears to be more stable than the radical anion of the BDY-PbS NPs because ECL was observed in the cathodic region, from Figure 7.3 when the potential reached -1.60 V, in blue. The amount of ECL produced *via* pulsing was around 150 nA.

The spectrum of the BDY-PbS NPs was accumulated over 15 s during pulsing experiments using the visible spectrometer set, centered at 850 nm, Figure 7.4. Two peaks were observed, the first at 700 nm and the second at 975 nm. By functionalizing the PbS NPs with BDY, dual ECL emissions were observed. Two mechanisms for

generating ECL in this annihilation pathway are proposed. When alternating the potential between -1.60 V to 0.74 V, a BDY radical cation, $\text{BDY}^{\bullet+}\text{-PbS}$, Eq. 7.2, and a BDY radical anion, $\text{BDY}^{\bullet-}\text{-PbS}$, Eq. 7.1, were generated from the BDY-PbS NPs. Through electron transfer between the radical cation and anion, the excited species, $\text{BDY}^*\text{-PbS}$, Eq. 7.3, was generated and emit light at 700 nm, $h\nu_1$, Eq. 7.4. This is close to the reported PL emission at 645 nm.² The red shifted ECL spectrum to lower energy may be due to an inner filter effect (self-absorption) and high concentrations of the NPs for ECL compared to PL, in addition to the difference in resolution between the instruments used for the PL and ECL studies.⁹

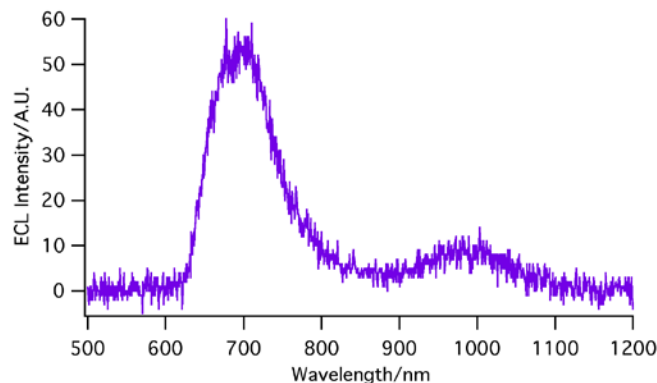


Figure 7.4. ECL visible spectrum of BDY-PbS NPs from pulsing between -1.60 V to 0.74 V for 15 s, visible CCD camera cooled to -55 °C, centered at 850 nm, T = 15 s.

The ECL emission at 975 nm, might be generated *via* energy transfer from the excited species, BDY^* to the PbS moiety, forming the BDY-PbS^* excited species, Eq. 7.5. The emission was then observed at 975 nm, $h\nu_2$, Eq. 7.6, when the BDY-PbS^* excited species relaxed to the ground state. There appears to be electronic communication/interaction between the PbS NPs with the surface ligand BDY when ECL is generated at 975 nm, Eq. 7.6. The PL emission of the PbS at 1100 nm,² is in close

agreement to the ECL emission at 975 nm, which is similar to the PL emission at 912 nm¹ for PbS QDs capped with oleic acid (see latter).



Since there is a possibility that the PbS moiety is also oxidized and reduced, even though the CV does not show the peaks, due to overlap, another route to generate the light, $h\nu_2$, could be through Eqs. 7.7 to 7.9.



ECL via TPrA Co-reactant. Tri-*n*-propylamine, TPrA, a common co-reactant, was added to enhance ECL of the BDY-PbS NPs while reducing the potential window and the duration of scanning time, Figure 7.5. The potential was scanned from 0.00 V to 1.58 V. The photocurrent started to gradually increase around 1.00 V. The ECL onset was around 0.50 V. Since the concentration of TPrA was much larger than the BDY-PbS NPs concentration, the first oxidation peaks of the BDY-PbS NPs were not observed. The oxidation of TPrA reached its maximum at 1.25 V, and an increase in photocurrent was observed until 1.38 V, where the photocurrent reached a maximum of 154 nA, Figure 7.5. Afterwards, the photocurrent started to decrease after 1.38 V until it reached 1.58 V. On the reverse scan, the photocurrent continued to decrease until it was close to the baseline prior to 0.00 V.

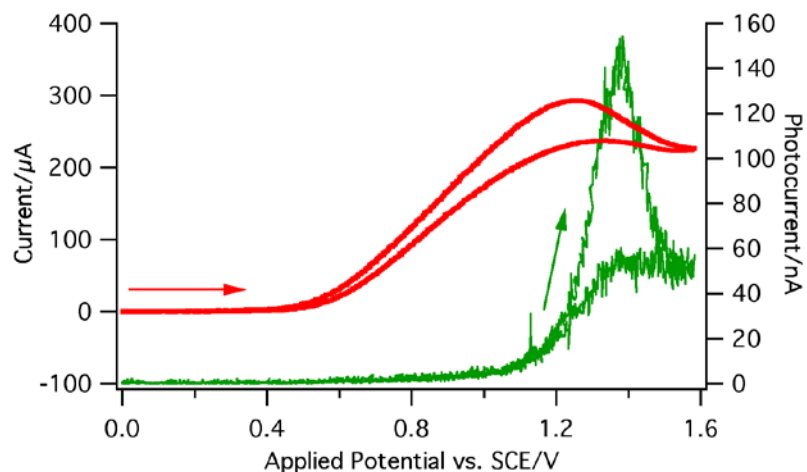


Figure 7.5. CV (in red) with ECL-voltage curve (in green) of BDY-PbS NPs in DCM with TPABF_6 as supporting electrolyte with 0.02 M TPrA, in a potential range of 0.00 V to 1.58 V, for one complete cycle, at a scan rate of 0.1 V/s.

When scanning the solution with TPrA between 0.00 V to 1.58 V, at a scan rate of 0.1 V/s, the spectrum of the BDY-PbS NPs with 0.02 M TPrA was accumulated over 82 s, using the NIR CCD camera cooled to $-75\text{ }^\circ\text{C}$, centered at 800 nm, Figure 7.6. Two peaks were observed similar to the annihilation pathway, the first at 733 nm and the second at 1028 nm.

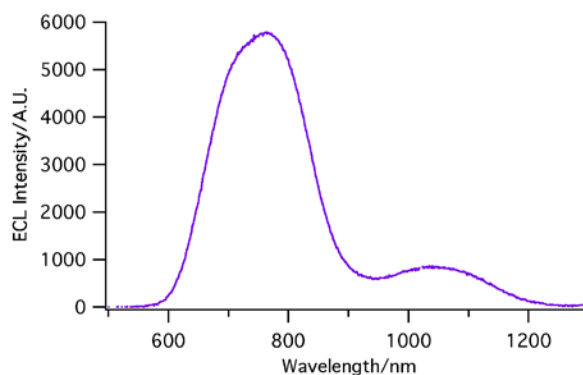


Figure 7.6. ECL NIR spectrum of BDY-PbS NPs with 0.02 M TPrA from scanning between 0.00 V to 1.58 V, at a scan rate of 0.1 V/s, NIR CCD camera cooled to $-75\text{ }^\circ\text{C}$, centered at 800 nm, $T = 82\text{ s}$.

From the accumulated spectrum, Figure 7.6, the mechanism of ECL emission was determined using our NIR spooling technique. Here each spectrum was recorded every 1 s, at a scan rate of 0.1 V/s between 0.00 V to 1.58 V, Figure 7.7. Two emissions were identified at 733 nm and 1028 nm, consistent with the accumulated spectrum, Figure 7.6. The spooling technique helps to identify which emission occurs first with less potential compared to the second emission that happens with greater positive applied potential.

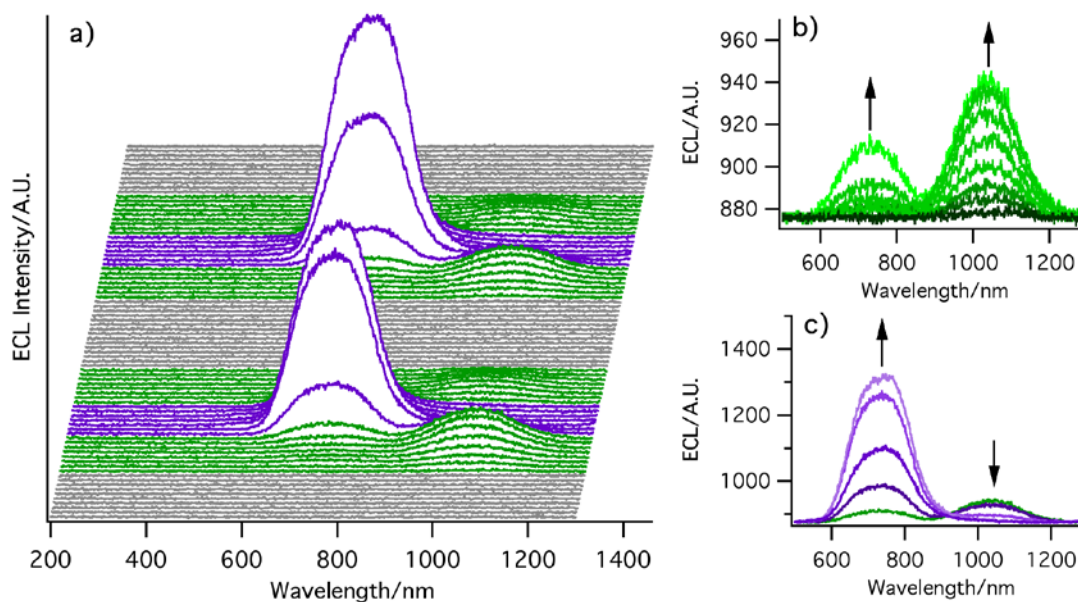
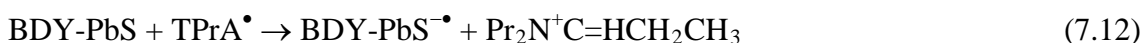


Figure 7.7. ECL NIR spooling of BDY-PbS NPs with 0.02 M TPrA, a) two cycles shown, between 0.00 V to 1.58 V, $T = 82$ s, at a scan rate of 0.1 V/s, b) evolution of 733 nm and 1028 nm from ECL onset at 0.38 V, first cycle shown, c) increase in 733 nm peak and decrease in 1028 nm peak (the point at which the 1028 nm started to decrease shown in green), first cycle shown.

ECL onset was observed at 0.38 V with an emission at 1028 nm. At 0.58 V, the second emission started to appear at 733 nm. The peak at 1028 nm continued to increase until 1.08 V, then the 733 nm peak started to increase until it reached maximum ECL intensity at 1.38 V. The intensity of the 733 nm peak started to decrease until 1.58 V and continued on the reverse scan until 1.38 V. At this potential, the 1028 nm appeared and continued to decrease until 0.68 V, then reached its baseline.

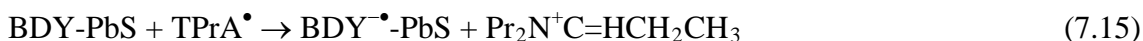
The ECL onset mechanisms are shown in Eqs. 7.10 to 7.13. Initially, TPrA is oxidized to $\text{TPrA}^{+\bullet}$, Eq. 7.10, then leads to the formation of the reducing radical, TPrA^\bullet , Eq. 7.11. From Figure 7.7, the onset of ECL, at 0.38 V, appears to be in the NIR at 1028 nm, most likely from the BDY-PbS^* excited species. The TPrA^\bullet radical will react with the BDY-PbS NPs and form $\text{BDY-PbS}^{-\bullet}$, Eq. 7.12. Then the radical anion, $\text{BDY-PbS}^{-\bullet}$, would react with $\text{TPrA}^{+\bullet}$ forming the BDY-PbS^* , Eq. 7.13.



Another route to generate the BDY-PbS^* excited species, starts with the BDY-PbS NPs being oxidized to $\text{BDY-PbS}^{+\bullet}$, Eq. 7.8. Once the TPrA has generated its strong reducing agent, TPrA^\bullet , Eq. 7.11, the two radicals will generate the BDY-PbS^* excited species, Eq. 7.14, that emits at 1028 nm, $h\nu_2$, Eq. 7.6.



When taking a closer look at the onset of ECL in Figure 7.7, a peak at 733 nm starts to form close to ECL onset at 0.58 V. This peak is consistent with the evolution of the BDY^*-PbS excited species. Here, the TPrA^\bullet radical could generate the $\text{BDY}^{-\bullet}-\text{PbS}$ radical anion, Eq. 7.15, which would react with the $\text{TPrA}^{+\bullet}$ radical cation, Eq. 7.16, and create the BDY^*-PbS excited species, emitting at 733 nm, $h\nu_1$, Eq. 7.4.



A similar mechanism with TPrA as in Eq. 7.14, involves the oxidized $\text{BDY}^{+\bullet}-\text{PbS}$, Eq. 7.2, reacting with the TPrA^\bullet radical to generate the BDY^*-PbS excited species, BDY^*-PbS .

PbS, Eq. 7.17. Once the BDY^*-PbS species relaxes to its ground state, an emission at 733 nm, $h\nu_1$, Eq. 7.4, was observed.



When the 733 nm peak started to increase until it reached maximum ECL intensity at 1.38 V, the BDY^*-PbS excited species was dominate. By this potential, the TPrA has completely oxidized thus the large increase in ECL was observed. During this time however, the $\text{BDY}-\text{PbS}^*$ excited species started to decrease until 1.38 V on the reverse scan. There is no reason why the $\text{BDY}-\text{PbS}^*$ excited species should decrease with maximum amount of TPrA oxidized. This leads us to the conclusion that in fact there is no intramolecular energy transfer between the BDY^* and PbS moieties to generate the $\text{BDY}-\text{PbS}^*$ excited species, as originally hypothesized in Eq. 7.5. The $\text{BDY}-\text{PbS}^*$ excited species emission at 1028 nm should not disappear if there is energy transfer, thus confirming that the PbS itself emits light at the same time as the BDY moiety, Eq. 7.6.

A comparison with BDY capped PbS NPs is with a commonly used surface ligand, oleic acid, OA, for OA-capped PbS NPs. Here, similar CV conditions were used with 0.02 M TPrA as co-reactant, Figure 7.8, as with the BDY-PbS NPs in Figure 7.5. Onset ECL occurred at 0.48 V, with 2 nA of ECL. Scanning more positive until 1.58 V increased the amount of ECL to 16 nA. The intensity of ECL was significantly less than the BDY-PbS NPs with the OA capped NPs, however, we were able to collect the spectrum, even with weak ECL.

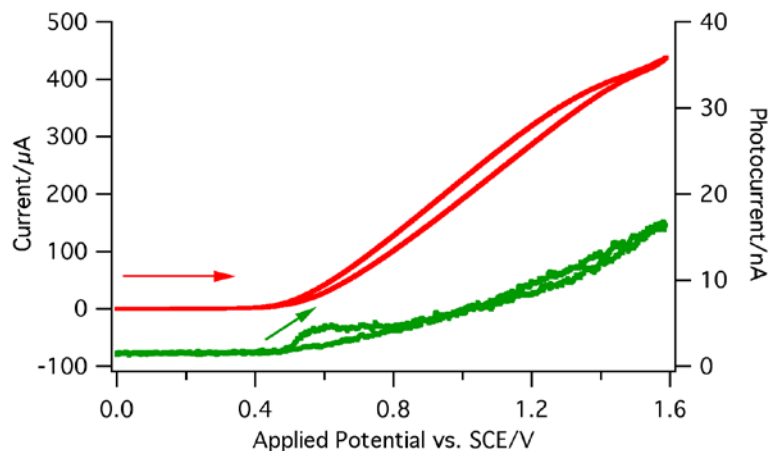


Figure 7.8. CV (in red) with ECL-voltage curve (in green) of OA-PbS NPs in DCM with TPABF_6 as supporting electrolyte with 0.02 M TPrA, in a potential range of 0.00 V to 1.58 V, for one complete cycle, with a scan rate of 0.1 V/s.

From the accumulated spectrum using the NIR CCD camera, only one peak after curve-fitting was observed at 1028 nm for the OA-PbS NPs, Figure 7.9a. This matches the peak observed in the BDY-PbS NPs accumulated spectrum. The spooling spectra, Figure 7.9b, showed slight shifts in the peak wavelength when the potential was scanned from 0.00 V to 1.58 V. At maximum intensity, 1.28 V, the peak was centered at 1015 nm, Figure 7.9b, close to the accumulated spectrum's wavelength of 1028 nm, Figure 7.9a, matching the NIR PL emission of 1100 nm². These experiments proved that OA capped PbS NPs can also produce ECL in the presence of TPrA. This further confirms the above ECL mechanism assessed by the spooling spectroscopy.

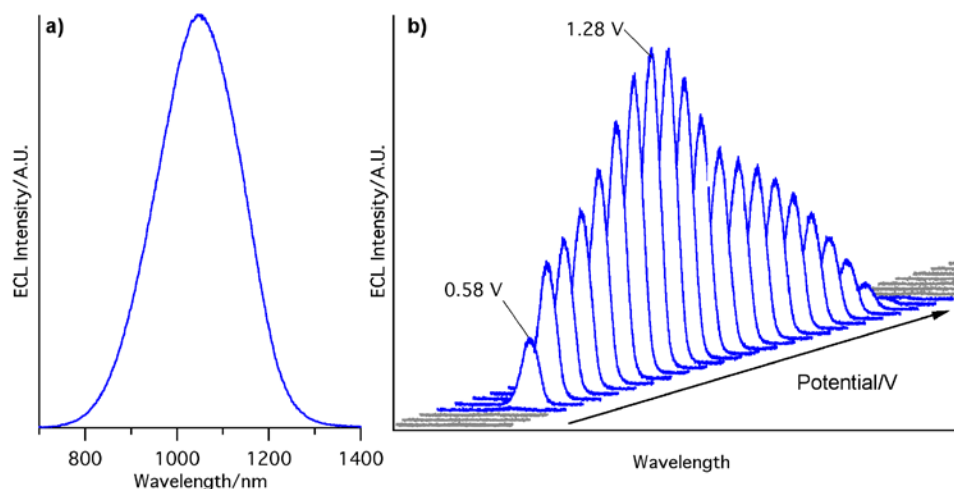


Figure 7.9. ECL spectra of OA-PbS NPs with 0.02 M TPrA from scanning between 0.00 V to 1.58 V, at a scan rate of 0.1 V/s, a) accumulated spectrum, b) spooling spectrum side profile, one cycle shown, NIR CCD camera cooled to $-75\text{ }^{\circ}\text{C}$, centered at 800 nm, $T = 80\text{ s}$.

7.4 Conclusions

We have demonstrated that BDY-PbS NPs generate ECL weakly through the annihilation pathway by pulsing the potential and stronger by using TPrA as a co-reactant and scanning the potential. Both pathways generated two excited species from the BDY-PbS NPs that emit in the visible, BDY excited species, $\text{BDY}^*\text{-PbS}$, at 733 nm, and NIR, PbS excited species, BDY-PbS^* , at 1028 nm using the NIR CCD camera. By comparison of the OA-PbS NPs, where there was only one excited species from PbS, with the BDY-PbS NPs, it is plausible that the two emissions originating from the BDY excited species and the PbS excited species were generated independently.

7.5 References

- (1) Sun, L.; Bao, L.; Hyun, B.-R.; Bartnik, A. C.; Zhong, Y.-W.; Reed, J. C.; Pang, D.-W.; Abruña, H. D.; Malliaras, G. G.; Wise, F. W. *Nano Lett.* **2009**, *9*, 789.
- (2) Lu, J.-S.; Fu, H.; Zhang, Y.; Jakubek, Z. J.; Wang, S. *Angew. Chem. Int. Ed.* **2011**, *50*, 11658.

- (3) Treibs, A.; Kreuzer, F. H. *Justus Liebigs Ann. Chem.* **1968**, 718, 208.
- (4) Loudet, A.; Burgess, K. *Chem. Rev.* **2007**, 107, 4891.
- (5) Ziessel, R.; Ulrich, G.; Harriman, A. *New J. Chem.* **2007**, 31, 496.
- (6) Ulrich, G.; Ziessel, R.; Harriman, A. *Angew. Chem. Int. Ed.* **2008**, 47, 1184.
- (7) Benniston, A. C.; Copley, G. *Phys. Chem. Chem. Phys.* **2009**, 11, 4124.
- (8) Lai, R. Y.; Bard, A. J. *J. Phys. Chem. B* **2003**, 107, 5036.
- (9) Nepomnyashchii, A. B.; Bröring, M.; Ahrens, J.; Krüger, R.; Bard, A. J. *J. Phys. Chem. C* **2010**, 114, 14453.
- (10) Nepomnyashchii, A. B.; Bröring, M.; Ahrens, J.; Bard, A. J. *J. Am. Chem. Soc.* **2011**, 133, 19498.
- (11) Rosenthal, J.; Nepomnyashchii, A. B.; Kozhukh, J.; Bard, A. J.; Lippard, S. J. *J. Phys. Chem. C* **2011**, 115, 17993.
- (12) Suk, J.; Omer, K. M.; Bura, T.; Ziessel, R.; Bard, A. J. *J. Phys. Chem. C* **2011**, 115, 15361.
- (13) Nepomnyashchii, A. B.; Bard, A. J. *Acc. Chem. Res.* **2012**, 45, 1844.
- (14) Nepomnyashchii, A. B.; Pistner, A. J.; Bard, A. J.; Rosenthal, J. *J. Phys. Chem. C* **2013**, 117, 5599.
- (15) Venkatanarayanan, A.; Martin, A.; Keyes, T. E.; Forster, R. J. *Electrochem. Commun.* **2012**, 21, 46.
- (16) Swanick, K. N.; Dodd, D. W.; Price, J. T.; Brazeau, A. L.; Jones, N. D.; Hudson, R. H. E.; Ding, Z. *Phys. Chem. Chem. Phys.* **2011**, 13, 17405.
- (17) Booker, C.; Wang, X.; Haroun, S.; Zhou, J.; Jennings, M.; Pagenkopf, B. L.; Ding, Z. *Angew. Chem. Int. Ed.* **2008**, 47, 7731.
- (18) Sahami, S.; Weaver, M. J. *J. Electroanal. Chem.* **1981**, 122, 155.
- (19) Nepomnyashchii, A. B.; Bröring, M.; Ahrens, J.; Bard, A. J. *J. Am. Chem. Soc.* **2011**, 133, 8633.

Chapter 8

8 Concluding Remarks and Future Work

As highlighted in this thesis, ECL is a powerful analytical technique that has high sensitivity and selectivity and has gained interests in a variety of applications. Using DPA and $[\text{Ru}(\text{bpy})_3]^{2+}$ as bench marks in ECL efficiency, the quest to find compounds that were stable in solution and could achieve high efficiencies while covering the visible and NIR spectra were desirable. The research presented in this thesis has demonstrated the possibilities of a wide range of ECL emitters, from modified nucleosides, to metal complexes, and nanoparticles.

The electrochemical behavior and ECL of four triazole-containing deoxycytidine nucleosides were studied that generated blue-green ECL emission, red-shifted compared to its PL spectra, due to excimer formation, with low relative ECL efficiencies. Another series of thienyltriazoles were synthesized and their redox chemistry and ECL mechanisms were analyzed. Again, blue-green ECL emission was observed, red-shifted compared to their PL spectra, possibly due to excimers, with relatively low ECL efficiencies. Overall, these studies provided information on how thienyltriazole containing complexes can be tuned to blue-green ECL emission and for understanding of their electronic and redox properties.

A large study was undertaken correlating electronic structure to ECL using iridium(III)-containing metal complexes. For some of the iridium(III) metal complexes, the generation of the excited triplet state appeared to be advantageous. It required less energy to yield higher ECL relative efficiencies. The installation of different substituents on the ligands increased or decreased the electrochemical gap, thus tuning the ECL emission. Complexes containing ppy ligands showed higher relative efficiencies than the phtl ligand containing iridium(III) complexes. With the use of the co-reactant BPO, we were able to achieve some relative efficiencies higher than that of $[\text{Ru}(\text{bpy})_3]^{2+}$, and have discovered that iridium(III) complexes containing the dma substituents on the bpy ligand

show self-enhancement and dramatically high relative ECL efficiencies, well surpassing the absolute efficiency of $[\text{Ru}(\text{bpy})_3]^{2+}$ with blue-green ECL emission. We used a newly developed ECL spooling spectroscopic technique to determine the mechanism for the self-enhancement due to multiple ECL emissions. Lastly for this iridium(III) complex study, we saw communication between the $[\text{Ru}]^{2+}$ and $[\text{Ir}]^-$ moieties in the $[\text{Ir}][\text{Ru}][\text{Ir}]$ soft salt during electrochemical reactions, reducing the energy required to produce ECL, with enhancement when using TPrA as the co-reactant.

In the study involving the Au_{25} clusters, we observed NIR ECL emission that was enhanced when using BPO as the co-reactant. Using the ECL spooling technique, we discovered there were different mechanisms, even for the same ECL emission, depending on the potential at which light was emitted. The ECL of Au_{25}^0 clusters is quite complex, with multiple pathways for ECL emission. It was discovered that the Au_{25}^0 clusters generated two excited species, Au_{25}^{-*} and Au_{25}^{0*} when using BPO as the co-reactant.

For the final study in this thesis, we demonstrated that BDY-PbS NPs generate ECL weakly *via* annihilation and stronger using the co-reactant TPrA. Prior to this study, only the ECL of PbS NPs and ECL of BDY type dyes have been studied separately. Combining the two into the BDY-PbS NPs produces ECL in the visible and NIR regions. Electronic communication between the BDY-capped ligand and the PbS core was observed. Dual emissions and electronic communication could be potentially useful in electronic or medical applications.

The field of ECL has been rapidly developing, thus proving to be a useful and powerful analytical technique. Future work may include additional electrochemical and ECL studies on iridium(III) metal complexes, progress towards light-emitting electrochemical cells (LEECs) as potential light sources and displays, and NIR NPs for bioanalytical applications. NIR ECL emission will not be absorbed by tissues, something important and may brightly lead the pathway into future ECL studies. New techniques are being designed to help understand the mechanisms of ECL generation that could lead to further insight into this complex analytical field.

Appendices

Appendix I. Chapter 2: Electrogenenerated Chemluminescence of Triazole-Modified Deoxycytidine Analogues in N,N-Dimethylformamide

CV and ECL Experimental Parameters

In annihilation systems, the CV potential window was 2.069 to -1.889 V for **2.1**, 1.861 to -2.435 V for **2.2**, 1.787 to -2.231 V for **2.3**, and 1.828 to -2.940 V for **2.4**. In co-reactant systems, the CV potential window was 0.000 to -2.278 V for **2.1**, 0.000 to -2.452 V for **2.2**, 0.000 to -2.517 V for **2.3**, and 0.000 to -2.126 V for **2.4**.

Curve-Fitting for ECL Spectra

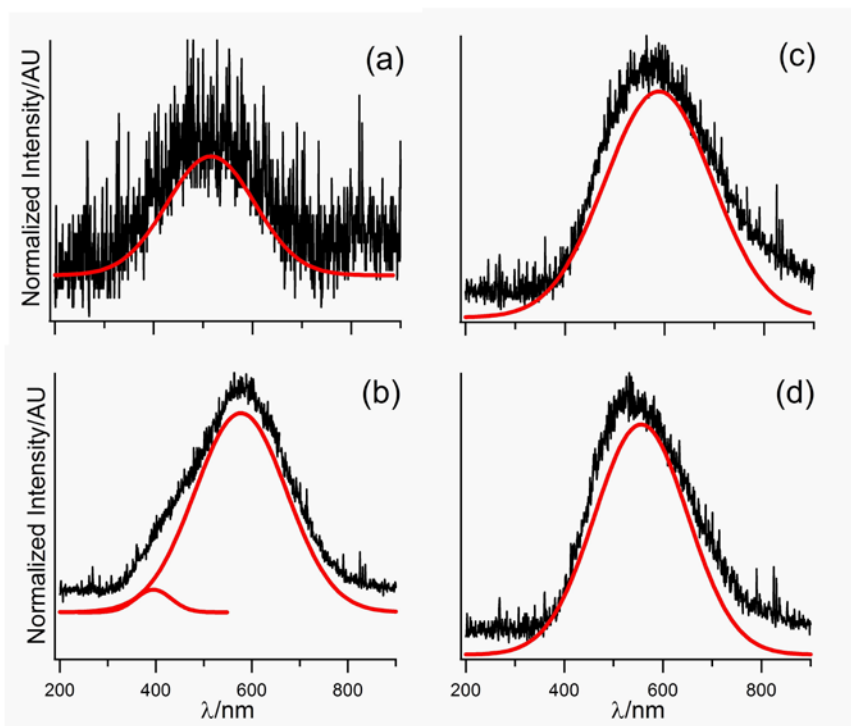


Figure S2.1. ECL spectra and their curve-fitting for **2.1-2.4** in DMF containing 5.0×10^{-3} M BPO and 0.1 M TBAP as supporting electrolyte and pulsing between potential ranges from (a) 0.000 to -2.278 V, $t = 60$ s for **2.1**, (b) 0.000 to -2.452 V, $t = 60$ s for **2.2**, (c) 0.000 to -2.517 V, $t = 60$ s for **2.3**, and (d) 0.000 to -2.126 V, $t = 60$ s for **2.4**.

Crystallographic Details for **2.1** • 2 H₂O

Crystals of [C₁₅H₁₆N₆O₄S] • 2 H₂O were grown from a concentrated aqueous solution (refer to Figure S2.2. for crystal structure of **2.1**). A colourless needle was mounted on a glass fibre. Data were collected at low temperature (-123°C) on a Nonius Kappa-CCD area detector diffractometer with COLLECT (Nonius B.V., 1997-2002). The unit cell parameters were calculated and refined from the full data set. Crystal cell refinement and data reduction were carried out using HKL2000 DENZO-SMN (Otwinowski & Minor, 1997). The absorption correction was applied using HKL2000 DENZO-SMN (SCALEPACK). The crystal data and refinement parameters for [C₁₅H₁₆N₆O₄S] • 2 H₂O are listed in Table S2.1. The reflection data and systematic absences were consistent with an orthorhombic space group: P2(1)2(1)2(1). Bond lengths and angles are listed in Table S2.2.

The SHELXTL/PC V6.14 for Windows NT (Sheldrick, G.M., 2001) suite of programs was used to solve the structure by direct methods. Subsequent difference Fourier syntheses allowed the remaining atoms to be located. Independent molecules were formed and are interconnected via H-bonding interactions involving the molecule itself and the two water molecules of solvation. All of the non-hydrogen atoms were refined with anisotropic thermal parameters. Some soft restraints were used for the thermal parameters and the disordered thiophene rings. The hydrogen atom positions were calculated geometrically and were included as riding on their respective carbon atoms.

The largest residue electron density peak (0.244 e/Å³) was associated with the disordered thiophene ring (Table S2.1). Full-matrix least squares refinement on F² gave R₁ = 5.26 for 2σ data and wR₂ = 11.96 for all data as seen in Table S2.1 (GOOF = 1.086). The final solution was submitted to the IUCR checkCIF program and had some Alert level A's or B's associated with the lack of complete data.

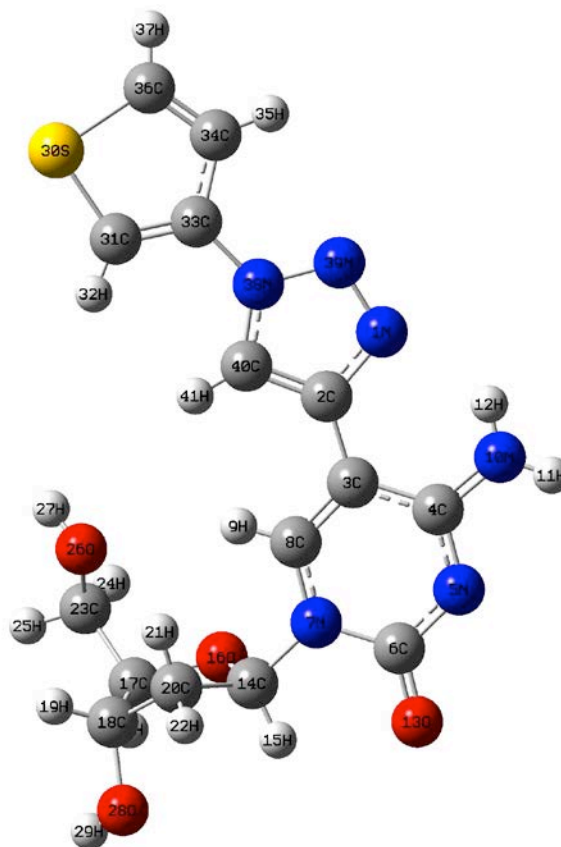


Figure S2.2. Ball-and-stick representation of **2.1**. Carbon atoms are in grey, sulfur in yellow, nitrogen in blue, oxygen in red, and hydrogen in white. The final solution was submitted to the IUCR CIF checking program and had some Alert level A's or B's associated with the lack of complete data, however the general structure can be observed for **2.1**, similar to our previously reported solid state structure of **2.2**.

Table S2.1. Crystal data and structure refinement for **2.1** • 2 H₂O

Empirical formula	C ₁₅ H ₂₀ N ₆ O ₆ S
Formula weight	412.43
Temperature	150(2) K
Wavelength	0.71073 Å
Crystal system	Orthorhombic
Space group	P 2 ₁ 2 ₁ 2 ₁

Unit cell dimensions	$a = 4.8367(6) \text{ \AA}$	
	$b = 12.1128(18) \text{ \AA}$	$\alpha = 90^\circ$.
	$c = 30.967(5) \text{ \AA}$	$\beta = 90^\circ$.
Volume	$1814.2(5) \text{ \AA}^3$	$\gamma = 90^\circ$.
Z	4	
Density (calculated)	1.510 Mg/m^3	
Absorption coefficient	0.227 mm^{-1}	
F(000)	864	
Crystal size	$0.75 \times 0.13 \times 0.03 \text{ mm}^3$	
Theta range for data collection	2.59 to 18.84° .	
Index ranges	$-4 \leq h \leq 4$, $-11 \leq k \leq 10$, $-27 \leq l \leq 27$	
Reflections collected	6165	
Independent reflections	1347 [R(int) = 0.0910]	
Completeness to $\theta = 18.84^\circ$	97.80%	
Absorption correction	Semi-empirical from equivalents	
Max. and min. transmission	0.9943 and 0.8482	
Refinement method	Full-matrix least-squares on F ²	
Data / restraints / parameters	1347 / 366 / 279	
Goodness-of-fit (GOOF) on F ²	1.086	
Final R indices [I > 2 σ (I)]	$R_1 = 0.0526$, $wR_2 = 0.1052$	
R indices (all data)	$R_1 = 0.0752$, $wR_2 = 0.1196$	
Absolute structure parameter	0.0(3)	
Largest diff. peak and hole	0.244 and -0.211 e\AA^{-3}	

Table S2.2. Hydrogen bonds for **2.1**• 2 H₂O [\AA and $^\circ$]

D-H...A	d(D-H)	d(H...A)	d(D...A)	<(DHA)
N(17)-H(17A)...O(41)#1	0.88	2.54	3.261(8)	139.5
N(17)-H(17B)...N(8)	0.88	2.08	2.764(10)	134.4
O(25)-H(25A)...O(31)#2	0.84	1.98	2.813(8)	171.4
O(26)-H(26A)...O(18)#3	0.84	1.82	2.625(7)	160.8
O(31)-H(31A)...O(26)	0.87(4)	1.90(5)	2.724(8)	157(9)
O(31)-H(31B)...O(41)	0.87(4)	2.59(9)	2.778(10)	93(6)
O(41)-H(41A)...N(13)#2	0.88(4)	2.05(6)	2.833(8)	147(8)
O(41)-H(41B)...O(31)#4	0.87(4)	2.12(5)	2.968(9)	162(9)

Symmetry transformations used to generate equivalent atoms:

#1 $-x+1, y-1/2, -z+3/2$ #2 $-x+1, y+1/2, -z+3/2$ #3 $-x+2, y+1/2, -z+3/2$

#4 $x-1, y, z$

Electrogenerated chemiluminescence of triazole-modified deoxycytidine analogues in N,N-dimethylformamide

K. N. Swanick, D. W. Dodd, J. T. Price, A. L. Brazeau, N. D. Jones, R. H. E. Hudson and Z. Ding, *Phys. Chem. Chem. Phys.*, 2011, **13**, 17405, DOI: 10.1039/C1CP22116G

If you are not the author of this article and you wish to reproduce material from it in a third party non-RSC publication you must formally request permission using RightsLink. Go to our Instructions for using RightsLink page for details.

Authors contributing to RSC publications (journal articles, books or book chapters) do not need to formally request permission to reproduce material contained in this article provided that the correct acknowledgement is given with the reproduced material.

Reproduced material should be attributed as follows:

- For reproduction of material from NJC: Reproduced from Ref. XX with permission from the Centre National de la Recherche Scientifique (CNRS) and The Royal Society of Chemistry.
- For reproduction of material from PCCP: Reproduced from Ref. XX with permission from the PCCP Owner Societies.
- For reproduction of material from PPS: Reproduced from Ref. XX with permission from the European Society for Photobiology, the European Photochemistry Association, and The Royal Society of Chemistry.
- For reproduction of material from all other RSC journals and books: Reproduced from Ref. XX with permission from The Royal Society of Chemistry.

If the material has been adapted instead of reproduced from the original RSC publication "Reproduced from" can be substituted with "Adapted from".

In all cases the Ref. XX is the XXth reference in the list of references.

If you are the author of this article you do not need to formally request permission to reproduce figures, diagrams etc. contained in this article in third party publications or in a thesis or dissertation provided that the correct acknowledgement is given with the reproduced material.

Reproduced material should be attributed as follows:

- For reproduction of material from NJC: [Original citation] - Reproduced by permission of The Royal Society of Chemistry (RSC) on behalf of the Centre National de la Recherche Scientifique (CNRS) and the RSC
- For reproduction of material from PCCP: [Original citation] - Reproduced by permission of the PCCP Owner Societies
- For reproduction of material from PPS: [Original citation] - Reproduced by

permission of The Royal Society of Chemistry (RSC) on behalf of the European Society for Photobiology, the European Photochemistry Association, and RSC

- For reproduction of material from all other RSC journals: [Original citation] - Reproduced by permission of The Royal Society of Chemistry

If you are the author of this article you still need to obtain permission to reproduce the whole article in a third party publication with the exception of reproduction of the whole article in a thesis or dissertation.

Information about reproducing material from RSC articles with different licences is available on our

[Permission Requests page](#).

Appendix II. Chapter 3: Synthesis, Structure, Electrochemistry, and Electrochemiluminescence of Thienyltriazoles

NMR peak assignments of 3.1-3.4.

[1-(2,2'-bithien-4-yl)-1H-1,2,3-triazol-4-yl]methanol (3.1, BiTTM).

^1H NMR ($(\text{CD}_3)_2\text{CO}$) δ : 8.43 (s, 1H, CH), 7.82 (d, 1H, CH, $J = 1.2$ Hz), 7.80 (d, 1H, CH, $J = 1.6$ Hz), 7.53 (dd, 1H, CH, $J = 1.2$ Hz, $J = 5.2$ Hz), 7.44 (dd, 1H, CH, $J = 0.8$ Hz, $J = 3.6$ Hz), 7.14 (dd, 1H, CH, $J = 3.6$ Hz, $J = 5.2$ Hz), 4.76 (dd, 2H, CH, $J = 0.4$ Hz, $J = 6.0$ Hz), 4.34 (t, 1H, OH, $J = 6.0$ Hz). ^{13}C NMR ($(\text{CD}_3)_2\text{CO}$) δ : 148.8, 137.9, 135.6, 135.4, 128.5, 126.6, 125.1, 121.3, 116.8, 112.7, 54.9.

[1-(3-thienyl)-1H-1,2,3-triazol-4-yl]methanol (3.2, TTM).

^1H NMR ($(\text{CD}_3)_2\text{SO}$) δ : 8.59 (s, 1H, CH), 8.02 (dd, 1H, CH, $J = 1.2$ Hz, $J = 2.8$ Hz), 7.78 (dd, 1H, CH, $J = 3.2$ Hz, $J = 5.2$ Hz), 7.64 (dd, 1H, CH, $J = 1.6$ Hz, $J = 5.2$ Hz), 5.33 (t, 1H, OH, $J = 5.6$ Hz), 4.69 (dd, 2H, CH, $J = 0.4$ Hz, $J = 5.2$ Hz). ^{13}C NMR ($(\text{CD}_3)_2\text{SO}$) δ : 148.7, 138.5, 128.3, 121.3, 120.6, 114.2, 54.9.

2-[1-(2,2'-bithien-4-yl)-1H-1,2,3-triazol-4-yl]phenol (3.3, BiTTP).

^1H NMR ($(\text{CD}_3)_2\text{SO}$) δ : 10.26 (s, 1H, OH), 8.07 (m, 2H, CH), 8.93 (s, 1H, CH), 7.95 (d, 1H, CH, $J = 1.6$ Hz), 7.61 (dd, 1H, CH, $J = 1.2$ Hz, $J = 5.2$ Hz), 7.49 (dd, 1H, CH, $J = 1.2$ Hz, $J = 3.6$ Hz), 7.21 (t, 1H, CH, $J = 8.4$ Hz), 7.14 (dd, 1H, CH, $J = 4.0$ Hz, $J = 5.2$ Hz), 7.01 (dd, 1H, CH, $J = 0.8$ Hz, $J = 8.4$ Hz), 6.93 (t, 1H, CH, $J = 7.2$ Hz). ^{13}C NMR ($(\text{CD}_3)_2\text{SO}$) δ : 154.1, 143.4, 137.9, 135.5, 135.4, 129.2, 138.6, 126.9, 126.6, 125.2, 121.4, 119.4, 117.0, 116.6, 116.1, 113.2.

2-[1-(3-thienyl)-1H-1,2,3-triazol-4-yl]phenol (3.4, TTP).

^1H NMR (CDCl_3) δ : 10.71 (s, 1H, OH), 8.19 (s, 1H, CH), 7.67 (t, 1H, CH, $J = 2.0$ Hz), 7.51 (m, 3H, CH), 7.28 (t, 1H, CH, $J = 7.6$ Hz), 7.08 (d, 1H, CH, $J = 8.0$ Hz), 6.94 (t, 1H, CH, $J = 7.6$ Hz). ^{13}C NMR (CDCl_3) δ : 156.1, 148.0, 135.5, 130.2, 127.8, 126.0, 120.9, 119.8, 117.9, 117.4, 115.2, 113.6.

ORTEP Figures

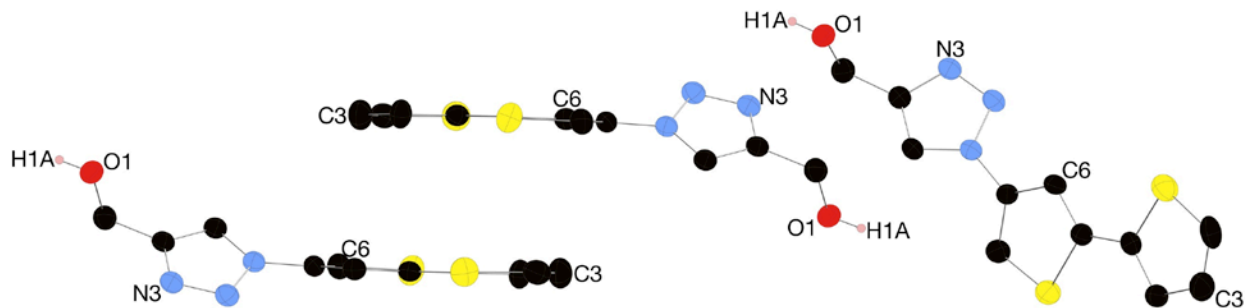


Figure S3.1. An ORTEP representation of **3.1** with three crystallographically adjacent molecules of **3.1**.

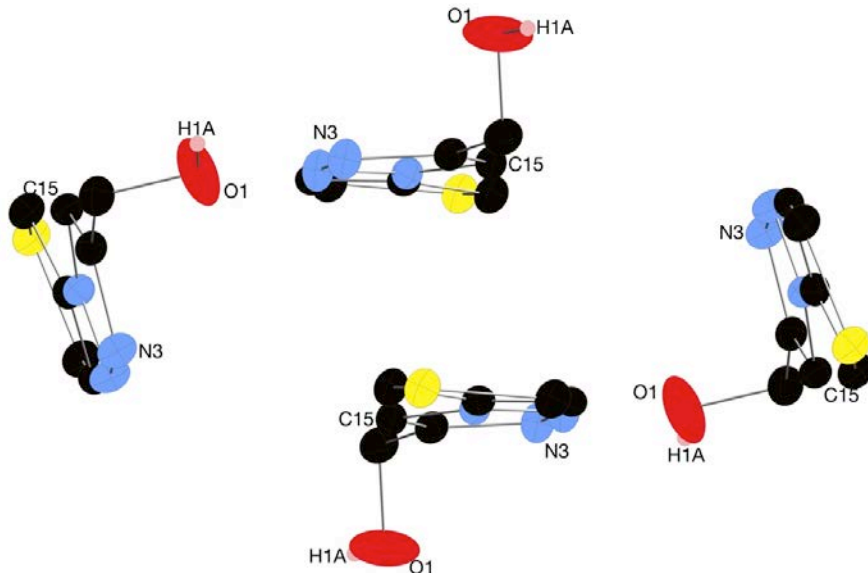


Figure S3.2. An ORTEP representation of **3.2** with four crystallographically adjacent molecules of **3.2**.

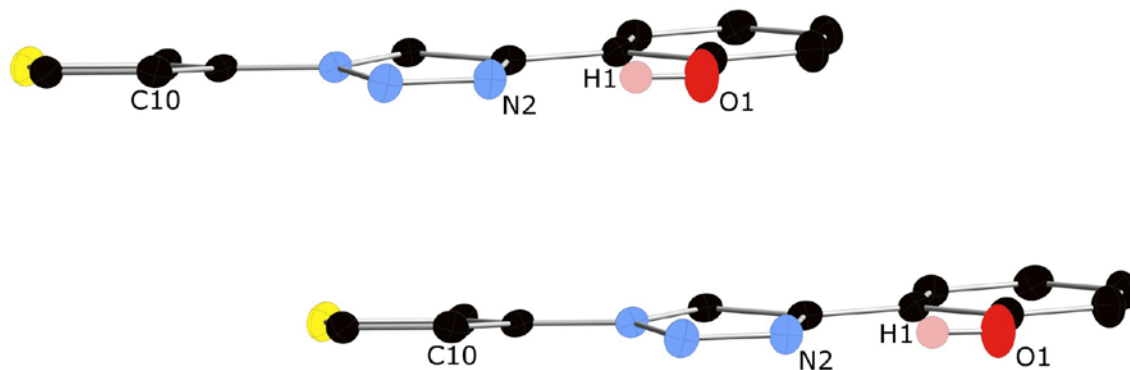


Figure S3.3. An ORTEP representation of **3.4** with two crystallographically adjacent molecules of **3.4**.

UV-Visible Absorption and Photoluminescence Spectra

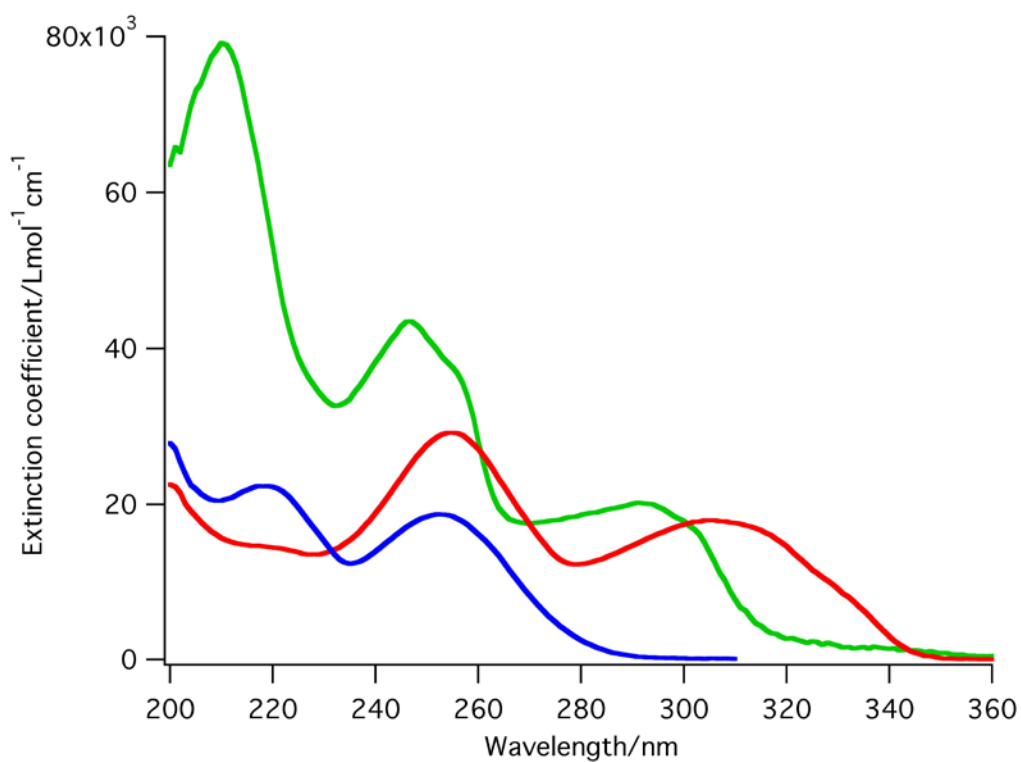


Figure S3.4. UV-visible absorption spectra of **3.1** in red, **3.2** in blue, and **3.4** in green, in MeOH.

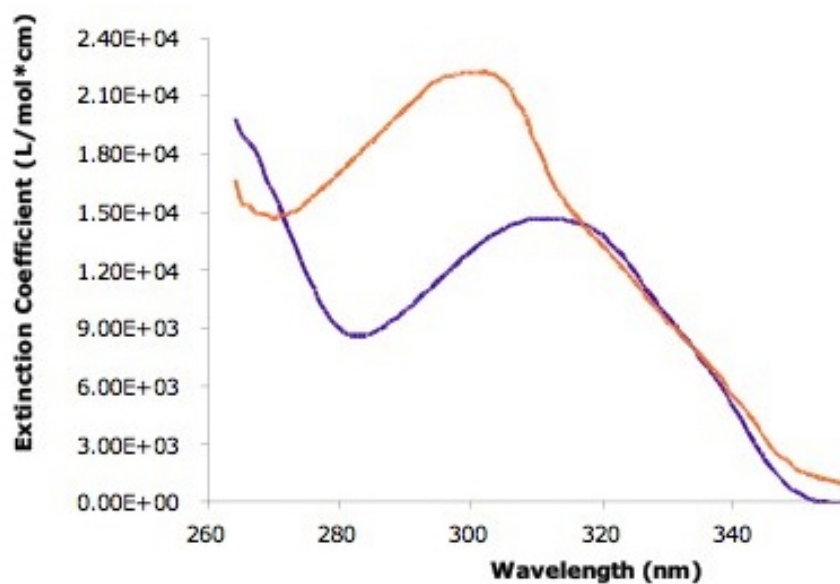


Figure S3.5. UV-visible absorption spectra of **3.1** in purple, and **3.3** in orange in DMF.

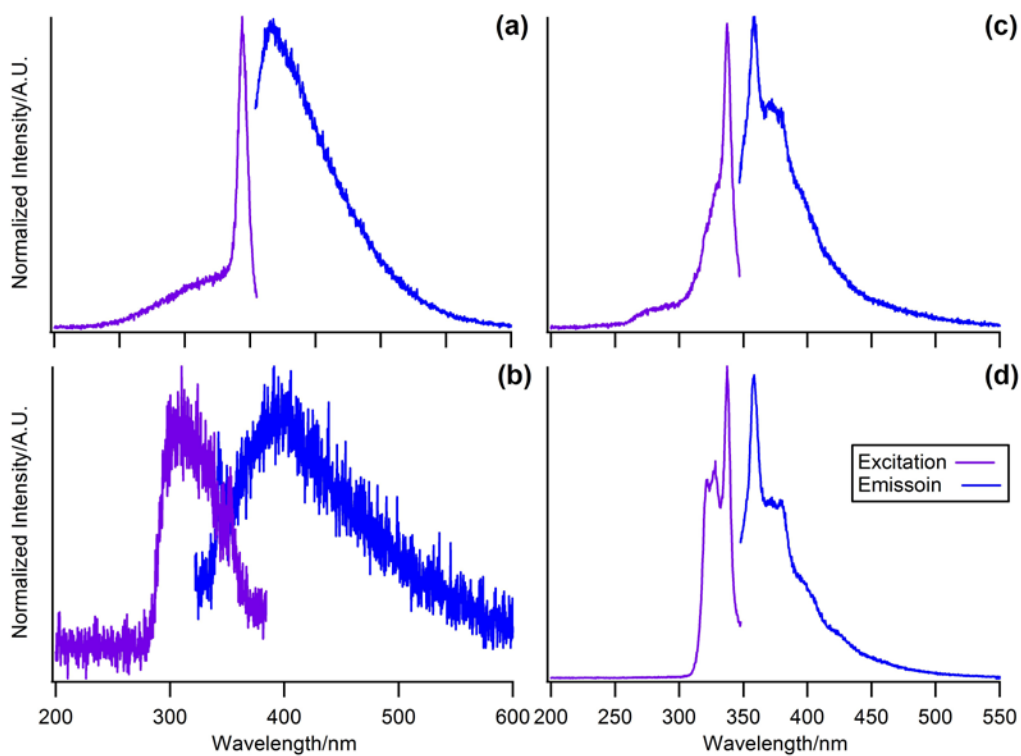


Figure S3.6. Normalized photoluminescence spectra, excitation in purple and emission in blue, of **3.1-3.4** in MeOH.

DFT Data

S3.7. Crystal structure Cartesian coordinates for the B3LYP/6-31+G* calculation of neutral compound **3.1**.

%mem=512MB

%chk=A6P3bithiopheneA.chk

B3LYP/6-31+G* SCF=Tight Opt Freq

bithioN3OH ligand

0 1

O	-2.19394486	2.93048333	0.00000000
H	-2.88333259	2.95967707	-0.44324099
C	-2.50944512	3.10170067	1.37584703
H	-3.12276629	2.40341797	1.65259140
H	-2.95271950	3.95542031	1.49959451
S	6.00727710	2.08915130	4.21157688
C	4.92005849	1.21199777	5.18051968
C	5.61179976	0.39772913	6.09175115
H	5.21035093	-0.14906173	6.72848821
C	7.00213093	0.52949547	5.90387997
H	7.62667669	0.05371641	6.40224484
C	7.34147028	1.38716021	4.95889918

H	8.22187025	1.58283717	4.73165380
S	2.41912211	0.39196928	6.00051551
C	3.47458702	1.33824097	5.01964795
C	2.76829417	2.09570017	4.13879086
H	3.15679698	2.67799693	3.52567832
C	1.37514134	1.89528909	4.26478829
C	1.03553889	0.98712707	5.24914328
H	0.16491939	0.74016381	5.46513889
N	0.41586137	2.53439529	3.44692992
N	0.51196312	3.85915987	3.17918537
N	-0.53112726	4.16293257	2.42432571
C	-0.69290585	2.00969699	2.86644172
H	-0.98191561	1.12599459	2.89794108
C	-1.29181855	3.05199241	2.22857969

S3.8. Crystal structure Cartesian coordinates for the B3LYP/6-31+G* calculation of neutral compound **3.2**.

%mem=512MB

%nproc=8

%chk=thioN3OH1.chk

B3LYP/6-31+g(d) SCF=Tight Opt=Tight Freq

thiopheneN3OH ligand

0 1

S	-4.39882335	-1.13355514	-2.18686459
---	-------------	-------------	-------------

C	-2.71170465	-1.42235914	-2.04090748
H	-2.33172874	-2.16823114	-1.63621500
C	-2.79851963	0.55154486	-3.26614372
H	-2.46216504	1.26002486	-3.76457012
C	-4.11549860	0.30357686	-3.08537116
H	-4.79291204	0.84969686	-3.41195204
C	-2.00884544	-0.39624394	-2.60554276
C	0.28041854	-1.09714714	-1.86608628
H	0.08027366	-1.81792714	-1.31260980
C	2.86070515	-0.95692714	-1.63100756
H	2.82371256	-1.86122314	-1.28136516
N	-0.58986956	-0.33375994	-2.56671014
N	1.34037385	0.47085686	-2.99833252
N	0.06060130	0.62426246	-3.25275316
C	1.51229317	-0.58320394	-2.14580020
O	3.32642689	-0.10281514	-0.62894732
H	4.06820316	-0.34979914	-0.38122196
H	2.99251970	-0.06355494	-1.98579861

S3.9. Crystal structure Cartesian coordinates for the B3LYP/6-31+G* calculation of neutral compound **3.3**.

%mem=512MB

%chk=bithioN3PhOHb.chk

opt freq b3lyp/6-31+g* geom=connectivity

bithioN3PhOH ligand

0 1			
S	-2.60330584	-0.28925619	0.00000000
O	-6.93884041	-5.88429051	4.86634115
H	-6.39649034	-5.24598427	4.80243537
N	-4.63372484	-2.83032531	2.16173367
N	-5.42543915	-4.07742363	3.69586304
N	-4.56977001	-3.10795851	3.48384160
C	-3.67941574	-1.58922987	0.28477773
H	-4.13007336	-2.07746411	-0.39462800
C	-3.80077423	-1.82534315	1.61833924
C	-5.53159803	-3.62320571	1.54297987
H	-5.75958476	-3.62320571	0.62057596
C	-6.04806741	-4.42959259	2.52421355
C	-7.05207788	-5.48259779	2.47423428
C	-7.63788661	-5.85027419	1.25963384
H	-7.37340987	-5.40706155	0.46308919
C	-8.59055101	-6.84024915	1.19455666
H	-8.97701262	-7.07436147	0.35896571
C	-8.98336449	-7.49306235	2.34642270
H	-9.64501095	-8.17288851	2.30477331
C	-2.29459248	-0.07650411	1.66571543
C	-3.01644096	-0.96493035	2.42581686
H	-2.99209128	-0.99844643	3.37464210
C	-7.45842508	-6.16442491	3.63625235

C	-8.41243283	-7.15740131	3.55815974
H	-8.67956774	-7.61512091	4.34689513
C	-1.32940614	0.97637716	2.24143789
C	-0.59343876	1.87881332	1.50616717
S	-1.05467969	1.15101146	3.88167066
C	0.20350307	2.71803231	2.34970582
H	-0.60079549	1.96200031	0.41787452
C	0.03046093	2.40720506	3.68019230
H	0.85963058	3.50036097	1.96396870
H	0.52366481	2.89911746	4.51622917

S3.10. Crystal structure Cartesian coordinates for the B3LYP/6-31+G* calculation of neutral compound **3.4**.

%mem=512MB

%chk=thioN3PhOHb.chk

opt freq b3lyp/6-31+g* geom=connectivity

thioN3PhOH ligand

0 1			
S	4.21487612	0.28925619	0.00000000
O	-0.12065845	-5.30577813	4.86634115
H	0.42169162	-4.66747189	4.80243537
N	2.18445712	-2.25181293	2.16173367
N	1.39274281	-3.49891125	3.69586304
N	2.24841195	-2.52944613	3.48384160

C	3.13876622	-1.01071749	0.28477773
H	2.68810860	-1.49895173	-0.39462800
C	3.01740773	-1.24683077	1.61833924
C	1.28658393	-3.04469333	1.54297987
H	1.05859720	-3.04469333	0.62057596
C	0.77011455	-3.85108021	2.52421355
C	-0.23389592	-4.90408541	2.47423428
C	-0.81970465	-5.27176181	1.25963384
H	-0.55522791	-4.82854917	0.46308919
C	-1.77236905	-6.26173677	1.19455666
H	-2.15883066	-6.49584909	0.35896571
C	-2.16518253	-6.91454997	2.34642270
H	-2.82682899	-7.59437613	2.30477331
C	4.52358948	0.50200827	1.66571543
H	5.11927814	1.15182003	2.02103681
C	3.80174100	-0.38641797	2.42581686
H	3.82609068	-0.41993405	3.37464210
C	-0.64024312	-5.58591253	3.63625235
C	-1.59425087	-6.57888893	3.55815974
H	-1.86138578	-7.03660853	4.34689513

S3.11. Calculated Cartesian coordinates optimized using the B3LYP/6-31+G* geometry of neutral compound **3.1**.

%mem=512MB

%chk=A6P3bithiopheneA.chk

B3LYP/6-31+G* SCF=Tight Opt Freq

bithioN3OH ligand

0 1

O,	0,	-3.306020774,	2.3623103952,	1.632513016
H,	0,	-4.154901743,	2.5081036687,	1.1897171138
C,	0,	-2.407334797,	3.4096409433,	1.264491129
H,	0,	-2.8023821273,	4.3921034169,	1.5621409417
H,	0,	-2.2478196312,	3.4285805418,	0.176305234
S,	0,	5.8523724158,	2.6906923297,	5.1481502128
C,	0,	4.905537081,	1.2227419356,	5.2967106843
C,	0,	5.6901429306,	0.1917821443,	5.7723921719
H,	0,	5.3130503503,	-0.8143792518,	5.9253116734
C,	0,	7.0427737862,	0.5722457241,	6.0079316231
H,	0,	7.8055102168,	-0.1065851829,	6.3743509522
C,	0,	7.2828108401,	1.8882028871,	5.708883398
H,	0,	8.2135192199,	2.4352606263,	5.7855252303
S,	0,	2.4104381819,	0.0266153205,	5.6574807167
C,	0,	3.4963690664,	1.2057565904,	4.9426960766
C,	0,	2.8180611575,	2.0271263499,	4.0715305362
H,	0,	3.2765906644,	2.8221752496,	3.497507234
C,	0,	1.432527295,	1.6992239759,	3.9747179682
C,	0,	1.0606085639,	0.6394645618,	4.7623115388
H,	0,	0.0831036137,	0.1934226465,	4.8801083778

N,	0,	0.5508342625,	2.4095242874,	3.1288727488
N,	0,	0.9624774406,	3.5507428561,	2.5147695405
N,	0,	-0.0379237272,	3.9985917648,	1.8109989728
C,	0,	-0.7445469498,	2.135471152,	2.7999471957
H,	0,	-1.2855027471,	1.2748325009,	3.1571932812
C,	0,	-1.1064113999,	3.1607366858,	1.9583546822

S3.12. Calculated Cartesian coordinates optimized using the B3LYP/6-31+G* geometry of neutral compound **3.2**.

%mem=512MB

%nproc=8

%chk=thioN3OH1.chk

B3LYP/6-31+g(d) SCF=Tight Opt=Tight Freq

thiopheneN3OH ligand

0 1

S,	0,-4.4057347009,	-1.0457562197,	-1.9659870226
C,	0,-2.6995276645,	-1.2070290657,	-1.7193971217
H,	0,-2.3154783043,	-1.9144980784,	-0.9978444294
C,	0,-2.8396538978,	0.4196119609,	-3.403289793
H,	0,-2.455254263,	1.1320660913,	-4.1215720573
C,	0,-4.163826958,	0.1529269887,	-3.1967011546
H,	0,-5.0150088904,	0.5978195858,	-3.6949755679
C,	0,-2.0012965025,	-0.3652827988,	-2.5484173101

C,	0,0.326602905,	-0.7270623896,	-1.6785013896
H,	0,0.0680336313,	-1.2426739818,	-0.7683342073
C,	0,2.9198248421,	-0.5780864918,	-1.6820689188
H,	0,3.5129494445,	-1.138827019,	-2.4194180076
N,	0,-0.5918722432,	-0.2623117173,	-2.573531391
N,	0,1.312800527,	0.3063768078,	-3.3837248373
N,	0,0.0304485753,	0.365061873,	-3.606751742
C,	0,1.5390007894,	-0.357060655,	-2.2117499293
O,	0,2.8062596553,	-1.3030343973,	-0.4566651067
H,	0,3.6931681443,	-1.450611899,	-0.0967386812
H,	0,3.4140258405,	0.3915871459,	-1.5225309127

S3.13. Calculated Cartesian coordinates optimized using the B3LYP/6-31+G* geometry of neutral compound **3.3**.

%mem=512MB

%chk=bithioN3PhOHb.chk

opt freq b3lyp/6-31+g* geom=connectivity

bithioN3PhOH ligand

0 1

S,	0,	-2.5177855294,	-0.2859048517,	0.0080418403
O,	0,	-6.666804206,	-6.2029759435,	4.7943500589
H,	0,	-5.9730040049,	-5.5047175566,	4.7312528728
N,	0,	-4.543073904,	-2.8921497796,	2.1559353436

N,	0,	-5.2199641033,	-4.2660385526,	3.6390727924
N,	0,	-4.3535001203,	-3.3176904929,	3.4250991388
C,	0,	-3.5609302938,	-1.6391669256,	0.2809332202
H,	0,	-3.9617132021,	-2.1976846577,	-0.5534038375
C,	0,	-3.7314244031,	-1.8619818877,	1.6235726082
C,	0,	-5.5504557289,	-3.5868856497,	1.5580322033
H,	0,	-5.8763474665,	-3.3765559067,	0.5523645428
C,	0,	-5.9884969311,	-4.4817395896,	2.5207419084
C,	0,	-7.0481913246,	-5.4925159587,	2.4872272462
C,	0,	-7.811883059,	-5.6873461729,	1.3200239163
H,	0,	-7.6017773652,	-5.0774023556,	0.4445429211
C,	0,	-8.8247705031,	-6.636916497,	1.2564229902
H,	0,	-9.3967536799,	-6.7640401713,	0.3418944651
C,	0,	-9.0956328773,	-7.4249499226,	2.3841507837
H,	0,	-9.8840545112,	-8.1725476333,	2.3514705158
C,	0,	-2.2798205925,	-0.0426898118,	1.7305705789
C,	0,	-3.0047030476,	-0.9607077426,	2.4560669872
H,	0,	-3.0078446681,	-1.0213624779,	3.537127403
C,	0,	-7.3338444276,	-6.2981548287,	3.6189096132
C,	0,	-8.3580860453,	-7.2559833058,	3.5499569665
H,	0,	-8.5511463383,	-7.8558689143,	4.4343412798
C,	0,	-1.4216376976,	1.0256142047,	2.2132020393
C,	0,	-0.3617721391,	1.6362116196,	1.5739802038
S,	0,	-1.6563755763,	1.7205504404,	3.8052924224
C,	0,	0.2640001616,	2.6480210109,	2.3573060003

H,	0,	-0.02616977,	1.3499752112,	0.5823302305
C,	0,	-0.319462501,	2.8016290192,	3.5881734046
H,	0,	1.1173189512,	3.228511288,	2.0233227581
H,	0,	-0.0449017059,	3.4857802524,	4.3805712917

S3.14. Calculated Cartesian coordinates optimized using the B3LYP/6-31+G* geometry of neutral compound **3.4**.

%mem=512MB

%chk=thioN3PhOHb.chk

opt freq b3lyp/6-31+g* geom=connectivity

thioN3PhOH ligand

0 1

S,	0,	4.3616891718,	0.2254541074,	-0.0079531351
O,	0,	-0.0527305823,	-5.4168955446,	4.8741393885
H,	0,	0.6309761575,	-4.7085452154,	4.8115428184
N,	0,	2.2258552066,	-2.2758622608,	2.1591882289
N,	0,	1.4536463036,	-3.5462344158,	3.687462591
N,	0,	2.3140531387,	-2.5930002956,	3.4704619065
C,	0,	3.320992405,	-1.1266299758,	0.2774537177
H,	0,	2.9868798369,	-1.7446487783,	-0.5443009734
C,	0,	3.0566612869,	-1.2664634587,	1.6168319105
C,	0,	1.2900272583,	-3.0454355558,	1.5373155658

H,	0,	1.0490135011,	-2.9267725136,	0.4934999682
C,	0,	0.7901000586,	-3.8730859181,	2.5296537238
C,	0,	-0.2395538868,	-4.9142331146,	2.4897148946
C,	0,	-0.8893579512,	-5.2296730607,	1.2806204173
H,	0,	-0.6142255135,	-4.6898757832,	0.3775284057
C,	0,	-1.8706670063,	-6.211344441,	1.210166998
H,	0,	-2.3541744041,	-6.4324784585,	0.2630568117
C,	0,	-2.2251083453,	-6.9093652801,	2.3734697391
H,	0,	-2.9902128964,	-7.6805941244,	2.3357295735
C,	0,	4.44075709,	0.5864413392,	1.6869843858
H,	0,	5.0258145812,	1.4273920428,	2.0350586068
C,	0,	3.6995229318,	-0.2843974162,	2.435024762
H,	0,	3.6026233954,	-0.2491460336,	3.512492891
C,	0,	-0.6086242218,	-5.6300901721,	3.6570727191
C,	0,	-1.6006202149,	-6.6207357315,	3.5810536966
H,	0,	-1.8594580809,	-7.149753001,	4.4933976781

Table S3.1. Summary of Calculated Thermochemistry Values from Gaussian (B3LYP/6-31+G*) for **3.1-3.4** in Hartree/Particle at T=289.15 K, P=1 Atm.

	3.1	3.2	3.3	3.4
ϵ_e	-1460.39603295	-908.576926167	-1652.16397298	-1100.34493788
ϵ_{ZPE}	0.185492	0.138428	0.238733	0.191679
E_{tot}	0.200679	0.149062	0.256513	0.204885
H_{corr}	0.201623	0.150006	0.257457	0.205830
G_{corr}	0.138864	0.099539	0.189275	0.149604
$E_0 = \epsilon_e + \epsilon_{ZPE}$	-1460.210541	-908.438498	-1651.925240	-1100.153259
$E_T = \epsilon_e + E_{tot}$	-1460.195354	-908.427864	-1651.907460	-1100.140052
$H_T = \epsilon_e + H_{corr}$	-1460.194410	-908.426920	-1651.906516	-1100.139108
$G_T = \epsilon_e + G_{corr}$	-1460.257169	-908.477387	-1651.974698	-1100.195334

S3.15. Crystal data tables for compound **3.1**, N09013b

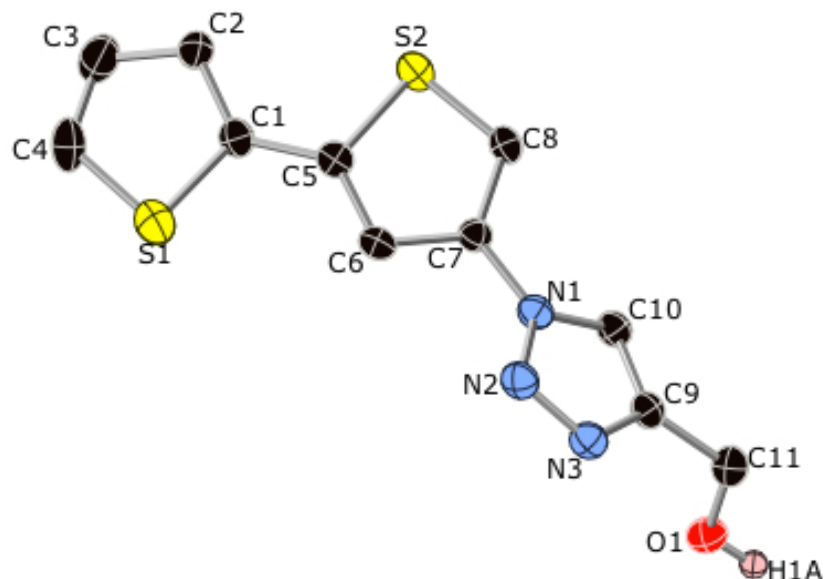


Table S3.2. Crystal data and structure refinement for N09013b.

Identification code	n09013b
Empirical formula	C ₁₁ H ₉ N ₃ O S ₂
Formula weight	263.33
Temperature	293(2) K
Wavelength	0.71073 Å
Crystal system, space group	Monoclinic, P2(1)/c
Unit cell dimensions	a = 13.321(3) Å alpha = 90 deg. b = 7.8902(16) Å beta = 92.32(3) deg. c = 11.259(2) Å gamma = 90 deg.
Volume	1182.4(4) Å ³
Z, Calculated density	4, 1.479 Mg/m ³
Absorption coefficient	0.436 mm ⁻¹
F(000)	544
Crystal size	0.25 x 0.15 x 0.10 mm

Theta range for data collection	3.00 to 27.45 deg.
Limiting indices	-17<=h<=17, -10<=k<=10, -14<=l<=14
Reflections collected / unique	4654 / 2679 [R(int) = 0.0355]
Completeness to theta = 27.45	99.4 %
Absorption correction	Semi-empirical from equivalents
Max. and min. transmission	0.9577 and 0.8989
Refinement method	Full-matrix least-squares on F ²
Data / restraints / parameters	2679 / 0 / 155
Goodness-of-fit on F ²	1.033
Final R indices [I>2sigma(I)]	R1 = 0.0607, wR2 = 0.1546
R indices (all data)	R1 = 0.1086, wR2 = 0.1836
Largest diff. peak and hole	.423 and -.435 e.A ⁻³

Table S3.3. Atomic coordinates ($\times 10^4$) and equivalent isotropic displacement parameters ($\text{\AA}^2 \times 10^3$) for N09013b. $U(\text{eq})$ is defined as one third of the trace of the orthogonalized U_{ij} tensor.

	x	y	z	$U(\text{eq})$
S(1)	4211(1)	2631(2)	9614(1)	70(1)
C(1)	4998(3)	1519(4)	8753(3)	49(1)
C(2)	4451(3)	487(5)	7943(4)	60(1)
C(3)	3413(4)	654(6)	8110(5)	78(1)
C(4)	3187(3)	1741(6)	8950(4)	69(1)
S(2)	6850(1)	480(2)	8024(1)	64(1)
C(5)	6088(3)	1679(4)	8896(3)	46(1)

C(6)	6645(3)	2639(4)	9679(3)	47(1)
C(7)	7687(3)	2385(4)	9567(3)	42(1)
C(8)	7912(3)	1234(5)	8692(3)	52(1)
O(1)	10496(2)	3697(3)	13358(2)	54(1)
N(1)	8432(2)	3195(3)	10294(2)	43(1)
N(2)	8368(2)	4874(4)	10532(3)	49(1)
N(3)	9174(2)	5259(4)	11203(3)	48(1)
C(10)	9282(3)	2530(4)	10810(3)	46(1)
C(11)	10691(3)	3914(5)	12135(3)	55(1)
C(9)	9751(3)	3851(4)	11377(3)	45(1)

Table S3.4. Bond lengths [Å] and angles [deg] for N09013b.

S(1)-C(4)	1.683(5)
S(1)-C(1)	1.701(4)
C(1)-C(2)	1.404(5)
C(1)-C(5)	1.460(5)
C(2)-C(3)	1.409(6)
C(2)-H(2)	0.9300
C(3)-C(4)	1.321(6)
C(3)-H(3A)	0.9300
C(4)-H(4)	0.9300
S(2)-C(8)	1.684(4)
S(2)-C(5)	1.724(4)

C(5)-C(6)	1.360(5)
C(6)-C(7)	1.413(5)
C(6)-H(6A)	0.9300
C(7)-C(8)	1.381(5)
C(7)-N(1)	1.413(4)
C(8)-H(8)	0.9300
O(1)-C(11)	1.422(4)
O(1)-H(1A)	0.8200
N(1)-N(2)	1.355(4)
N(1)-C(10)	1.356(4)
N(2)-N(3)	1.323(4)
N(3)-C(9)	1.361(4)
C(10)-C(9)	1.361(5)
C(10)-H(10A)	0.9300
C(11)-C(9)	1.487(5)
C(11)-H(11A)	0.9700
C(11)-H(11B)	0.9700
C(4)-S(1)-C(1)	92.2(2)
C(2)-C(1)-C(5)	127.6(3)
C(2)-C(1)-S(1)	110.7(3)
C(5)-C(1)-S(1)	121.7(3)
C(1)-C(2)-C(3)	110.2(4)
C(1)-C(2)-H(2)	124.9
C(3)-C(2)-H(2)	124.9
C(4)-C(3)-C(2)	114.2(4)

C(4)-C(3)-H(3A)	122.9
C(2)-C(3)-H(3A)	122.9
C(3)-C(4)-S(1)	112.7(3)
C(3)-C(4)-H(4)	123.7
S(1)-C(4)-H(4)	123.7
C(8)-S(2)-C(5)	93.14(18)
C(6)-C(5)-C(1)	129.4(3)
C(6)-C(5)-S(2)	110.9(3)
C(1)-C(5)-S(2)	119.7(3)
C(5)-C(6)-C(7)	112.0(3)
C(5)-C(6)-H(6A)	124.0
C(7)-C(6)-H(6A)	124.0
C(8)-C(7)-C(6)	113.6(3)
C(8)-C(7)-N(1)	122.8(3)
C(6)-C(7)-N(1)	123.6(3)
C(7)-C(8)-S(2)	110.4(3)
C(7)-C(8)-H(8)	124.8
S(2)-C(8)-H(8)	124.8
C(11)-O(1)-H(1A)	109.5
N(2)-N(1)-C(10)	110.6(3)
N(2)-N(1)-C(7)	120.5(3)
C(10)-N(1)-C(7)	128.9(3)
N(3)-N(2)-N(1)	106.3(3)
N(2)-N(3)-C(9)	109.6(3)
N(1)-C(10)-C(9)	105.3(3)

N(1)-C(10)-H(10A)	127.3
C(9)-C(10)-H(10A)	127.3
O(1)-C(11)-C(9)	111.7(3)
O(1)-C(11)-H(11A)	109.3
C(9)-C(11)-H(11A)	109.3
O(1)-C(11)-H(11B)	109.3
C(9)-C(11)-H(11B)	109.3
H(11A)-C(11)-H(11B)	107.9
C(10)-C(9)-N(3)	108.1(3)
C(10)-C(9)-C(11)	130.9(3)
N(3)-C(9)-C(11)	120.9(3)

Symmetry transformations used to generate equivalent atoms:

Table S3.5. Anisotropic displacement parameters ($\text{Å}^2 \times 10^3$) for N09013b. The anisotropic displacement factor exponent takes the form: $-2 \pi^2 [h^2 a^{*2} U_{11} + \dots + 2 h k a^* b^* U_{12}]$

	U11	U22	U33	U23	U13	U12
S(1)	62(1)	73(1)	77(1)	-6(1)	10(1)	9(1)
C(1)	50(2)	43(2)	53(2)	6(2)	3(2)	3(2)
C(2)	46(2)	61(2)	72(3)	-16(2)	-5(2)	2(2)
C(3)	60(3)	71(3)	102(4)	-4(3)	-14(3)	-2(2)
C(4)	45(2)	67(3)	96(3)	22(3)	5(2)	10(2)
S(2)	60(1)	72(1)	60(1)	-22(1)	9(1)	-3(1)

C(5)	50(2)	43(2)	46(2)	4(2)	4(2)	2(2)
C(6)	54(2)	42(2)	44(2)	-4(2)	6(2)	3(2)
C(7)	44(2)	42(2)	41(2)	-1(2)	4(1)	-2(2)
C(8)	43(2)	63(2)	53(2)	-7(2)	14(2)	2(2)
O(1)	62(2)	52(2)	49(1)	0(1)	-5(1)	0(1)
N(1)	47(2)	38(2)	44(2)	-1(1)	5(1)	1(1)
N(2)	52(2)	39(2)	57(2)	-1(1)	3(2)	5(1)
N(3)	53(2)	39(2)	53(2)	0(1)	5(1)	0(1)
C(10)	48(2)	40(2)	50(2)	1(2)	5(2)	4(2)
C(11)	49(2)	58(2)	60(2)	2(2)	3(2)	-2(2)
C(9)	45(2)	47(2)	44(2)	5(2)	10(2)	-2(2)

Table S3.6. Hydrogen coordinates ($\times 10^4$) and isotropic displacement parameters ($\text{\AA}^2 \times 10^3$) for N09013b.

	x	y	z	U(eq)
H(2)	4733	-206	7377	72
H(3A)	2929	51	7667	94
H(4)	2533	1989	9152	83
H(6A)	6372	3377	10224	56
H(8)	8559	921	8500	63
H(1A)	11027	3734	13752	82
H(10A)	9498	1410	10782	55
H(11A)	11143	3029	11889	66

H(11B) 11020 4996 12025 66

Table S3.7. Torsion angles [deg] for N09013b.

C(4)-S(1)-C(1)-C(2)	1.0(3)
C(4)-S(1)-C(1)-C(5)	-178.7(3)
C(5)-C(1)-C(2)-C(3)	178.2(4)
S(1)-C(1)-C(2)-C(3)	-1.5(5)
C(1)-C(2)-C(3)-C(4)	1.4(6)
C(2)-C(3)-C(4)-S(1)	-0.7(6)
C(1)-S(1)-C(4)-C(3)	-0.2(4)
C(2)-C(1)-C(5)-C(6)	-178.8(4)
S(1)-C(1)-C(5)-C(6)	0.8(5)
C(2)-C(1)-C(5)-S(2)	-1.3(5)
S(1)-C(1)-C(5)-S(2)	178.3(2)
C(8)-S(2)-C(5)-C(6)	0.2(3)
C(8)-S(2)-C(5)-C(1)	-177.8(3)
C(1)-C(5)-C(6)-C(7)	177.4(3)
S(2)-C(5)-C(6)-C(7)	-0.3(4)
C(5)-C(6)-C(7)-C(8)	0.3(4)
C(5)-C(6)-C(7)-N(1)	-178.4(3)
C(6)-C(7)-C(8)-S(2)	-0.2(4)
N(1)-C(7)-C(8)-S(2)	178.5(3)
C(5)-S(2)-C(8)-C(7)	0.0(3)

C(8)-C(7)-N(1)-N(2)	136.5(4)
C(6)-C(7)-N(1)-N(2)	-45.0(5)
C(8)-C(7)-N(1)-C(10)	-41.4(5)
C(6)-C(7)-N(1)-C(10)	137.1(4)
C(10)-N(1)-N(2)-N(3)	-0.5(4)
C(7)-N(1)-N(2)-N(3)	-178.7(3)
N(1)-N(2)-N(3)-C(9)	0.9(4)
N(2)-N(1)-C(10)-C(9)	-0.2(4)
C(7)-N(1)-C(10)-C(9)	177.9(3)
N(1)-C(10)-C(9)-N(3)	0.7(4)
N(1)-C(10)-C(9)-C(11)	177.3(3)
N(2)-N(3)-C(9)-C(10)	-1.1(4)
N(2)-N(3)-C(9)-C(11)	-178.1(3)
O(1)-C(11)-C(9)-C(10)	-91.8(4)
O(1)-C(11)-C(9)-N(3)	84.5(4)

Symmetry transformations used to generate equivalent atoms:

S3.16. Crystal data tables for compound **3.2**, N09024b.

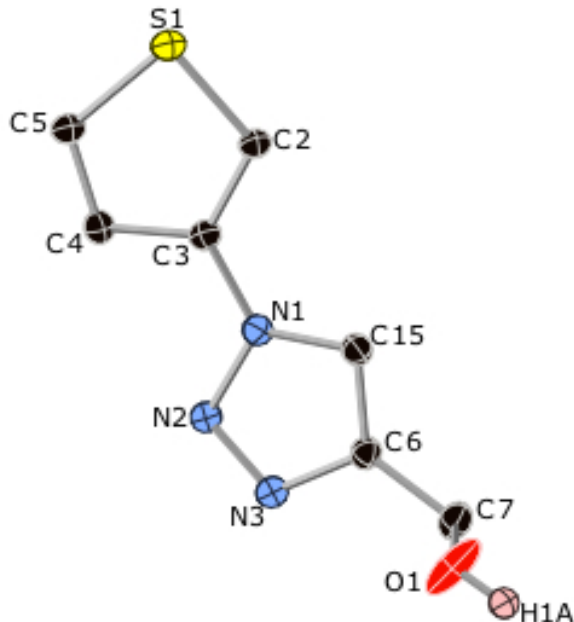


Table S3.8. Crystal data and structure refinement for N09024b.

Identification code	n09024b
Empirical formula	C7 H7 N3 O S
Formula weight	181.22
Temperature	150(2) K
Wavelength	0.71073 Å
Crystal system, space group	Orthorhombic, Pbc _a
Unit cell dimensions	a = 21.383(4) Å alpha = 90 deg. b = 9.840(2) Å beta = 90 deg. c = 7.4392(15) Å gamma = 90 deg.
Volume	1565.3(5) Å ³
Z, Calculated density	8, 1.538 Mg/m ³
Absorption coefficient	0.362 mm ⁻¹
F(000)	752

Crystal size	0.25 x 0.10 x 0.10 mm
Theta range for data collection	2.81 to 30.07 deg.
Limiting indices	-30<=h<=30, -13<=k<=13, -10<=l<=10
Reflections collected / unique	8274 / 2296 [R(int) = 0.0365]
Completeness to theta = 30.07	99.6 %
Absorption correction	Semi-empirical from equivalents
Max. and min. transmission	0.9647 and 0.9150
Refinement method	Full-matrix least-squares on F ²
Data / restraints / parameters	2296 / 0 / 123
Goodness-of-fit on F ²	1.078
Final R indices [I>2sigma(I)]	R1 = 0.0541, wR2 = 0.1567
R indices (all data)	R1 = 0.0716, wR2 = 0.1709
Extinction coefficient	0.022(6)
Largest diff. peak and hole	.608 and -.451 e.A ⁻³

Table S3.9. Atomic coordinates ($\times 10^4$) and equivalent isotropic displacement parameters ($\text{\AA}^2 \times 10^3$) for N09024b. $U(\text{eq})$ is defined as one third of the trace of the orthogonalized U_{ij} tensor.

	x	y	z	$U(\text{eq})$
S(1)	2486(1)	4584(1)	1903(2)	36(1)
C(2)	1697(1)	4878(5)	2098(8)	34(2)
C(4)	1737(2)	2873(6)	451(9)	30(2)
C(5)	2353(1)	3124(3)	694(5)	36(1)
S(1B)	2498(1)	3106(2)	664(3)	34(1)

C(2B)	1714(2)	2726(14)	660(20)	25(3)
C(4B)	1748(4)	4813(14)	2120(20)	43(4)
C(5B)	2362(4)	4610(6)	1771(14)	34(1)
C(3)	1368(1)	3834(2)	1339(2)	29(1)
C(15)	297(1)	4547(2)	2334(2)	32(1)
C(7)	-909(1)	4404(2)	2650(3)	40(1)
N(1)	704(1)	3771(2)	1392(2)	29(1)
N(3)	-198(1)	2953(2)	813(2)	36(1)
N(2)	400(1)	2797(2)	470(2)	36(1)
C(6)	-279(1)	4024(2)	1958(2)	32(1)
O(1)	-1127(1)	3536(2)	3997(3)	74(1)

Table S3.10. Bond lengths [Å] and angles [deg] for N09024b.

S(1)-C(2)	1.7178
S(1)-C(5)	1.7182
C(2)-C(3)	1.367(4)
C(2)-H(2)	0.9500
C(4)-C(5)	1.3522
C(4)-C(3)	1.398(4)
C(4)-H(4)	0.9500
C(5)-H(5)	0.9500
S(1B)-C(5B)	1.7182
S(1B)-C(2B)	1.7186

C(2B)-C(3)	1.411(9)
C(2B)-H(2B)	0.9500
C(4B)-C(5B)	1.3524
C(4B)-C(3)	1.388(11)
C(4B)-H(4B)	0.9500
C(5B)-H(5B)	0.9500
C(3)-N(1)	1.421(2)
C(15)-N(1)	1.353(2)
C(15)-C(6)	1.364(3)
C(15)-H(15A)	0.9500
C(7)-O(1)	1.397(2)
C(7)-C(6)	1.491(2)
C(7)-H(7A)	0.9900
C(7)-H(7B)	0.9900
N(1)-N(2)	1.346(2)
N(3)-N(2)	1.314(2)
N(3)-C(6)	1.366(2)
O(1)-H(1A)	0.8400
C(2)-S(1)-C(5)	91.3
C(3)-C(2)-S(1)	110.09(16)
C(3)-C(2)-H(2)	125.0
S(1)-C(2)-H(2)	125.0
C(5)-C(4)-C(3)	111.27(9)
C(5)-C(4)-H(4)	124.4
C(3)-C(4)-H(4)	124.4

C(4)-C(5)-S(1)	112.6
C(4)-C(5)-H(5)	123.7
S(1)-C(5)-H(5)	123.7
C(5B)-S(1B)-C(2B)	91.3
C(3)-C(2B)-S(1B)	110.0(4)
C(3)-C(2B)-H(2B)	125.0
S(1B)-C(2B)-H(2B)	125.0
C(5B)-C(4B)-C(3)	112.62(18)
C(5B)-C(4B)-H(4B)	123.7
C(3)-C(4B)-H(4B)	123.7
C(4B)-C(5B)-S(1B)	112.6
C(4B)-C(5B)-H(5B)	123.7
S(1B)-C(5B)-H(5B)	123.7
C(2)-C(3)-C(4B)	5.3(5)
C(2)-C(3)-C(4)	114.41(14)
C(4B)-C(3)-C(4)	109.7(2)
C(2)-C(3)-C(2B)	117.33(18)
C(4B)-C(3)-C(2B)	112.3(3)
C(4)-C(3)-C(2B)	8.9(11)
C(2)-C(3)-N(1)	122.37(14)
C(4B)-C(3)-N(1)	127.1(2)
C(4)-C(3)-N(1)	123.17(14)
C(2B)-C(3)-N(1)	119.93(17)
N(1)-C(15)-C(6)	105.18(15)
N(1)-C(15)-H(15A)	127.4

C(6)-C(15)-H(15A)	127.4
O(1)-C(7)-C(6)	113.30(16)
O(1)-C(7)-H(7A)	108.9
C(6)-C(7)-H(7A)	108.9
O(1)-C(7)-H(7B)	108.9
C(6)-C(7)-H(7B)	108.9
H(7A)-C(7)-H(7B)	107.7
N(2)-N(1)-C(15)	110.78(14)
N(2)-N(1)-C(3)	119.99(14)
C(15)-N(1)-C(3)	129.17(15)
N(2)-N(3)-C(6)	109.49(15)
N(3)-N(2)-N(1)	106.78(14)
C(15)-C(6)-N(3)	107.77(15)
C(15)-C(6)-C(7)	130.66(18)
N(3)-C(6)-C(7)	121.51(17)
C(7)-O(1)-H(1A)	109.5

Symmetry transformations used to generate equivalent atoms:

Table S3.11. Anisotropic displacement parameters ($\text{Å}^2 \times 10^3$) for N09024b. The anisotropic displacement factor exponent takes the form: $-2 \pi^2 [h^2 a^{*2} U_{11} + \dots + 2 h k a^* b^* U_{12}]$

U11	U22	U33	U23	U13	U12
-----	-----	-----	-----	-----	-----

S(1)	27(1)	35(1)	47(1)	-2(1)	1(1)	-4(1)
C(2)	25(2)	31(3)	46(4)	-1(3)	5(2)	-3(2)
C(4)	34(2)	29(2)	27(2)	1(2)	3(1)	1(2)
C(5)	27(1)	35(1)	47(1)	-2(1)	1(1)	-4(1)
S(1B)	28(1)	37(1)	37(1)	4(1)	-1(1)	-1(1)
C(2B)	22(4)	28(5)	26(4)	11(4)	1(3)	-3(3)
C(4B)	46(6)	28(7)	55(10)	-6(6)	-22(6)	3(5)
C(5B)	28(1)	37(1)	37(1)	4(1)	-1(1)	-1(1)
C(3)	27(1)	30(1)	30(1)	3(1)	-1(1)	-1(1)
C(15)	32(1)	30(1)	32(1)	-3(1)	3(1)	1(1)
C(7)	33(1)	39(1)	46(1)	4(1)	5(1)	6(1)
N(1)	28(1)	28(1)	31(1)	-1(1)	-1(1)	0(1)
N(3)	28(1)	35(1)	46(1)	-6(1)	0(1)	0(1)
N(2)	28(1)	34(1)	48(1)	-10(1)	0(1)	-1(1)
C(6)	31(1)	29(1)	35(1)	2(1)	1(1)	2(1)
O(1)	32(1)	120(2)	70(1)	51(1)	18(1)	23(1)

Table S3.12. Hydrogen coordinates ($\times 10^4$) and isotropic displacement parameters ($\text{\AA}^2 \times 10^3$) for N09024b.

	x	y	z	U(eq)
H(2)	1516	5653	2653	41
H(4)	1576	2138	-235	36

H(5)	2677	2556	246	44
H(2B)	1538	1891	262	31
H(4B)	1594	5546	2826	52
H(5B)	2682	5230	2101	41
H(15A)	393	5295	3094	38
H(7A)	-892	5342	3130	47
H(7B)	-1210	4398	1639	47
H(1A)	-1482	3793	4338	111

Table S3.13. Torsion angles [deg] for N09024b.

C(5)-S(1)-C(2)-C(3)	3.4(4)
C(3)-C(4)-C(5)-S(1)	-3.3(4)
C(2)-S(1)-C(5)-C(4)	0.0
C(5B)-S(1B)-C(2B)-C(3)	6.2(11)
C(3)-C(4B)-C(5B)-S(1B)	-6.4(12)
C(2B)-S(1B)-C(5B)-C(4B)	0.0
S(1)-C(2)-C(3)-C(4B)	21(11)
S(1)-C(2)-C(3)-C(4)	-6.0(8)
S(1)-C(2)-C(3)-C(2B)	3.4(8)
S(1)-C(2)-C(3)-N(1)	176.5(2)
C(5B)-C(4B)-C(3)-C(2)	-152(13)
C(5B)-C(4B)-C(3)-C(4)	2.2(11)
C(5B)-C(4B)-C(3)-C(2B)	11(2)

C(5B)-C(4B)-C(3)-N(1)	-177.8(5)
C(5)-C(4)-C(3)-C(2)	6.1(8)
C(5)-C(4)-C(3)-C(4B)	3.6(7)
C(5)-C(4)-C(3)-C(2B)	-105(3)
C(5)-C(4)-C(3)-N(1)	-176.4(2)
S(1B)-C(2B)-C(3)-C(2)	-9.3(13)
S(1B)-C(2B)-C(3)-C(4B)	-11(2)
S(1B)-C(2B)-C(3)-C(4)	63.7(17)
S(1B)-C(2B)-C(3)-N(1)	177.4(5)
C(6)-C(15)-N(1)-N(2)	-0.3(2)
C(6)-C(15)-N(1)-C(3)	-177.53(16)
C(2)-C(3)-N(1)-N(2)	173.2(4)
C(4B)-C(3)-N(1)-N(2)	175.9(11)
C(4)-C(3)-N(1)-N(2)	-4.0(5)
C(2B)-C(3)-N(1)-N(2)	-13.8(10)
C(2)-C(3)-N(1)-C(15)	-9.8(4)
C(4B)-C(3)-N(1)-C(15)	-7.1(11)
C(4)-C(3)-N(1)-C(15)	173.0(4)
C(2B)-C(3)-N(1)-C(15)	163.2(10)
C(6)-N(3)-N(2)-N(1)	-0.2(2)
C(15)-N(1)-N(2)-N(3)	0.3(2)
C(3)-N(1)-N(2)-N(3)	177.80(14)
N(1)-C(15)-C(6)-N(3)	0.2(2)
N(1)-C(15)-C(6)-C(7)	177.08(18)
N(2)-N(3)-C(6)-C(15)	0.0(2)

N(2)-N(3)-C(6)-C(7)	-177.25(17)
O(1)-C(7)-C(6)-C(15)	-100.5(3)
O(1)-C(7)-C(6)-N(3)	76.0(2)

Symmetry transformations used to generate equivalent atoms:

S3.17. Crystal data tables for compound **3.4**, B09049a.

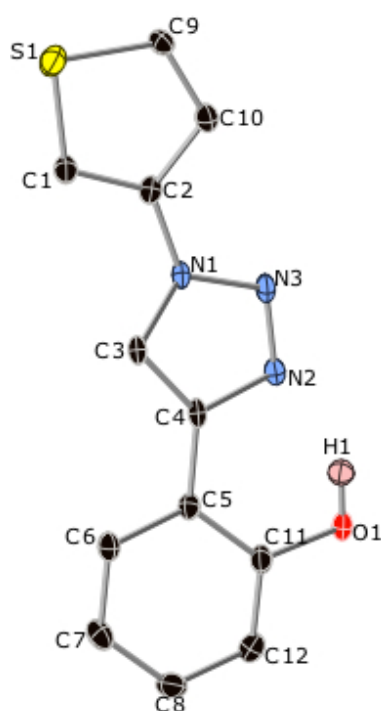


Table S3.14. Crystal data and structure refinement for B09049a.

Identification code	b09049a
Empirical formula	C ₁₂ H ₉ N ₃ O S
Formula weight	243.29
Temperature	150(2) K
Wavelength	0.71073 Å
Crystal system, space group	Monoclinic, P2(1)/c

Unit cell dimensions	a = 16.8378(18) Å alpha = 90 deg. b = 5.0024(5) Å beta = 98.840(3) deg. c = 13.1719(13) Å gamma = 90 deg.
Volume	1096.28(19) Å ³
Z, Calculated density	4, 1.486 Mg/m ³
Absorption coefficient	0.280 mm ⁻¹
F(000)	512
Crystal size	0.20 x 0.08 x 0.05 mm
Theta range for data collection	2.45 to 25.00 deg.
Limiting indices	-19<=h<=19, -5<=k<=5, -8<=l<=15
Reflections collected / unique	6400 / 1898 [R(int) = 0.0348]
Completeness to theta = 25.00	98.5 %
Absorption correction	Semi-empirical from equivalents
Max. and min. transmission	0.9861 and 0.9461
Refinement method	Full-matrix least-squares on F ²
Data / restraints / parameters	1898 / 0 / 155
Goodness-of-fit on F ²	1.040
Final R indices [I>2sigma(I)]	R1 = 0.0432, wR2 = 0.1021
R indices (all data)	R1 = 0.0659, wR2 = 0.1111
Largest diff. peak and hole	0.257 and -0.258 e.Å ⁻³

Table S3.15. Atomic coordinates ($\times 10^4$) and equivalent isotropic displacement parameters ($\text{Å}^2 \times 10^3$) for B09049a. $U(\text{eq})$ is defined as one third of the trace of the orthogonalized U_{ij} tensor.

x	y	z	$U(\text{eq})$
---	---	---	----------------

S(1)	4127(1)	11901(2)	2358(1)	37(1)
O(1)	2002(1)	716(4)	6097(1)	43(1)
N(1)	3121(1)	6821(4)	4019(1)	23(1)
N(2)	2792(1)	4329(5)	5198(2)	30(1)
N(3)	3281(1)	6266(5)	5035(2)	30(1)
C(1)	3514(2)	9303(5)	2578(2)	29(1)
C(2)	3566(2)	8829(5)	3602(2)	25(1)
C(3)	2531(2)	5236(5)	3544(2)	24(1)
C(4)	2314(2)	3624(5)	4298(2)	25(1)
C(5)	1714(2)	1519(5)	4259(2)	25(1)
C(6)	1253(2)	784(6)	3326(2)	29(1)
C(7)	682(2)	-1195(6)	3276(2)	35(1)
C(8)	555(2)	-2499(6)	4161(2)	37(1)
C(9)	4464(2)	12326(6)	3638(2)	28(1)
C(10)	4106(2)	10549(5)	4222(2)	29(1)
C(11)	1579(2)	156(6)	5152(2)	30(1)
C(12)	1006(2)	-1829(6)	5092(2)	38(1)

Table S3.16. Bond lengths [Å] and angles [deg] for B09049a.

S(1)-C(9)	1.707(3)
S(1)-C(1)	1.711(3)
O(1)-C(11)	1.365(3)

O(1)-H(1)	0.8400
N(1)-C(3)	1.348(3)
N(1)-N(3)	1.353(3)
N(1)-C(2)	1.414(3)
N(2)-N(3)	1.310(3)
N(2)-C(4)	1.373(3)
C(1)-C(2)	1.359(3)
C(1)-H(1A)	0.9500
C(2)-C(10)	1.416(4)
C(3)-C(4)	1.371(3)
C(3)-H(3)	0.9500
C(4)-C(5)	1.455(4)
C(5)-C(6)	1.398(4)
C(5)-C(11)	1.408(4)
C(6)-C(7)	1.375(4)
C(6)-H(6)	0.9500
C(7)-C(8)	1.381(4)
C(7)-H(7)	0.9500
C(8)-C(12)	1.380(4)
C(8)-H(8)	0.9500
C(9)-C(10)	1.374(4)
C(9)-H(9)	0.9500
C(10)-H(10)	0.9500
C(11)-C(12)	1.379(4)
C(12)-H(12)	0.9500

C(9)-S(1)-C(1)	92.61(13)
C(11)-O(1)-H(1)	109.5
C(3)-N(1)-N(3)	111.1(2)
C(3)-N(1)-C(2)	129.3(2)
N(3)-N(1)-C(2)	119.6(2)
N(3)-N(2)-C(4)	110.4(2)
N(2)-N(3)-N(1)	106.17(19)
C(2)-C(1)-S(1)	110.6(2)
C(2)-C(1)-H(1A)	124.7
S(1)-C(1)-H(1A)	124.7
C(1)-C(2)-N(1)	123.6(2)
C(1)-C(2)-C(10)	113.8(2)
N(1)-C(2)-C(10)	122.6(2)
N(1)-C(3)-C(4)	105.6(2)
N(1)-C(3)-H(3)	127.2
C(4)-C(3)-H(3)	127.2
C(3)-C(4)-N(2)	106.8(2)
C(3)-C(4)-C(5)	131.4(2)
N(2)-C(4)-C(5)	121.9(2)
C(6)-C(5)-C(11)	117.9(2)
C(6)-C(5)-C(4)	120.7(2)
C(11)-C(5)-C(4)	121.4(2)
C(7)-C(6)-C(5)	121.4(3)
C(7)-C(6)-H(6)	119.3
C(5)-C(6)-H(6)	119.3

C(6)-C(7)-C(8)	119.8(3)
C(6)-C(7)-H(7)	120.1
C(8)-C(7)-H(7)	120.1
C(12)-C(8)-C(7)	120.0(3)
C(12)-C(8)-H(8)	120.0
C(7)-C(8)-H(8)	120.0
C(10)-C(9)-S(1)	111.3(2)
C(10)-C(9)-H(9)	124.3
S(1)-C(9)-H(9)	124.3
C(9)-C(10)-C(2)	111.6(2)
C(9)-C(10)-H(10)	124.2
C(2)-C(10)-H(10)	124.2
O(1)-C(11)-C(12)	117.6(2)
O(1)-C(11)-C(5)	122.3(2)
C(12)-C(11)-C(5)	120.1(2)
C(11)-C(12)-C(8)	120.7(3)
C(11)-C(12)-H(12)	119.6
C(8)-C(12)-H(12)	119.6

Symmetry transformations used to generate equivalent atoms:

Table S3.17. Anisotropic displacement parameters ($\text{\AA}^2 \times 10^3$) for B09049a. The anisotropic displacement factor exponent takes the form: $-2 \pi^2 [h^2 a^{*2} U_{11} + \dots + 2 h k a^* b^* U_{12}]$

U ₁₁	U ₂₂	U ₃₃	U ₂₃	U ₁₃	U ₁₂
-----------------	-----------------	-----------------	-----------------	-----------------	-----------------

S(1)	48(1)	34(1)	29(1)	4(1)	10(1)	0(1)
O(1)	59(2)	53(1)	17(1)	2(1)	1(1)	-21(1)
N(1)	28(1)	27(1)	13(1)	0(1)	0(1)	2(1)
N(2)	38(1)	34(1)	18(1)	-1(1)	0(1)	-7(1)
N(3)	39(1)	34(1)	15(1)	0(1)	-2(1)	-3(1)
C(1)	38(2)	26(2)	23(1)	0(1)	2(1)	1(1)
C(2)	30(2)	24(1)	22(1)	0(1)	4(1)	6(1)
C(3)	29(2)	27(2)	14(1)	-2(1)	0(1)	5(1)
C(4)	29(2)	29(2)	14(1)	-2(1)	-1(1)	6(1)
C(5)	30(2)	26(2)	21(1)	-2(1)	4(1)	2(1)
C(6)	32(2)	33(2)	21(1)	2(1)	-2(1)	4(1)
C(7)	33(2)	36(2)	31(2)	-3(1)	-7(1)	0(1)
C(8)	31(2)	37(2)	42(2)	-2(1)	5(1)	-8(1)
C(9)	24(2)	30(2)	28(1)	-1(1)	-1(1)	-1(1)
C(10)	29(2)	33(2)	23(1)	-1(1)	0(1)	3(1)
C(11)	37(2)	33(2)	20(1)	-3(1)	3(1)	0(1)
C(12)	44(2)	42(2)	28(2)	2(1)	10(1)	-6(2)

Table S3.18. Hydrogen coordinates ($\times 10^4$) and isotropic displacement parameters ($\text{\AA}^2 \times 10^3$) for B09049a.

	x	y	z	U(eq)
--	---	---	---	-------

H(1)	2317	1994	6048	65
H(1A)	3184	8328	2056	35
H(3)	2311	5236	2835	28
H(6)	1337	1671	2714	35
H(7)	376	-1665	2634	42
H(8)	157	-3856	4130	44
H(9)	4851	13624	3911	33
H(10)	4208	10483	4951	35
H(12)	920	-2746	5697	45

Title: Synthesis, Structure, Electrochemistry, and Electrochemiluminescence of Thienyltriazoles

Author: Kalen N. Swanick, Jacquelyn T. Price, Nathan D. Jones, and Zhifeng Ding

Publication: The Journal of Organic Chemistry

Publisher: American Chemical Society **Date:** Jul 1, 2012

Copyright © 2012, American Chemical Society

PERMISSION/LICENSE IS GRANTED FOR YOUR ORDER AT NO CHARGE

This type of permission/license, instead of the standard Terms & Conditions, is sent to you because no fee is being charged for your order. Please note the following:

Permission is granted for your request in both print and electronic formats, and translations. If figures and/or tables were requested, they may be adapted or used in part. Please print this page for your records and send a copy of it to your publisher/graduate school.

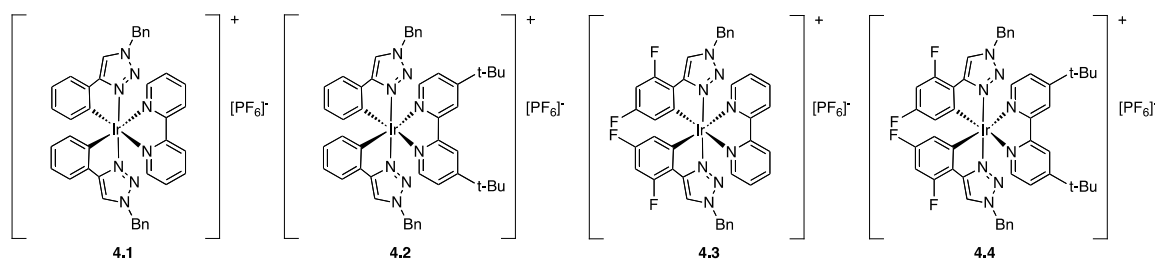
Appropriate credit for the requested material should be given as follows: "Reprinted (adapted) with permission from (COMPLETE REFERENCE CITATION). Copyright (YEAR) American Chemical Society." Insert appropriate information in place of the capitalized words.

One-time permission is granted only for the use specified in your request. No additional uses are granted (such as derivative works or other editions). For any other uses, please submit a new request.

Appendix III. Chapter 4: Electrochemiluminescence of Iridium(III) Complexes

Chapter 4.1: Bright Electrochemiluminescence of Iridium(III) Complexes

Synthesis of $[(C^*N)_2Ir(N^*N)]^+PF_6^-$ Complexes 4.1-4.4



The synthesis and characterization have been published in a previous report.¹

Electrochemical and Photophysical Data Summary

A brief summary of the electrochemical and photophysical data is given below.

Table S4.1. Electrochemical Properties of **4.1-4.4**^{a1}.

Compound	$E_{1/2, ox}$	ΔE_p	ΔE	$E_{1/2, red}$	ΔE_p
4.1	1.28 V	69 mV	2.75 V	-1.47 V	78 mV
4.2	1.26 V	84 mV	2.82 V	-1.56 V	84 mV
4.3	1.61 V	105 mV	3.01 V	-1.40 V	69 mV
4.4	1.60 V	96 mV	3.09 V	-1.49 V	75 mV

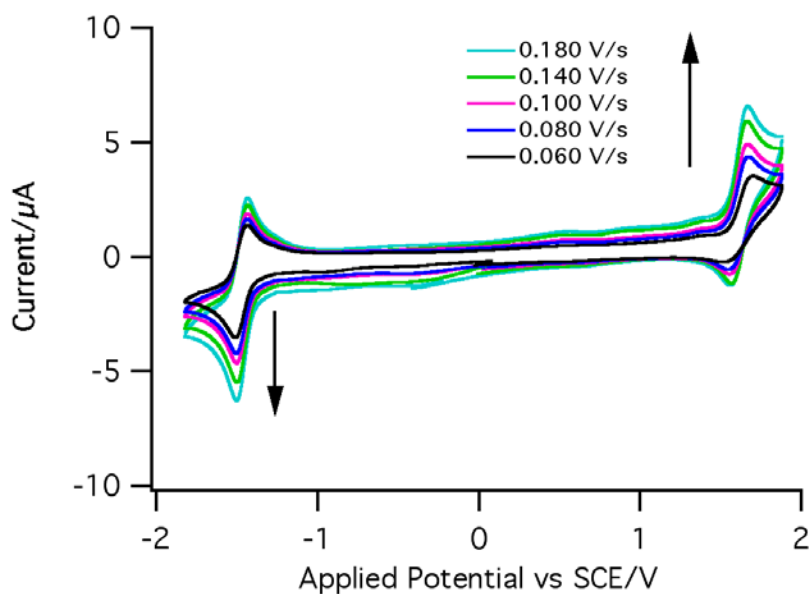
^a Measured in acetonitrile (ca. 1.5 mM) with NBu_4PF_6 (ca. 0.1 M) as supporting electrolyte. Potentials (V) are reported vs. SCE standard electrode and were calibrated using an internal standard Fc/Fc^+ redox couple (0.40 V in ACN).²

Table S4.2. Photophysical Properties of **4.1-4.4**¹.

Compound	Photoluminescence (PL, λ_{\max}) ^a	PL Quantum yield (ϕ) ^b
4.1	580 nm	25.1
4.2	575 nm	34.6
4.3	514 nm	73.1
4.4	498 nm	79.7

^a Measured in acetonitrile at 298 K. ^b Measured at 298 K using Ru(bpy)₃(PF₆)₂ $\phi = 9.5\%$ ³ in ACN.

Supplementary Cyclic Voltammetry Data

**Figure S4.1.** CV of **4.4** with varying scan rate from 0.06 V/s to 0.18 V/s.

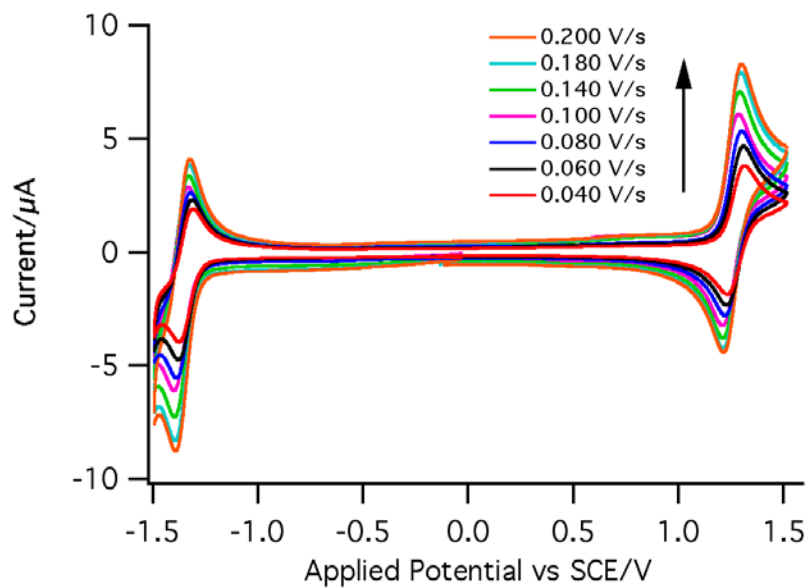


Figure S4.2. CV of $[\text{Ru}(\text{bpy})_3](\text{PF}_6)_2$ with varying scan rate from 0.04 V/s to 0.20 V/s.

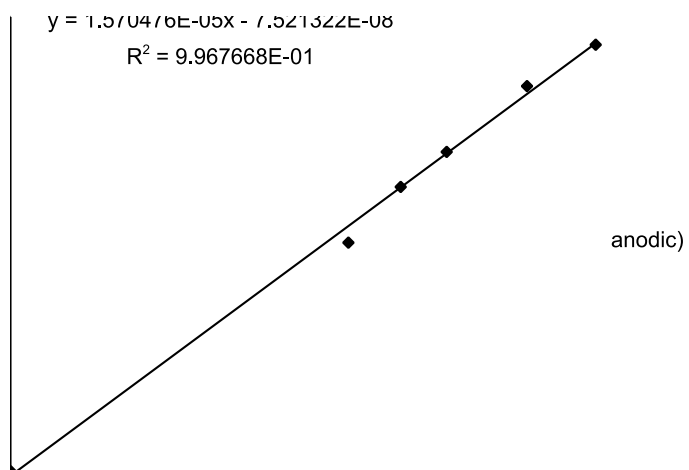


Figure S4.3. Plot of anodic peak current, i_{pa} , of **4.4** against $v^{1/2}$ (v = scan rate).

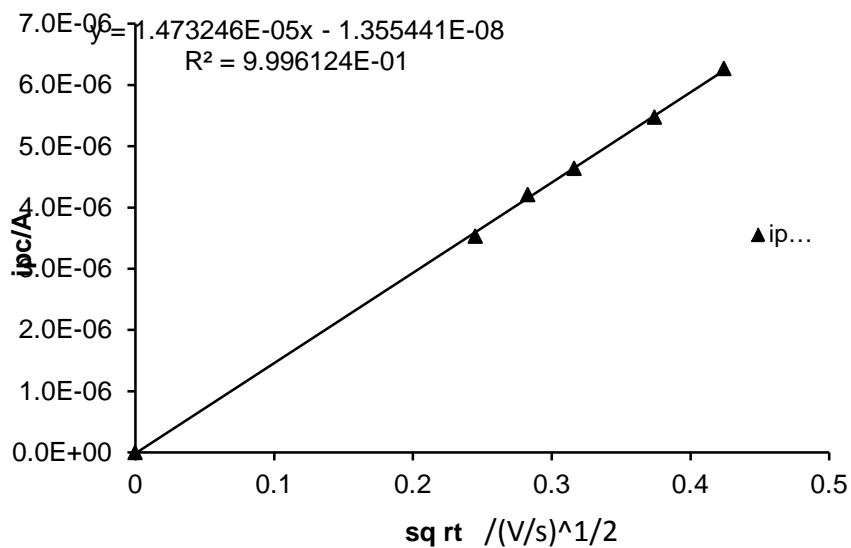


Figure S4.4. Plot of cathodic peak current, i_{pc} , of **4.4** against $v^{1/2}$ (v = scan rate).

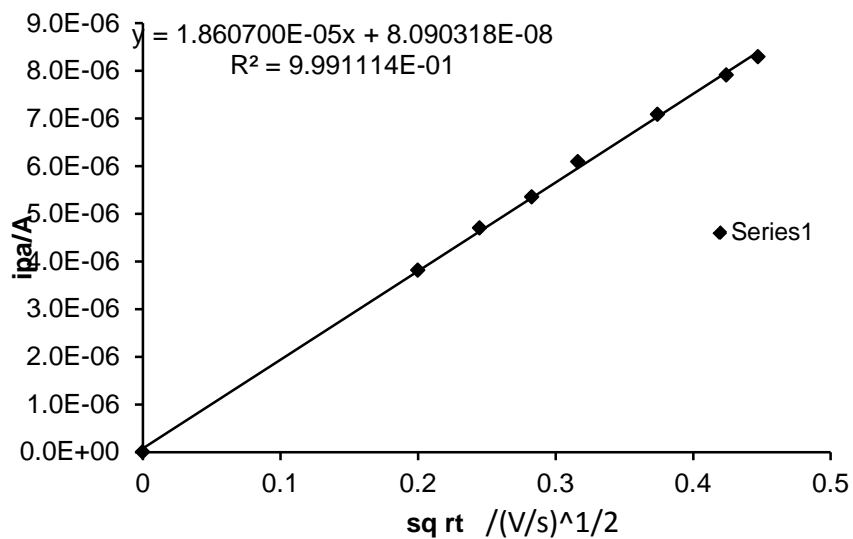


Figure S4.5. Plot of anodic peak current, i_{pa} , of $[\text{Ru}(\text{bpy})_3](\text{PF}_6)_2$ against $v^{1/2}$ (v = scan rate).

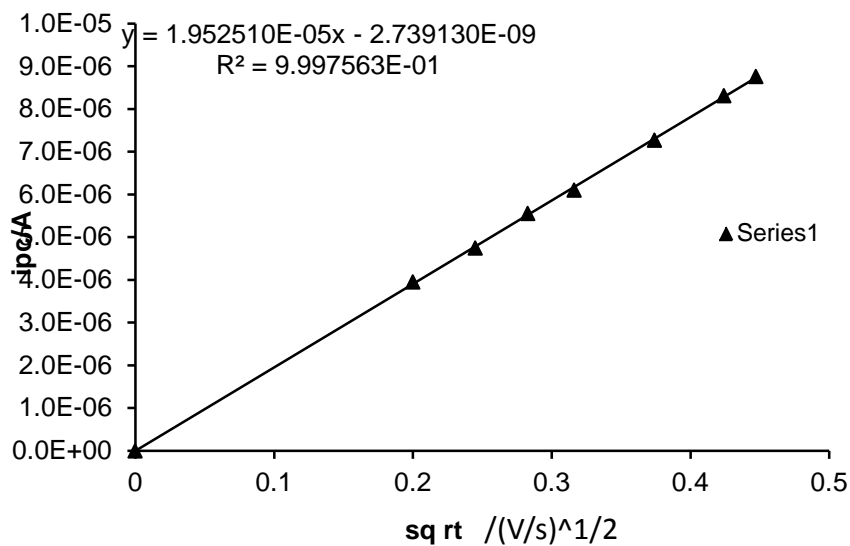


Figure S4.6. Plot of cathodic peak current, i_{pc} , of $[\text{Ru}(\text{bpy})_3](\text{PF}_6)_2$ against $v^{1/2}$ (v = scan rate).

Cyclic Voltammograms and ECL-Voltage Curves in the Co-reactant Path

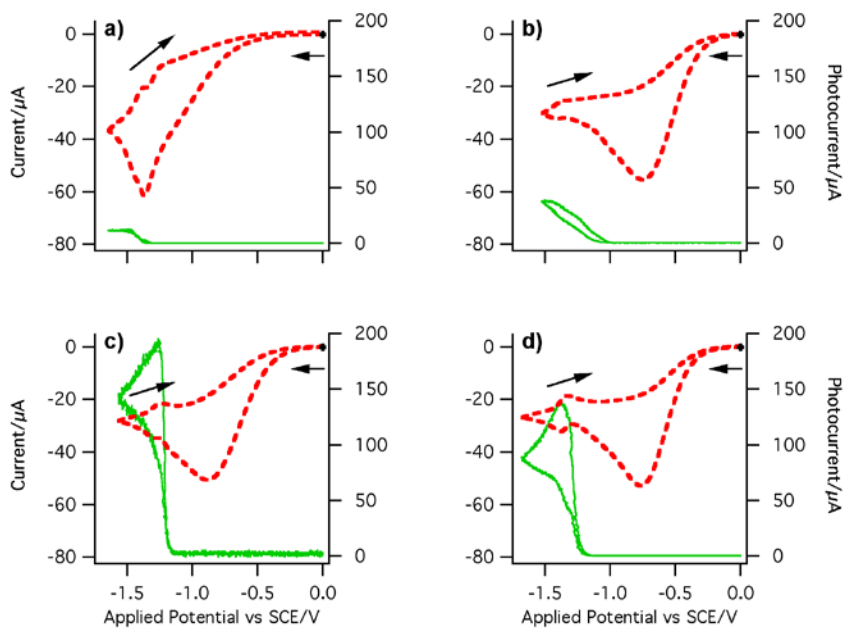


Figure S4.7. Cyclic voltammograms (dotted lines) overlaid with the ECL-voltage curves (solid lines) of compounds a) 4.1, b) 4.2, c) 4.3, and d) 4.4, in the co-reactant path.

Supplementary Video and Photograph

Please see the video in the ESI of complex **4.3** emitting green light electrochemically when pulsing between its oxidation and reduction potentials at the working electrode.⁴ In addition, please refer to the photograph of the electrochemical cell with complex **4.3** in solution illuminated by UV light, Figure S4.8.

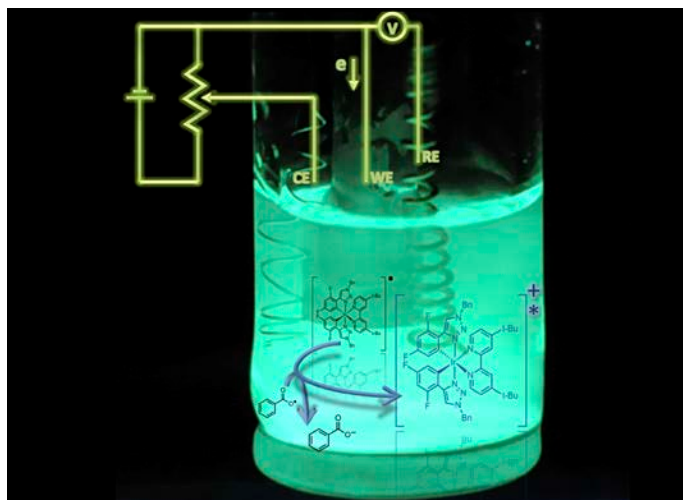


Figure S4.8. Electrochemical cell with complex **4.3** in solution illuminated by UV light.

References

- (1) Ladouceur, S.; Fortin, D.; Zysman-Colman, E. *Inorg. Chem.* **2011**, *50*, 11514.
- (2) Connelly, N. G.; Geiger, W. E. *Chem. Rev.* **1996**, *96*, 877.
- (3) Ishida, H.; Tobita, S.; Hasegawa, Y.; Katoh, R.; Nozaki, K. *Coord. Chem. Rev.* **2010**, *254*, 2449.
- (4) Swanick, K. N.; Ladouceur, S.; Zysman-Colman, E.; Ding, Z. *Chem. Commun.* **2012**, *48*, 3179.

Bright electrochemiluminescence of iridium(III) complexes

K. N. Swanick, S. Ladouceur, E. Zysman-Colman and Z. Ding, *Chem. Commun.*, 2012, **48**, 3179, DOI: 10.1039/C2CC16385C

If you are not the author of this article and you wish to reproduce material from it in a third party non-RSC publication you must formally request permission using RightsLink. Go to our Instructions for using RightsLink page for details.

Authors contributing to RSC publications (journal articles, books or book chapters) do not need to formally request permission to reproduce material contained in this article provided that the correct acknowledgement is given with the reproduced material.

Reproduced material should be attributed as follows:

- For reproduction of material from NJC: Reproduced from Ref. XX with permission from the Centre National de la Recherche Scientifique (CNRS) and The Royal Society of Chemistry.
- For reproduction of material from PCCP: Reproduced from Ref. XX with permission from the PCCP Owner Societies.
- For reproduction of material from PPS: Reproduced from Ref. XX with permission from the European Society for Photobiology, the European Photochemistry Association, and The Royal Society of Chemistry.
- For reproduction of material from all other RSC journals and books: Reproduced from Ref. XX with permission from The Royal Society of Chemistry.

If the material has been adapted instead of reproduced from the original RSC publication "Reproduced from" can be substituted with "Adapted from".

In all cases the Ref. XX is the XXth reference in the list of references.

If you are the author of this article you do not need to formally request permission to reproduce figures, diagrams etc. contained in this article in third party publications or in a thesis or dissertation provided that the correct acknowledgement is given with the reproduced material.

Reproduced material should be attributed as follows:

- For reproduction of material from NJC: [Original citation] - Reproduced by permission of The Royal Society of Chemistry (RSC) on behalf of the Centre National de la Recherche Scientifique (CNRS) and the RSC
- For reproduction of material from PCCP: [Original citation] - Reproduced by permission of the PCCP Owner Societies
- For reproduction of material from PPS: [Original citation] - Reproduced by permission of The Royal Society of Chemistry (RSC) on behalf of the European Society for Photobiology, the European Photochemistry Association, and RSC

- For reproduction of material from all other RSC journals:[Original citation] -
Reproduced by permission of The Royal Society of Chemistry

If you are the author of this article you still need to obtain permission to reproduce the whole article in a third party publication with the exception of reproduction of the whole article in a thesis or dissertation.

Information about reproducing material from RSC articles with different licences is available on our

[Permission Requests page](#).

Appendix IV. Chapter 5: Mechanistic Insight into Electrochemiluminescence of Iridium(III) Complexes *via* Spooling Spectroscopy

Chapter 5.1: Blue Strongly Luminescent Cationic Iridium(III) Complexes with an Electron-Rich Ancillary Ligand: Evaluation of Their Optoelectronic and Electrochemiluminescence Properties

ECL Spectra

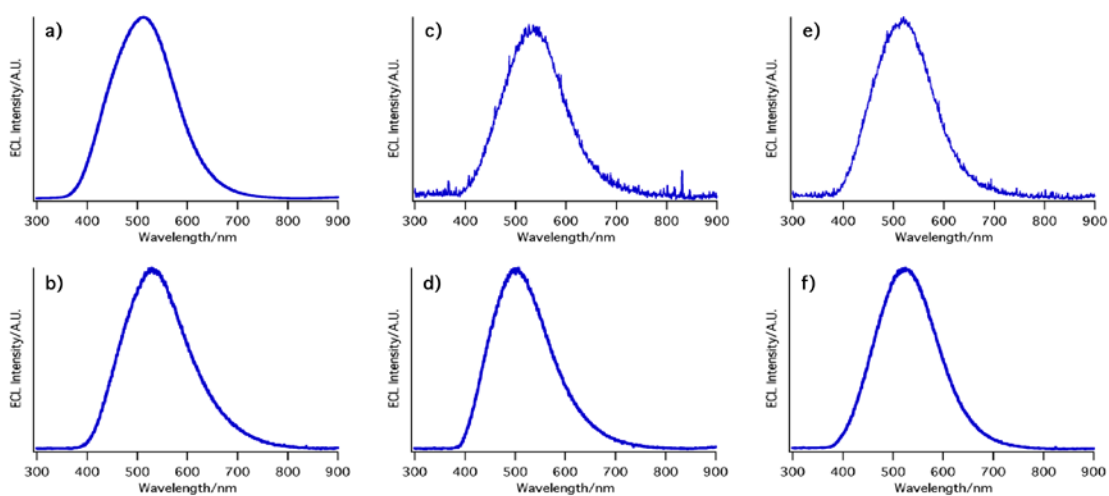


Figure S5.1. ECL spectra of complexes a) **5.1**, b) **5.2**, c) **5.3**, d) **5.4**, e) **5.5**, and f) **5.6**, in ACN.

Chapter 5.2: Self-Enhanced Electrochemiluminescence of an Iridium(III) Complex: Mechanistic Insight

Electrochemical and Spectroscopic Data

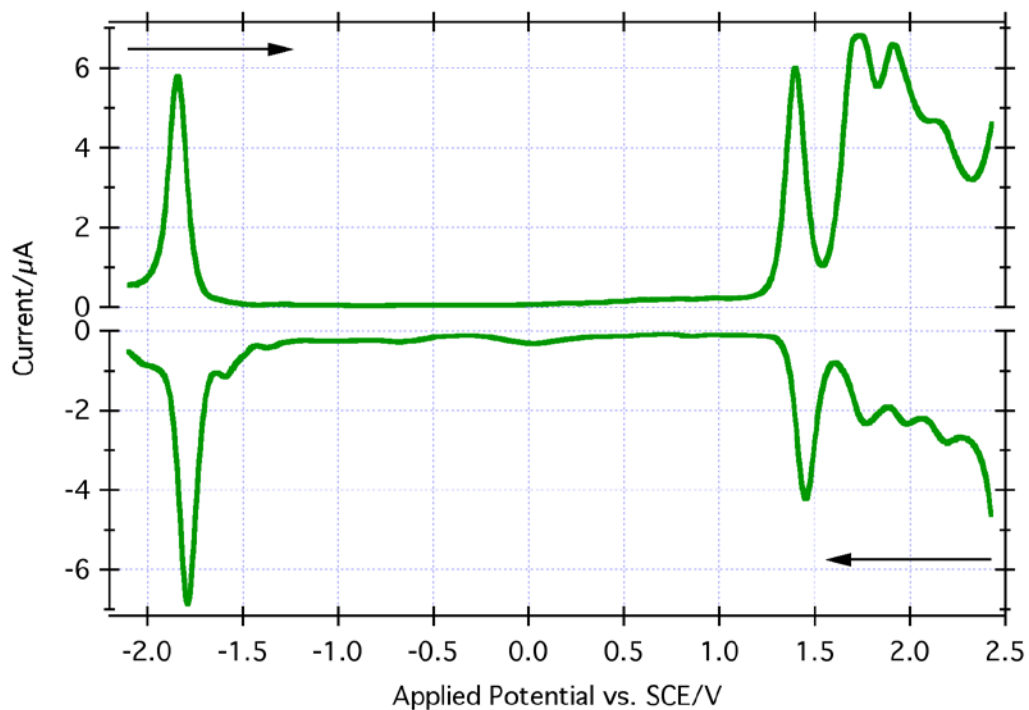


Figure S5.2. DPV of **5.2** from -2.10 V to 2.42 V and from 2.42 V to -2.10 V.

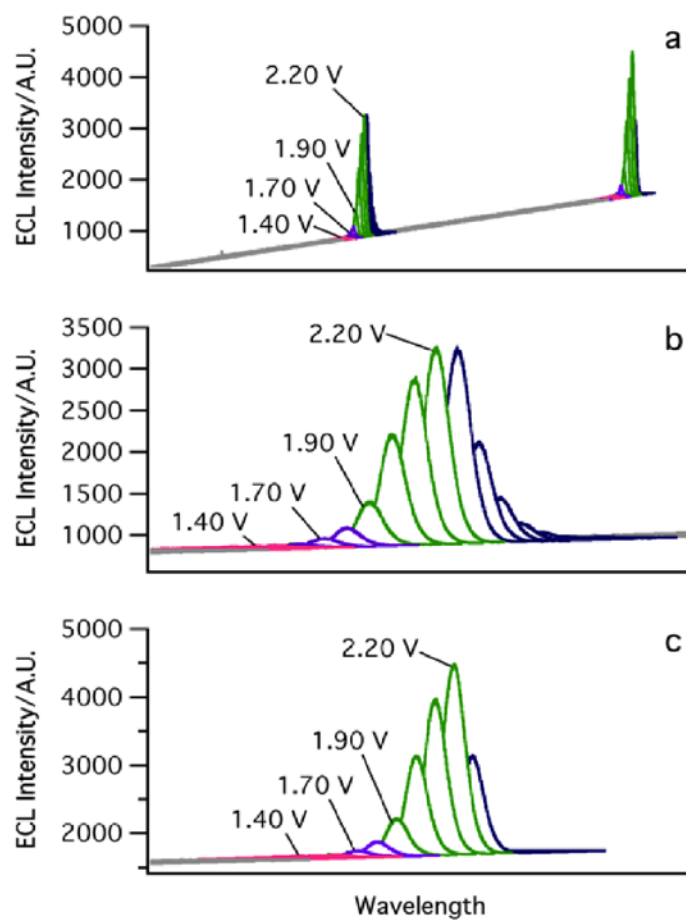


Figure S5.3. a) 2 cycles of ECL spooling spectra of **5.2**, one complete cycle started from 0.00 V to -2.10 V to 2.42 V and back to 0.00 V, scan rate of 0.1 V/s, time = 145 s for 2 cycles; Colors are coded in the same way as in Figure 1. b) Zoomed-in ECL spooling spectra in the first cycle in (a). c) Zoomed-in ECL spooling spectra in the second cycle in (a) showing the same pattern of evolution and devolution of ECL as in the first cycle in (b).

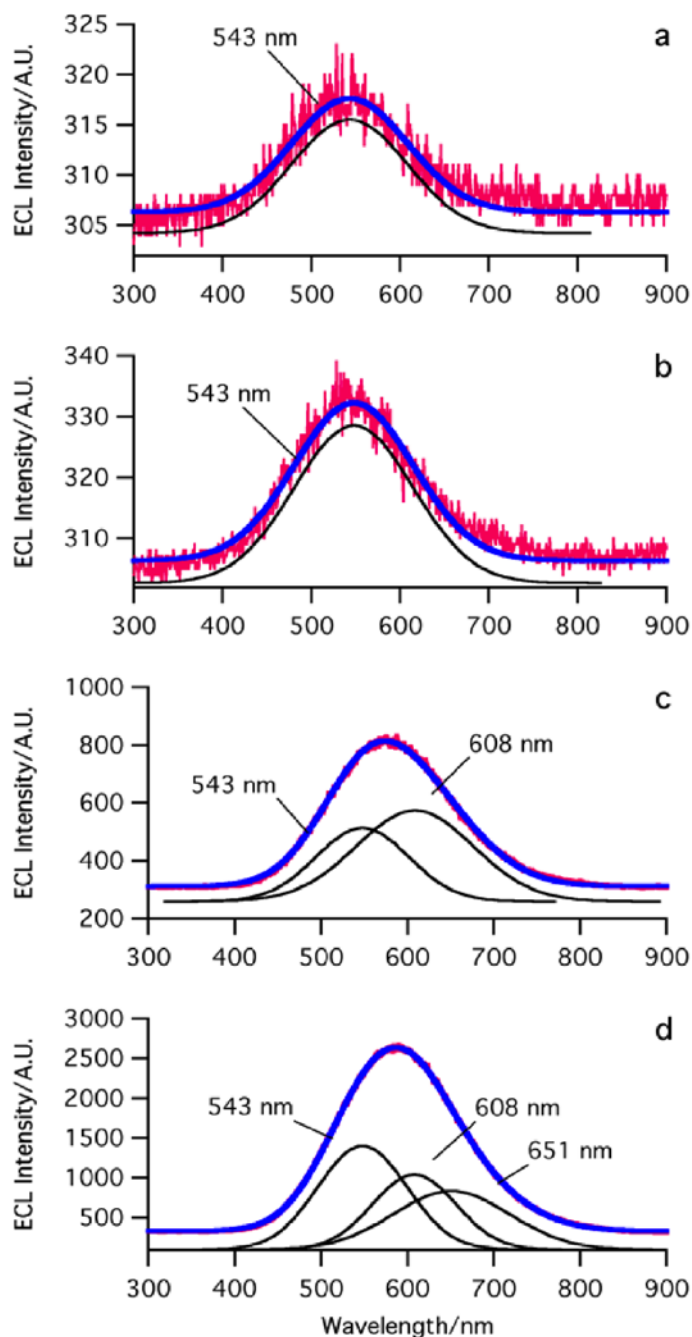


Figure S5.4. Curve-fitting of ECL spooling spectra of **5.2** in the first cycle of potential scanning; a) ECL onset curve fit at 1.20 V, 543 nm in black; b) first excited species curve fit at 1.40 V, 543 nm in black; c) second excited species curve fit to two peaks at 1.70 V, 543 nm and 608 nm in black; d) third excited species curve fit to three peaks at 1.90 V to 2.20 V, 543 nm, 608 nm and 651 nm in black. The actual spectra are shown in pink and the average of the curve fitted peaks are shown in blue.

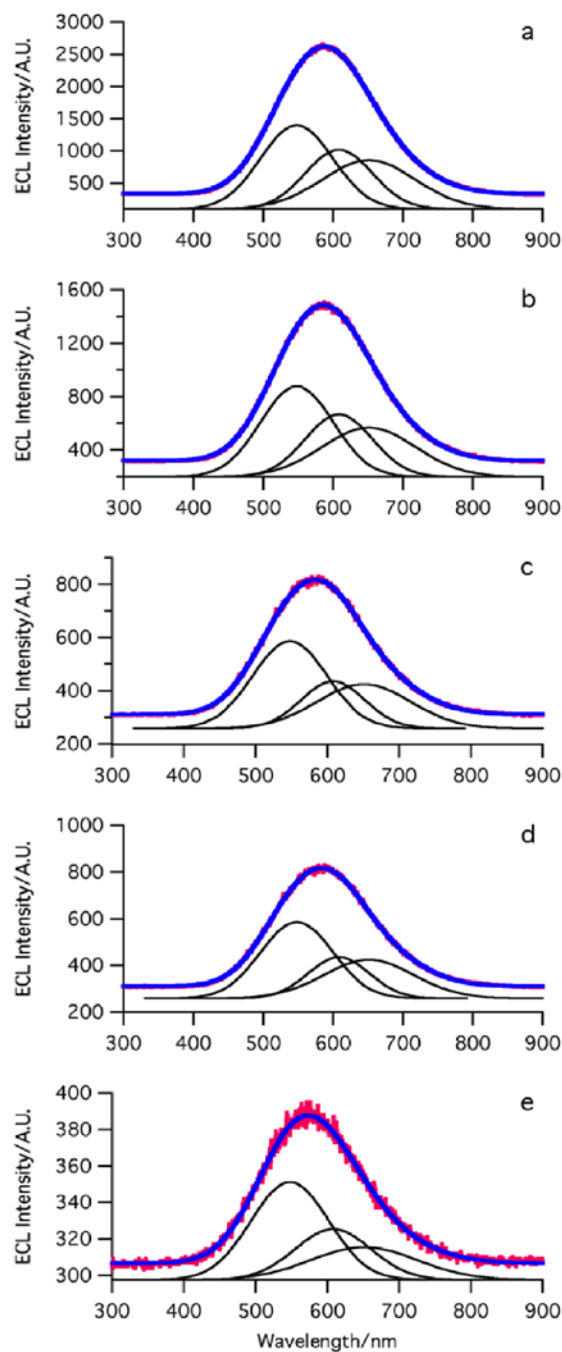


Figure S5.5. Curve-fitting of ECL spooling spectra decay of **5.2** (in black in Figure 2a); a) at 2.30 V; b) at 2.40 V; c) at 2.30 V, scan direction has changed to that moving towards negative potential now; d) at 2.20 V; e) at 2.10 V. The ECL intensity of curves fitted to 543 nm, 608 nm, and 651 nm decrease in all cases once past the point at which the radical cations are generated. The actual spectra are shown in pink and the average of the curve fitted peaks are shown in blue.

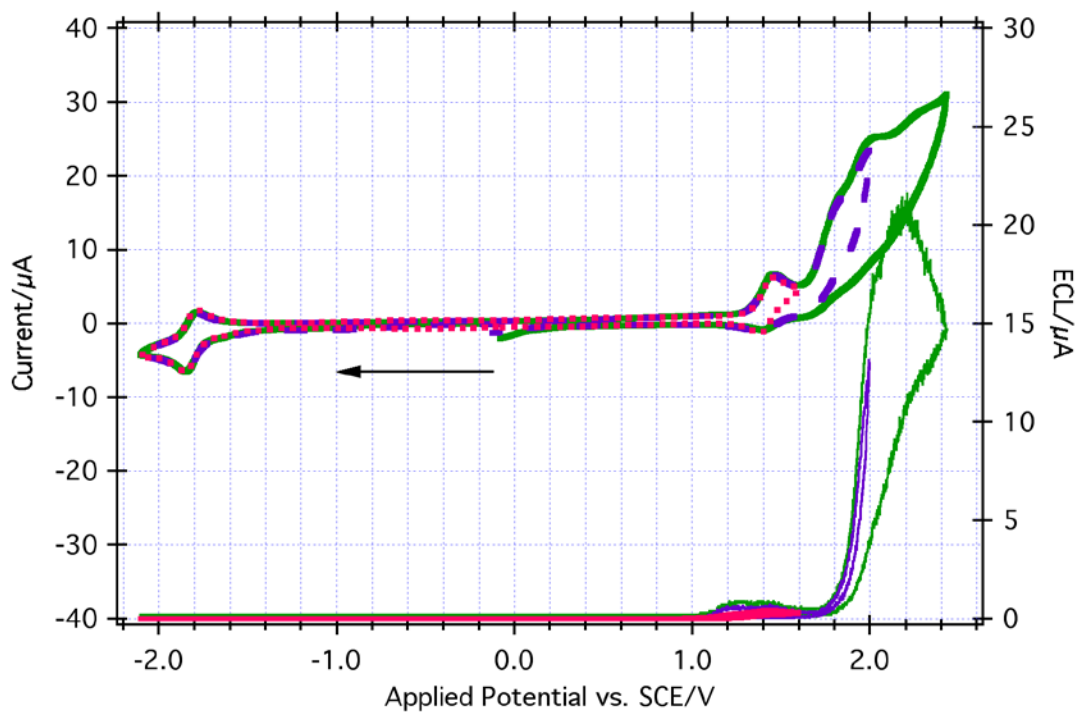


Figure S5.6. Extra CVs with ECL-voltage curves overlaid of complex **5.2** (dotted line in pink from 0.00 V to -2.10 V to 1.60 V and back to 0.00 V, dashed line in purple up to 2.00 V, and solid line in green until 2.42 V, scan rate of 0.1 V/s).

Title: Self-Enhanced Electrochemiluminescence of an Iridium(III) Complex: Mechanistic Insight

Author: Kalen N. Swanick, Sébastien Ladouceur, Eli Zysman-Colman, Zhifeng Ding

Publication: Angewandte Chemie International Edition

Publisher: John Wiley and Sons **Date:** Oct 4, 2012

Copyright © 2012 WILEY-VCH Verlag GmbH & Co. KGaA, Weinheim

Order Completed

Thank you very much for your order.

This is a License Agreement between Kalen N Swanick ("You") and John Wiley and Sons ("John Wiley and Sons"). The license consists of your order details, the terms and conditions provided by John Wiley and Sons, and the payment terms and conditions.

All payments must be made in full to CCC. For payment instructions, please see information listed at the bottom of this form.

License Number	3180860699097
License date	Jul 02, 2013
Licensed content publisher	John Wiley and Sons
Licensed content publication	Angewandte Chemie International Edition
Licensed content title	Self-Enhanced Electrochemiluminescence of an Iridium(III) Complex: Mechanistic Insight
Licensed copyright line	Copyright © 2012 WILEY-VCH Verlag GmbH & Co. KGaA, Weinheim
Licensed content author	Kalen N. Swanick,Sébastien Ladouceur,Eli Zysman-Colman,Zhifeng Ding
Licensed content date	Oct 4, 2012
Start page	11079
End page	11082
Type of use	Dissertation/Thesis
Requestor type	Author of this Wiley article
Format	Print and electronic
Portion	Full article
Will you be translating?	No
Total	0.00 USD
Terms and Conditions	

TERMS AND CONDITIONS

This copyrighted material is owned by or exclusively licensed to John Wiley & Sons, Inc. or one of its group companies (each a "Wiley Company") or a society for whom a Wiley Company has exclusive publishing rights in relation to a particular journal (collectively "WILEY"). By clicking "accept" in connection with completing this licensing transaction, you agree that the following terms and conditions apply to this transaction (along with the billing and payment terms and conditions established by the Copyright Clearance Center Inc., ("CCC's Billing and Payment terms and conditions"), at the time that you opened your RightsLink account (these are available at any time at <http://myaccount.copyright.com>).

Terms and Conditions

1. The materials you have requested permission to reproduce (the "Materials") are protected by copyright.
2. You are hereby granted a personal, non-exclusive, non-sublicensable, non-transferable, worldwide, limited license to reproduce the Materials for the purpose specified in the licensing process. This license is for a one-time use only with a maximum distribution equal to the number that you identified in the licensing process. Any form of republication granted by this license must be completed within two years of the date of the grant of this license (although copies prepared before may be distributed thereafter). The Materials shall not be used in any other manner or for any other purpose. Permission is granted subject to an appropriate acknowledgement given to the author, title of the material/book/journal and the publisher. You shall also duplicate the copyright notice that appears in the Wiley publication in your use of the Material. Permission is also granted on the understanding that nowhere in the text is a previously published source acknowledged for all or part of this Material. Any third party material is expressly excluded from this permission.
3. With respect to the Materials, all rights are reserved. Except as expressly granted by the terms of the license, no part of the Materials may be copied, modified, adapted (except for minor reformatting required by the new Publication), translated, reproduced, transferred or distributed, in any form or by any means, and no derivative works may be made based on the Materials without the prior permission of the respective copyright owner. You may not alter, remove or suppress in any manner any copyright, trademark or other notices displayed by the Materials. You may not license, rent, sell, loan, lease, pledge, offer as security, transfer or assign the Materials, or any of the rights granted to you hereunder to any other person.
4. The Materials and all of the intellectual property rights therein shall at all times remain the exclusive property of John Wiley & Sons Inc or one of its related companies (WILEY) or their respective licensors, and your interest therein is only that of having possession of and the right to reproduce the Materials pursuant to Section 2 herein during the continuance of this Agreement. You agree that you own no right, title or interest in or to the Materials or any of the intellectual property rights therein. You shall have no rights

hereunder other than the license as provided for above in Section 2. No right, license or interest to any trademark, trade name, service mark or other branding ("Marks") of WILEY or its licensors is granted hereunder, and you agree that you shall not assert any such right, license or interest with respect thereto.

5. NEITHER WILEY NOR ITS LICENSORS MAKES ANY WARRANTY OR REPRESENTATION OF ANY KIND TO YOU OR ANY THIRD PARTY, EXPRESS, IMPLIED OR STATUTORY, WITH RESPECT TO THE MATERIALS OR THE ACCURACY OF ANY INFORMATION CONTAINED IN THE MATERIALS, INCLUDING, WITHOUT LIMITATION, ANY IMPLIED WARRANTY OF MERCHANTABILITY, ACCURACY, SATISFACTORY QUALITY, FITNESS FOR A PARTICULAR PURPOSE, USABILITY, INTEGRATION OR NON-INFRINGEMENT AND ALL SUCH WARRANTIES ARE HEREBY EXCLUDED BY WILEY AND ITS LICENSORS AND WAIVED BY YOU.

6. WILEY shall have the right to terminate this Agreement immediately upon breach of this Agreement by you.

7. You shall indemnify, defend and hold harmless WILEY, its Licensors and their respective directors, officers, agents and employees, from and against any actual or threatened claims, demands, causes of action or proceedings arising from any breach of this Agreement by you.

8. IN NO EVENT SHALL WILEY OR ITS LICENSORS BE LIABLE TO YOU OR ANY OTHER PARTY OR ANY OTHER PERSON OR ENTITY FOR ANY SPECIAL, CONSEQUENTIAL, INCIDENTAL, INDIRECT, EXEMPLARY OR PUNITIVE DAMAGES, HOWEVER CAUSED, ARISING OUT OF OR IN CONNECTION WITH THE DOWNLOADING, PROVISIONING, VIEWING OR USE OF THE MATERIALS REGARDLESS OF THE FORM OF ACTION, WHETHER FOR BREACH OF CONTRACT, BREACH OF WARRANTY, TORT, NEGLIGENCE, INFRINGEMENT OR OTHERWISE (INCLUDING, WITHOUT LIMITATION, DAMAGES BASED ON LOSS OF PROFITS, DATA, FILES, USE, BUSINESS OPPORTUNITY OR CLAIMS OF THIRD PARTIES), AND WHETHER OR NOT THE PARTY HAS BEEN ADVISED OF THE POSSIBILITY OF SUCH DAMAGES. THIS LIMITATION SHALL APPLY NOTWITHSTANDING ANY FAILURE OF ESSENTIAL PURPOSE OF ANY LIMITED REMEDY PROVIDED HEREIN.

9. Should any provision of this Agreement be held by a court of competent jurisdiction to be illegal, invalid, or unenforceable, that provision shall be deemed amended to achieve as nearly as possible the same economic effect as the original provision, and the legality, validity and enforceability of the remaining provisions of this Agreement shall not be affected or impaired thereby.

10. The failure of either party to enforce any term or condition of this Agreement shall not constitute a waiver of either party's right to enforce each and every term and condition of this Agreement. No breach under this agreement shall be deemed waived or excused by either party unless such waiver or consent is in writing signed by the party

granting such waiver or consent. The waiver by or consent of a party to a breach of any provision of this Agreement shall not operate or be construed as a waiver of or consent to any other or subsequent breach by such other party.

11. This Agreement may not be assigned (including by operation of law or otherwise) by you without WILEY's prior written consent.

12. Any fee required for this permission shall be non-refundable after thirty (30) days from receipt

13. These terms and conditions together with CCC's Billing and Payment terms and conditions (which are incorporated herein) form the entire agreement between you and WILEY concerning this licensing transaction and (in the absence of fraud) supersedes all prior agreements and representations of the parties, oral or written. This Agreement may not be amended except in writing signed by both parties. This Agreement shall be binding upon and inure to the benefit of the parties' successors, legal representatives, and authorized assigns.

14. In the event of any conflict between your obligations established by these terms and conditions and those established by CCC's Billing and Payment terms and conditions, these terms and conditions shall prevail.

15. WILEY expressly reserves all rights not specifically granted in the combination of (i) the license details provided by you and accepted in the course of this licensing transaction, (ii) these terms and conditions and (iii) CCC's Billing and Payment terms and conditions.

16. This Agreement will be void if the Type of Use, Format, Circulation, or Requestor Type was misrepresented during the licensing process.

17. This Agreement shall be governed by and construed in accordance with the laws of the State of New York, USA, without regards to such state's conflict of law rules. Any legal action, suit or proceeding arising out of or relating to these Terms and Conditions or the breach thereof shall be instituted in a court of competent jurisdiction in New York County in the State of New York in the United States of America and each party hereby consents and submits to the personal jurisdiction of such court, waives any objection to venue in such court and consents to service of process by registered or certified mail, return receipt requested, at the last known address of such party.

Wiley Open Access Terms and Conditions

Wiley publishes Open Access articles in both its Wiley Open Access Journals program [<http://www.wileyopenaccess.com/view/index.html>] and as Online Open articles in its subscription journals. The majority of Wiley Open Access Journals have adopted the Creative Commons Attribution License (CC BY) which permits the unrestricted use, distribution, reproduction, adaptation and commercial exploitation of the article in any medium. No permission is required to use the article in this way provided that the article is properly cited and other license terms are observed. A small number of Wiley Open

Access journals have retained the Creative Commons Attribution Non Commercial License (CC BY-NC), which permits use, distribution and reproduction in any medium, provided the original work is properly cited and is not used for commercial purposes.

Online Open articles - Authors selecting Online Open are, unless particular exceptions apply, offered a choice of Creative Commons licenses. They may therefore select from the CC BY, the CC BY-NC and the Attribution-NoDerivatives (CC BY-NC-ND). The CC BY-NC-ND is more restrictive than the CC BY-NC as it does not permit adaptations or modifications without rights holder consent.

Wiley Open Access articles are protected by copyright and are posted to repositories and websites in accordance with the terms of the applicable Creative Commons license referenced on the article. At the time of deposit, Wiley Open Access articles include all changes made during peer review, copyediting, and publishing. Repositories and websites that host the article are responsible for incorporating any publisher-supplied amendments or retractions issued subsequently.

Wiley Open Access articles are also available without charge on Wiley's publishing platform, Wiley Online Library or any successor sites.

Conditions applicable to all Wiley Open Access articles:

The authors' moral rights must not be compromised. These rights include the right of "paternity" (also known as "attribution" - the right for the author to be identified as such) and "integrity" (the right for the author not to have the work altered in such a way that the author's reputation or integrity may be damaged).

Where content in the article is identified as belonging to a third party, it is the obligation of the user to ensure that any reuse complies with the copyright policies of the owner of that content.

If article content is copied, downloaded or otherwise reused for research and other purposes as permitted, a link to the appropriate bibliographic citation (authors, journal, article title, volume, issue, page numbers, DOI and the link to the definitive published version on Wiley Online Library) should be maintained. Copyright notices and disclaimers must not be deleted.

Creative Commons licenses are copyright licenses and do not confer any other rights, including but not limited to trademark or patent rights.

Any translations, for which a prior translation agreement with Wiley has not been agreed, must prominently display the statement: "This is an unofficial translation of an article that appeared in a Wiley publication. The publisher has not endorsed this translation."

Conditions applicable to non-commercial licenses (CC BY-NC and CC BY-NC-ND)

For non-commercial and non-promotional purposes individual non-commercial users may access, download, copy, display and redistribute to colleagues Wiley Open Access

articles. In addition, articles adopting the CC BY-NC may be adapted, translated, and text- and data-mined subject to the conditions above.

Use by commercial "for-profit" organizations

Use of non-commercial Wiley Open Access articles for commercial, promotional, or marketing purposes requires further explicit permission from Wiley and will be subject to a fee. Commercial purposes include:

Copying or downloading of articles, or linking to such articles for further redistribution, sale or licensing;

Copying, downloading or posting by a site or service that incorporates advertising with such content;

The inclusion or incorporation of article content in other works or services (other than normal quotations with an appropriate citation) that is then available for sale or licensing, for a fee (for example, a compilation produced for marketing purposes, inclusion in a sales pack)

Use of article content (other than normal quotations with appropriate citation) by for-profit organizations for promotional purposes

Linking to article content in e-mails redistributed for promotional, marketing or educational purposes;

Use for the purposes of monetary reward by means of sale, resale, license, loan, transfer or other form of commercial exploitation such as marketing products

Print reprints of Wiley Open Access articles can be purchased from:

corporatesales@wiley.com

The modification or adaptation for any purpose of an article referencing the CC BY-NC-ND License requires consent which can be requested from RightsLink@wiley.com.

Other Terms and Conditions:

BY CLICKING ON THE "I AGREE..." BOX, YOU ACKNOWLEDGE THAT YOU HAVE READ AND FULLY UNDERSTAND EACH OF THE SECTIONS OF AND PROVISIONS SET FORTH IN THIS AGREEMENT AND THAT YOU ARE IN AGREEMENT WITH AND ARE WILLING TO ACCEPT ALL OF YOUR OBLIGATIONS AS SET FORTH IN THIS AGREEMENT.

Chapter 5.3: Electrochemiluminescence of Heterometallic Ruthenium(II)-Iridium(III) Soft Salts

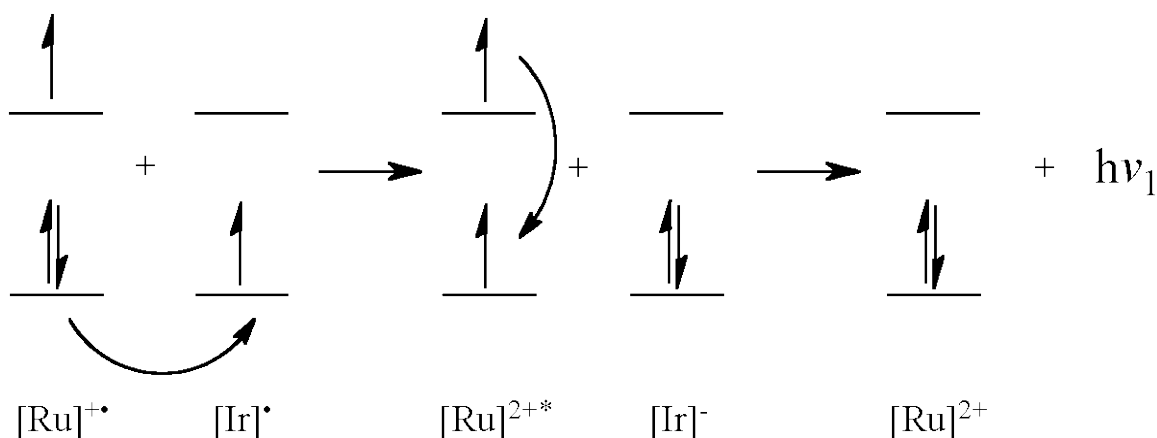
Electrochemical and ECL Data

Table S5.1. Electrochemical and ECL data^a

Complex	$E_{1/2}/V$	$\Delta E_{\text{redox}}/eV$	$\lambda_{\text{max}}(\text{ECL})/\text{nm}$
[Ru]Cl ₂	-1.45; 1.11	2.56	638
TBA[Ir]	-2.32; 0.98 ^b	3.30	517
[Ir][Ru][Ir]	-2.60; -2.33; -1.86; -1.61; -1.45; 0.97 ^b ; 1.14 ^b	2.42	634

^a CVs were recorded in dry, nitrogen purged ACN using 0.1 M TBAPF₆ as the supporting electrolyte. Potentials are reported in V vs. SCE and were calibrated using an Fc⁺/Fc internal standard (0.38 V in ACN).¹ ^b Irreversible, E_a is reported; ^c Partially reversible. ^d Annihilation ECL spectral data.

ECL Mechanism



Scheme S5.1. ECL mechanism for generation of $[Ru]^{2+*}$ excited species

ECL Spooling Spectroscopy

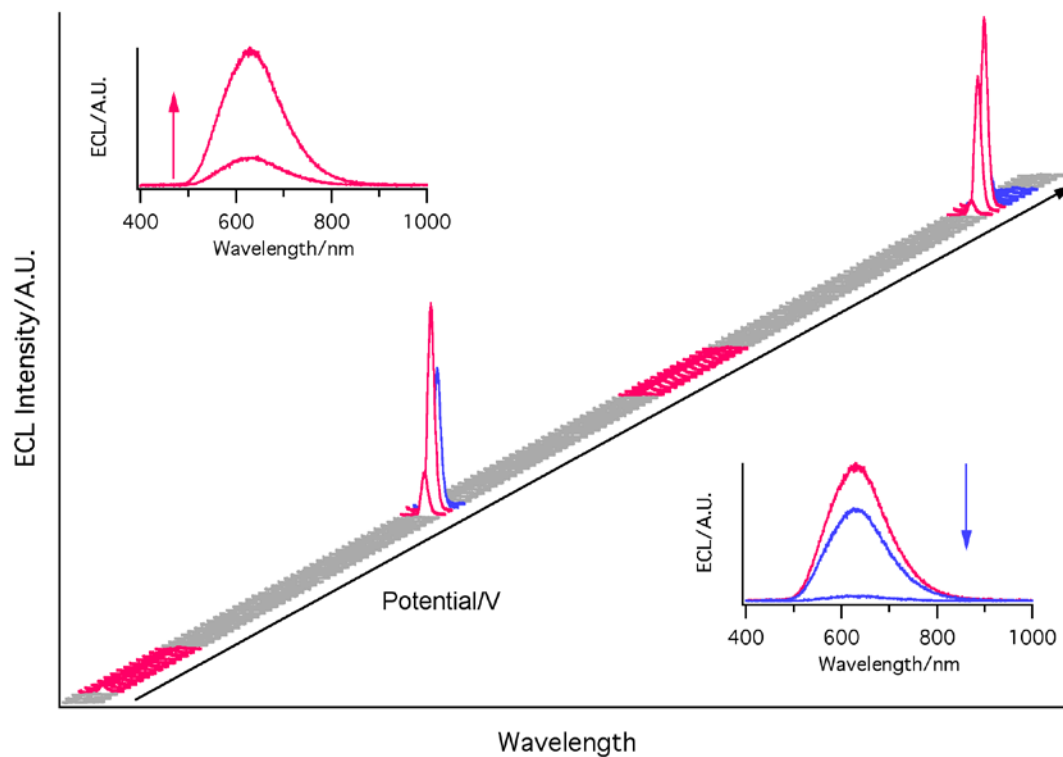


Figure S5.7. ECL spooling spectra of $[\text{Ir}][\text{Ru}][\text{Ir}]$ soft salt with an extended potential window showing the first oxidation of Ru moiety until the second reduction of Ir moiety (evolution of ECL in pink and devolution of ECL in purple) for two complete cycles with a scan rate of 0.1 V/s, inset: evolution of ECL in pink and devolution of ECL in purple.

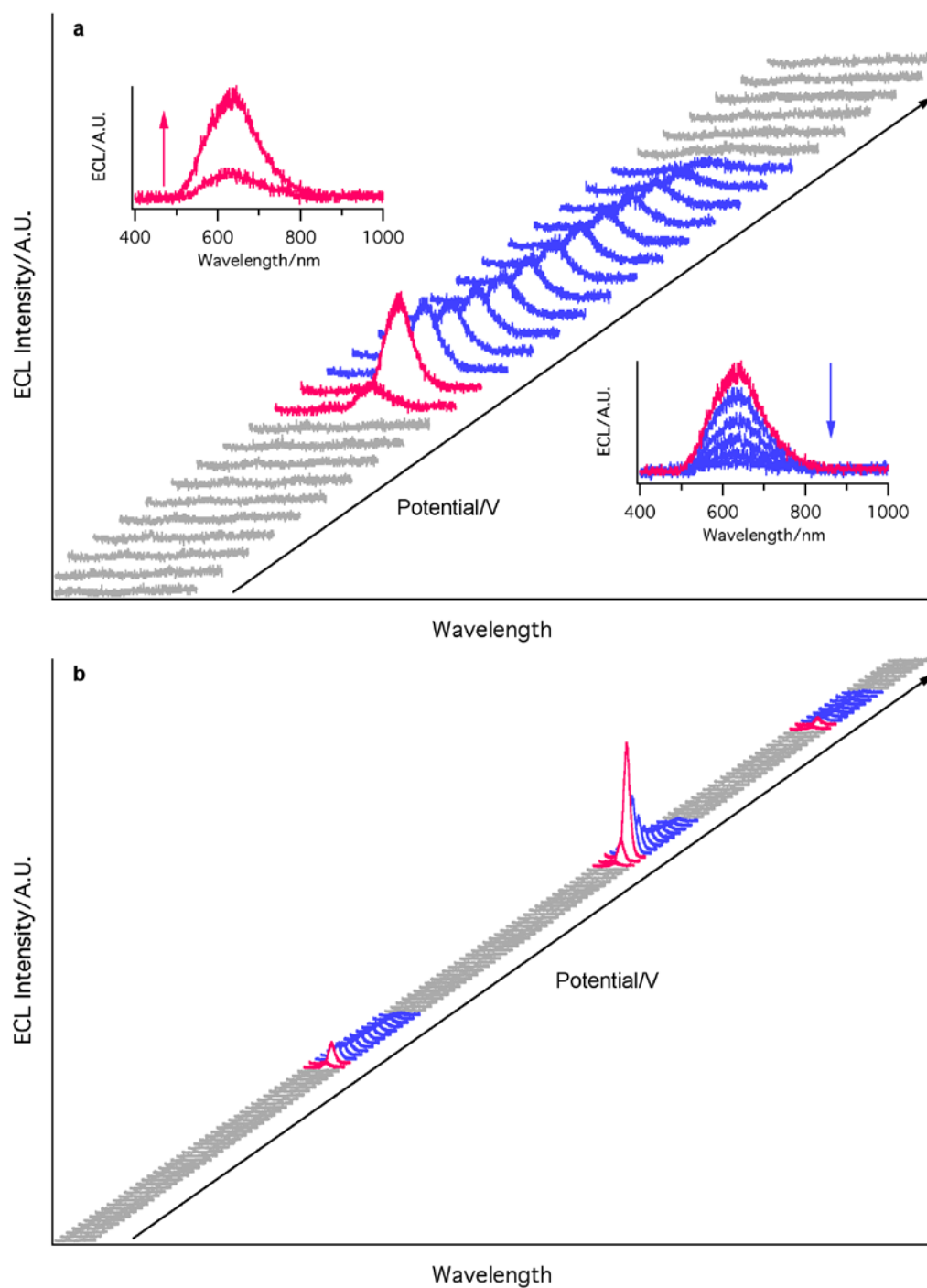


Figure S5.8. ECL spooling spectra of 1:2 $[\text{Ru}]\text{Cl}_2:\text{TBA}[\text{Ir}]$ mixture solution with an extended potential window showing the first oxidation of Ru moiety until the second reduction of Ir moiety (evolution of ECL in pink and devolution of ECL in purple) for a) one complete cycle, inset: evolution of ECL in pink and devolution of ECL in purple, and b) two complete cycles, with a scan rate of 0.1 V/s.

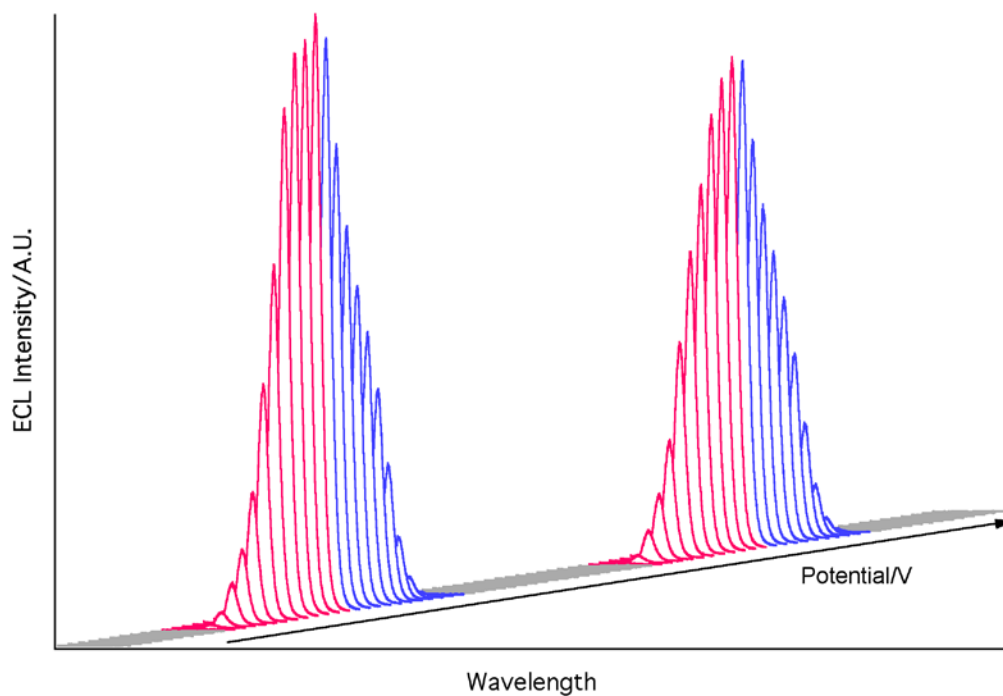


Figure S5.9. ECL spooling spectra of $[\text{Ir}][\text{Ru}][\text{Ir}]$ soft salt with 0.02 M TPrA co-reactant between 0.00 V to 1.52 V with a scan rate of 0.1 V/s for two complete cycles (evolution of ECL in pink and devolution of ECL in purple).

References

- (1) Pavlishchuk, V. V.; Addison, A. W. *Inorganica Chimica Acta* **2000**, 298, 97.

Appendix V. Chapter 6: Sensitive Detection of Au₂₅ Clusters by Electrochemiluminescence

Chapter 6.1: Interrogating Near-Infrared Electrogenerated Chemiluminescence of Au₂₅(SC₂H₄Ph)₁₈⁺ Clusters

Synthesis and Characterization of Au₂₅(SC₂H₄Ph)₁₈⁺ (z = -1 and +1) Clusters

Chemicals. Hydrogen tetrachloroaurate trihydrate (Aldrich, 99.9%), phenylethanethiol (Aldrich, 98%), tetra-*n*-octylammonium bromide (Aldrich, 98%), sodium borohydride (Aldrich, 99%), hydrogen peroxide (Caledon, 30%), sodium hydroxide (Caledon, 99%), tetrahydrofuran (THF) (Caledon, 99.9%), pentafluorobenzoyl chloride (Alfa Aesar, 99%), methanol (Caledon, 99.8%), dichloromethane (Caledon), chloroform (Caledon, 99.8%), ethanol (Caledon, 99.8%), and acetonitrile (Caledon) were used as received. Deuterated chloroform and dichloromethane was furnished by Cambridge Isotope Laboratories.

Instrumentation for Synthesis Characterization. UV-visible spectra were recorded using a Varian Cary 5000 spectrophotometer. ¹H and ¹⁹F NMR spectra were recorded on a Mercury and Inova 400 spectrometers (¹H: 400 MHz and ¹⁹F: 376 MHz) in CD₂Cl₂ or CDCl₃ to follow the completion of Au₂₅⁻ to Au₂₅⁺ reaction and in *d*-chloroform to characterize the final product of bis(pentafluorobenzyl) peroxide.

An AB Applied Biosystem mass spectrometer (4700 Proteomics Analyzer) was employed to obtain the MALDI-TOF spectra. The sample was prepared by mixing 0.2:1000 analyte:matrix ratio. Then, 7 μL of the mixture was casted on the target plate and air dried.¹ ESI mass spectra were recorded on MicroTOF (Bruker) in CH₂Cl₂/MeOH solvent mixture in the presence of cesium iodide electrolyte.

Synthesis of TOA·Au₂₅(SC₂H₄Ph)₁₈. TOA·Au₂₅(SC₂H₄Ph)₁₈ (Au₂₅⁻) has been synthesized with some modification on the methods introduced by Murray² and Maran.^{3,4} Briefly, 1.02 g (2.54 mmol) HAuCl₄·3H₂O and 1.66 g (3.04 mmol) tetraoctylammonium bromide (TOABr) were dissolved in 100 mL THF. The dark red solution was put in the ice-bath for 30 min and then 2.1 mL (15.67 mmol) of phenylethane thiol was added one drop at a time over 10 minutes. Meanwhile, the color of mixture turned yellowish while the ice bath was kept for 2 hours. The solution was heated up to room temperature and led to a colorless solution after 3 hours. At this point, the ice bath was put back and 0.998 g (26.69 mmol) NaBH₄, dissolved in 20 mL of ice cold distilled water was added to the mixture quickly under vigorous stirring. A dark solution formed with the addition of the

reducing agent. The solution was gravity filtered and the solvent volume was vacuum evaporated. The residual was settled down overnight. The excess of NaBH_4 and phenylethane thiol was removed by washing the crude sample with Water/EtOH mixture. The final product was extracted from $-(\text{Au-S-Au-S})$ -oligomer using acetonitrile to get an oily product which then recrystallized to obtained a dark-brown needle crystals. The purity and crystal structure were checked by different spectroscopic techniques, such as UV-vis,^{2,3} $^1\text{HNMR}$,³ X-ray crystallography^{5,6} and ESI-Mass.

Synthesis of Bis(pentafluorobenzoyl) Peroxide. To convert Au_{25}^- to its corresponding oxidized form, Au_{25}^+ , bis(pentafluorobenzoyl) peroxide was used as oxidizing agent. Recently, Maran's group showed that this compound is able to react with Au_{25}^- and Au_{25}^0 and produce the same mono-dispersed nanocluster.³ Synthesis of bis(pentafluorobenzoyl) peroxide (1) was performed by following Barson's⁷ procedure with some modification. Then, the purity of the sample was checked by TLC (15:1 petroleum ether/ ethyl acetate) and $^{19}\text{FNMR}$ (-133.74, -143.30, -158.15 ppm in CDCl_3).³ No explosion was observed during the peroxide preparation and the sample was kept in the freezer to prevent decomposition.

Conversion of Au_{25}^- to Au_{25}^+ . Maran and co-workers³ have discussed that upon addition of the peroxide (1) to the $\text{Au}_{25}(\text{SC}_2\text{H}_4\text{Ph})_{18}^-$ an oxidation reaction can happen via electron transfer between the nanocluster and the peroxide (1) which leads to formation $\text{Au}_{25}(\text{SC}_2\text{H}_4\text{Ph})_{18}^- \text{C}_6\text{F}_5\text{CO}_2^+$ cluster. In our work, the same methodology has been applied to get "1+" monodispersed cluster. Briefly, 1 mmol of crystallized Au_{25}^- was prepared in d_2 -dichloromethane in an NMR tube and $^1\text{HNMR}$ spectrum was recorded. Then 2 mmol of (1) (d_2 -dichloromethane) was added $^1\text{HNMR}$ and UV-vis spectra have been taken to monitor the reaction completion and purity of the final product. MALDI-TOF mass spectrum also proved that the original nanocluster exist over the course of reaction. To run the MALDI experiment, the sample was mixed with *trans*-2-[3-(4-*tert*-butylphenyl)-2-methyl-2-propenylidene]-malononitrile (DCTB), applying 1000/0.2 ratio of matrix/analyte and 7 mL of the prepared sample was placed on the target plate, dried at room temperature. The laser intensity was kept as low as possible to have a good signal to noise ratio, although some fragmentation observed among the sample analysis.

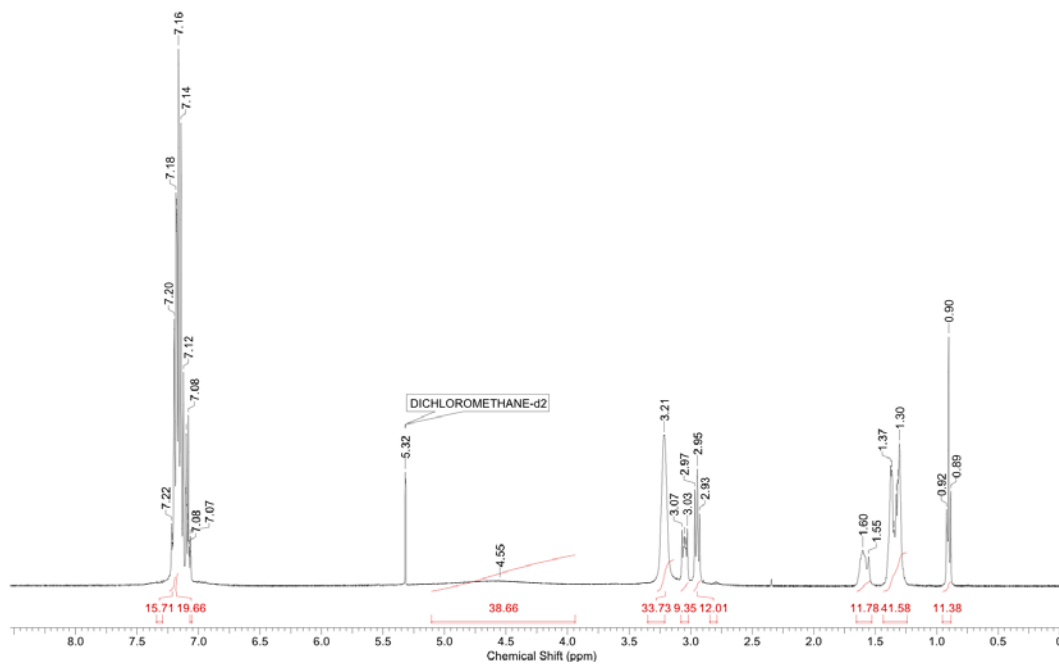


Figure S6.1. ^1H NMR spectrum of recrystallized $\text{TOA}\cdot\text{Au}_{25}(\text{SC}_2\text{H}_4\text{Ph})_{18}$ in CD_2Cl_2 .

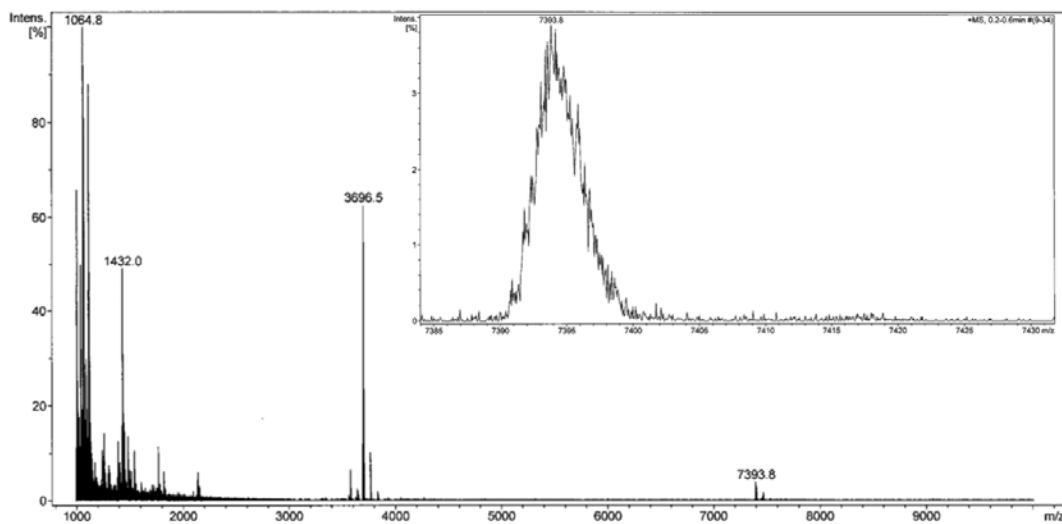
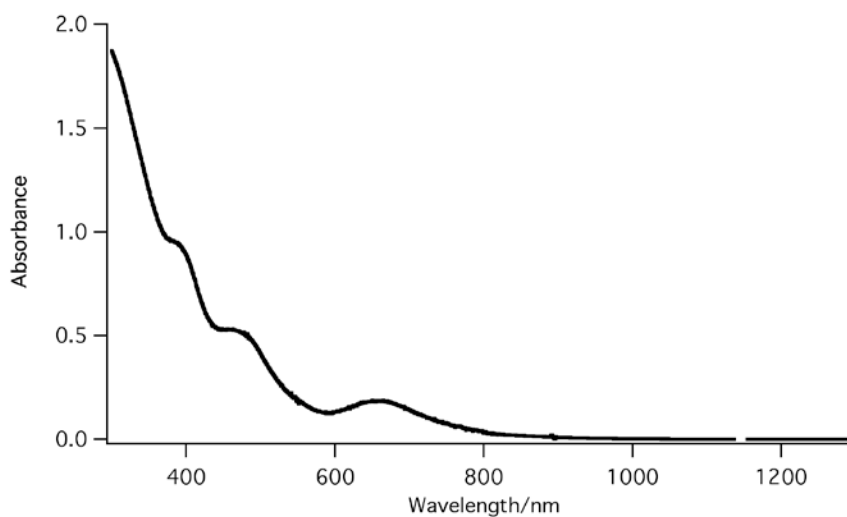


Figure S6.2. ESI mass spectrum of $\text{TOA}\cdot\text{Au}_{25}(\text{SC}_2\text{H}_4\text{Ph})_{18}$, taken in $\text{CH}_2\text{Cl}_2/\text{MeOH}$ mixture.

Table S6.1. X-ray crystallography data of TOA·Au₂₅(SC₂H₄Ph)₁₈.

	A	b	C	A	β	γ	V(A ⁰) ³	T (K)
This work	16.16	17.43	18.70	106.39	105.47	90.99	4845	150
Murray et al. 2008	16.1114	17.3313	18.5810	106.269	105.494	90.959	4776.1	99
Jin et al. 2009	16.234	17.395	18.697	106.349	105.659	90.859	4855	123

**Figure S6.3.** UV-vis spectrum of recrystallized Au₂₅(SC₂H₄Ph)₁₈⁺ C₆F₅CO₂⁻ in CH₂Cl₂.

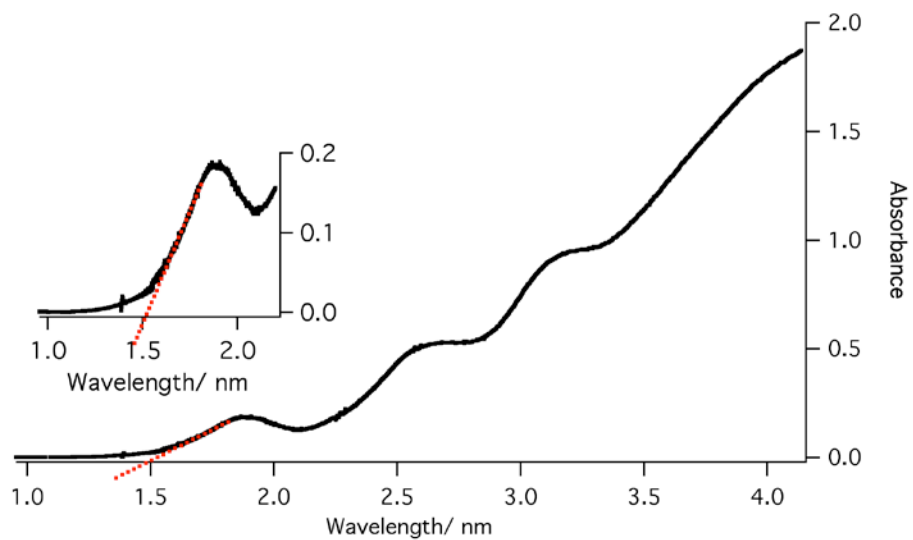


Figure S6.4. UV-vis spectrum using energy (eV) as x axis for recrystallized $\text{Au}_{25}(\text{SC}_2\text{H}_4\text{Ph})_{18}^+ \text{C}_6\text{F}_5\text{CO}_2^-$ in CH_2Cl_2 .

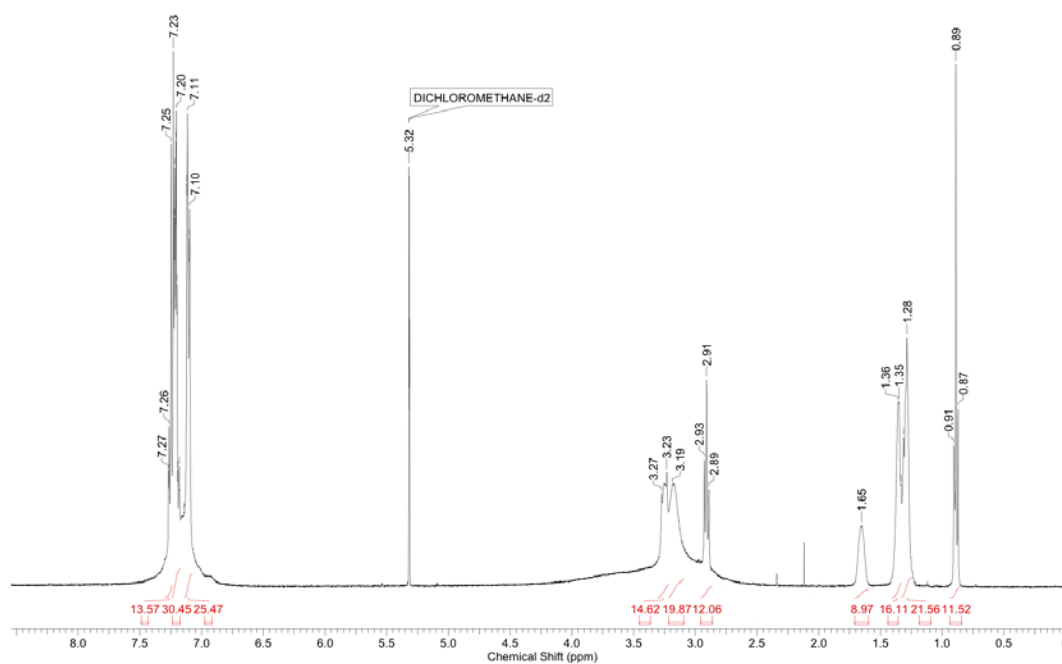


Figure S6.5. ^1H NMR spectrum of $\text{Au}_{25}(\text{SC}_2\text{H}_4\text{Ph})_{18}^+ \text{C}_6\text{F}_5\text{CO}_2^-$, CD_2Cl_2 , after in situ addition of bis(pentafluorobenzoyl) peroxide.

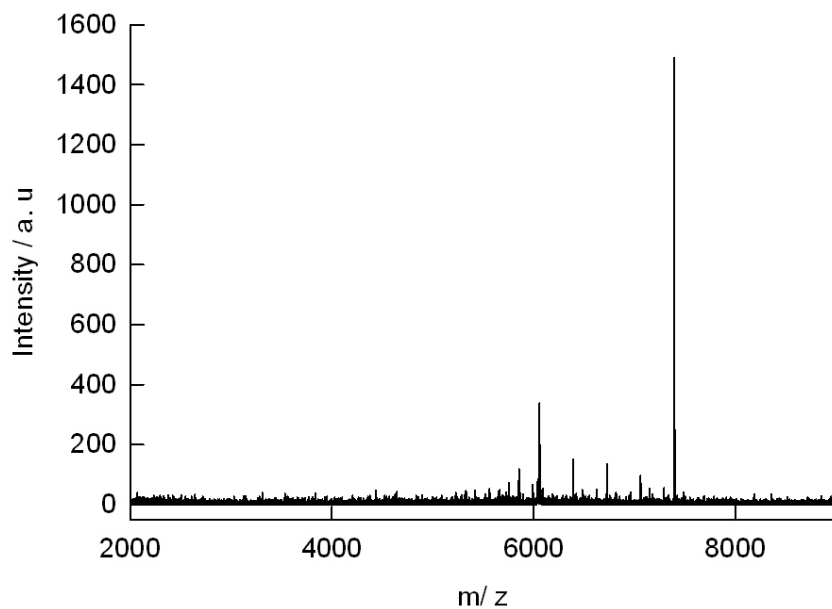


Figure S6.6. MALDI spectrum of $\text{Au}_{25}(\text{SC}_2\text{H}_4\text{Ph})_{18}^+ \text{C}_6\text{F}_5\text{CO}_2^-$, 1000:0.2 matrix/analyte, negative reflector mode.

ECL Data

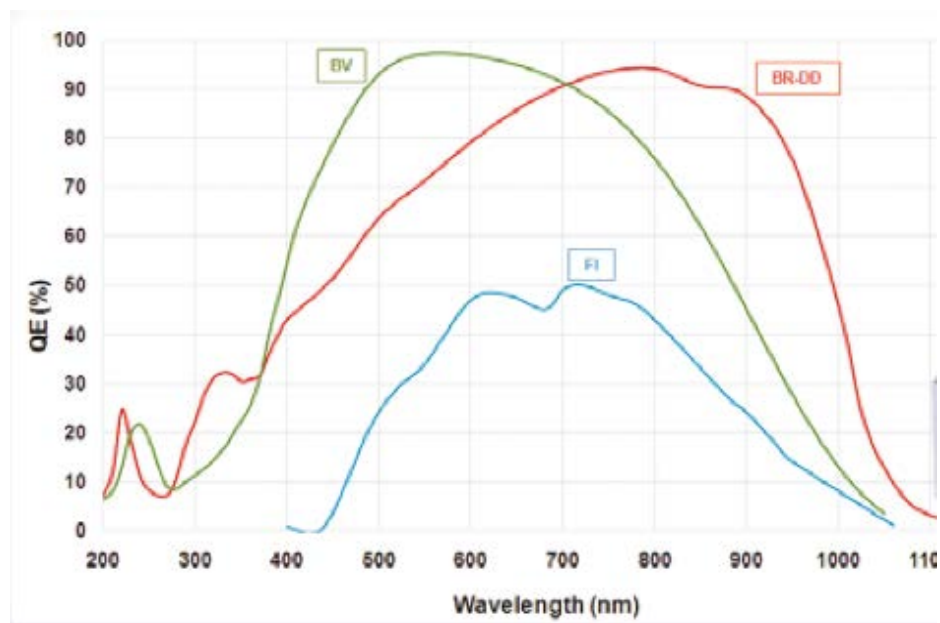


Figure S6.7. The iDus CCD camera response curve (BR-DD, red).

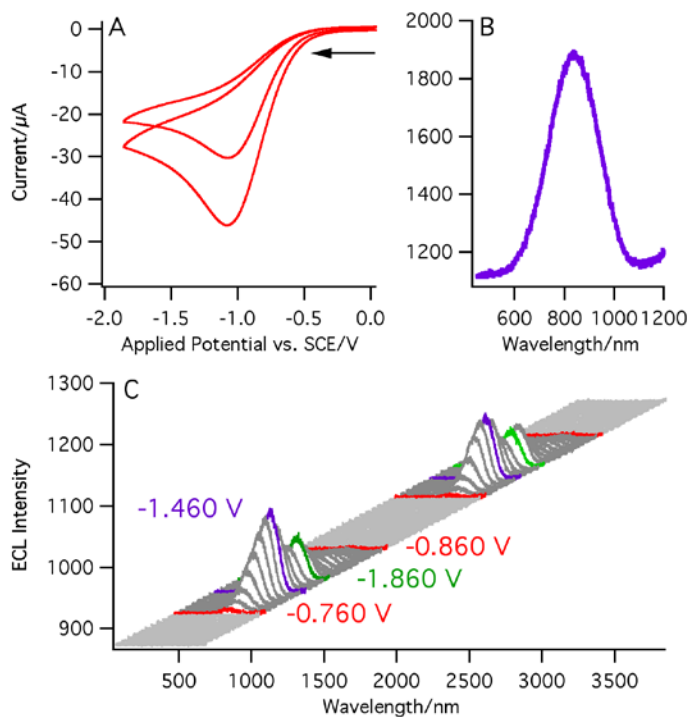


Figure S6.8. a) CV with BPO during two cycles of applied potential sweeping from 0.04 to -1.86 V then back to 0.04 V. b) A typical accumulated ECL spectrum of the same coreactant solution and CV collected over 80 s, two cycles, when scanning the potential between 0.04 to -1.86 V at a scan rate of 0.1 V/s. c) Spooled ECL spectra of Au_{25}^+ clusters with BPO during a sweep of the applied potential from 0.04 to -1.86 V then back to 0.04 V, for two cycles. Each spectrum was acquired for 1 s using an i-DUS NIR CCD camera cooled to $-75\text{ }^\circ\text{C}$.

PL Spectroscopy

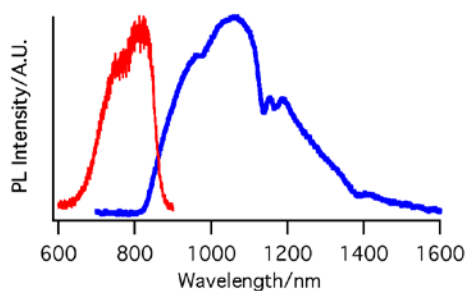


Figure S6.9. Photoluminescence of a Au_{25}^- 1:1 benzene/acetonitrile solution using a R928 PMT detector in wavelength range between 600 and 900 nm (red), and an InGaAs detector between 700 and 1600 nm (blue). The sample was excited at 480 nm.

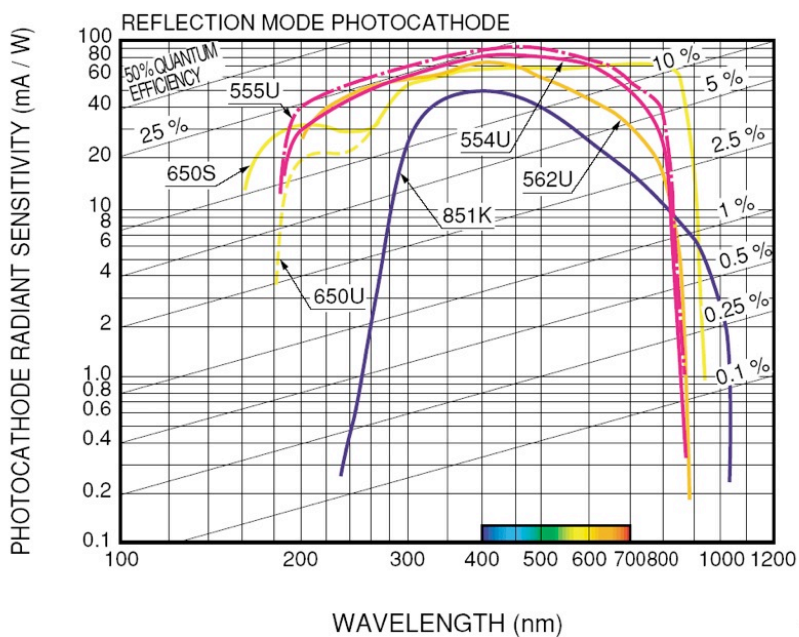


Figure S6.10. The spectral response curve, 562U for Hamamatsu R928 PMT used in our PL spectrometer.

▣ Spectral response

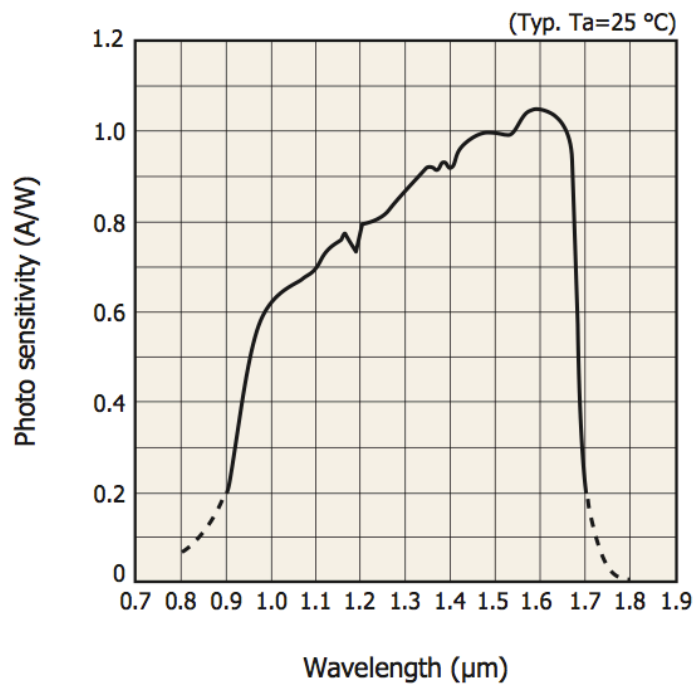


Figure S6.11. Hamamatsu InGaAs PIN photodiode spectral response curve.

Photoluminescence spectroscopy, Figure S6.9 was carried out on a PTI spectrometer equipped with both visible PMT and NIR InGaAs detectors. The PMT and InGaAs spectral response curves are illustrated in Figure S6.10 (curve 562U) and S6.11. Since in the PL spectrometer utilized, the PMT detector does not respond well after 830 nm (less than 1% in QE, Figure S6.10) and neither does the InGaAs detector before 850 nm (Figure S6.11), there is some misgiven PL intensity pattern in the PL spectra obtained in Figure S6.9. That is probably the case in the literature.

NIR PL Spectroscopy

NIR photoluminescence spectroscopy was conducted on a confocal microscope (Alpha SNOM, WITec, Germany) under ambient conditions. A He-Neon polarized laser with a 633 nm wavelength was used for excitation. A 50X objective with 10 mm focus length (Nikon Canada, Mississauga) was used to focus the laser beam onto the Au cluster solution and collect PL signals. An edge filter (RazorEdge filters from Semrock, NY) with band pass $> 160 \text{ nm}^{-1}$ was used to block the 633 nm excitation laser. A complete PL spectrum was recorded the iDUS CCD camera air-cooled at $-75 \text{ }^\circ\text{C}$, behind the grating of 300 l mm^{-1} spectrograph (Acton 2300i).

The CCD camera response QE is higher than 90% to the wavelength between 600 and 900 nm, while the PL peak intensity at 1080 nm is a couple of orders lower in addition to the detect response QE being less than 10%, Figure S6.7.

CVs and ECL-Voltage Curves in the Annihilation Path

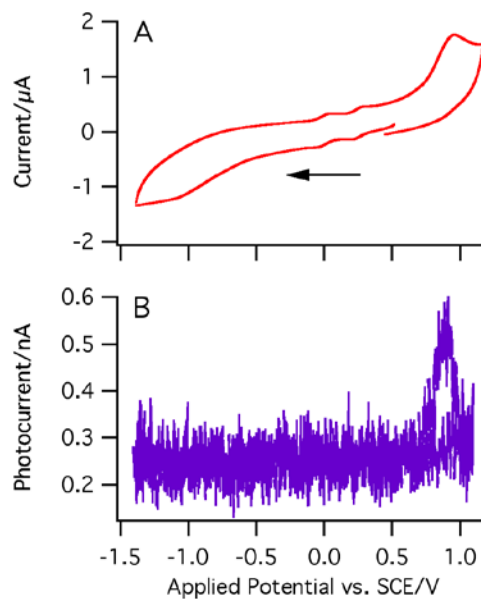


Figure S6.12. Cyclic voltammogram (A) and ECL-voltage curve (B) of Au_{25}^+ clusters in 1:1 benzene/acetonitrile solution at a scan rate of 0.1 V/s in the potential range of 1.16 and -1.38 V.

CVs and ECL-Voltage Curves of a Blank Solution with 5 mM BPO Solution

No ECL was observed in the absence of Au_{25}^+ clusters with the BPO electrolyte solution in the same potential range.

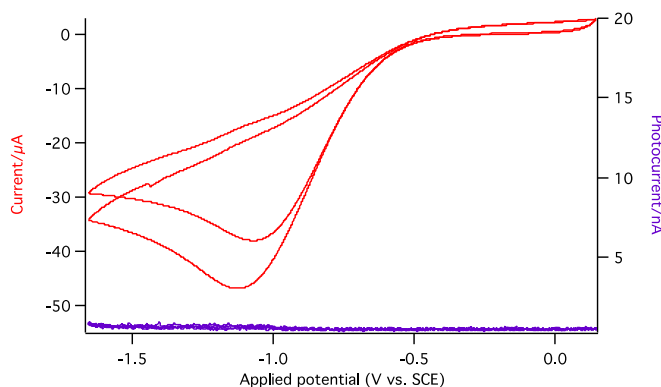


Figure S6.13. Cyclic voltammograms and ECL-voltage curves of a blank solution with 5 mM BPO solution containing 0.1 M TBAP. Other experimental conditions are the same as in Figure 6.1b.

Calculations of PL Quantum Yield for Au₂₅⁻

Relative PL quantum efficiency of the Au₂₅⁻ was estimated by comparing the integrated PL intensities and the absorbance value of the Au₂₅⁻ sample with the reference of relative to [Ru(bpy)₂]²⁺.⁸ The calculation was done according the following equation:⁹

$$\Phi_x = 100 n_x^2 \left(\frac{\int_a^b PL d\lambda}{\int_a^b Ab d\lambda} \right)_x / n_{St}^2 \left(\frac{\int_a^b PL d\lambda}{\int_a^b Ab d\lambda} \right)_{St}$$

where Φ is the quantum yield (%) relative to references, PL is the PL intensity, Ab is the absorbance value, St represents the standard and x stands for the sample, n_x is diffractive index of sample and n_{St} is diffractive index of standard solvent. Here both are the same. The relative PL efficiency value for Au₂₅⁻ is 2.6%, equivalent to an absolute efficiency value of 0.20%, given that the [Ru(bpy)₂]²⁺ PL efficiency is 7.5%.⁸

References

- (1) Dass, A.; Stevenson, A.; Dubay, G. R.; Tracy, J. B.; Murray, R. W. *J. Am. Chem. Soc.* **2008**, *130*, 5940.
- (2) Parker, J. F.; Fields-Zinna, C. A.; Murray, R. W. *Acc. Chem. Res.* **2010**, *43*, 1289.
- (3) Venzo, A.; Antonello, S.; Gascon, J. A.; Guryanov, I.; Leapman, R. D.; Perera, N. V.; Sousa, A.; Zamuner, M.; Zanella, A.; Maran, F. *Anal. Chem.* **2011**, *83*, 6355.
- (4) Antonello, S.; Hesari, M.; Polo, F.; Maran, F. *Nanoscale* **2012**, *4*, 5333.
- (5) Heaven, M. W.; Dass, A.; White, P. S.; Holt, K. M.; Murray, R. W. *J. Am. Chem. Soc.* **2008**, *130*, 3754.
- (6) Zhu, M.; Aikens, C. M.; Hollander, F. J.; Schatz, G. C.; Jin, R. *J. Am. Chem. Soc.* **2008**, *130*, 5883.
- (7) Barson, C. A.; Wisdom, R. A. *Eur. Polym. J.* **1972**, *8*, 1139.
- (8) Wallace, W. L.; Bard, A. J. *J. Phys. Chem.* **1979**, *83*, 1350.
- (9) Booker, C.; Wang, X.; Haroun, S.; Zhou, J.; Jennings, M.; Pagenkopf, B. L.; Ding, Z. *Angew. Chem. Int. Ed.* **2008**, *47*, 7731.

Title: Interrogating Near-Infrared Electrogenerated Chemiluminescence of $\text{Au}_{25}(\text{SC}_2\text{H}_4\text{Ph})_{18}^+$ Clusters

Author: Kalen N. Swanick, Mahdi Hesari, Mark S. Workentin, and Zhifeng Ding

Publication: Journal of the American Chemical Society

Publisher: American Chemical Society **Date:** Sep 1, 2012

Copyright © 2012, American Chemical Society

PERMISSION/LICENSE IS GRANTED FOR YOUR ORDER AT NO CHARGE

This type of permission/license, instead of the standard Terms & Conditions, is sent to you because no fee is being charged for your order. Please note the following:

Permission is granted for your request in both print and electronic formats, and translations. If figures and/or tables were requested, they may be adapted or used in part. Please print this page for your records and send a copy of it to your publisher/graduate school.

Appropriate credit for the requested material should be given as follows: "Reprinted (adapted) with permission from (COMPLETE REFERENCE CITATION). Copyright (YEAR) American Chemical Society." Insert appropriate information in place of the capitalized words.

One-time permission is granted only for the use specified in your request. No additional uses are granted (such as derivative works or other editions). For any other uses, please submit a new request.

Chapter 6.2: Spooling ECL Spectroscopy of $\text{Au}_{25}\text{L}_{18}^0$ in the presence of BPO

Materials and Methods for Synthesis and Characterization of $\text{Au}_{25}(\text{SCH}_2\text{CH}_2\text{Ph})_{18}^0$

Chemicals. Tetrachloroaurate (III) trihydrate, sodium borohydrate, ethanol, dichloromethane, tri-propylamine, benzoyl peroxide, dry acetonitrile and dry benzene purchased from Aldrich. Tetrahydrofurane was provided from Caledon. Ethanol was provided by Commercial alcohol. Tetra-*n*-butylammonium perchlorate (TBAP) electrolyte purchased from Fluka.

Synthesis. $\text{HAuCl}_4 \cdot 3\text{H}_2\text{O}$, 1.02 g dissolved in 100 mL tetrahydrofurane in a tri-neck rounded flask. The solution was cooled using ice-bath and 2.1 mL phenylethane thiol was added to the solution under slow stirring. The yellowish solution color was turned to colorless within next 45 minutes. At this point, 998 mg NaBH_4 was dissolved to 20 mL ice-cold water and added to the mixture all at once under vigorous stirring. The dark solution was formed upon reducing agent addition, indication of large nanoparticle formation. The mixture stirred for 4-5 days to complete aging step. Then, the sample was gravity filtered and solvent volume reduced yields an oily product. The excess of sodium borohydride and capping thiol was removed by washing with water/ethanol mixture. Purity of sample was examined *via* UV-vis spectroscopy, $^1\text{HNMR}$ spectroscopy and mass spectrometry.

Electrochemistry of Au_{25}^0 during annihilation process. Figure S6.14 shows cyclic voltammogram (CV) and differential pulse voltammograms of 0.1mM Au_{25}^0 at a Pt disk working electrode in 1:1 benzene:acetonitrile mixture containing 0.1 M tetra-*n*-butylammonium perchlorate (TBAP) as supporting electrolyte. Coiled platinum wires served as counter and reference electrodes. The electrochemistry of $\text{Au}_{25}\text{L}_{18}^z$ (where L= $\text{HSC}_2\text{H}_4\text{Ph}$, $\text{HSC}_6\text{H}_{13}$, $z = -1, 0$ and $1+$) clusters have been well investigated and documented.¹⁻³

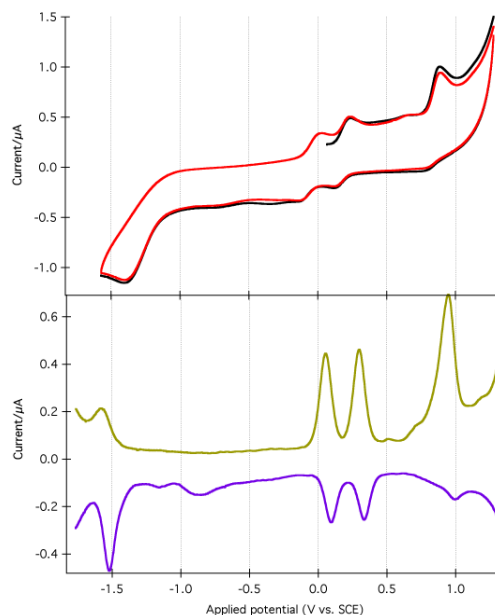


Figure S6.14. Cyclic voltammograms (the black and red lines are indication of 1st and 2nd scans) and differential pulse voltammograms (the yellow and purple curves are indication as oxidation and reduction scans) of Au₂₅⁰ in 1:1 benzene:acetonitrile, 0.1 M TBAP as supporting electrolyte, scan rate: 0.1 V/s.

Spectroscopy and photoelectrochemistry

UV-vis-NIR spectrum of 0.016 mM of Au₂₅(SC₂H₄Ph)₁₈⁰ was recorded using a Varian Cary 5G absorption spectrometer in the wavelength range of 300-1300 nm (4.13-0.95 eV).

The electrochemistry and ECL experiments carried out in a 25 cm glass cylinder equipped with a quartz window at the bottom. The conventional three-electrode system has been employed, a 2 mm home-made platinum disk and Pt coils served as working, reference and counter electrodes, respectively. The ECL set-up and instrumentation details have been published elsewhere.³

In a typical ECL cell set-up 0.1 mM Au₂₅(SC₂H₄Ph)₁₈⁰ dissolved in 1:1 benzene:acetonitrile mixture. A CHI610a electrochemical workstation coupled with a photomultiplier tube (PMT) has been used to record the ECL-voltage. The recorded photocurrent transformed to a voltage signal, using a picoammeter/voltage source (Keithley 6487, Cleveland, OH). The potential, current signals from the electrochemical workstation, and the photocurrent signal from the picoammeter were sent simultaneously through a DAQ board (DAQ 6052E, National Instruments, Austin, TX) in a computer. The data acquisition system was controlled from a custom-made LabVIEW program (ECL_PMT610a.vi, National Instruments, Austin, TX). The photosensitivity on the picoammeter was set manually in order to avoid the saturation.

The intensities versus wavelengths (ECL spectra) were recorded by Andor Technology program. Similar to the CV experiments, the samples were scanned between their redox potentials. Since the ECL is in NIR region, ECL spectroscopy was conducted on an Acton 2300i spectrograph with two gratings (50 l/mm blazed at 600 nm and 300 l/mm blazed at 700 nm) and an Andor iDUS CCD camera (Model DU401-BR-DD-352), see Figure S6.7.

To calibrate the cyclic voltammograms, before running the experiment at each BPO concentration, the two quasi-reversible redox waves of the Au₂₅ in the middle of potential window ($E_{pa}^0 = 0.185$ and $E_{pc}^0 = -0.065$ V vs. SCE) were recorded as an internal standard. Then, ferrocene was added to the solution to calibrate peak potentials vs. SCE ($E^0_{(Fc/Fc^+)} = 0.424$ V vs. SCE in acetonitrile: benzene 1:1) after each ECL experiment.⁴

ECL Data

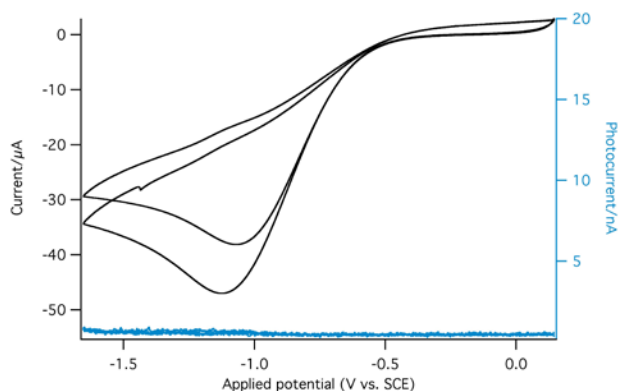


Figure S6.15. ECL-voltage curve of 0.005 M BPO blank solution in ACN:Bz (1:1), with 0.1 M TBAP supporting electrolyte, scan rate of 0.1 V/s, T = 25°C.

References

- (1) Lee, D.; Donkers, R. L.; Wang, G.; Harper, A. S.; Murray, R. W. *J. Am. Chem. Soc.* **2004**, *126*, 6193.
- (2) Garcia-Raya, D.; Madueno, R.; Blazquez, M.; Pineda, T. *J. Phys. Chem. C* **2009**, *113*, 8756.
- (3) Swanick, K. N.; Hesari, M.; Workentin, M. S.; Ding, Z. *J. Am. Chem. Soc.* **2012**, *134*, 15205.
- (4) Cao, W.; Zhang, X.; Bard, A. J. *J. Electroanal. Chem.* **2004**, *566*, 409.

Curriculum Vitae

Name: Kalen N. Swanick

Post-secondary Education and Degrees: The University of Western Ontario
London, Ontario, Canada
2003-2008 B.Sc. with Honors in Chemistry, Minor in Psychology

The University of Western Ontario
London, Ontario, Canada
2008-2013 Ph.D.

Honours and Awards: Western Graduate Research Scholarship (WGRS)
2010-2013

Related Work Experience: Teaching Assistant
The University of Western Ontario
2008-2013

Publications:

“Correlating Electronic Structures to Electrochemiluminescence of Cationic Ir Complexes” Kalen N. Swanick, Sébastien Ladouceur, Eli Zysman-Colman, and Zhifeng Ding, **2013**, submitted.

“Electrochemiluminescence of Heterometallic Ruthenium(II)-Iridium(III) Soft Salts” Kalen N. Swanick, Martina Sandroni, Zhifeng Ding and Eli Zysman-Colman, **2013**, submitted.

“Strongly Blue Luminescent Cationic Iridium(III) Complexes with an Electron-rich Ancillary Ligand: Evaluation of their Optoelectronic and Electrochemiluminescence Properties” Sébastien Ladouceur, Kalen N. Swanick, Shawn Gallagher-Duval, Zhifeng Ding and Eli Zysman-Colman, *Eur. J. Inorg. Chem.*, **2013**, accepted, DOI: 10.1002/ejic.201300849.

“Self-Enhanced Electrochemiluminescence of an Iridium(III) Complex: Mechanistic Insight” Kalen N. Swanick, Sébastien Ladouceur, Eli Zysman-Colman, and Zhifeng Ding, *Angew. Chem. Int. Ed.*, **2012**, *51*, 11079-11082.

“Interrogating the Near-infrared Electrogenerated Chemiluminescence of $\text{Au}_{25}(\text{SC}_2\text{H}_4\text{Ph})_{18}^+$ Clusters” Kalen N. Swanick, Mahdi Hesari, Mark S. Workentin and Zhifeng Ding, *J. Am. Chem. Soc.*, **2012**, *134*, 15205-15208.

“Synthesis, Structure, Electrochemistry, and Electrochemiluminescence of Thienyltriazoles” Kalen N. Swanick, Jacquelyn T. Price, Nathan D. Jones, and Zhifeng Ding, *J. Org. Chem.*, **2012**, *77*, 5646-5655.

“Bright electrochemiluminescence of iridium(III) complexes” Kalen N. Swanick, Sébastien Ladouceur, Eli Zysman-Colman, and Zhifeng Ding, *Chem. Commun.*, **2012**, *48*, 3179-3181.

“Electrogenerated chemiluminescence of iridium(III) complexes” Kalen N. Swanick, Sébastien Ladouceur, Eli, Zysman-Colman, and Zhifeng Ding, *Luminescence*, **2012**, *27*, 162-163.

“Electrogenerated chemiluminescence of triazole-modified deoxycytidine analogues in N,N-dimethylformamide” Kalen N. Swanick, David W. Dodd, Jacquelyn T. Price, Allison L. Brazeau, Nathan D. Jones, Robert H.E. Hudson, and Zhifeng Ding, *Phys. Chem. Chem. Phys.*, **2011**, *13*, 17405-17412.

“A multi-channel sensor based on 8-hydroxyquinoline ferrocenoate for probing Hg(II) ion” Lei Shi, Wei Song, Yang Li, Da-Wei Li, Kalen N. Swanick, Zhifeng Ding, Yi-Tao Long, *Talanta*, **2011**, *84*, 900–904.

“Blue fluorescent deoxycytidine analogues: convergent synthesis, solid-state and electronic structure, and solvatochromism” D.W. Dodd, K.N. Swanick, J.T. Price, A.L. Brazeau, M.J. Ferguson, N.D. Jones, R.H.E. Hudson, *Org. Biomol. Chem.*, **2010**, *8*, 663-666.

Conferences Presentations:

“Electrochemiluminescence of a Heterometallic Ion Pair” Kalen N. Swanick, Martina Sandroni, Eli Zysman-Colman, and Zhifeng Ding, Surface Canada 2013, University Community Centre, Western University, London ON, Canada. May 08, **2013** (poster).

“Electrochemiluminescence of a Heterometallic Ion Pair” Kalen N. Swanick, Martina Sandroni, Eli Zysman-Colman, and Zhifeng Ding, 4th Georgian Bay International Conference on Bioinorganic Chemistry (CanBIC), Charles W. Stockey Centre, Parry Sound, ON. May 23, **2013** (poster).

“Electrochemiluminescence of Bright Cationic Iridium(III) Complexes” Kalen N. Swanick, Sébastien Ladouceur, Eli Zysman-Colman, and Zhifeng Ding, CAMBR Distinguished Lecturer and Research Day, University Community Centre, Western University, London ON, Canada. November 13, **2012** (oral).

“Near-Infrared Electrochemiluminescence of Au₂₅ Clusters” Kalen N. Swanick, Mahdi Hesari, Mark S. Workentin and Zhifeng Ding, 63rd Annual Meeting of the International Society of Electrochemistry (ISE) 2012, Clarion Congress Hotel, Prague, Czech Republic. August 21, **2012** (oral).

“Synthesis, Structure, Electrochemistry and Electrochemiluminescence of Thienyltriazoles” Kalen N. Swanick, Jacquelyn T. Price, Nathan D. Jones, Zhifeng Ding, 39th Ontario-Québec Physical Organic Mini-Symposium (POMS), The University of Western Ontario, London, ON. November 06, **2011** (oral).

“Efficient Electrogenenerated Chemiluminescence of Polyfluorenes” K.N. Swanick, Z. Ding, S.L. McFarlane, L.S. Coumont, J.G.C. Veinot, 94th Canadian Chemistry Conference and Exhibition, Palais des congrès de Montréal, Montréal, QC. June 02, **2011** (oral).

“Electrogenenerated chemiluminescence of dissymmetric siloles” Kalen N. Swanick, Mahmoud Moustafa, Brian L. Pagenkopf, Zhifeng Ding, 3rd Georgian Bay International Conference on Bioinorganic Chemistry (CanBIC), Charles W. Stockey Centre, Parry Sound, ON. June 09, **2011** (poster).

“Thiophene-Containing N,O-Donor Ligands for Metal Complexes” K.N. Swanick, J.T. Price, Z. Ding and N.D. Jones. 2009 IDW, University of Guelph, Guelph, ON. November 28, **2009** (poster)

“Intrinsically Photoluminescent and Electrochemiluminescent Cytidine Analogs Accessed via the Huisgen Cycloaddition” Dodd, D.W., Swanick, K.N., Price, J.T, Brazeau, A.L., Ding, Z., Jones, N.D., Hudson, R.H.E. 92nd Canadian Chemistry Conference and Exhibition, Hamilton Convention Centre, Hamilton, ON. May 31, **2009** (oral). David W. Dodd received the "Nucleic Acids Presentation Award (oral)" from the organizers of the Nucleic Acids Symposium.

“A new class of fluorophore-labelled nucleobases for electrogenerated chemiluminescence” Kalen N. Swanick, David W. Dodd, Robert H.E. Hudson, Zhifeng Ding, Nathan D. Jones. QOMSBOC 2008, University of Toronto, Toronto, ON. November 08, **2008** (poster)

“Modified Cytosine Nucleobases for Biosensing Applications” Kalen N. Swanick, R.H.E. Hudson and N.D. Jones. 36th Annual Southern Ontario Undergraduate Student Chemistry Conference, Queen’s University, Kingston, ON. March 15, **2008** (oral)